



HAL
open science

Microwaves as a probe of quantum dot circuits : from Kondo dynamics to mesoscopic quantum electrodynamics

Laure Bruhat

► **To cite this version:**

Laure Bruhat. Microwaves as a probe of quantum dot circuits : from Kondo dynamics to mesoscopic quantum electrodynamics. Physics [physics]. Université Paris sciences et lettres, 2016. English. NNT : 2016PSLEE012 . tel-01430414

HAL Id: tel-01430414

<https://theses.hal.science/tel-01430414>

Submitted on 9 Jan 2017

HAL is a multi-disciplinary open access archive for the deposit and dissemination of scientific research documents, whether they are published or not. The documents may come from teaching and research institutions in France or abroad, or from public or private research centers.

L'archive ouverte pluridisciplinaire **HAL**, est destinée au dépôt et à la diffusion de documents scientifiques de niveau recherche, publiés ou non, émanant des établissements d'enseignement et de recherche français ou étrangers, des laboratoires publics ou privés.

THÈSE DE DOCTORAT
de l'Université de recherche
Paris Sciences Lettres –
PSL Research University

préparée à
l'École normale supérieure

Microwaves as a probe
of quantum dot circuits:
from Kondo dynamics to
mesoscopic quantum
electrodynamics

par Laure Bruhat

École doctorale n°564
Spécialité: Physique
Soutenue le 01.04.2016

Composition du Jury :

M. Silvano DE FRANCESCHI
CEA Grenoble
Rapporteur

M. Christian SCHÖNENBERGER
University of Basel
Rapporteur

M. Leonid GLAZMAN
Yale University
Examineur

M. Hugues POTHIER
CEA Saclay
Examineur

M. Jean-Michel RAIMOND
Collège de France
Examineur

M. Takis KONTOS
Ecole Normale Supérieure
Directeur de thèse

Mme. Audrey COTTET
École normale supérieure
Membre invité

Abstract

This thesis uses microwaves as probe of carbon nanotube quantum dot circuits. In a first experiment, a microwave excitation is directly applied to a circuit electrode for a quantum dot in the Kondo regime. We provide the first frequency-amplitude characterisation of the Kondo zero-bias conductance. Preliminary data are consistent with predicted universal behaviour. We present two other experiments, where quantum dot circuits are embedded in microwave resonators. Cavity photons probe charge relaxation resistance and photon emission in a quantum dot coupled to normal and superconducting reservoirs in presence of Coulomb repulsion. Our observations validate a modelling in terms of the circuit linear response. We also present the first implementation of a Cooper pair splitter in cavity. The strong coupling regime is achieved, a premiere with quantum dot circuits. Our findings support the idea, that mesoscopic quantum electrodynamics is a fruitful toolbox in the context of both fields of quantum transport and quantum information science.

Key words: Carbon nanotube quantum dots; Cavity quantum electrodynamics; Kondo effect; Charge relaxation resistance; Photon-assisted tunnelling; Cooper pair splitter.

Résumé

Cette thèse utilise les micro-ondes pour étudier des circuits de boîtes quantiques à base de nanotubes de carbone. Dans une première expérience, l'excitation micro-onde est appliquée directement sur une électrode du circuit pour une boîte quantique dans le régime Kondo. Nous réalisons la première caractérisation fréquence-amplitude de la conductance Kondo à biais nul. Des données préliminaires sont en accord avec la prédiction de réponse universelle. Nous présentons deux autres expériences, où les boîtes quantiques sont insérées dans des résonateurs micro-ondes. Les photons de la cavité sondent la résistance de relaxation de charge et l'émission de photon dans une boîte quantique couplée à des réservoirs normaux et supraconducteurs, en présence de répulsion coulombienne. Nos observations valident une modélisation en terme de réponse linéaire du circuit. Nous présentons aussi la première implémentation d'une lame séparatrice à paires de Cooper en cavité. Le régime de couplage fort est atteint, une première avec des circuits de boîtes quantiques. Nos résultats renforcent l'idée que l'électrodynamique quantique mésoscopique est une boîte à outils fructueuse, aussi bien dans le contexte du domaine du transport quantique que dans celui de l'information quantique.

Mots clés : Boîtes quantiques en nanotubes de carbone ; Electrodynamique quantique en cavité ; Effet Kondo ; Résistance de relaxation de charge ; Effet tunnel photo-assisté ; Lame séparatrice à paires de Cooper.

Acknowledgements

Let me first thank the committee members for agreeing to review this work. I will write the full acknowledgement section after the defence.

Contents

	Page
Abstract	ii
Acknowledgements	iii
Acronyms and notations	1
Introduction	4
1 Quantum transport in quantum dot circuits	15
1.1 Transport phenomenology in quantum dots	16
1.1.1 Energy scales	16
1.1.2 Transport regimes	18
1.2 "Closed" quantum dots	20
1.2.1 Coulomb blockade	20
1.2.2 Double quantum dots as qubits	25
1.3 Kondo physics	29
1.3.1 From Anderson model to Kondo physics	30
1.3.2 Kondo resonance conductance and universality	32
1.4 Quantum dot circuits with superconducting contacts	33
1.4.1 Proximity effect in a quantum dot	35
1.4.2 Cooper pair splitter	38
2 cQED architecture as a probe of dynamics of mesoscopic systems	42
2.1 Microwave response of mesoscopic circuits	43
2.1.1 Universal charge relaxation	44
2.1.2 Dynamics of Kondo physics	45
2.1.3 ABS spectroscopy	45
2.2 Mesoscopic circuit QED	46
2.2.1 Cavity description : Input-output theory	46
2.2.2 Different coupling schemes to the cavity electromagnetic field	48
2.2.3 Dissipationless description of a superconducting qubit-cavity system	50
2.2.4 Mesoscopic circuit QED experiments	53
2.3 Linear response of circuit to microwave field	55
2.3.1 Cavity transmission in the circuit linear response regime	55
2.3.2 Adiabatic limit	56

2.4	Master equation treatment of coherent coupling between cavity and circuit electronic transitions	57
2.4.1	Isolated two-level system	57
2.4.2	Case of a three-level system in a ladder geometry	59
3	Experimental methods	61
3.1	Nanofabrication	62
3.1.1	Sample description and outlook of the fabrication process	62
3.1.2	Sample cleaning	64
3.1.3	Patterning of gold alignment crosses, contacting pads and sample number	65
3.1.4	Niobium coplanar wave-guide resonator and circuit bonding pads and precontacts	66
3.1.5	Carbon nanotube stamping	67
3.1.6	Patterning of the device electrodes	71
3.1.7	Sample mounting and wire-bonding	71
3.2	Measurement setup	72
3.2.1	Cryogenics	72
3.2.2	DC measurements	78
3.2.3	Microwave measurements	80
4	Dynamics of Kondo effect at finite frequency	83
4.1	Predictions and existing measurements on Kondo dynamics	84
4.2	Kondo phenomenology	85
4.2.1	Sample	85
4.2.2	Resonance in absence of excitation	86
4.2.3	Phenomenology under microwave excitation	87
4.3	Power-frequency dependance of Kondo conductance peak under microwave excitation	88
4.3.1	In situ microwave amplitude calibration	88
4.3.2	Scaled amplitude-frequency conductance map	90
4.3.3	Ansatz proposed for quantitative analysis	92
4.4	Test of universality	93
5	Charge dynamics of a single level coupled to fermionic reservoirs	96
5.1	An S-QD-N device embedded in a microwave resonator	97
5.2	Equilibrium charge dynamics in a N-dot junction at finite frequency	99
5.2.1	Cavity signals as a probe of charge susceptibility	99
5.2.2	Investigation of charge relaxation universality	101
5.3	Non equilibrium charge dynamics in an S-dot-N bijunction	104
5.3.1	Crossed measurement of dot conductance and cavity response	104
5.3.2	Photon-assisted tunnelling between a dot and a superconductor	107
5.4	Summary and discussion	108
6	Strong coupling of a Cooper pair splitter to cavity photons	111
6.1	Sample and setup	112
6.2	DC transport	113
6.3	Cavity response	115

6.3.1	Resonant behaviour	115
6.3.2	Strong coupling	117
6.4	Preliminary microscopic interpretation	118
6.4.1	Three-level ladder scenario	118
6.4.2	Sub-gap transitions	120
Conclusion and perspectives		122
A	QD-S and splitter effective hamiltonian	125
A.1	Schrieffer-Wolff transformation	125
A.2	S-QD device	126
A.3	Cooper pair splitter	128
B	Nanofabrication processes	129
B.1	CPSRES fabrication roadmap	129
B.2	Quartz stamps with CNT fabrication	130
B.3	Nb cavity fabrication	132
B.4	CNT stamping	132
C	Photon number evaluation	134
C.1	Input power P_{in} calibration	134
C.2	Output power P_{out} calibration	137
C.3	Photon number	141
D	Supplementary materials on AC Kondo	143
D.1	Raw data description	143
D.2	Power calibration and frequency set	143
D.3	Data extraction and scaling	146
E	Supplementary materials on charge relaxation	148
E.1	Experimental supplementary	148
E.2	Theoretical supplementary	150
Bibliography		154

Acronyms

AC	Alternative current
ABS	Andreev Bound States
AFM	Atomic force microscope
B/AB	Bonding/Anti-bonding
CNT	Carbon nanotube
CPS	Cooper pair splitter
CPW	Coplanar waveguide
cQED	Circuit quantum electrodynamics
CQED	Cavity quantum electrodynamics
CVD	Chemical vapour deposition
DC	Direct current
DOS	Density of states
DQD	Double quantum dot
ENS	Ecole Normale Superieure
FWHM	Full width at half maximum
IF	Intermediate frequency
IPA	Isopropanol
LO	Local oscillator
MC	Mixing chamber
MIBK	Methyl-iso-butyl ketone
MW	Microwave
NMR	Nuclear magnetic resonance
NW	Nanowire
PAT	Photon-assisted tunnelling
PCB	Printed circuit board
PMMA	Poly methyl methacrylate
QD	Quantum dot
QED	Quantum electrodynamics
RF	Radio frequency
RIE	Reactive ion etching
RMS	Root mean square
RWA	Rotating wave approximation
SEM	Scanning electron microscope
SIS	Superconductor-Insulator-Superconductor
SMA	SubMiniature version A (microwave connector norm)
SWNT	Single wall carbon nanotube
UHV	Ultra high vacuum
UV	Ultra-violet
VNA	Vectorial network analyser
2DEG	Two-dimensional electron gas

Notations

α_g	Capacitive lever-arm of gate electrode on dot
Δ	Superconducting gap
Δ_E	Energy level spacing in a dot
Δ_{cd}	Frequency detuning between cavity and drive frequency
Δ_{qd}	Frequency detuning between qubit and drive frequency
ϵ_0	Vacuum dielectric permittivity (unless specified)
ϵ_i	Energy of the dot bare energy level i
ϵ_d	Dressed orbital level in the single level case
ϵ_δ	Energy detuning between the dots of the double quantum dot
ϵ_Σ	Energy direction perpendicular to ϵ_{delta} , (average energy of the two dots)
ϵ_{in}	Driving amplitude at the input of the cavity
γ	Relaxation rate of a qubit
Γ	Sum of tunnelling energies between dot and left and right leads
$\tilde{\Gamma}_i$	$\Gamma_{L/R}$ Tunnelling energy between dot and lead i, dressed by the Fermi distribution in the lead.
$\Gamma_{N/S}$	Tunnelling rate between dot and normal/superconducting lead
Γ_2	Decoherence rate of a qubit (inverse of T_2^*)
Γ_ϕ	Pure dephasing rate of a qubit
λ	Wavelength
Λ_0	Half of κ (half-FWHM of square amplitude for a bare cavity pulsation spectrum)
$\Delta\Lambda_0$	Cavity linewidth shift (change in Λ_0 induced by the circuit)
κ	Cavity decay rate (or bandwidth)
κ_i	Cavity decay rate due to loss at the port i of the cavity
$\mu(N)$	Electrochemical potential of dot with N electrons
$\mu_{L/R}$	Electrochemical potential of left/right lead
μ_B	Bohr magneton
ν	Density of states in a normal lead (unless specified)
χ	Charge susceptibility of a dot single-level
χ_{qb}	Susceptibility of qubit coupled to the resonator (a nought index refers to ground state)
φ	Microwave phase
$\Delta\varphi$	Microwave phase variation induced by the circuit
Ω	Larmor frequency of a qubit
ω_c	Cavity resonance pulsation (ω_0 in chapter 5)
$\Delta\omega_0$	Cavity pulsation shift induced by the circuit with respect to bare cavity
ω_d	Cavity drive pulsation (ω_{RF} in chapter 5)

A	Amplitude of microwave transmitted signal
A_0	Amplitude of transmitted signal for a bare cavity
ΔA	Change in amplitude induced by the circuit with respect to bare cavity
\hat{a}	Photonic field annihilation operator
B	Magnetic field
ΔB_z^{nuc}	Zeeman energy difference between left and right dot, caused by nuclear spins
C_g	Capacitance from dot d to its local gate
$C_{L/R}$	Capacitance from dot d to left/right lead
C_m	Capacitance between two coupled dots
C_Σ	Sum of all capacitances on dot d
e	Electron charge
$E_{add}(N)$	addition energy in the N -electron ground state (so to add electron $N+1$)
f_c	Cavity fundamental mode frequency
Δf_{-3dB}	FWHM of square amplitude, or equivalently width of transmitted signal at -3dB, for a bare cavity frequency spectrum
g	Coupling strength between cavity and qubit, or cavity and a dot single-orbital
g_i	Coupling to cavity field of the dot orbital i (level modulation)
G	Differential conductance through the device
G_Q	Conductance quantum
$G_{ON/OFF}$	Kondo conductance with/without microwave excitation
h	Planck constant
I	Current through the device; cavity field quadrature
\tilde{I}	Current calculated from numerical integration of the conductance
J	Energy separation between singlet S and spin 0 triplet T_0 , called exchange coupling
k_B	Boltzmann constant
n_0	Number of photons in a bare cavity at the resonance frequency
n	Cavity average photon number (unless specified)
\hat{n}_i	Charge number operator of level i in a single dot
N	Average number of electrons on the dot (unless specified)
Q	Quality factor; cavity field quadrature
R_{AC}	Quantum charge relaxation resistance
t	inter-dot tunnel coupling; time (unless specified)
t_{eh}	Non-local Cooper pair injection matrix element
t_{ee}^{ind}	Superconducting induced inter-dot tunnel coupling
t_i	tunnelling matrix element between dot and lead i for a single dot
$t_{L/R}$	tunnelling matrix element between superconductor and left/right dot in a CPS
T	temperature; cavity transmission
T_K	Kondo temperature
T_2^*	Coherence time
U	Coulomb charging energy on the dot
U_m	Mutual charging energy between two coupled dots
$V_{g(i)}$	Gate voltage (labelled i)
V_{SD}	Source-drain or bias voltage (V_b in chapter 5)
V_i	Electrical potential on electrode i
V_Σ, V_δ	Axis of the rotated frame $V_{g,L}-V_{g,R}$
V_\perp	Photonic pseudopotential

Introduction

This thesis work lies at the intersection of quantum transport [1], light-matter interaction [2] and quantum information science [3]. In the following we provide a brief overview of these fields, which does not target exhaustiveness, but rather aims at highlighting the links between this thesis and its larger scientific context.

Quantum transport

Quantum transport refers to the study of electrical circuits, which cannot be described by the classical laws of electronics. Quantum effects typically occur for small ($\sim \mu m$) and cold circuits. Consequently, quantum transport experiments require the fabrication of low-dimensional objects, where at least one of the three object dimensions (height, length, width) is small. Because of their intermediate size between macroscopic and microscopic scales, these circuits are called *mesoscopic*. Experimentally, they are cooled down to cryogenic temperature (below 4K or equivalently below $-269^\circ C$) and usually characterised by electrical current measurements.

Since the 1980s, the diversity of circuits displaying quantum features has constantly broadened, renewing the field. Mesoscopic circuits can be made exclusively out of metals, deposited in layers or wires. A metallic circuit (so-called atomic contact) can even be done by creating a single atom contact between two pieces of metal. Metals can also be used as electrodes, contacting other materials. Semiconductors have been widely used to create two-dimensional electron gas (a plane where electrons can move), semiconducting wires and self-assembled quantum dots. Molecule-based circuits have been studied, in particular using carbon structures like fullerenes and carbon nanotubes. Another carbon-based material, graphene, is the archetype of single- or few-atomic-layer thick materials, which are a current active research topic. Quantum transport studies in other recently discovered materials (e.g. topological insulators, oxide interfaces) are also topical.

Quantum transport is not only characterised by a large variety of circuits but also of phenomena. Here we stress two important properties of electrons to understand quantum transport. First, one should think of electrons as waves and not only as particles. Interferences between electronic waves account for several phenomena (e.g. electronic Fabry-Perot, weak/strong localization, Aharonov-Bohm effect), and allows to make quantum optics experiments with electrons instead of photons. A key parameter to quantify the importance of the wavy nature of electrons is the phase coherence length L_φ . This parameter corresponds to the length over which the phase of an electronic wave is preserved. If L_φ is longer than the circuit size, one needs to take the electron wavy nature into account.

Second, the possible states for electrons in low-dimensional objects are constrained. Each electron is described by a unique set of discrete numbers, which values are allowed/forbidden depending on the circuit properties. In a wire, each allowed set of numbers is a channel. The number of channels N in a conductor determines the electrical conductance, a bit like the number of lanes on the highway determines the traffic fluidity. Consequently, the conductance is quantised in integer multiples of the conductance quantum ($G = NG_Q$ with $G_Q = e^2/h$), the hallmark of quantum transport [4].

The variety of quantum transport phenomena is nourished by the variety of electrodes, which can be used in mesoscopic circuits. Indeed, the nature of the circuit metallic elements strongly affects the rules governing electron transport. The use of ferromagnetic metals enables to engineer spin-dependent electronic transport properties, a field called spintronics [5, 6]. The use of superconductors is also broad enough to be a field on its own, called mesoscopic superconductivity. It allows to engineer non-dissipative circuits, the base element being the Josephson junction, which is made of two superconductors separated by a thin oxide layer. The study of superconductors in proximity with various non-superconducting elements has been a long-standing research interest. Chapter 5 and 6 of this thesis fit in this context. Since the 2000's, some circuits based on Josephson junctions appeared as promising in the context of quantum information processing, as reviewed below.

In this thesis, we study a particular class of mesoscopic circuits called quantum dots circuits [7]. Quantum dots are zero-dimensional objects, meaning that their size is reduced in the three spatial dimensions (height, width, length). Quantum dots play the role of electron boxes. They can be realised starting from higher-dimensional objects, provided that electrodes are used to ultimately confine electrons in small volumes. For example we use carbon nanotubes as base material to fabricate our quantum dots circuits [8]. Carbon nanotubes are relatively easily produced and offer the additional advantage of good quantisation of the transverse wave-vector. Because of both their specific crystalline structure and one-dimensional character, they have only four conduction

channels. Quantum dot circuits display most of the quantum transport phenomena mentioned above, with the advantage of parameters tunability, provided by gate electrodes. An important effect, which can be studied in quantum dots, is Kondo physics, one of condensed matter core topic, as it is the simplest situation with many-body interactions. The spin of an electron confined in the quantum dot is interacting with the many electron spins of the contacting electrodes, which models the presence of a magnetic impurity in a metal. This phenomenon is considered in chapter 4. Finally, the fact that electrons in quantum dots have specific states with discrete energies, is a common point with natural atoms and molecules. This explains, why they may be seen as artificial atoms and molecules. Those "atomic-like" energy levels make quantum dots a candidate platform for quantum computing.

More generally, quantum transport can be viewed today as an ensemble of both emerging and mature fields, depending on whether the circuits under study are poorly or exquisitely controlled and understood. If one masters the quantum transport properties of mesoscopic circuits, one can envision exploiting this quantum behaviour to engineer quantum machines. The community of superconducting circuits is currently the most advanced along this path, followed by the quantum dot circuits community. In the next section, we make a rough state of the art of the use of superconducting circuits and quantum dots circuits for quantum information processing. We particularly stress on how these two fields relate to each other.

Solid-state quantum information processing

Quantum algorithms are theoretically more efficient than classical ones to solve certain classes of problems. In particular they are naturally well suited to deal with quantum systems. The base element is a logical qubit, the counterpart of the classical bit, which can be either 0 or 1. In contrast, a qubit is not solely either in $|0\rangle$ or in $|1\rangle$, but it can be in any superposition of the two quantum states $|0\rangle$ and $|1\rangle$. The hardware realisation of logical qubits, which states can be controlled both jointly and separately, has fostered intense research over the last two decades. A logical qubit relies on one or several physical qubits, which are quantum systems with two states (called two-level systems). In practice suitable physical systems may have more states, as long as two of them can be selectively addressed. Historically, experimental quantum information emerged in the late 90's in the Nuclear Magnetic Resonance (NMR) [9] and Atomic Molecular and Optical (AMO) [10] physics communities. Since then, others systems have been proposed and investigated for building physical qubits, like for instance electronic circuits or defects in solid, and the list does not stop there. Before focusing on circuits, which are our system of interest, we want to stress that they are candidates among

many others in the world-wide active research quest for quantum computing. These fields progress in parallel, and feed each other. Superconducting circuits and quantum dots circuits are the two circuit families, which are being investigated for building a solid-state quantum information processing platform, with the advantages of versatility and potential scalability.

Superconducting qubits are based on quantum states of macroscopic electrical quantities, like currents and voltages. The existence of such quantum states with possibly long life times relies on superconductivity special properties. Originally these qubits were controlled by applying electrical microwave pulses on the circuit electrodes. Since 2004 the field has taken over the tools of cavity quantum electrodynamics (CQED)[11], and qubits are now routinely controlled using the microwave photons of superconducting cavities [12]. Historically, CQED developed in atomic physics to study the interaction between a single atom and a single photon in a cavity. These pioneer studies of light-matter interaction at the most elementary level allowed to test fundamental laws of quantum physics [13]. The concepts and methods developed in this framework [14, 15] resulted in exquisite control over quantum individual systems [16], rewarded by Serge Haroche's nobel Prize in 2012. CQED originally inspired its circuit version (labelled cQED), and the two fields remain close in their present development [17–19]. cQED benefits from tunability of qubit frequencies and light-matter coupling strengths, which are fixed by nature for atoms. In addition, nanofabrication techniques enable the more versatile realisation of complex systems, with multiple qubits and cavities. cQED is a very active research field, where progress in microwave quantum optics (e.g quantum-limited detection, single-photon pulse shaping) goes hand-by-hand with a better control over an increasing number of qubits (e.g state stabilization, qubit entanglement). We will see in the last section, that the tremendous success of applying CQED methods to superconducting qubits recently inspired the "neighbour" quantum dot qubit community.

In contrast to superconducting qubits, qubits in quantum dots are based on quantum states of microscopic quantities. In particular the use of electron spins trapped in quantum dots for quantum computing was proposed in 1998 [20], and has been explored experimentally ever since. Indeed the electron spin is a good variable to encode a qubit state, as it has naturally two states (up or down), and is not easily affected by environment charge fluctuations. The other side of the coin is that it is not easily controlled and measured. The manipulation of one qubit involves magnetic and/or electric microwave excitations, and is now well controlled for several qubit types [21]. However, in comparison with superconducting circuits, there is a lack of reliable coupling between two qubits in conventional quantum dots [22–25]. This has only been achieved very recently with quantum dots based on single defects in silicon [26]. In all these experiments, the

coupling between qubits was local and concerned neighbouring spins. This thesis is related to two proposed strategies to couple more distant spins.

First, the use of a superconductor coupled to two dots has been suggested to couple moderately separated spin qubits [27, 28]. In chapter 6, we present an experiment on such a device, the so-called Cooper pair splitter. The principle is to extract a Cooper pair from a central superconducting electrode, and to split the two electrons forming the pair into two separated dots. If the Cooper pair splitter circuit is suitably designed, it is predicted to preserve the entanglement of the split Cooper pairs. Entanglement is the "most quantum" and counter-intuitive property of quantum physics, at the basis of quantum computing efficiency. While distant entangled photons pairs are routinely produced in quantum optics laboratories [29], it is interesting to note that the same has not been achieved with individual electrons, so far. Cooper pair splitters have been studied in quantum transport experiments [30–37] which assessed the splitting of particle pairs, but could not state on injection coherence, nor on spins entanglement.

Alternatively spin qubits could be coupled over macroscopic length scales by using microwave cavity photons as "quantum bus". This strategy is directly inspired by the superconducting qubits community, which improved such cavity-mediated two-qubits coupling since the early demonstration in 2007 [38, 39]. The coupling between distant qubits is one important reason, that originally motivated the study of quantum dots coupled to microwave resonators [40, 41]. Chapters 5 and 6 present some experiments belonging to this new field of mesoscopic QED, which combines mesoscopic circuits and cQED techniques. Along with former experiments, our work supports the idea that mesoscopic QED is a prolific toolbox in the context of both fields of quantum transport and quantum information science, as we discuss in the following section.

Mesoscopic QED

Mesoscopic QED consists in coupling mesoscopic conductors to microwave cavity photons. The field is still emerging, since the original experiments of 2011-2012, where quantum dots [42–44] and a superconductor-insulating-superconductor (SIS) junction [45] were first embedded into microwave cavities. We focus on quantum dots, which are the circuits under study in this thesis. Experiments carried out over the five past years (~ 20) are shortly reviewed in section 2.2.4 of this thesis, and more extensively in the review [46]. Below, we give general arguments, highlighting the diversity of situations, in which cavities presently appear as, or are predicted to be, instrumental.

Historically, the idea of placing quantum dot circuits in cavities came along with the proposals of using quantum dots for quantum information [40, 41, 47, 48]. Transport measurements require the coupling to many degrees of freedom (the electrode electrons),

which often weakens quantum states (a phenomenon called decoherence). In contrast, cavities can reveal electrons moving from one dot to the other, in the absence of any charge transfer to electrodes. This allows to study the internal dynamics of almost isolated artificial molecules. Most experiments focused on charge transfer in double dots [43, 49–53], the artificial equivalent of diatomic molecules. Photon-emission induced by double dots was recently observed, a step towards the realisation of a quantum-dot-based laser, which ranges among early expectations of mesoscopic QED [47].

However, the realisation of long distance two-qubits coupling via the cavity remains a long-term goal of the community. The control of spin qubits with microwave cavity photons has not been demonstrated so far. This is challenging, since the spin intrinsic coupling to the cavity electromagnetic field is far too small to be exploited. Recently the coupling of a single electron spin to cavity photons has been achieved, by engineering a coupling between the electron spin and electron spatial position [54]. This is a promising step towards the control of spin qubits with microwaves. However, using cavity photons to control the state of a circuit is more demanding than using photons as a probe of the circuit state. A prerequisite for control is to reach the so-called strong coupling regime, characterised by the possibility of coherent excitation transfer between qubit and cavity. Before this work (see chapter 6), this regime had not been realised in the mesoscopic community.

However, weaker coupling regimes are sufficient for cavity measurements to be instrumental in probing "atomic-like" mesoscopic circuits with cavity photons. For example, cavities have been proposed theoretically to investigate the coherence of Cooper pair injection in Cooper pair devices [55, 56]. As discussed in previous section, coherent Cooper pair splitting is still an open issue, which is strongly related to demonstrating the possibility of generating distant entangled electrons in a solid-state environment. The main original goal of this thesis was to address this question by embedding a Cooper pair splitter in a microwave cavity. Chapter 6 presents the first experimental crossed-characterisation of a Cooper pair splitter device, combining currents and cavity field measurements.

Another motivation for placing circuits in cavities is to probe quantum transport in a complementary way, as usual continuous current measurements do. The relevance of mesoscopic QED tools applied to this purpose was revealed experimentally, rather than anticipated in early proposals. One aspect is to study the circuit frequency response to the GHz excitation caused by the cavity electromagnetic field. However, experimental studies of electronic transport dynamics started way before the advent of mesoscopic QED, by applying microwave excitations directly to the circuit electrodes. Historically, the first experiment of this type was performed in 1963 with a SIS junction [57]. It revealed that microwaves can induce DC transport by so-called photon-assisted-tunnelling

(PAT) processes. Since then, PAT has been widely explored in various systems, like junctions and quantum dots [58]. The input of microwaves to investigate quantum transport is further illustrated in section 2.1. One example is the investigation of the Kondo effect under microwave excitation, which started a decade ago [59–61] and is further explored in our chapter 4.

Nevertheless a cQED architecture offers more than a mode of circuit excitation at finite-frequency. Due to the circuit-cavity coupling, measuring the resonator transmission reveals information about the circuit, which could not be accessed by transport measurements alone. Resonant cavities with high finesse can be a more sensitive probe to electronic transport than current measurements, as the experiment of chapter 5 illustrates for PAT between a dot and a superconductor. Beyond quantitative differences, cavity and transport signals can be qualitatively different, even in a transport situation with measurable currents. Such a situation was first reported in a crossed cavity-current study of transport through a double quantum dot [52]. The combination of both cavity and current measurements appeared as beneficial for characterising the device more completely. Finally, cavities reveal charge displacements, which are intrinsically absent of electrical current signals, because they do not result in net charge transport from one contacting electrode to another. For example, the cavity electromagnetic field is sensitive to back-and-forth electron transfer between a quantum dot level and a single contacting electrode. This situation was first studied in [62], and is explored in greater details in our chapter 5, giving strong insight into charge tunnelling dynamics.

The manuscript is organized as follows. Chapter 1 is dedicated to the description of quantum transport in quantum dot circuits. In addition to introducing general basic concepts, we specifically focus on Kondo physics and the effect of superconducting contacts, which correspond to the physical situations investigated in this thesis. Chapter 2 details the scientific context and specific theoretical tools of mesoscopic QED. Experimental methods are the object of chapter 3, from sample fabrication to transport and cavity measurement techniques at cryogenic temperature. The next three chapters present original results, which have been obtained during this thesis. We summarize below the main achievements for each of them.

Dynamics of Kondo effect at finite frequency

Chapter 4 belongs to the long-standing studies of finite-frequency effects in mesoscopic circuits, where microwaves excitations are applied directly to the circuit electrode. Here, we do not use a cavity but a fast gate to probe the finite-frequency response of a quantum dot in the Kondo regime. We report the second observation of radiation-induced Kondo satellite peaks, primarily observed in a GaAs two-dimensional electron gas [60] (figure

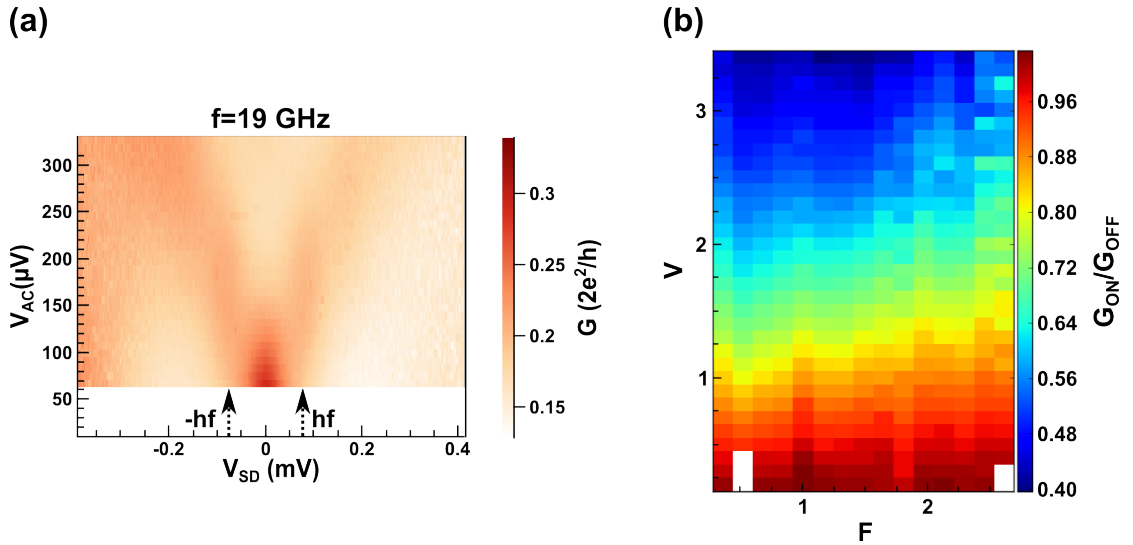


FIGURE 1: (a) Phenomenology of the finite-frequency response of the Kondo conductance vs bias voltage V_{SD} , as a function of the microwave excitation amplitude V_{AC} , at $f=19$ GHz. (b) Scaled Amplitude-frequency evolution of Kondo resonance. G_{ON}/G_{OFF} is the ratio between the Kondo conductances at zero-bias, with and without microwave excitation. The axis are the scaled amplitude $V = eV_{AC}/k_B T_K$ and scaled frequency $F = hf/k_B T_K$.

1a). Using an independent in-situ amplitude calibration, we provide the first quantitative measurement of the amplitude-frequency dependence of the Kondo conductance with an AC bias (figure 1b). The Kondo resonance is found to be less affected at higher excitation frequencies, in agreement with Kaminski et al theoretical paper [63]. We describe our data quantitatively using an Ansatz, which bridges between expressions given in this paper for two limiting regimes of parameters. Measurement on two Kondo resonances with very different T_K allows to make some statements on universality. We find a good scaling of the conductance with the scaled amplitude $V = eV_{AC}/k_B T_K$. In the more limited parameter range we could explore, our data is also consistent with a scaling of the conductance with the scaled frequency $F = hf/k_B T_K$.

Cavity photons as a probe of tunnelling dynamics between a discrete level and fermionic reservoirs

In chapter 5, we present experimental data and theoretical modelling of the behaviour of a single quantum dot in a carbon nanotube, coupled to normal metal (N) and superconducting (S) reservoirs, and embedded in a high finesse microwave cavity. We observe a large variety of effects depending on the values of the tunnel rates and on the bias voltage applied to the device. In any case transport and cavity signals differ clearly, supporting the idea that a crossed-measurements of both yields a more accurate characterisation of the device.

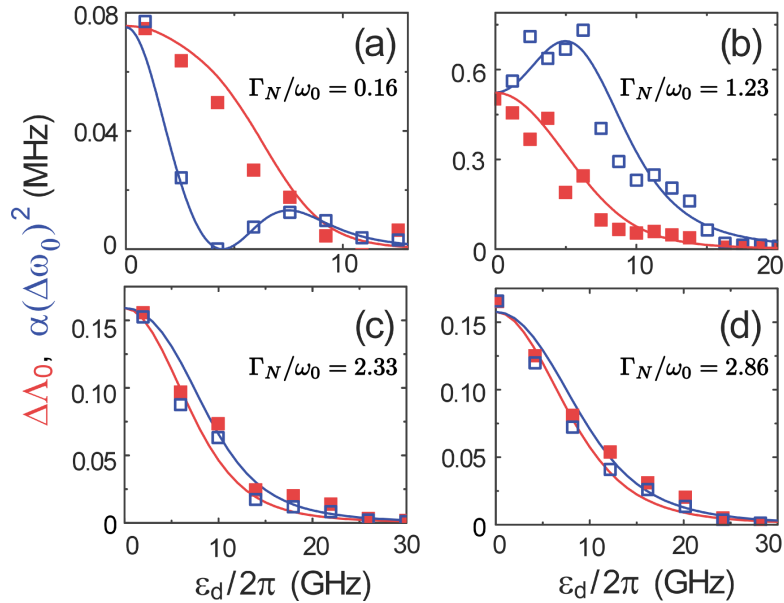


FIGURE 2: Comparison between the experimental cavity linewidth shift $\Delta\Lambda_0$ and square cavity frequency shift $(\Delta\omega_0)^2$ using a scaling factor α . These shifts result from dissipation and dispersion induced by a S-dot-N circuit at zero-bias. The scaling factor α depends on the tunnelling rate Γ_N between the dot and the normal electrode N. We also show as blue and red full lines the calculated $\Delta\Lambda_0$ and $(\Delta\omega_0)^2$.

For intermediate tunnel rates Γ_N and zero-bias voltage, current is zero, while the cavity frequency shift $\Delta\omega_0$ and linewidth shift $\Delta\Lambda_0$ follow a relation, which is independent of the quantum dot orbital energy ϵ_d (figure 2c and d). This behaviour is related to the universality of the quantum charge relaxation resistance R_{AC} predicted by Büttiker et al. [64, 65], and observed only in a strongly spin-polarised GaAs quantum dot so far [66]. We present the first experimental investigation of quantum charge relaxation in the spin-degenerate interacting case. Our observations are consistent with recent theory works, which suggest that the universality of the charge relaxation resistance R_{AC} persists in this limit [67, 68]. More precisely, our experiment confirms that R_{AC} is independent from the dot orbital energy, a property which could not be probed in reference [66], and which is already valid for intermediate tunnel rates ($\Gamma_N/\omega_0 \sim 2.5$). Panels a and b of figure 2 show that the scaling behaviour breaks down for smaller tunnel rates.

For bias voltage eV_b out of the superconducting gap Δ , there can be an increase in the cavity amplitude A (blue areas), which reveals photon-assisted tunnelling between the dot and the BCS peaks of the superconducting reservoir (figure 3e). In contrast, the experimental conductance map shown in figure 3a can be reproduced by a model (3b), which does not include any microwave excitation. As PAT a priori leads to specific signatures in conductance measurements, this indicates the cavity superior sensitivity to detect PAT events with respect to current measurements. PAT between a dot and a superconductor was never observed experimentally before, even with DC transport.

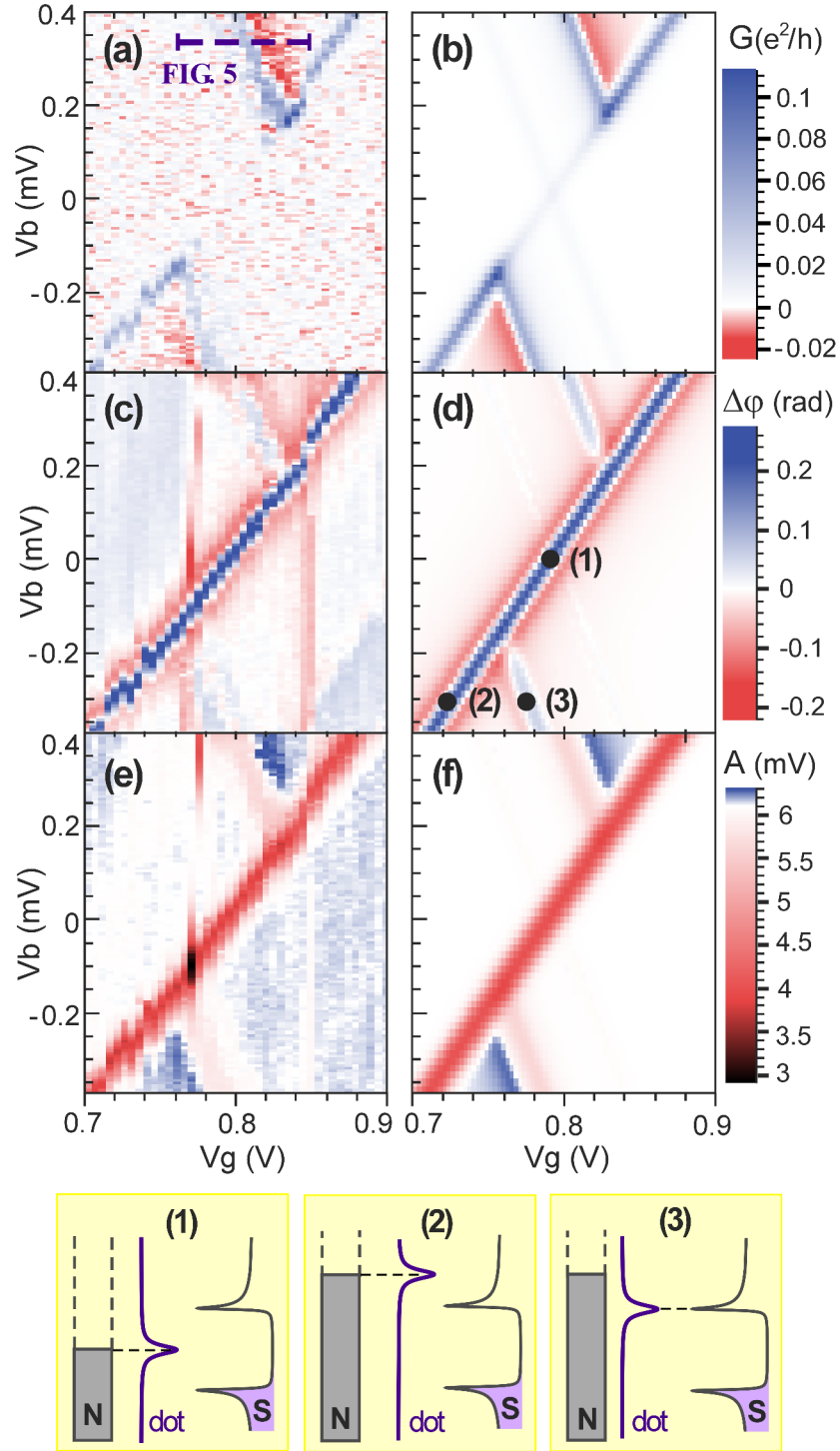


FIGURE 3: Panels (a), (c) and (e): Measured linear conductance G , phase shift $\Delta\phi$ and total amplitude A of the transmitted microwave signal, versus the dot gate voltage V_g and the bias voltage V_b . Panels (b), (d) and (d): Predictions based on calculations of the charge susceptibility for a S-dot-N system. The white colour in the amplitude colour code corresponds to the bare cavity amplitude in panels (e) and (f). Panels (1), (2) and (3): Electric potential configuration corresponding to the black points in panel (d).

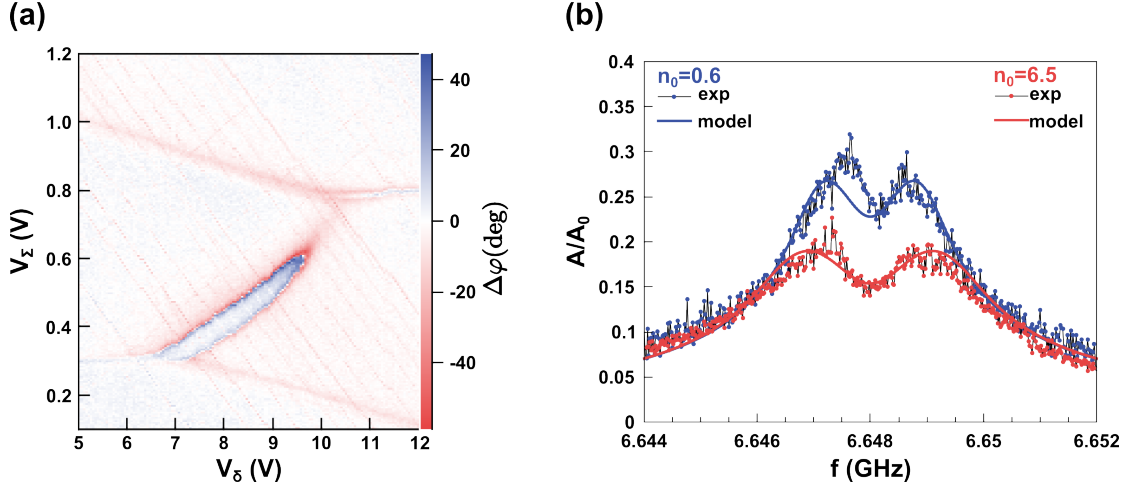


FIGURE 4: **(a)** Cavity phase shift $\Delta\varphi$ colour plot in the gate-gate rotated plane V_Σ - V_δ for a bias voltage $V_{SD} = -0.16mV$. Here, the sign change reveals a resonance between an electronic transition of the CPS device and the cavity mode. **(b)** Observation of Rabi splitting in the cavity spectrum, indicating a strong coupling of the CPS device to cavity photons. The influence of the cavity input power is measured and modelled (full lines) for $n_0 \approx 0.6$ and $n_0 \approx 6.5$ (bare cavity equivalent photon numbers).

Here, we report the possibility of photon emission by a dot coupled to reservoirs, against the common idea that reservoirs are synonym of dissipation only.

Remarkably, the formalism we use is able to reproduce quantitatively all the measured quantities, in the large variety of effects we observe (figures 2 and 3). Our work is the first experimental test of the cavity response theoretical description in terms of charge susceptibility. The validation of this recently proposed approach [69–72] lays the foundations for the study of others nanocircuits coupled to cavities, involving any type of fermionic reservoirs (normal, superconducting, ferromagnetic).

Strong coupling of a Cooper pair splitter to cavity photons

In chapter 6, we present the first implementation of a Cooper pair splitter in a microwave resonator. The cavity appears as a powerful probe, as it reveals features which are either absent or hardly resolvable in transport signals. We observe the resonant coupling between electronic transitions of the device and cavity photons (figure 4a). From an energetic analysis, we show that this observation is conditioned to the subgap position of the electronic states involved in the resonant transition(s). Importantly, the strong coupling regime is achieved, which had never been realised before with quantum dot circuits. We provide a semi-classical modelling of the non-trivial Rabi splitting dependence with the photon number (figure 4b). A full interpretation of the CPS microscopic states, which are involved in this strong coupling to cavity photons, needs further analysis.

Chapter 1

Quantum transport in quantum dot circuits

1.1	Transport phenomenology in quantum dots	16
1.1.1	Energy scales	16
1.1.2	Transport regimes	18
1.2	"Closed" quantum dots	20
1.2.1	Coulomb blockade	20
1.2.2	Double quantum dots as qubits	25
1.3	Kondo physics	29
1.3.1	From Anderson model to Kondo physics	30
1.3.2	Kondo resonance conductance and universality	32
1.4	Quantum dot circuits with superconducting contacts	33
1.4.1	Proximity effect in a quantum dot	35
1.4.2	Cooper pair splitter	38

In macroscopic conductors, electronic transport is well described by treating electrons as particles. Their dual wave nature has to be taken into account as soon as the phase of the electronic wavefunction is preserved along the conductor size. Research on quantum transport boomed in the 90's with the advent of nano-lithography techniques. Mesoscopic circuits could be fabricated to be smaller than the phase coherence length, which typically reaches a few microns below 1K.

One branch of quantum transport is the study of quantum dot circuits. They consist in artificial zero-dimensional objects made out of molecules, single-wall carbon nanotubes, graphene, semiconducting nanowires or two-dimensional electron gases (2DEG), which are contacted with electrodes. Versatility of nanolithography offers the possibility to realise different circuit geometries from single to multiple dot. These dots can be connected to various conductors like normal metals, superconductors or ferromagnetic metals.

This chapter introduces the concepts of quantum transport, that are involved in the understanding of this thesis work. The basics of quantum dot circuits are introduced in 1.1. The ability to exchange electrons with the electrodes defines two classes of systems, that are further addressed. "Closed dots" (section 1.2) exploits the long lifetime of electrons on the dots to realise two-level systems, which can be used as qubits in the context of quantum information. "Open dots" give rise to many-body phenomena and in particular to Kondo physics (section 1.3), considered as the archetype of many-body effects. 1.4 is dedicated to quantum dots connected to superconductors.

1.1 Transport phenomenology in quantum dots

A quantum dot (QD) is a zero-dimensional system, which has discrete energy levels. The energy levels of a quantum dot can be filled with electrons very much like an atom [73], which explains why quantum dots are sometimes referred to as artificial atoms. Transport measurement is a way to perform the quantum dot spectroscopy since the 90's. The quantum dot is contacted to reservoirs, with which it can exchange electrons, and it is capacitively coupled to one or more gate electrodes, which vary the dot electrostatic potential (figure 1.1). Along with the extrinsic energy scale $k_B T$ imposed by temperature, three intrinsic energy scales mainly characterise electronic transport through QDs.

1.1.1 Energy scales

Thermal energy All experiments presented in this thesis were performed in a dilution refrigerator cryostat with base temperature close to 16 mK. The relevant temperature

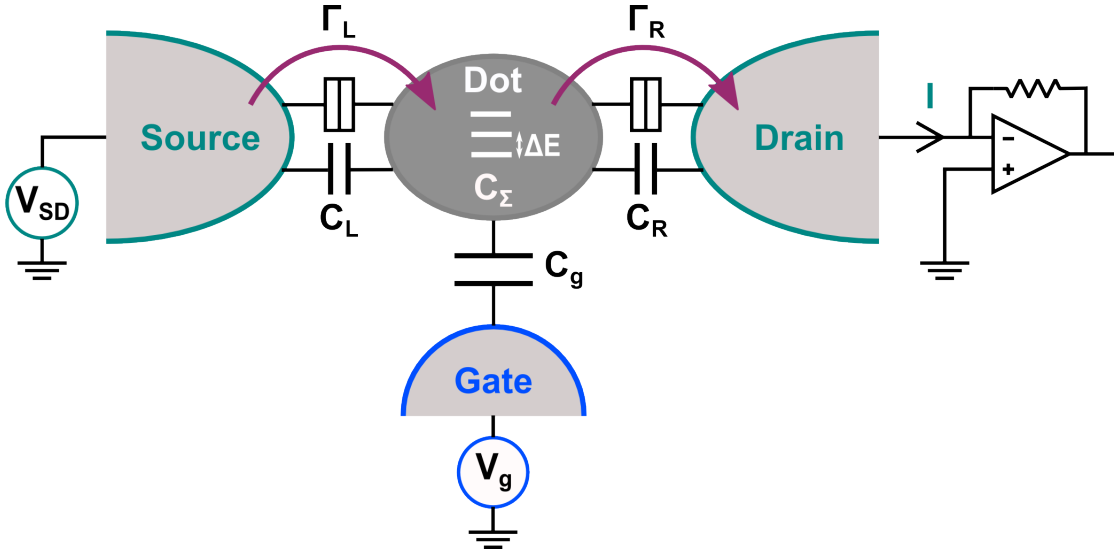


FIGURE 1.1: **Principle of quantum dot transport spectroscopy.** A quantum dot is a zero-dimensional object (dark grey), which has discrete energy levels, separated by ΔE . In transport experiments, it is contacted to source and drain electrodes. Each contact $i \in (R, L)$ is characterised by a tunnelling rate Γ_i/\hbar and a capacitance C_i . A gate electrode is capacitively coupled to the dot via the capacitance C_g . The gate voltage V_g enables to tune the position of the energy levels with respect to the reservoirs chemical potential. The ability to charge the dot is basically captured by the dot total capacitance C_Σ , which is the sum of C_L , C_R and C_g . Standard transport measurement are performed by applying a bias voltage V_{SD} to the source electrode, while the current is amplified and measured through the drain electrode.

to interpret transport measurements is the electronic temperature. From conductance measurement, an upper bound for the electronic temperature around 50 mK ($k_B T_{el} \approx 4 \mu\text{eV} \sim \text{GHz}$) has been extracted (section 3.2.2.2).

Energy-level spacing In objects of finite size, electrons have a discrete spectrum. The energy-level spacing in a quantum dot with typical size L is given by the interference condition $\Delta E = \frac{\hbar v_F}{2L}$ where v_F is the Fermi velocity. In principle, the size of the dot is set by the electrode geometry, but disorder may induce smaller effective dots. The discrete levels created by confinement form the dot main spectrum and are referred to as orbitals by analogy with real atomic orbitals. Like their natural counterparts, orbital levels in QDs can be degenerate in presence of internal electronic degrees of freedom. In principle, orbitals in carbon nanotubes exhibit a four-fold degeneracy coming from spin and valley two-fold degeneracies, arising from the graphene structure of the nanotube wall. A small object behaves as a quantum dot, if the separation between energy levels ΔE is observable at the experiment temperature ($\Delta E > k_B T$). In carbon nanotubes $v_F \approx 10^6 \text{ms}^{-1}$, so $L = 400 \text{nm}$ gives $\Delta E \approx 5 \text{meV}$ ($\sim \text{THz}$). The resulting condition on the temperature is $T \lesssim 10 \text{K}$, which is reached with liquid ^4He .

Charging energy Confining electrons in a small island costs energy because of Coulomb repulsion. The presence of each extra electron on the island costs the charging energy U corresponding to a capacitance C_Σ . It can be estimated by calculating the geometrical capacitance of a 100nm x 100nm island facing a 100nm distant gate electrode : $C_\Sigma = \epsilon_0 \epsilon_r S/d \approx 10^{-18} \epsilon_r F$. Depending on the material relative permittivity, this gives $U = \frac{e^2}{C_\Sigma} \approx 10 - 100 meV$. Typically, in our carbon nanotube QDs, $U \approx 10 meV$ (\sim few THz). The charging energy is often thought about as the energy to add an extra electron on a confined object. This is true for small metallic islands, where charging effects are important but energy levels quantisation can be neglected ($\Delta E \ll U$). However, this is generally not correct for quantum dots. There the addition energy $E_{add}(N)$ required to add a $(N + 1)^{th}$ electron on the quantum dot involve the charging energy U and the energy spacing $\Delta E(N)$ between levels N and $N + 1$. This term can be zero if the levels N and $N + 1$ are degenerate.

Tunnelling rate Electrodes can be seen as electron reservoirs, which can exchange electrons with the dot at the tunnel rate Γ/\hbar . This parameter is mainly set by the electronic density in the leads, and the overlap between lead and dot wavefunctions. The latter depends on the electron potential landscape, which is partly set by the fabrication process and partly tuned by gate voltages. The degree of tunability depends on materials and processes, and is currently higher for 2DEGs and nanowires than for carbon nanotubes. If $\Gamma > k_B T$, the barriers transparency rules the electrons degree of confinement in the dot, hence the energy levels width. Discrete levels can be observed in a dot provided that $\Gamma < \Delta E$. If the thermal energy is dominating, the level broadening is controlled by $k_B T$. Tunnelling rates between dot and leads measured in our nanotube devices are in the $\mu eV - meV$ range (\sim 100 MHz to few hundreds of GHz).

1.1.2 Transport regimes

The interplay between ΔE , U and Γ determines the transport regime and the conductance features in the plane defined by gate voltage V_g and bias voltage V_{SD} axis (figure 1.2).

- **Coulomb blockade regime** : $\Gamma, kT \ll \Delta E \lesssim U$. In this regime (detailed in 1.2.1), transport is dominated by Coulomb repulsion between electrons. Colour plot of the differential conductance as a function of V_g and V_{SD} shows diamond-shaped patterns. In the diamond-shaped blockade regions, no current flows and the number of electrons N is fixed, while within the cross-shaped regions, the patterns reflect the spectra of transitions between N and $N+1$ electrons.

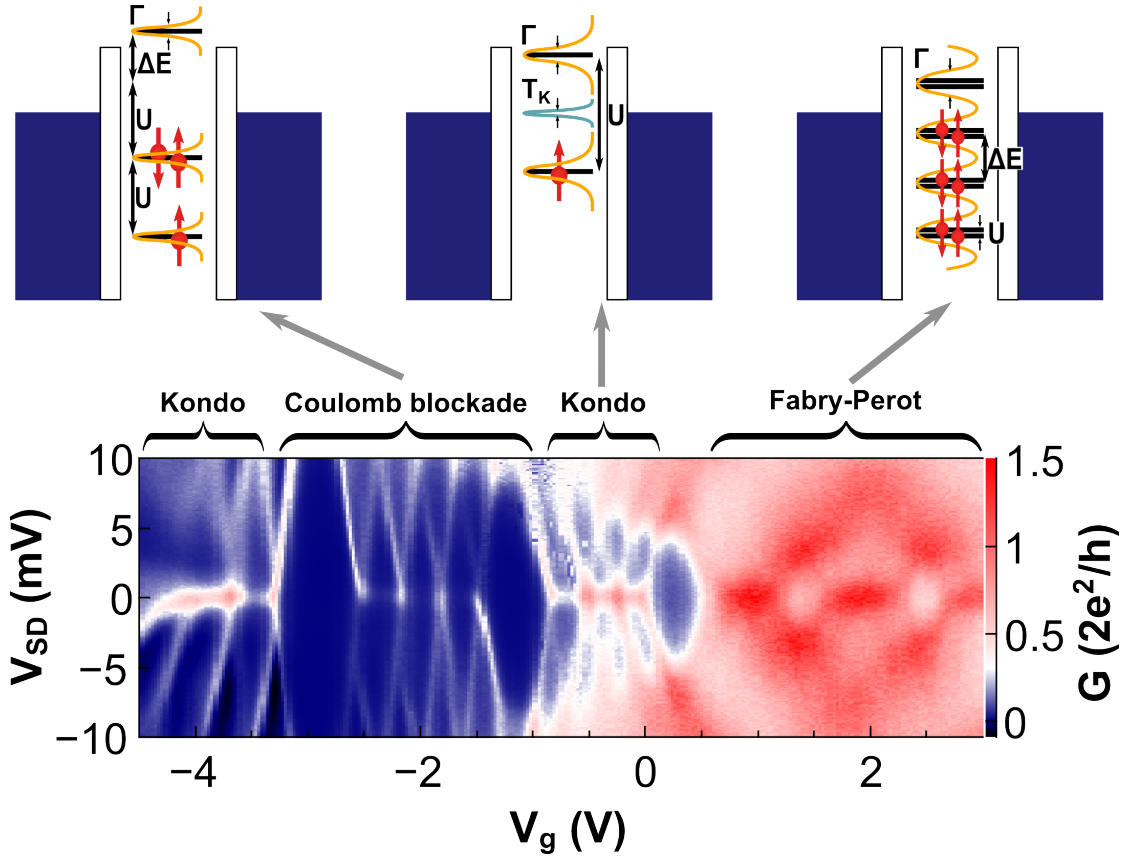


FIGURE 1.2: Electronic spectroscopy of a carbon nanotube exhibiting the three regimes of transport : Coulomb blockade, Kondo and Fabry-Perot. The corresponding characteristic features in a conductance colour plot versus gate and bias voltage are respectively : Coulomb diamonds, Kondo ridges and Fabry-Perot checker-board. For each regime a schematics of the QD recalls the relevant parameter hierarchy between the level energy spacing ΔE , the Coulomb energy U and the tunnelling energy Γ . The Kondo resonance results in an effective peak in the density of states at zero-bias, which width defines the Kondo temperature T_K . Here the thermal energy is the smallest energy scale.

- **Kondo regime** : $kT < \Gamma < \Delta E \lesssim U$. This regime (object of section 1.3) appears in carbon nanotubes with fairly transparent tunnel barriers, but still in the Coulomb blockade regime. It is characterised by the Kondo ridge, a zero bias conductance resonance inside the Coulomb diamonds.
- **Fabry-Perot regime** : $kT, U \ll \Gamma \lesssim \Delta E$. In this regime, the barriers transmission dominates over charging effects. The dot is open and interference phenomena take place in the nanotube waveguide, like Fabry-Perot interferences occur in optical cavities. This results in a checker-board pattern for the differential conductance.

1.2 ”Closed” quantum dots

”Closed” quantum dots have low tunnelling rates to reservoirs, which means that they are nearly isolated from the leads. Coulomb blockade physics dominates : the dot state is essentially defined by the number of charges. Charge stability diagram for single and double QD are explained in 1.2.1.1 and 1.2.2.1. In nearly isolated dots¹, transport is described by the master equation approach (1.2.1.2). As electron dwell time in dots is rather long ($0.05ms \sim 20kHz$ in [74]), charge is a good quantum number. This is exploited to make charge qubits in double QDs (1.2.2.2). Because of its higher robustness to decoherence, the electron spin degree of freedom is at the core of many qubits proposals as illustrated in 1.2.2.3.

1.2.1 Coulomb blockade

1.2.1.1 Coulomb diamonds

On an isolated island the number of charge must be an integer because of charge quantisation. A quantum dot contacted to reservoirs remains a Coulomb blockade system where the charge number is well defined, provided that it is ”isolated enough”. More precisely the energy fluctuations must be much lower than the charging energy : $max(\Gamma, k_B T) \ll U$. In this case electron transport through the dot is blocked except if the addition energy is supplied by an external voltage source. Conductance map in the V_g - V_{SD} plane shows Coulomb diamonds, where the charge number on the dot is fixed (no transport). Each diamond corresponds to the N-electron ground state. Boundaries of N-electron diamond can be found using the constant interaction model. It is based on the two following assumptions. Electronic interactions inside the dot and between dot and its environment are constant and parametrized by the total capacitance of the dot : $C_\Sigma = C_g + C_L + C_R$ where C_g is the dot capacitance to the gate and C_L/C_R the dot capacitance to the left/right lead. Effects of interactions on the ”chemical” energy-level spectrum are neglected, and the single-particle energy-level spectrum (the set of $\{\epsilon_i\}$) holds, whatever the electron number. In this framework, the total energy of the dot with N electrons in the ground state is :

$$E(N) = E_{el}(N) + \sum_{i=1}^N \epsilon_i \quad (1.1)$$

¹when Γ is the smallest energy scale in the system

The first term is the electrostatic energy :

$$E_{el}(N) = \frac{e^2}{2C_\Sigma} \left(N - \frac{C_g V_g + C_L V_L + C_R V_R}{e} \right)^2 \quad (1.2)$$

The second term is a "chemical" part : it is the sum of the single-particle spectrum energy ϵ_i over all occupied orbital levels i . The N-electron ground state is stable if all four single-electron transfer processes between dot and leads are forbidden for energetic reasons. The energy difference caused by a tunnelling event has two terms : the electrochemical potential $\mu(N+1)$ for adding ($-\mu(N)$ for extracting) one electron to (from) the dot and the electrostatic energy eV_i ($-eV_i$) for adding (extracting) an electron to (from) the electrode i .

$$\mu(N) = E(N) - E(N-1) \quad (1.3)$$

The set of following inequalities define the Coulomb blockade regime because single-electron transfers cannot happen if they cost energy.

$$\begin{aligned} \text{From left lead to dot : } \Delta E &= \mu(N+1) - eV_L > 0 \\ \text{From dot to left lead : } \Delta E &= -\mu(N) + eV_L > 0 \\ \text{From right lead to dot : } \Delta E &= \mu(N+1) - eV_R > 0 \\ \text{From dot to right lead : } \Delta E &= -\mu(N) + eV_R > 0 \end{aligned} \quad (1.4)$$

In our experimental situation, $V_L = V_{SD}$ and $V_R = 0$, so conditions 1.4 result in :

$$\begin{aligned} eV_{SD} &< \left(N + \frac{1}{2} \right) \frac{e^2}{C_L} - \frac{C_g}{C_L} eV_g + \frac{C_\Sigma}{C_L} \epsilon_{N+1} \\ eV_{SD} &< - \left(N - \frac{1}{2} \right) \frac{e^2}{C_\Sigma - C_L} + \frac{C_g}{C_\Sigma - C_L} eV_g - \frac{C_\Sigma}{C_\Sigma - C_L} \epsilon_N \\ eV_{SD} &> \left(N - \frac{1}{2} \right) \frac{e^2}{C_L} - \frac{C_g}{C_L} eV_g + \frac{C_\Sigma}{C_L} \epsilon_N \\ eV_{SD} &> - \left(N + \frac{1}{2} \right) \frac{e^2}{C_\Sigma - C_L} + \frac{C_g}{C_\Sigma - C_L} eV_g - \frac{C_\Sigma}{C_\Sigma - C_L} \epsilon_{N+1} \end{aligned} \quad (1.5)$$

In the eV_g - eV_{SD} plane, each condition of 1.5 is a straight line (figure 1.3). The four lines delimit a diamond, where transport is blocked. The N-diamond height and width reveal important parameters of the dot. We define the gate voltage $V_{g,N}$ as the zero-bias degeneracy condition between the N-1 and N-electron ground states, that is $\mu(N, V_{g,N}, V_{SD} = 0) = 0$. For each $V_{g,N}$ there is a conductance peak (see data of figure 1.2). The difference $e(V_{g,N+1} - V_{g,N})$ corresponds to the distance between consecutive peaks, thus to

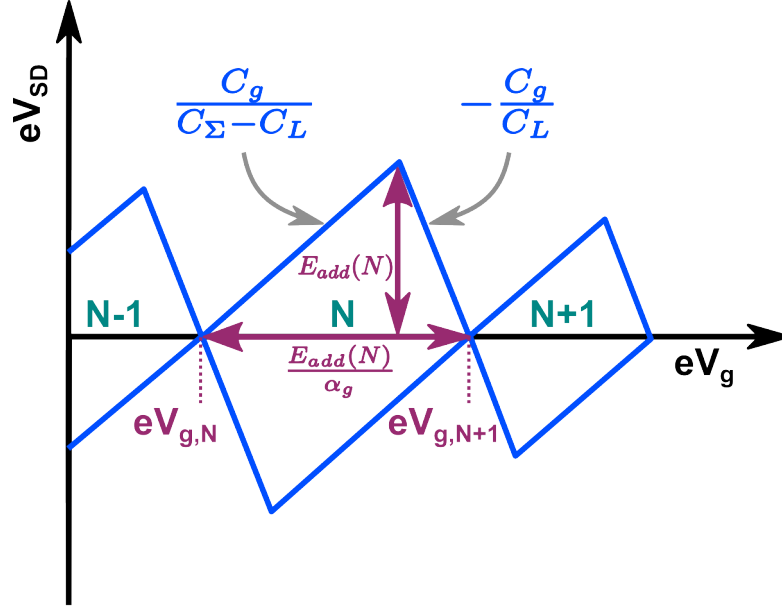


FIGURE 1.3: **Charge stability diagram of a single dot depending on gate voltage V_g and bias voltage V_{SD} .** The blue lines correspond to the set of conditions 1.5. If the bias voltage V_{SD} is applied to the left electrode as depicted in figure 1.1, the positive and negative slopes are respectively $C_g/(C_{\Sigma} - C_L)$ and $-C_g/C_L$. Within a diamond delimited by the lines, the charge on the dot is fixed, and takes an integer value labelled in green. The N-diamond half-height equals the addition energy $E_{add}(N)$ required to add a N+1 electron. The N-diamond width $e(V_{g,N+1} - V_{g,N})$ equals E_{add}/α_g where $\alpha_g = C_g/C_{\Sigma}$ is the gate capacitive lever arm.

the zero-bias diamond width. Equations 1.1, 1.2 and 1.3 lead to :

$$\mu(N+1, V_g, V_{SD} = 0) = \epsilon_{N+1} + U \left(N + \frac{1}{2} \right) - e\alpha_g V_g \quad (1.6)$$

with the gate capacitive lever arm $\alpha_g = \frac{C_g}{C_{\Sigma}}$.

From this, we deduce $eV_{g,N} \equiv \left(\epsilon_{N+1} + U \left(N + \frac{1}{2} \right) \right) / \alpha_g$. Consequently, the zero-bias width $e(V_{g,N+1} - V_{g,N})$ is equal to $E_{add}(N)/\alpha_g$, with the addition energy in the N-electron state:

$$E_{add}(N) = \frac{e^2}{C_{\Sigma}} + \epsilon_{N+1} - \epsilon_N = U + \Delta E(N) \quad (1.7)$$

Diamond slopes are related to capacitances : the positive one is $\frac{C_g}{C_{\Sigma} - C_L}$ and the negative one is $-\frac{C_g}{C_L}$. The diamond half-height is found to be equal to E_{add} . As a result, the gate capacitive lever arm α_g is the ratio between diamond half-height and zero-bias width.

Note that equation 1.6 shows that the gate voltage actually tunes the dot zero-bias electrochemical potential. However, it is convenient and wide-spread to say that the gate voltage tunes the dot level energy. Then equation 1.6 for a certain level d is written

:

$$\epsilon_d = \epsilon_0 - e\alpha_g V_g = e\alpha_g (V_{g,0} - V_g) \quad (1.8)$$

This formulation will be the one further used in this thesis.

1.2.1.2 Master equation for transport : $\Gamma \ll k_B T$

Consider a QD in the Coulomb blockade regime, with the additional condition $\Gamma \ll k_B T$. In this case single-electron tunnelling events are sequential and random. This is why a probabilistic approach to describe transport is appropriate [75]. The system is described by probabilities $p_\alpha(t)$ to be in the state α at time t and tunnelling rates $\tilde{\Gamma}_{\alpha \rightarrow \beta}/\hbar$ giving the probability per unit time for the system to go from α to β . The master equation is a balance equation for the probabilities. In the most general case it writes :

$$\hbar \frac{dp_\alpha}{dt} = - \sum_{\beta} \tilde{\Gamma}_{\alpha \rightarrow \beta} p_\alpha + \sum_{\beta} \tilde{\Gamma}_{\beta \rightarrow \alpha} p_\beta \quad (1.9)$$

In the most simple case of non-degenerate levels, transport at the N-N+1 ground states degeneracy is ruled by the probabilities p_0 and p_1 for the last level to be empty or occupied. In this single level picture, the energy ϵ_{N+1} of the last level is further labelled ϵ_d . Transport from (to) the lead $i \in L, R$ to (from) the dot happens at a rate $\tilde{\Gamma}_i^\pm$ ($\tilde{\Gamma}_i^-$). The total ingoing and outgoing rates are (in energy units) $\tilde{\Gamma}^\pm = \tilde{\Gamma}_L^\pm + \tilde{\Gamma}_R^\pm$. Counting incoming and outgoing electrons gives the following master equations :

$$\begin{aligned} \hbar \frac{dp_0}{dt} &= -\tilde{\Gamma}^+ p_0 + \tilde{\Gamma}^- p_1 \\ \hbar \frac{dp_1}{dt} &= -\tilde{\Gamma}^- p_1 + \tilde{\Gamma}^+ p_0 \end{aligned} \quad (1.10)$$

The stationary condition $\frac{dp_\alpha}{dt} = 0$ for all α 's and the normalization condition $\sum_\alpha p_\alpha = 1$ yield the following probabilities :

$$\begin{aligned} p_0 &= \frac{\tilde{\Gamma}^-}{\tilde{\Gamma}^- + \tilde{\Gamma}^+} \\ p_1 &= \frac{\tilde{\Gamma}^+}{\tilde{\Gamma}^- + \tilde{\Gamma}^+} \end{aligned} \quad (1.11)$$

Due to current conservation, it is equivalent to count current through left or right lead.

$$I = \frac{e}{\hbar} \left(\tilde{\Gamma}_L^+ p_0 - \tilde{\Gamma}_L^- p_1 \right) \quad (1.12)$$

$$I = \frac{e}{\hbar} \left(\frac{\tilde{\Gamma}_L^+ \tilde{\Gamma}_R^- - \tilde{\Gamma}_L^- \tilde{\Gamma}_R^+}{\tilde{\Gamma}^- + \tilde{\Gamma}^+} \right) \quad (1.13)$$

The tunnelling energies are obtained using Fermi's Golden rule, treating the tunnelling hamiltonian as a perturbation :

$$\tilde{\Gamma}_i^\pm = \Gamma_i f(\pm(\epsilon_d + eV_i)) \text{ with } \Gamma_i = 2\pi |t_i|^2 \nu_i \quad (1.14)$$

where V_i is the potential applied on lead $i \in (L, R)$, $\epsilon_d = \epsilon_{d,0} - e\alpha_g V_g$ is the gate tunable dot level energy and f the Fermi function. ν_i is the density of state in reservoir i . t_i is the hopping term between an electronic band k_i of lead i and the dot, which is taken constant for all k 's. Taking $V_L = V_{SD}$ and $V_R = 0$, and using the identity $f(x) + f(-x) = 1$, the current simplifies as :

$$I = \frac{e}{\hbar} \frac{\Gamma_L \Gamma_R}{\Gamma_L + \Gamma_R} (f(\epsilon_d + eV_{SD}) - f(\epsilon_d)) \quad (1.15)$$

Assuming $V_{SD} \ll k_B T$, the following Fermi function expansion can be used :

$$f(\epsilon_d + eV_{SD}) = f(\epsilon_d) + eV_{SD} \frac{1}{4k_B T \cosh^2\left(\frac{\epsilon_d}{2k_B T}\right)} \quad (1.16)$$

The resulting current writes $I = GV$ with the low-bias conductance :

$$G = \frac{e^2}{\hbar} \frac{\Gamma_L \Gamma_R}{\Gamma_L + \Gamma_R} \frac{1}{4k_B T \cosh^2\left(\frac{\epsilon_d}{2k_B T}\right)} \quad (1.17)$$

This corresponds to a symmetric peak centred in $\epsilon_d = 0$. Its maximum is a fraction of the conductance quantum $G_Q = \frac{e^2}{\hbar}$, which is equal to $\frac{1}{16} \frac{\Gamma}{k_B T}$ for symmetric tunnelling energies $\Gamma = \Gamma_L + \Gamma_R$. The Full Width at Half Maximum (FWHM) in energy units is $FWHM = 4k_B T \operatorname{arccosh}(\sqrt{2}) \approx 3.5 k_B T$.

In practice, our experiments are mostly in the regime $k_B T \lesssim \Gamma$. However equation 1.17 for the conductance is interesting to give an upper bound for the electron temperature (see 3.2.2.2). Considering spin degeneracy would not invalid this method, as it would make the peak slightly asymmetric and wider.

1.2.1.3 Resonant tunnelling in the regime: $k_B T \leq \Gamma$

In the regime $k_B T \lesssim \Gamma$, more quantum effect occur. The situation remains simple near a Coulomb crossing, if we assume again non-degenerate levels, and treat the filled

electronic states as a background. It means that a single level with occupancy 0 or 1 is resonant with the leads. This allows to disregard Coulomb interaction, which would need at least two electrons. In this non-interacting case, the conductance can be derived exactly either using the Green's function formalism or the scattering matrix approach :

$$G = \frac{e^2}{h} \frac{\Gamma_L \Gamma_R}{\left(\frac{\Gamma_L + \Gamma_R}{2}\right)^2} \frac{1}{1 + \left(\frac{2\epsilon_d}{\Gamma_L + \Gamma_R}\right)^2} \quad (1.18)$$

The peak shape is Lorentzian with $FWHM = \Gamma = \Gamma_L + \Gamma_R$. The maximum is a fraction of the conductance quantum, which is set by the asymmetry between left and right tunnel energies. In the fully symmetric case, the conductance reaches G_Q . For degenerate levels where interactions come into play, Coulomb peaks qualitatively have the same features : $G_{max} \sim \frac{e^2}{h}$ and $FWHM \sim \Gamma$. Conductance cannot be calculated exactly by analytical methods in this many-body situation. Numerous theoretical approaches are currently used to treat many-body problems approximately. In practice, experimental Coulomb peaks are often fit by a Lorentzian, knowing that height and width are renormalized by interactions. The Lorentzian shape assumption is convenient, and it is a rather good approximation, if the peaks are well separated.

1.2.2 Double quantum dots as qubits

The simplest qubit is a two-level system. Examples of natural two-level systems are spins $\frac{1}{2}$ (up and down states) and diatomic molecules (bonding and anti-bonding states). These can be realised artificially in quantum dot devices : single electron spins in single quantum dots and double quantum dots.

1.2.2.1 Stability diagram

A double quantum dot consists of two dots $i \in L, R$ in series, each tunnel coupled to a reservoir at rate Γ_i/\hbar and capacitively coupled to a local gate V_{gi} . The coupling between the two dots has two origins : the Coulomb repulsion parametrized by the mutual charging energy U_m and the tunnelling rate t/\hbar between the two dots. We assume the dots to be sufficiently isolated from the leads to be in the Coulomb blockade regime. If $t < k_B T$, tunnelling can be neglected and the state of the double dot is given by the occupancies (N, M) of the two dots. Invoking electrostatic arguments similarly to 1.2.1.1, one finds the stable charge state as a function of the gates and bias voltages. At zero bias, the stability diagram in the gate-gate plane exhibits the so-called honeycomb pattern (figure 1.4a). The V_{gi} axis controls the electron number in dot i. The diagonal

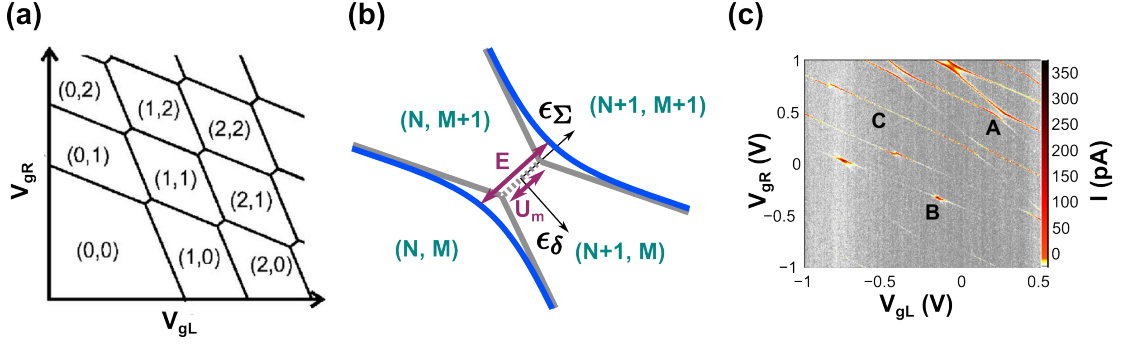


FIGURE 1.4: Charge stability diagram of a double dot depending on gate voltages V_{gL} and V_{gR} . **(a)** displays lines delimiting hexagons, within which a DQD charge state (N, M) is stable based on electrostatic arguments. N (M) is the electron number on the left (right) dot. N and M are well defined as long as tunnelling between the dots t can be neglected. **(b)** is a zoom showing how the presence of substantial interdot tunnelling $t > k_B T$ modifies the stability diagram close to the degeneracy line between $(N, M+1)$ and $(N+1, M)$ (dotted grey line). The straight plain grey lines corresponding to negligible t (like in **(a)**) turn into an anti-crossing (blue lines). In the first case, the distance between the lines is given by the mutual charging energy U_m , while in the latter case it accounts for the energy difference $E = U_m + \sqrt{\epsilon_\delta^2 + 4t^2}$ between bonding and anti-bonding hybrid states. ϵ_δ is the detuning between left and right energy levels. The perpendicular axis ϵ_Σ indicates the sum of the dot energies. **(c)** is a current colour plot as a function of left and right gate voltages. As expected, transport is maximum close to anti-crossings, no matter if they are clearly resolved (like A) or merged (like B). Indeed both dots are there resonant with the leads. Current may also be measured along cotunnelling lines, where only one dot is resonant with the leads (feature C).

axis ϵ_Σ controls the double dot total energy and corresponds to a symmetric charging of the two dots. The antidiagonal axis ϵ_δ , usually referred to as detuning, controls the energy difference between the two dots, and corresponds to internal charge transfer from one dot to the other.

The stability diagram is often measured by transport measurements (figure 1.4b,c). There is no current inside any (N, M) hexagon. Single-electron transfer can only occur if the electrochemical potentials of both dots are aligned with the Fermi level. This situation is realised at the hexagon vertices called triple points. On the hexagon edges, only two out of three electrochemical potentials are aligned. The edges in the diagonal direction are called degeneracy lines or zero-detuning lines : $(N, M+1)$ and $(N+1, M)$ charge states have the same energy along this segment of length U_m . An electron can oscillate between left and right dots, but current is zero because the energy state does not lie at the Fermi energy. On the other edges, one dot is resonant with its neighbouring lead. These edges, called cotunnelling lines, are named after the physical mechanism that allows transport through the non-resonant dot (see section 1.3.1 for a detailed explanation).

In presence of substantial interdot tunnelling $t > k_B T$ and close to degeneracy ($\epsilon_\delta < t$), left and right dot charge states hybridise, and the double dot eigenstates are no longer

($N, M+1$) and ($N+1, M$) states but superpositions of these, namely bonding and anti-bonding states. This leads to level repulsion, which can be measured in the current in the gate-gate plane (figure 1.4b). The spacing between the lines corresponds to the energy to pay to change the charge ground state between adjacent total number of electrons (from a state with ($N+M+1$) electrons to $((N+M+1)\pm 1)$ electrons):

$$E = U_m + \sqrt{\epsilon_\delta^2 + 4t^2} \quad (1.19)$$

Like the addition energy in a single dot, it has an electrostatic part U_m and a chemical part corresponding to the energy difference between B and AB states.

1.2.2.2 Charge qubit

Close to zero-detuning, B and AB states form a two-level system, that can be used as a qubit. The anti-crossing control parameter is the detuning ϵ_δ . The qubit frequency is given by $\hbar\Omega = \sqrt{\epsilon_\delta^2 + 4t^2}$. Preparing, manipulating and detecting the qubit state are the elementary operations required by quantum information processing. This was first achieved in 2003 [76] in GaAs 2DEG applying DC voltage pulses on the drain electrode and measuring current. The qubit coherence time $T_2 \sim ns$ given in this experiment remained of the same order of magnitude in following works in GaAs 2DEG ([77], [78]) as well as in Si [79] and carbon nanotube [52]. Although experiments differ from their qubit operation schemes and host material, charge noise is the shared limiting decoherence process. Charge noise is due to local charge hopping between potential minima created by defects. It causes fluctuations in gate potentials, thus in detuning and qubit frequency. The amplitude of the corresponding $1/f$ noise density is estimated to be few $10^{-4}e/\sqrt{Hz}$ with little variations between host materials.

1.2.2.3 Singlet-triplet spin qubit

Poor coherence properties of charge qubits foster research on qubits exploiting the electron spin degree of freedom. Single spin $\frac{1}{2}$ qubit, singlet-triplet qubit in double QD, exchange-only qubit with 3 electron spins are well established spin qubit architectures. Other proposals like spin-orbit or valley-spin qubits combine spin with other degrees of freedom. In the prospect of quantum information processing, current research issues in the field include operation fidelity, coherence properties, error correction, up-scaling. The purpose of this section is not to make a review on spin qubits, but to give an insight into this major topic of QDs by focusing on the singlet-triplet qubit. This particular choice provides the opportunity to introduce key concepts ruling spin physics in double dots.

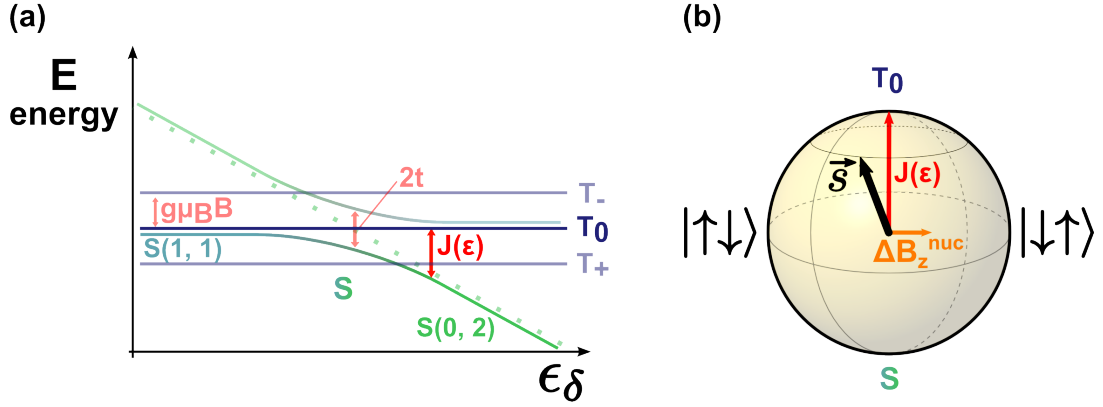


FIGURE 1.5: **Singlet-triplet qubit principle.** (a) depicts the energy level diagram of a double quantum dot close to the degeneracy line between (0, 2) and (1, 1) as a function of detuning ϵ_δ between the two states. Inter-dot tunnelling t results in an anticrossing between the singlet states $S(1, 1)$ and $S(0, 2)$ and leaves triplets unchanged. A magnetic field splits the three triplets by the Zeeman splitting $|g|\mu_B B$. The two energy levels S and T_0 defining the singlet-triplet qubit appear at the first front over the half-transparent rest of the spectrum. The energy level separation $J(\epsilon_\delta)$ is electrically controlled by ϵ_δ , which offer the possibility to perform qubit rotation around the z-axis of the Bloch sphere sketched in (b). Rotation around the x-axis is provided by the energy difference $2\Delta B_Z^{nuc}$ between $|\uparrow\downarrow\rangle$ and $|\downarrow\uparrow\rangle$ caused by the inhomogeneity of random nuclear magnetic fields between left and right dot.

We focus on the degeneracy line between (0, 2) and (1, 1) states. According to Pauli exclusion principle, two electron on the same orbital level must be in the singlet state $|S\rangle = \frac{|\uparrow\downarrow\rangle - |\downarrow\uparrow\rangle}{\sqrt{2}}$ (antisymmetric spin wavefunction). For the (0, 2) charge configuration to be in a spin triplet $T(0, 2)$, the two electron have to sit on different orbitals. Thus the orbital energy separates $T(0, 2)$ states from singlet ground state $S(0, 2)$. In the (1, 1) charge configuration, spins sit on different orbitals, so the four spin states are degenerate: there is one singlet state $S(1, 1)$ (spin 0) and three triplets (spin 1) $T_- = |\downarrow\downarrow\rangle$, $T_0 = \frac{|\uparrow\downarrow\rangle + |\downarrow\uparrow\rangle}{\sqrt{2}}$, $T_+ = |\uparrow\uparrow\rangle$. Electron tunnelling between the two dots preserves spin, so it can only hybridise $S(0, 2)$ with $S(1, 1)$, while triplets remain unchanged. Applying a magnetic field lifts the triplet degeneracy by separating T_\pm from T_0 by the Zeeman splitting $\Delta B_Z = \mp |g|\mu_B B$. Under this condition, T_0 and the hybridised singlet labelled S form a two-level system that can be operated as a qubit. For commodity the qubit state is depicted on a Bloch sphere with T_0 and S as north and south poles and $|\uparrow\downarrow\rangle$ and $|\downarrow\uparrow\rangle$ as eigenstates of the x-axis.

First implementation of such singlet-triplet qubit has been realised in GaAs 2DEG double QD [22]. Initialization, manipulation sequences like Rabi oscillations and spin-echo, as well as readout were demonstrated. Initialization of a singlet state close to $S(1, 1)$

consists in two steps : first go to positive detuning to obtain $S(0, 2)$, second apply a pulse to end up in the negative detuning region. Full manipulation of a qubit requires to control the energy difference between z-axis eigenstates as well as between x-axis eigenstates corresponding to rotation around z or x axis of the Bloch sphere. Here rotation around the z axis is electrically controlled. The energy separation $J(\epsilon_\delta)$ between S and T_0 strongly depends on ϵ_δ : for large negative detuning $J(\epsilon_\delta) \rightarrow 0$ and close to zero-detuning J becomes large $J(\epsilon = 0) = t$. J-pulse can be easily performed by applying gate voltage pulses. Rotation around the x-axis is much less controlled. Due to the inhomogeneity of nuclear spins orientation, electron spins in each dot experience a different local magnetic field. ΔB_Z^{nuc} is the Zeeman energy difference between left and right dot. $|\downarrow\uparrow\rangle$ and $|\uparrow\downarrow\rangle$ are eigenstates of this hamiltonian term with energies $\pm\Delta B_Z^{nuc}$. ΔB_Z^{nuc} varies on a typical time scale, which limits the coherence time : $T_2^* \approx 10ns$. Spin-echo experiments enable to compensate the effect of random nuclear fields and gives access to the enhanced coherence time $T_2 = 1.2\mu s$. The readout of the qubit state after manipulation is a projective measurement on $S(0, 2)$ and relies on Pauli blockade. A pulse is applied towards $S(0, 2)$ stability region. If the qubit is in the S state, it has a finite projection to $S(0, 2)$ and ends up in $S(0, 2)$ state. In contrast a qubit in T_0 is orthogonal to $S(0,2)$, and stays in $T(0)$, that is a $(1, 1)$ charge state. Using this spin-to-charge conversion mechanism, the qubit state is inferred from a charge sensing measurement of the dot charge state.

1.3 Kondo physics

Kondo physics occurs whenever a discrete degenerate state interacts with a fermionic reservoir. This general situation is a model system for many-body problems. That is why Kondo effect is a central issue in condensed matter, and has a long and rich history on both experimental and theoretical sides. The historical Kondo effect concerns a spin $\frac{1}{2}$ interacting with an electron gas. First experimental observations were made in metals containing magnetic impurities back in the 1930s [80]. In such metals, resistivity increases below a certain temperature (usually around 10K), which is unexpected as all standard scattering processes (electron-phonon and electron-electron) get frozen at low-temperature. An explanation was brought by Kondo in 1964 [81] based on an antiferromagnetic exchange interaction between the impurity and the electron spins. Refined theoretical description was provided by the renormalization group theory developed by Wilson in 1975 on the particular case of the Kondo problem [82]. The field has been renewed in the late 90s in the context of quantum dots. In the odd occupancy regime, a single electron sits on the last occupied spin-degenerate level, and plays the role of the magnetic impurity. The tunnel coupling to the leads mediates the exchange

interaction between dot and reservoirs spins (1.3.1). The advantages of such artificial impurities lie in the variety and tunability of devices. More exotic Kondo systems can be explored based on spin 1 [83] or orbital [84] degeneracies. Only spin $\frac{1}{2}$ Kondo effect will be described in this section.

1.3.1 From Anderson model to Kondo physics

The Anderson hamiltonian addresses the problem of an impurity in a metal. It is adapted to describe quantum dots in the following way :

$$H = H_d + H_{leads} + H_t \quad (1.20)$$

The dot hamiltonian H_d disregards all levels except the last occupied. It describes a single spin-degenerate level at energy ϵ_d with occupation $\hat{n}_d = \sum_{\sigma \in (\uparrow, \downarrow)} d_\sigma^\dagger d_\sigma$ (d_σ annihilates an electron with spin σ) and charging energy U .

$$H_d = \epsilon_d \hat{n}_d + \frac{U}{2} \hat{n}_d (\hat{n}_d - 1) \quad (1.21)$$

The lead hamiltonian writes :

$$H_{leads} = \sum_{\alpha \in (L, R), k, \sigma} (\epsilon_{k\sigma} - \mu_\alpha) c_{\alpha k \sigma}^\dagger c_{\alpha k \sigma} \quad (1.22)$$

where k labels the orbital degree of freedom in the leads, and $\alpha \in (L, R)$ refers to the left/right lead. Finally, the tunnelling hamiltonian writes :

$$H_t = \sum_{\alpha \in (L, R), k, \sigma} t_\alpha d_\sigma^\dagger c_{\alpha k \sigma} + h.c \quad (1.23)$$

Consider the situation when the gate voltage is tuned inside a Coulomb diamond with an odd number of electrons. This so-called "local moment" regime corresponds to $\langle \hat{n}_d \rangle = 1$. Single-electron processes are blocked because both empty and doubly-occupied states have energies $E_0 = 0$ and $E_2 = 2\epsilon_d + U$ higher than the single-occupied state energy $E_1 = \epsilon_d$. However second-order tunnelling processes occur involving a zero or double occupancy virtual state. To describe the local moment regime, it is convenient to derive an effective hamiltonian in the single occupancy subspace. Schrieffer and Wolf proposed a canonical transformation $H_S = e^{iS} H e^{-iS}$ [85] that removes tunnelling linear terms, which pull the system out of the single-occupancy subspace. The term H_S is developed to second order in tunnelling, and only processes conserving single-occupancy are kept

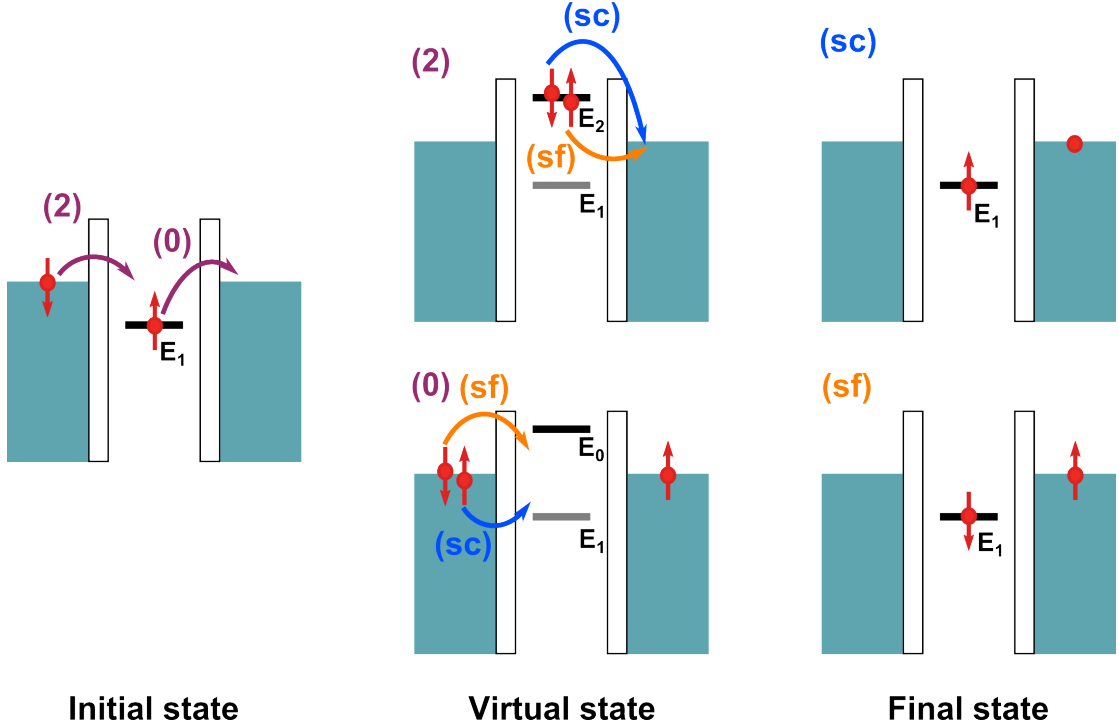


FIGURE 1.6: **Second-order tunnelling processes occurring within the single-occupancy subspace.** At each step the black level indicates the dot state. From an initial state with one spin-up electron at energy E_1 the dot can spend a short time in a doubly-occupied (2) or empty (0) states at energies E_2 or E_0 higher than E_1 (virtual state). Depending on which spin goes in or out of the dot, the dot ends up in a final state with the same or opposite spin as in the initial state. Spin-conserving processes are labelled (sc) and depicted with blue arrows while spin-flipping processes are labelled (sf) and depicted with orange arrows.

(figure 1.6). This yields to the effective low-energy Anderson hamiltonian :

$$H_{\text{eff}} = H_d + H_{\text{leads}} + H_{\text{scattering}} \quad (1.24)$$

with :

$$H_{\text{scattering}} = \sum_{\alpha\alpha'} J_{\alpha\alpha'} \left(\vec{s}_{\alpha\alpha'} \cdot \vec{S} \right) + \sum_{kk',\alpha\alpha',\sigma} W_{\alpha\alpha'} c_{\alpha k\sigma}^\dagger c_{\alpha' k'\sigma} \quad (1.25)$$

Both terms come from second-order tunnelling involving empty and doubly-occupied virtual states, as illustrated by the expressions for the scattering energies :

$$J_{\alpha\alpha'} = 2 \left(\frac{t_\alpha t_{\alpha'}}{E_2 - E_1} + \frac{t_\alpha t_{\alpha'}}{E_0 - E_1} \right) = \frac{2U t_\alpha t_{\alpha'}}{(\epsilon_d + U)(-\epsilon_d)} > 0 \quad (1.26)$$

and

$$W_{\alpha\alpha'} = -\frac{1}{2} \left(\frac{t_\alpha t_{\alpha'}}{E_2 - E_1} + \frac{t_\alpha t_{\alpha'}}{E_1 - E_0} \right) = \frac{(2\epsilon_d + U) t_\alpha t_{\alpha'}}{2(\epsilon_d + U)(-\epsilon_d)} > 0 \quad (1.27)$$

However the two terms account for different scattering processes, whether or not the

spin plays a role. The first term is called the Kondo hamiltonian and expresses an antiferromagnetic spin-spin interaction between the dot spin $\frac{1}{2} \vec{S}$ and the local spin density of itinerant electron $\vec{s}_{\alpha\alpha'} = \sum_{k,k',\sigma,\sigma'} c_{\alpha k\sigma}^\dagger \frac{\vec{\sigma}_{\sigma\sigma'}}{2} c_{\alpha' k'\sigma'}$. It involves joint dot and lead electron spin-flips, while the second term is independent of spin and acts as a potential scattering.

The picture of a many-body antiferromagnetic exchange interaction is obvious in the Kondo hamiltonian formula. Replacing the spin density \vec{s} by a single reservoir electron spin, we see immediately that at half-filling ($\epsilon_d = -U/2$), the ground state will be a singlet formed by the spin sitting on the dot and the reservoir spin. In fact, many conduction electron spins take part in the formation of a many-body singlet ground state. They constitute the so-called Kondo cloud.

Current flowing through the device is related to tunnelling rates between reservoirs, which can be calculated perturbatively with respect to $H_{scattering}$. To first order in $H_{scattering}$, the tunnelling amplitude is given by the standard cotunnelling formula. However, the tunnelling amplitude calculated to second order in $H_{scattering}$ (fourth order in tunnelling matrix elements) diverges below a certain energy $k_B T_K$, defining the Kondo temperature T_K . This low-energy divergence is caused by the spin-flip scattering term. Because it was pointed out by Kondo, it was named "the Kondo problem".

1.3.2 Kondo resonance conductance and universality

The Kondo problem reveals two main properties of the Kondo effect. Firstly conductance is high, though inside a Coulomb blocked region. Despite its finite value predicted by more evolved theoretical models, the conductance at $T < T_K$ remains greatly enhanced, and can reach the value for a perfected transmitted channel $\frac{2e^2}{h}$ [86]. The low-energy divergence condition also requires $eV_{SD} < k_B T_K$. The Kondo resonance thus manifests itself by a zero-bias line inside a Coulomb diamond in the $V_g - V_{SD}$ conductance map. This is the characteristic Kondo ridge. Secondly the emergence of a single energy scale characterizing the divergence suggests scaling laws involving T_K . This makes the success of the renormalization group theory. All physical quantities are universal functions of dimensionless parameters, $k_B T_K$ being the scaling energy. Conductance and current noise spectral density are functions of $\frac{T}{T_K}$, $\frac{eV_{SD}}{k_B T_K}$, $\frac{g\mu_B B}{k_B T_K}$. Conductance versus bias voltage exhibits a peak of width $\sim T_K$. Measurements for several samples with different T_K collapse on a single function as illustrated on figure 1.7.

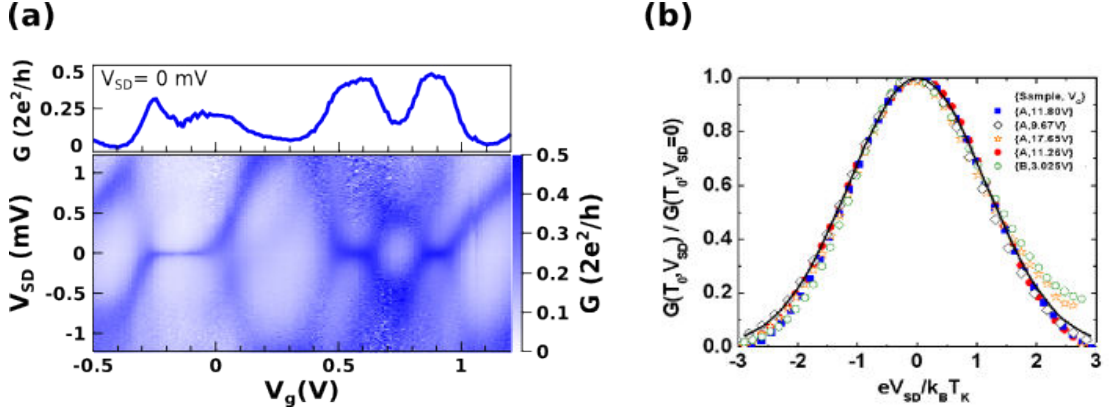


FIGURE 1.7: **Phenomenology of Kondo effect.** (a) lower panel displays a conductance colour plot in the bias-gate voltages plane, while the upper panel shows a gate line scan at zero bias. Kondo ridges are visible at zero-bias within every other Coulomb diamond characteristic of double degeneracy (Kondo SU(2)). This means that spin-degeneracy is the only degeneracy in the system in contrast with four-degeneracy when additional valley degeneracy matters (Kondo SU(4)). On a gate line scan the Kondo effect manifests itself as a conductance plateau between Coulomb peaks, which can either be constant or exhibit a shallow dip. (b) shows universality of conductance vs bias voltage at the Kondo resonance. Curves obtained for different samples with different T_K collapse onto a single curve once eV_{SD} is rescaled by T_K graph taken from [87].

1.4 Quantum dot circuits with superconducting contacts

Transport in hybrid structures combining normal metals and superconductors was studied extensively in thin films geometry. Proximity effect was demonstrated, namely the fact that a normal metal in contact with a superconductor becomes superconducting over a certain length. Contacting quantum dots with superconducting electrodes was expected to yield new features in transport.

Some can be intuited by considering the sequential tunnelling regime, where electrons tunnel one by one because of Coulomb interaction. Considering only quasiparticle transport, formula 1.14 in section 1.2.1.2 shows that the tunnelling energy Γ is dressed by the density of states of the leads. In case of superconducting contacts, the quasiparticle density of states is zero at low-energy over a 2Δ -wide gap, and for higher energies writes $\nu_S(E) = \frac{|E|}{\sqrt{E^2 - \Delta^2}} \nu_N$, Δ being the superconducting gap. In this so-called "semiconductor picture" depicted in figure 1.8a and b, current through a S-QD-N device is expected to exhibit a 2Δ -wide gap around zero-bias and maxima at $eV_{SD} = \pm\Delta$ reflecting peaks in the superconducting density of states (figure 1.8 c). In a S-QD-S device, these features appear at $eV_{SD} = \pm 2\Delta$ and were observed for the first time in 1995 on metallic grains [89]. They have been reproduced in QDs based on NW, CNT, self-assembled quantum dots and molecules like fullerenes (see [90] for a review).

In addition to quasiparticle transport, supercurrent carried by Cooper pair may flow through quantum dots. This can be understood easily in a non-interacting quantum

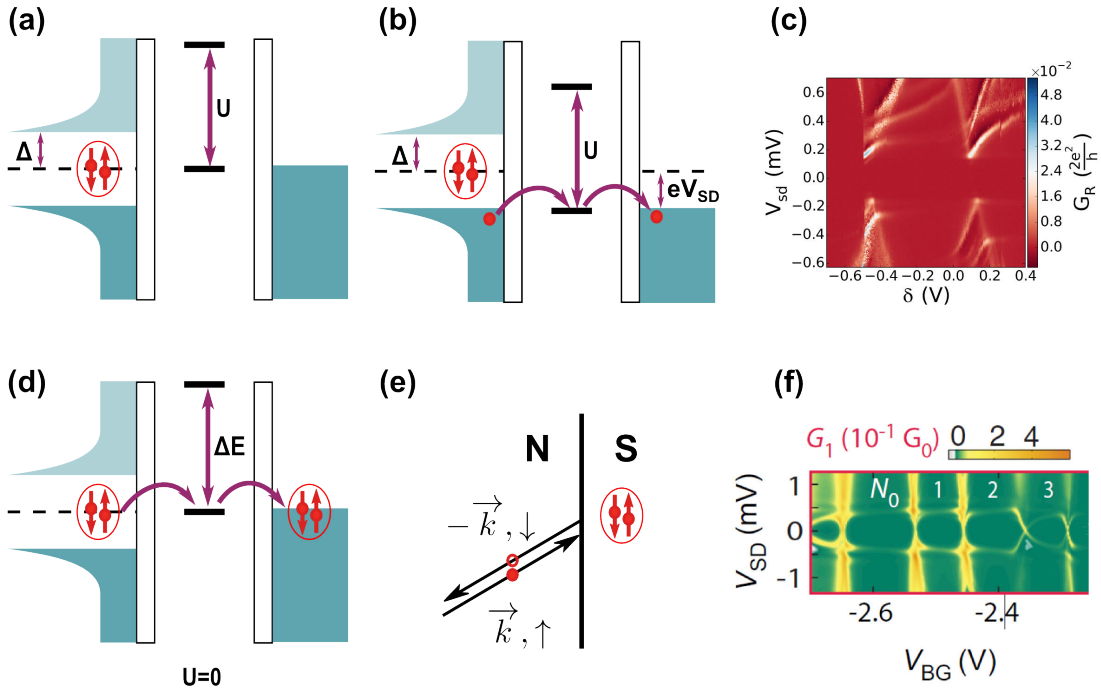


FIGURE 1.8: **Simple explanation of different transport features observed in S-QD-N devices.** In the presence of strong interactions transport is dominated by single-particle sequential tunnelling. It is blocked when the dot energy lies within the superconducting gap (sketch (a)) and it flows when the bias voltage exceeds the gap (sketch (a)). (c) shows experimental data corresponding to such parameter regime. In the opposite regime where Coulomb interactions are negligible, Cooper pairs can tunnel through the dot ((d)). This can be understood using a scattering formalism using the concept of Andreev reflection sketched on (e). The existence of sub-gap states named Andreev Bound States is predicted, which results in sub-gap transport (f) (data taken from [88]).

dot. Because two electrons with opposite spin can sit on the same energy level, a Cooper pair can travel through the dot each time an energy level ϵ_d is resonant with the Cooper pairs condensate lying at the superconducting chemical potential μ_S (figure 1.8 d). A common theoretical approach to derive the sub-gap current is a scattering formalism invoking Andreev reflections. An Andreev reflection happens at the interface between a normal metal and a superconductor and consists in the reflection of an electron \vec{k}, \uparrow into a hole $-\vec{k}, \downarrow$ (figure 1.8 e). The result is the transfer of a Cooper pair from normal metal to superconductor, or vice-versa via the reverse mechanism. For a confined conductor like a QD, interfaces between the circuit elements also lead to Andreev and/or normal reflections. The resonance condition predicts the existence of discrete energy states inside the gap, called Andreev Bound States (ABS). These states carry sub-gap current, as shown in the data presented in figure 1.8 f.

An alternative theoretical approach to describe quantum dots contacted to superconducting electrodes is the hamiltonian formalism. In section 1.4.1 we derive an effective hamiltonian for a Dot-S device in the large gap limit. In section 1.4.2 we address the

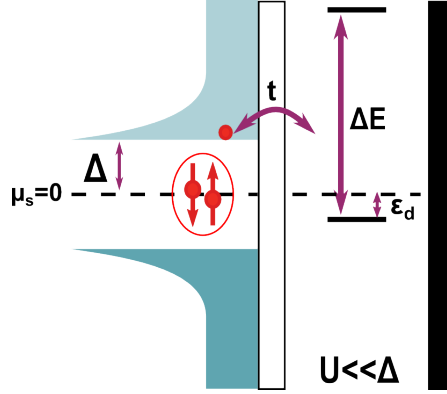


FIGURE 1.9: Parameters regime for the effective description of the S-QD device given by equation 1.34 to be valid. $\Gamma = 2\pi|t|^2\nu_N$ has also to be much smaller than Δ .

Cooper pair splitter device, which is a central topic of this thesis. While the splitting of Cooper pairs into two different quantum dots can be described as crossed Andreev reflections, the hamiltonian approach is better suited to understand the device microscopic states.

1.4.1 Proximity effect in a quantum dot

We consider a spin-degenerate single-level non-interacting quantum dot connected to one superconducting electrode with a large gap Δ . The energy reference is the superconductor chemical potential, which is set to zero. The dot energy level ϵ_d lies deep inside the gap. This implies $\Delta E \gg \Delta \gg \Gamma \gg U$ and $\epsilon_d \ll \Delta$. The situation is depicted on figure 1.9 and is described by the following hamiltonian :

$$H = H_d + H_{sc} + H_t \quad (1.28)$$

$H_d = \epsilon_d \hat{n}_d$ is the dot hamiltonian with $U=0$ (section 1.3.1). The superconducting electrode is described by :

$$H_{sc} = \sum_{k,\sigma} E_{k\sigma} \gamma_{k\sigma}^\dagger \gamma_{k\sigma} \quad (1.29)$$

where $\gamma_{k\sigma}$ annihilates a Bogoliubov quasiparticle with energy $E_k = \sqrt{\xi_k^2 + \Delta^2}$. ξ_k is the normal state single electron energy. Bogoliubov quasiparticles are excitations of the BCS ground state and thus verify $\gamma_{k\sigma} |BCS\rangle = 0$. They are superpositions of electron and hole excitations. More precisely :

$$\begin{aligned} \gamma_{k,\uparrow} &= u_k c_{k\uparrow} - v_k c_{-k\downarrow}^\dagger \\ \gamma_{-k\downarrow}^\dagger &= u_k^* c_{-k\downarrow}^\dagger + v_k^* c_{k\uparrow} \end{aligned} \quad (1.30)$$

with

$$\begin{aligned} u_k &= e^{-i\frac{\phi}{2}} \sqrt{\frac{1}{2} \left(1 + \frac{\xi_k}{\sqrt{\Delta^2 + \xi_k^2}} \right)} \\ v_k &= -e^{i\frac{\phi}{2}} \sqrt{\frac{1}{2} \left(1 - \frac{\xi_k}{\sqrt{\Delta^2 + \xi_k^2}} \right)} \end{aligned} \quad (1.31)$$

H_t describes electron tunnelling between the dot and the superconducting contact. Adapting formula 1.23 to the single contact case yields $H_t = t \sum_{k,\sigma} d_\sigma^\dagger c_{k\sigma} + h.c.$

At low-temperature there are no excitations in the superconductor. An effective hamiltonian can be derived in this subspace. As H_t is linear in γ , it creates Bogoliubov excitations. It can be eliminated to first order by performing a Schrieffer-Wolff transformation similarly to section 1.3.1 : $H_S = e^{iS} H e^{-iS}$ with :

$$S = i \sum_{k\sigma} (X_{k\sigma} \gamma_{k\sigma} - h.c.) \quad (1.32)$$

and :

$$\begin{aligned} X_{k\uparrow} &= \frac{t u_k^*}{E_k - \epsilon_d} d_\uparrow^\dagger + \frac{t^* v_k^*}{E_k + \epsilon_d} d_\downarrow \\ X_{k\downarrow} &= \frac{t u_k^*}{E_k - \epsilon_d} d_\downarrow^\dagger - \frac{t^* v_k^*}{E_k + \epsilon_d} d_\uparrow \end{aligned} \quad (1.33)$$

The general principle of a Schrieffer-Wolff transformation and the mathematical check of the specific transformation given by 1.32 and 1.33 are presented in appendix A. After calculation detailed in appendix A, the expansion of H_S to second-order in t yields the following effective hamiltonian $H_{d,\text{eff}}$ for the QD :

$$H_{d,\text{eff}} = \tilde{\epsilon}_d \hat{n}_d + \left(\Gamma_C d_\uparrow^\dagger d_\downarrow^\dagger + h.c. \right) + \text{constant} \quad (1.34)$$

The dot energy

$$\tilde{\epsilon}_d = \epsilon_d \left(1 - \pi |t|^2 \nu \frac{1}{\sqrt{\Delta^2 - \epsilon_d^2}} \right) \quad (1.35)$$

is renormalized by the presence of the superconductor. However the main effect of the superconductor is to hybridise the dot empty and doubly-occupied states via the matrix element $\Gamma_C = \pi t^2 e^{i\phi} \nu \frac{1}{\sqrt{1 - \left(\frac{\epsilon_d}{\Delta}\right)^2}}$, where ν is the normal density of states at the Fermi

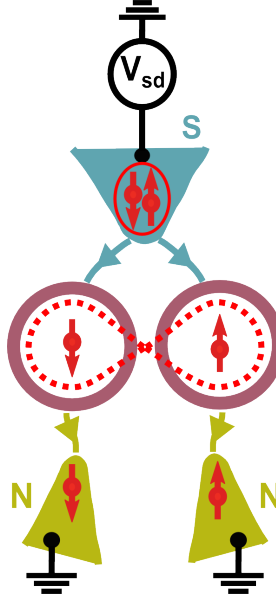


FIGURE 1.10: **Sketch of a Cooper pair splitter device.** A central superconducting electrode (blue) is contacted to both left and right dot of a double dot (purple). The two lateral contacts of the double dot are normal electrodes (green). Electrons transport in the desired working regime is drawn in red : Cooper pairs from the superconductor get split into spatially separated orbitals, while keeping the spin singlet character of the pair. Each electron then tunnels independently to the closest lead.

level. The matrix representation of $H_{d,\text{eff}}$ in the $(|0\rangle, |\uparrow\downarrow\rangle, |\uparrow\rangle, |\downarrow\rangle)$ basis is :

$$H_{d,\text{eff}} = \begin{pmatrix} 0 & \Gamma_C^* & 0 & 0 \\ \Gamma_C & 2\tilde{\epsilon}_d & 0 & 0 \\ 0 & 0 & \tilde{\epsilon}_d & 0 \\ 0 & 0 & 0 & \tilde{\epsilon}_d \end{pmatrix} \quad (1.36)$$

By diagonalizing the even occupancy block, one finds the following eigenstates :

$$|\Psi_{\pm}\rangle = \left(\frac{\Gamma_C^*}{\sqrt{|\Gamma_C|^2 + E_{\pm}}} + \frac{E_{\pm}}{\sqrt{|\Gamma_C|^2 + E_{\pm}}} d_{\uparrow}^{\dagger} d_{\downarrow}^{\dagger} \right) |0\rangle \quad (1.37)$$

with eigenenergies :

$$E_{\pm} = \tilde{\epsilon}_d \pm \sqrt{\tilde{\epsilon}_d^2 + |\Gamma|^2} \quad (1.38)$$

Equation 1.37 shows that the dot states in presence of a superconductor have a very similar structure as Cooper pairs $u_k + v_k c_{k\uparrow}^{\dagger} c_{-k\downarrow}^{\dagger}$. Superconducting correlations are induced on the dot : this can be seen as an "atomistic" proximity effect.

1.4.2 Cooper pair splitter

A Cooper pair splitter exploits the proximity effect in a beamsplitter geometry (figure 1.10). A central superconducting electrode is contacted to both left and right dot of a double dot. The two lateral contacts of the double dot are normal electrodes. We first discuss the superconducting-double-dot system alone and forget about the normal reservoirs. Superconducting correlations may be induced locally in each dot as described in the single dot case. In addition non-local superconducting correlations are induced: the two electrons forming a Cooper pair are split and one sits on each dot. Strong Coulomb interactions make on-site double-occupancy unlikely, which highly favours non-local correlations with respect to local correlations. Taking the same path as in previous section an effective hamiltonian can be derived in the large gap limit from the following original double-dot-S hamiltonian :

$$H = \sum_{i \in L, R} \epsilon_i \hat{n}_i + \sum_{k, \sigma} E_{k\sigma} \gamma_{k\sigma}^\dagger \gamma_{k\sigma} + \sum_{i \in L, R} \left(t_i \sum_{k, \sigma} d_{i, \sigma}^\dagger c_{k\sigma} e^{i\mathbf{k} \cdot \mathbf{r}_i} + h.c \right) \quad (1.39)$$

with \mathbf{r}_i the spatial coordinate, where tunnelling occurs between the superconductor and dot i . We perform a Schrieffer-Wolff transformation similarly to the single dot case (see Appendix A for the explicit formula). Expanding to second order in tunnelling rates and assuming that on-site double occupancy is forbidden, leads to the effective hamiltonian :

$$H_{\text{eff}} = \sum_{i \in L, R} \epsilon_i \hat{n}_i + \left[t_{eh} \left(d_{L\uparrow}^\dagger d_{R\downarrow}^\dagger - d_{L\downarrow}^\dagger d_{R\uparrow}^\dagger \right) + t_{ee}^{\text{ind}} \sum_{\sigma} d_{L\sigma}^\dagger d_{R\sigma} + h.c. \right] \quad (1.40)$$

with the Cooper pair splitting term :

$$t_{eh} = \pi t_L t_R e^{i\phi} \nu f(\delta x) \sum_{i \in L, R} \frac{1}{2} \frac{1}{\sqrt{1 - \left(\frac{\epsilon_i}{\Delta} \right)^2}} \quad (1.41)$$

and the superconducting-induced interdot tunnel element :

$$t_{ee}^{\text{ind}} = -\pi t_L t_R^* \nu f(\delta x) \frac{\epsilon_L + \epsilon_R}{\Delta} \sum_{i \in L, R} \frac{1}{2} \frac{1}{\sqrt{1 - \left(\frac{\epsilon_i}{\Delta} \right)^2}} \quad (1.42)$$

which both depend on the geometrical factor :

$$f(\delta x) = \cos(k_F \delta x) \frac{\sum_i F(\epsilon_i) e^{-\frac{|\delta x|}{F(\epsilon_i) \xi_0}}}{\sum_i F(\epsilon_i)} \quad (1.43)$$

with $F(\epsilon_i) = \frac{1}{\sqrt{1 - \left(\frac{\epsilon_i}{\Delta}\right)^2}}$ and k_F the Fermi wavevector. The geometrical factor depends on the dimension and is given here in the one-dimensional case. Cooper pairs are injected in the two dots at a distance $|\delta x| = |x_L - x_R|$. $f(\delta x)$ is normalized, such that $f(\delta x = 0) = 1$. For $f(\delta x)$ not to cancel t_{eh} and t_{ee}^{ind} , $|\delta x|$ which should be smaller than the superconducting coherence length ξ_0 ($\xi_0 \sim 100nm$ in Aluminium).

Note that Coulomb repulsion was invoked to favour non-local versus local Cooper pair injection, but was not treated explicitly in the original hamiltonian. We do not expect the presence of splitting and superconducting-induced interdot tunnelling effects in the effective hamiltonian to be affected by a full treatment of interactions. However, the dependence of the coefficients t_{eh} and t_{ee}^{ind} with respect to parameters will be affected by interactions. This statement extends to the presence of an intrinsic interdot tunnelling t , which we have not considered above.

The matrix representation in the $(|0\rangle, |S\rangle, |T_0\rangle, |T_+\rangle, |T_-\rangle, |\uparrow 0\rangle, |0 \uparrow\rangle, |\downarrow 0\rangle, |0 \downarrow\rangle)$ basis is block-diagonal $H_{\text{eff}} = \begin{pmatrix} H_e & 0 \\ 0 & H_o \end{pmatrix}$. The decoupling between even and odd blocks is expected, because in our description, particles going in or out the double dot can only be Cooper pairs. The matrix representation in the even sector writes :

$$H_e = \begin{pmatrix} 0 & \sqrt{2}t_{eh}^* & 0 & 0 & 0 \\ \sqrt{2}t_{eh} & \epsilon_\Sigma & 0 & 0 & 0 \\ 0 & 0 & \epsilon_\Sigma & 0 & 0 \\ 0 & 0 & 0 & \epsilon_\Sigma & 0 \\ 0 & 0 & 0 & 0 & \epsilon_\Sigma \end{pmatrix} \quad (1.44)$$

The superconductor main effect is to hybridise the double dot empty $|0\rangle = (0,0)$ and singlet $|S\rangle = S(1,1)$ states via the matrix element t_{eh} . Triplets remain eigenstates. Diagonalization of the $(|0\rangle, |S\rangle)$ sector yields eigenstates :

$$|V_{1(2)}\rangle = \frac{\sqrt{2}t_{eh}^*}{\sqrt{2|t_{eh}|^2 + E_{1(2)}}} |0\rangle + \frac{E_{1(2)}}{\sqrt{2|t_{eh}|^2 + E_{1(2)}}} |S\rangle \quad (1.45)$$

with eigenenergies :

$$E_{V_{1(2)}} = \frac{1}{2} \left(\epsilon_\Sigma \pm \sqrt{\epsilon_\Sigma^2 + 8|t_{eh}|^2} \right) \quad (1.46)$$

The energy levels diagram is shown on figure 1.11. Equation 1.41 shows that to first order in ϵ_i/Δ , t_{eh} does not depend on the dot energies. Taking t_{eh} constant, V_1 and V_2 anti-crossing parameter control is the energy sum $\epsilon_\Sigma = \epsilon_L + \epsilon_R$ and the minimum energy splitting between V_1 and V_2 is $2\sqrt{2}t_{eh}$. V_1 and V_2 contain the entangled state $|S\rangle$, which

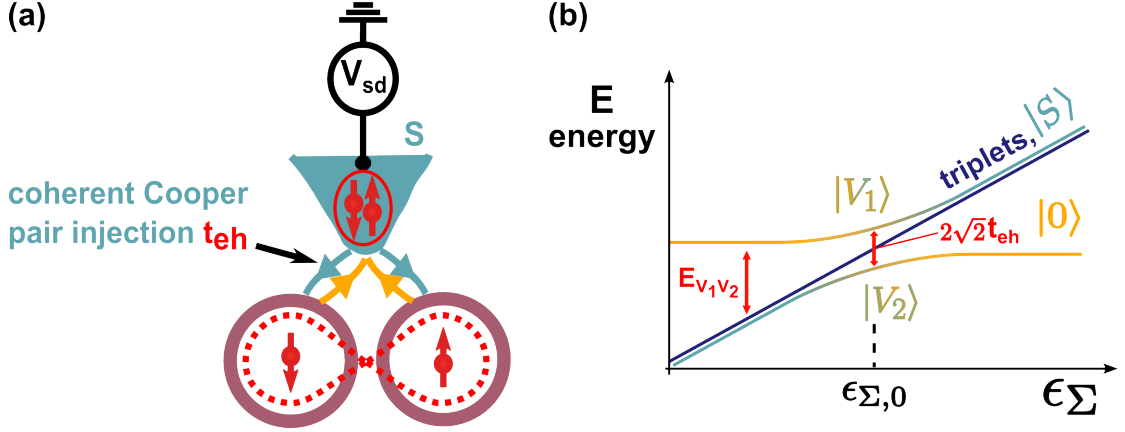


FIGURE 1.11: Sketch (a) and simplified level diagram (b) of the S-DQD device. The coherent injection of Cooper pair quantified by the matrix element t_{eh} hybridises empty (yellow) and singlet $S(1,1)$ (blue) states. This results in an anti-crossing of hybrid states V_1 and V_2 as a function of the dots energy sum ϵ_Σ . Minimum energy separation $E_{V_1V_2} = 2\sqrt{2}t_{eh}$ between these levels happens at $\epsilon_{\Sigma,0}$. Triplets energy dispersion is not affected by the superconductor and remains linear in ϵ_Σ .

explains why a Cooper pair splitter is considered as a source of distant entangled spins.

In the odd sector, the matrix representation reads :

$$H_o = \begin{pmatrix} \epsilon_L & t_{ee}^{ind} & 0 & 0 \\ t_{ee}^{ind*} & \epsilon_R & 0 & 0 \\ 0 & 0 & \epsilon_L & t_{ee}^{ind} \\ 0 & 0 & t_{ee}^{ind*} & \epsilon_R \end{pmatrix} \quad (1.47)$$

An interesting effect is the induced energy-dependant hopping term t_{ee}^{ind} between left and right dots. This corresponds to a cotunnelling process : an electron from one dot can virtually excite a quasiparticle in the superconductor and tunnel to the other dot. Equations 1.42 and 1.41 show that Cooper pair splitting and induced interdot tunnelling are related by $\left| \frac{t_{ee}^{ind}}{t_{eh}} \right| = \frac{\epsilon_\Sigma}{\Delta}$. To first order in ϵ_i/Δ , t_{ee}^{ind} is linear with ϵ_Σ . Diagonalization of each $(|\sigma, 0\rangle, |0, \sigma\rangle)$ block leads to spin-degenerate bonding $|\Psi_{B,\sigma}\rangle$ and antibonding $|\Psi_{AB,\sigma}\rangle$ states :

$$|\Psi_{B(AB),\sigma}\rangle = \frac{1}{\sqrt{(E_{B(AB)} - \epsilon_R)^2 + |t_{ee}^{ind}|^2}} \left(t_{ee}^{ind} |\sigma, 0\rangle + \frac{|t_{ee}^{ind}|^2}{E_{B(AB)} - \epsilon_R} |0, \sigma\rangle \right) \quad (1.48)$$

with eigenenergies :

$$E_{B(AB)} = \frac{1}{2} \left(\epsilon_\Sigma \pm \sqrt{\epsilon_\Sigma^2 + 4|t_{ee}^{ind}|^2} \right) \quad (1.49)$$

Ideally, the presence of normal leads in the isolated limit $\Gamma_{L/R} \ll k_B T \ll t_{eh}$ acts as

a spectroscopic probe, and reveals the level diagram structure without affecting it. At $\epsilon_\Sigma = \epsilon_{\Sigma,0}$ hybridization between singlet and empty states is maximum. There the charge can fluctuate most, and one expects a maximum in the current from the superconductor to any lead. This is the so-called two-particle resonance as it happens at a fixed value $\epsilon_{\Sigma,0}$ of the sum of the dot energies $\epsilon_\Sigma = \epsilon_L + \epsilon_R$. In our simplified model, we see that $\epsilon_{\Sigma,0} = 0$, which means that the current resonance due to pair splitting occurs when $\epsilon_L = -\epsilon_R$. In more complex cases, $\epsilon_{\Sigma,0}$ is non-zero and may be related to spin-orbit interaction or coupling between valleys K and K' [91]. The two-particle resonance is predicted by a master equation approach [91], which is valid in the sequential tunnelling regime and when the dot-lead coupling is weaker than the dot-superconductor coupling. The two-particle resonance in the current was also predicted in the opposite regime, where the normal contacts are more transparent than the superconducting contact, provided that $\Delta, U, \Delta E > eV_{SD} > \Gamma_{L/R}, k_B T$ [27].

In practice, transport experimental studies of Cooper pair splitter devices [30–35] were all performed with rather "open" dots with $\Gamma_{L,R} \sim \Delta$ and do not fully correspond to the two parameter regimes mentioned above. This explains why the two-particle resonance has not been reported so far. In most studies, pair splitting processes were demonstrated and evaluated by comparing simultaneously measured left and right current. Based on a probabilistic analysis, such experiments enable to state that charge pairs preferably split and go each through a different dot. However they investigate neither coherent splitting, nor entanglement of the split pairs. Positive noise current cross-correlations were measured [34]. Historically considered as a proof of the singlet - thus entangled - nature of the split pairs [92], it was later demonstrated that such positive correlations still hold if the splitter is replaced by a chaotic cavity, which destroys phase coherence [93, 94]. The focus was put on increasing pair splitting compared to competing processes such as local-pair-injection and elastic cotunnelling. 90% splitting efficiency was achieved [33]. Recent progress in the field includes the implementation of CPS in graphene [36, 37], while original experiments were performed with CNT [31] and InAs NW [30].

Further experiments are needed to investigate the coherence of splitting, and entanglement of split pairs. Exploring coherence properties by transport measurements is very challenging, as tunnelling rate should be high enough for the current to be measurable, and low enough for the coherence to be preserved. On the contrary, cavity QED is a natural probe of closed systems, as light-matter interaction was historically exploited to probe and manipulate atomic degrees of freedom. These tools and concepts have been applied to on-chip circuit-based "artificial atoms" embedded in microwave superconducting resonators. This led to the emergence of the circuit QED field, which brings further insight into the dynamics of mesoscopic systems.

Chapter 2

cQED architecture as a probe of dynamics of mesoscopic systems

2.1	Microwave response of mesoscopic circuits	43
2.1.1	Universal charge relaxation	44
2.1.2	Dynamics of Kondo physics	45
2.1.3	ABS spectroscopy	45
2.2	Mesoscopic circuit QED	46
2.2.1	Cavity description : Input-output theory	46
2.2.2	Different coupling schemes to the cavity electromagnetic field	48
2.2.3	Dissipationless description of a superconducting qubit-cavity system	50
2.2.4	Mesoscopic circuit QED experiments	53
2.3	Linear response of circuit to microwave field	55
2.3.1	Cavity transmission in the circuit linear response regime	55
2.3.2	Adiabatic limit	56
2.4	Master equation treatment of coherent coupling between cavity and circuit electronic transitions	57
2.4.1	Isolated two-level system	57
2.4.2	Case of a three-level system in a ladder geometry	59

Beyond DC transport measurements, one interest of microwave measurements is to probe the dynamics of mesoscopic systems by using frequencies of the same order of magnitude as the system relevant energy scales. 2.1 illustrates this principle : the microwave photon energy is typically close to the tunnelling rate to study charge tunnelling dynamics in a quantum dot coupled to a single reservoir, it is close to the Kondo temperature to study Kondo dynamics, and it is close to ABS energy spacing to perform ABS spectroscopy.

On top of providing information about dynamics, the use of microwave resonators has two main motivations. First, coupling a system to a high quality factor resonator is a widely used strategy to measure it with high sensitivity. This principle is for example exploited in Atomic Force Microscopy or in mass measurement using piezoelectricity. In the mesoscopic community, a pioneer work used this strategy in 1995 by coupling a microwave resonator to mesoscopic rings [95]. Second, the cavity can be in the quantum regime, and one can perform cQED experiments to explore rich physics about quantum light-matter interaction. This idea is being developed in atomic physics for several decades. It entered the field of superconducting qubits a decade ago. More recently cQED architecture were implemented in the mesoscopic circuits community. Finally, even in the classical regime, cavities probe transport processes in a complementary way than current measurements. Consequently, simultaneous cavity-current crossed characterisation can be instrumental in the complete understanding of a device. Key concepts and a brief review of mesoscopic QED are provided in 2.2, as starting point to address the field. Quantitative theoretical approaches are detailed in 2.3 and 2.4 for two different coupling regimes.

2.1 Microwave response of mesoscopic circuits

Microwave measurements of mesoscopic circuits provide further knowledge on quantum transport, in addition to DC measurements. The idea is to probe the system dynamics by applying an excitation, which frequency is comparable to a device characteristic energy scale. Microwave resonators are not the only way to apply microwaves to a mesoscopic circuit. For fifty years, the finite-frequency response of mesoscopic circuits has been investigated by applying microwave voltage/current signals directly to the circuit electrodes [57, 58]. In addition to their fundamental interest, such studies also have a technological interest, as operating nano-electronic devices at high-frequency is valuable. In the context of quantum information, the operating speed is even more crucial for fighting decoherence. In this section, we do not aim at reviewing the long-standing use of microwaves to probe quantum transport. The idea is rather to give a flavour of it, by presenting selected experiments closely related to this thesis work.

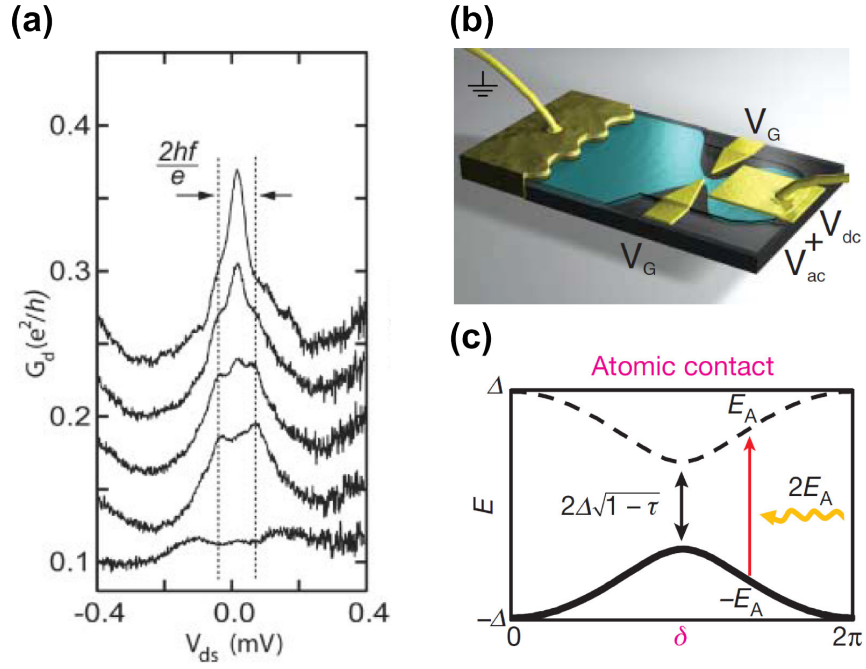


FIGURE 2.1: **Some experiments using microwaves to probe the dynamics of mesoscopic circuits.** (a) displays the conductance versus bias voltage V_{ds} in the Kondo regime, while a microwave voltage V_{ds}^{ac} is applied between source and drain. From top to bottom the curves are respectively measured with V_{ds}^{ac} equal to 29, 45, 60, 67, 144 μV . The scale is correct for the bottom curve and each successive curve is offset by $0.04 e^2/h$ for clarity. Source: [60]. (b) is a sketch of the 2DEG based device, where charge relaxation was first explored. Gate electrodes polarised with V_G form a quantum point contact which connects a quantum dot (on the right) to a reservoir (on the left). A large gate electrode is depicted in gold on the quantum dot. It can be AC biased with a microwave voltage V_{ac} . AC current is collected through the reservoir electrode. Source: [66]. (c) displays the energy dispersion of the Andreev doublet as a function of the phase difference δ . A yellow arrow represents a microwave photon, that can be resonant with the energy $2E_A$ of the doublet transition. Such ABS spectroscopy was performed in an atomic contact. Source: [96].

2.1.1 Universal charge relaxation

The DC conductance of a non-interacting coherent quantum conductor connected to two macroscopic reservoirs is given by the Landauer formula :

$$G = N \frac{e^2}{h} D \quad (2.1)$$

where D is the contact transmission and N the number of channels. This formula predicts conductance quantisation and is at the basis of mesoscopic transport. It was first observed experimentally in 1988 [4]. The conductor resistance for a single-channel is transmission dependent and reaches a maximum at perfect transmission $R_q = \frac{h}{e^2}$, which defines the quantum of resistance.

The simplest system to investigate AC transport is a quantum dot tunnel coupled to a single reservoir. This has been realised experimentally in a 2DEG [66] (figure 2.1b). The dot can be charged via the geometrical capacitance C_g of a gate electrode, on which both DC and microwave voltages can be applied. The measured circuit admittance is equivalent to the low-frequency response of a series RC circuit ($\omega \ll \frac{1}{RC}$). The total capacitance is the association of the geometrical capacitance C_g and the quantum capacitance C_q in series. C_q is associated with the dot level density of states and depends on the contact transmission as expected. The counter-intuitive though theoretically predicted result [65, 97] of this experiment is the universality of the associated series resistance R . Whatever the contact transmission D , this so-called charge relaxation resistance takes a constant value equal to half a resistance quantum : $R = \frac{R_q}{2}$. Chapter 5 presents a related experiment on a S-dot-N device in cavity, where charge dynamics is explored in a wider range of parameters beyond the limit $\omega \ll \frac{1}{RC}$.

2.1.2 Dynamics of Kondo physics

Applying voltages at microwave frequencies on quantum dots electrodes enables to probe the dynamics of more complex systems. The AC response of a many-body Kondo resonance has been addressed theoretically and experimentally. In [60] two modifications of the Kondo resonance in presence of a microwave bias voltage were reported : a reduction of the zero-bias resonance peak amplitude and the appearance of satellite peaks at $eV_{SD} = \pm \hbar\omega$ (figure 2.1a). Further characterisation of the Kondo resonance response as a function of amplitude and frequency of the microwave voltage is motivated by the theoretical prediction of universal behaviour. This study is the object of chapter 4.

2.1.3 ABS spectroscopy

As mentioned in section 1.4 sub-gap states called Andreev Bound States may exist when small conductors are connected to superconductors. Their existence has been demonstrated in superconducting atomic contacts by spectroscopic measurements [96, 98]. In such system ABS are predicted to come in doublet with energies $\pm E_A$:

$$E_A = \Delta \sqrt{1 - \tau \sin^2 \frac{\delta}{2}} \quad (2.2)$$

where τ is the transmission probability of a single conduction channel and δ is the phase difference across the atomic contact. The energy transition $2E_A$ between the Andreev doublet is thus smaller than $2\Delta \approx 400\mu\text{eV} \sim 100\text{GHz}$. This is why microwaves

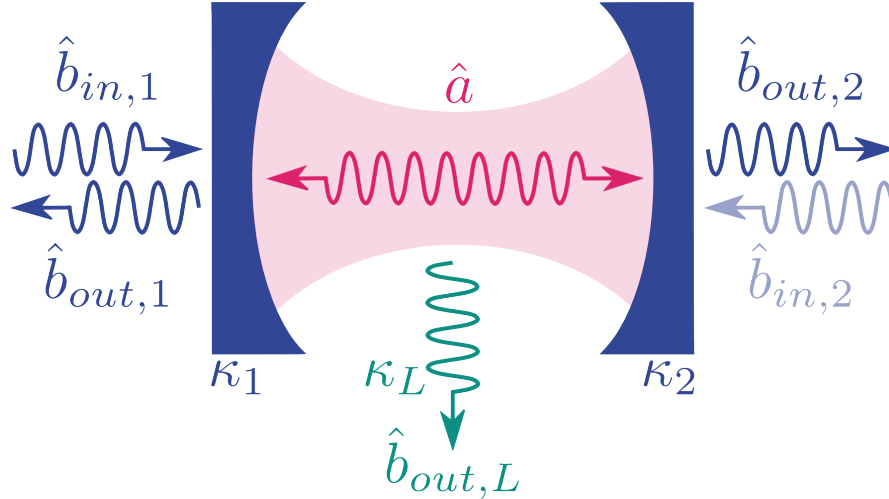


FIGURE 2.2: **Input-output formalism.** The cavity photonic field \hat{a} can be probed thanks to its coupling to external modes. A two-sided cavity is described by the coupling κ_1 and κ_2 to physical ports 1 and 2 plus the coupling κ_L to an effective third mode accounting for internal losses. The corresponding ingoing $\hat{b}_{in,i}$ and outgoing $\hat{b}_{out,i}$ square root photon fluxes are shown. Equations 2.8 and 2.9 were obtained by neglecting the half-transparent flux $\hat{b}_{in,2}$. This is valid if a sufficient drive is applied on port 1.

are required to perform ABS spectroscopy (figure 2.1c). In the experiment [96, 98] a voltage-biased Josephson junction was used as on-chip microwave source and detector. Later on, similar atomic contacts were embedded in a microwave resonator, leading to the coherent manipulation of ABS by cavity photons [99].

2.2 Mesoscopic circuit QED

Coupling mesoscopic circuits to the GHz electromagnetic field of high-finesse superconducting microwave resonators provides a sensitive probe of their dynamics. Moreover quantum experiments involving hybrid light-matter states can be envisioned. We start by describing the cavity field in absence of mesoscopic circuit (section 2.2.1). 2.2.2 presents how mesoscopic circuits can couple to the cavity field. The illustrative case of a superconducting qubit is exposed in 2.2.3. As dissipation is negligible the coupled qubit-cavity system can simply be treated by a Jaynes-Cummings hamiltonian. In 2.2.4 experimental results obtained with mesoscopic circuits are reviewed.

2.2.1 Cavity description : Input-output theory

In this section, we consider a bare cavity, without mesoscopic circuit. The input-output theory is a usual approach to describe the quantum regime of a cavity coupled to external modes. We focus on our experimental situation of a two-sided cavity coupled to input

port 1 and output port 2. Possible internal losses are modelled by the coupling to a third port labelled L (figure 2.2). Most important quantities are the cavity transmission, which is measured experimentally and the cavity photon number, which has to be evaluated for data analysis. We put forward the key steps and assumptions of the derivation starting from the system hamiltonian (see [100] for more details):

$$H = H_{cav} + H_{bath} + H_{coupling} \quad (2.3)$$

with :

$$\begin{aligned} H_{cav} &= \hbar\omega_c \left(\hat{a}^\dagger \hat{a} + \frac{1}{2} \right) \\ H_{bath} &= \sum_{q,i} \hbar\omega_{q,i} \hat{b}_{q,i}^\dagger \hat{b}_{q,i} \\ H_{c,bath} &= -i \sum_{q,i} (f_{q,i} \hat{a}^\dagger \hat{b}_{q,i} - f_{q,i}^* \hat{b}_{q,i}^\dagger \hat{a}) \end{aligned} \quad (2.4)$$

H_{cav} corresponds to a single-mode cavity, which is characterised by a resonance pulsation ω_c and a creation operator \hat{a}^\dagger . Operator $\hat{b}_{q,i}^\dagger$ creates a photon in mode q and bath $i \in (1, 2, L)$. The coupling term $H_{c,bath}$ is expressed in the rotating-wave approximation (RWA). We use the Heisenberg representation $\hat{A}(t) = e^{iHt/\hbar} \hat{A} e^{-iHt/\hbar}$. Writing the evolution equation $\dot{\hat{A}}(t) = \frac{i}{\hbar} [\hat{H}, \hat{A}(t)]$ for cavity operator \hat{a} and external ports operators $\hat{b}_{q,i}$ leads to a set of coupled equations. Assuming $|f_{q,i}|^2 = |f_i|^2$ and noting η_i the density of states in bath i, it can be rewritten as :

$$\dot{\hat{a}}(t) = -i\omega_c \hat{a}(t) - \sum_{i \in (1,2,L)} \frac{\kappa_i}{2} \hat{a}(t) - \sum_{i \in (1,2,L)} \sqrt{\kappa_i} \hat{b}_{in,i}(t, t_0) \quad (2.5)$$

$$\hat{b}_{out,i}(t, t_1) = \hat{b}_{in,i}(t, t_0) + \sqrt{\kappa_i} \hat{a}(t) \text{ for } i \in (1, 2, L) \quad (2.6)$$

with $\kappa_i = \frac{2\pi}{\hbar} \eta_i |f_i|^2$, $t_0 < t < t_1$ and :

$$\begin{aligned} \hat{b}_{in,i}(t, t_0) &\equiv \frac{f_i}{\hbar \sqrt{\kappa_i}} \sum_q e^{-i\omega_q(t-t_0)} \hat{b}_q(t_0) \\ \hat{b}_{out,i}(t, t_1) &\equiv \frac{f_i}{\hbar \sqrt{\kappa_i}} \sum_q e^{-i\omega_q(t-t_1)} \hat{b}_q(t_1) \end{aligned} \quad (2.7)$$

The cavity is driven only by port 1 because thermal fluctuations of the output port are supposed to be negligible $\hat{b}_{in,2} \approx 0$. The third port L is an effective description of losses so by definition $\hat{b}_{in,L} = 0$. The coupled system of equation simplifies and can be solved

in the Fourier domain :

$$\hat{a}(\omega) = -\frac{\sqrt{\kappa_1}}{-i(\omega - \omega_c) + \frac{\kappa}{2}} \hat{b}_{in,1}(\omega) \quad (2.8)$$

$$\hat{b}_{out,2}(\omega) = -\frac{\sqrt{\kappa_1 \kappa_2}}{-i(\omega - \omega_c) + \frac{\kappa}{2}} \hat{b}_{in,1}(\omega) \quad (2.9)$$

with $\kappa = \kappa_1 + \kappa_2 + \kappa_L$. Note that $\hat{b}_{in,i}$ and $\hat{b}_{out,i}$ have dimensions $[T]^{-1/2}$ and can be interpreted as square roots of ingoing and outgoing photon fluxes. As a result the cavity input power in case of a monochromatic beam writes $P_{in} = \hbar\omega \langle \hat{b}_{in,1}^\dagger \hat{b}_{in,1} \rangle$. Similarly the cavity output power is $P_{out} = \hbar\omega \langle \hat{b}_{out,2}^\dagger \hat{b}_{out,2} \rangle$. The cavity transmission T is the ratio between outgoing and ingoing propagating fields :

$$T = \frac{\langle \hat{b}_{out,2} \rangle}{\langle \hat{b}_{in,1} \rangle} = -\frac{\sqrt{\kappa_1 \kappa_2}}{-i(\omega - \omega_c) + \frac{\kappa}{2}} \quad (2.10)$$

The bare cavity mean photon number at resonance $n_0 \equiv \langle \hat{a}^\dagger \hat{a} \rangle_{\omega=\omega_c}$ can be related to the cavity input or output power using relations 2.8 and 2.9 :

$$n_0 = \frac{|T|^2 P_{in}}{\hbar\omega_c \kappa_2} = \frac{P_{out}}{\hbar\omega_c \kappa_2} \quad (2.11)$$

For a symmetric cavity $\kappa_1 = \kappa_2$ and n simplifies as :

$$n_0 = \frac{2\sqrt{P_{in} P_{out}}}{\hbar\omega_c \kappa} \quad (2.12)$$

This formula is at the basis of our practical evaluation of n_0 , which is detailed in Appendix C.

2.2.2 Different coupling schemes to the cavity electromagnetic field

2.2.2.1 Electric coupling

As mesoscopic circuits contain charges, they naturally couple to the cavity electric field. This electric coupling between tunnelling charges and cavity photons can be expressed in terms of a scalar photonic pseudopotential [69] :

$$H_{e-ph} = -e \int d^3r \underbrace{\hat{\Psi}^\dagger(\vec{r}) \hat{\Psi}(\vec{r})}_{\text{tunnelling electron density}} \underbrace{V_\perp(\vec{r})}_{\text{quantum photonic pseudopotential}} (\hat{a} + \hat{a}^\dagger) \quad (2.13)$$

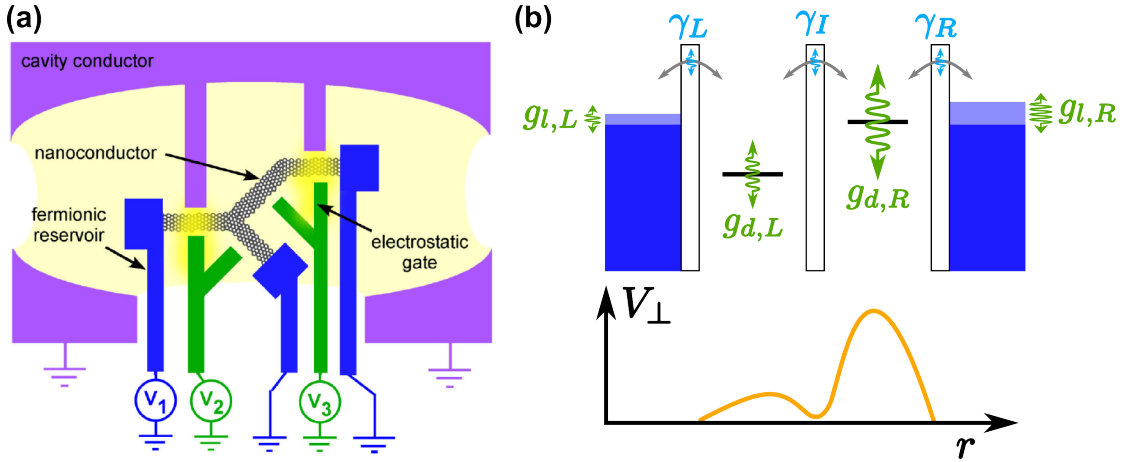


FIGURE 2.3: **Electric coupling between a mesoscopic circuit and the photonic field of a cavity.** (a) is a sketch of a mesoscopic circuit contacted to gates (green) and reservoirs (blue), which is embedded in a cavity (purple). The cavity has protrusions, which shape the photonic potential profile over the circuit. Such spatial variations are encoded in yellow tones : the higher the photonic potential the brighter the colour. (b) Qualitative effects of the electrical coupling of a double dot circuit to the cavity field. In general energy levels are modulated both in the dots and in the reservoirs (g terms, green arrows). Tunnel couplings are expected to be modulated to a lesser extent (γ terms, light blue arrows). As g and γ terms are related to spatial overlap between the level wavefunctions and the photonic potential (equations 2.16 and 2.17), the specific profile of V_\perp plotted in yellow favours coupling to the dot levels compared to coupling to leads, and asymmetries the coupling between left and right dots.

where the field operator $\hat{\Psi}(\vec{r})$ includes all tunnelling charges in the circuit and \hat{a} is the single cavity mode annihilation operator. The possibly strong spatial dependence of the scalar photonic pseudopotential $V_\perp(\vec{r})$ over the circuit length is a particularity of mesoscopic circuits, which justifies the adapted formalism developed in [69] (figure 2.3a). In contrast, atomic cavity QED frequently assumes a linear spatial dependence of the photonic potential $V_\perp(\vec{r}) = \vec{E}_0 \cdot \vec{r}$, while the superconducting qubit community uses a capacitive circuit model equivalent to coarse-grained spatial variations of V_\perp . In mesoscopic QED V_\perp inhomogeneity mainly comes from the presence of gate and contact electrodes. Its spatial profile crucially affects the circuit microscopic degrees of freedom to which photons couple.

This idea is illustrated by expressing H_{e-ph} in a tunnelling formalism. The dot circuit D and each reservoir R_p ($p \in 1, 2, \dots, N$) are diagonalized independently in the absence of tunnelling. Each eigenstate j of a subsystem $o \in \{D, R_1, R_2, \dots, R_N\}$ is characterised by the creation operator $\hat{c}_{o,j}^\dagger$, the wavefunction $\phi_{o,j}(\vec{r})$ and the eigenenergy $\epsilon_{o,j}$. If the dot/reservoirs tunnel couplings are small, the basis formed by the isolated orbitals is almost orthogonal and can be used to expand the charge field operator :

$$\hat{\Psi}^\dagger(\vec{r}) = \sum_{o,j} \phi_{o,j}^*(\vec{r}) \hat{c}_{o,j}^\dagger \quad (2.14)$$

Using this decomposition the coupling hamiltonian rewrites $H_{e-ph} = h_{int}(\hat{a} + \hat{a}^\dagger)$ with :

$$h_{int} = \sum_{o,j} g_{o,j} \hat{c}_{o,j}^\dagger \hat{c}_{o,j} + \sum_{oj \neq o'j'} \left(\gamma_{oj,o'j'} \hat{c}_{o,j}^\dagger \hat{c}_{o',j'} + h.c. \right) \quad (2.15)$$

and :

$$\hbar g_{oj} = -e \int d^3r |\phi_{o,j}(\vec{r})|^2 V_\perp(\vec{r}) \quad (2.16)$$

$$\gamma_{oj,o'j'} = -e \int d^3r \phi_{o,j}^*(\vec{r}) \phi_{o',j'}(\vec{r}) V_\perp(\vec{r}) \quad (2.17)$$

In this framework the effect of cavity field is interpreted in terms of AC modulation $\hbar g_{o,i}(\hat{a} + \hat{a}^\dagger)$ of energy level $\epsilon_{o,j}$ and AC modulation $\gamma_{oj,o'j'}$ of tunnel coupling $t_{oj,o'j'}$ (figure 2.3b). Photo-induced energy shifts affect both dot eigenenergies and reservoir chemical potentials. Photo-induced tunnel couplings affect tunnelling between dot and reservoirs, and can also produce internal transitions within the dot. The g terms are expected to be much larger than the γ term which are proportional to wavefunctions overlap. Note that a completely homogeneous cavity field is equivalent to a global modulation of the energy scale, thus has no physical effect. In contrast strong heterogeneities of the photonic potential over the circuit length favours the cavity sensitivity to the circuit dynamics. For example an asymmetric potential such as depicted on figure 2.3b allows to probe interdot hopping, as will be shown in section 2.2.4. Ultimately an adequate design of the electrodes geometry would shape at will the photonic potential profile. This would enable to engineer a wide variety of coupling schemes corresponding to different physics to be explored.

2.2.2.2 Magnetic coupling

One can think about coupling either the spin momentum or the orbital momentum to the cavity magnetic field. Direct magnetic coupling between the cavity magnetic field and a single spin is weak, of order of magnitude going from $10mHz$ to $50 Hz$ depending on the cavity mode volume. Such coupling has been observed using spin ensembles containing a high number of spins N [101, 102]. State of the art sensitivity is quantum limited and corresponds to $N \approx 10^3$ spins [103].

2.2.3 Dissipationless description of a superconducting qubit-cavity system

The simplest description of a coupled qubit-cavity system is the Jaynes-Cummings model (figure 2.4a):

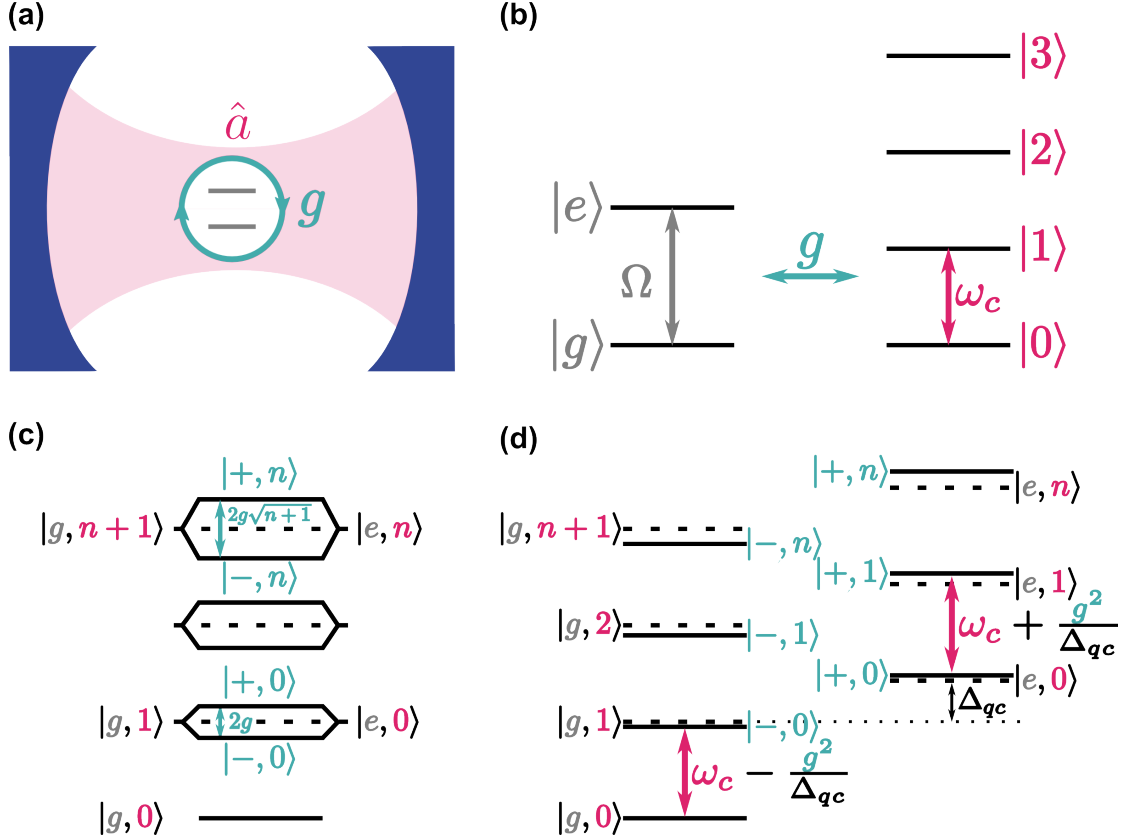


FIGURE 2.4: **Description of a non-dissipative qubit-cavity system.** (a) Sketch of a qubit (grey) coupled to the cavity field (pink) with coupling strength g (turquoise-blue). (b) Level diagrams (in pulsation unit) of bare qubit (grey) and bare cavity (pink) coupled by g . Energy level diagrams (in pulsation unit) in the resonant ($\Delta_{qc} = 0$) (c) and dispersive regime ($\Delta_{qc} \gg g$) (d). Uncoupled states are recalled with dashed lines and grey/pink labels on the sides. Dressed states are represented with plain lines and labelled in blue in the center.

$$H_{JC} = \underbrace{\hbar\omega_c \left(\hat{a}^\dagger \hat{a} + \frac{1}{2} \right)}_{H_{cav}} + \underbrace{\frac{\hbar\Omega}{2} \sigma_z}_{H_{qbit}} + \underbrace{\hbar g \left(\hat{a}^\dagger \hat{\sigma}^- + \hat{\sigma}^+ \hat{a} \right)}_{H_c} \quad (2.18)$$

The first term is the cavity hamiltonian. The qubit is described by the Pauli operator σ_z in the ($|e\rangle, |g\rangle$) basis formed by the qubit excited and ground states, separated by energy $\hbar\Omega$. The last term describes the qubit-cavity electrical coupling characterised by the coupling constant g (figure 2.4b). It is linear and is obtained under the rotating-wave-approximation (RWA). The Jaynes-Cummings model is a pure hamiltonian description, where energy is conserved. Both the cavity decay rate κ and the qubit relaxation rate γ are neglected. The use of superconductors for the fabrication of qubits and cavities minimizes dissipation, and makes this assumption relevant in first approximation. Typically $g \sim 100\text{MHz} > \kappa \sim 10\text{MHz} > \gamma \sim 1\text{MHz}$. In the case of mesoscopic circuits dissipation has to be taken into account. However the Jaynes-Cummings model is instructive, as it captures some physical effects, that will also appear in mesoscopic cQED.

Here the system is described by the state $|q, n\rangle$, where the qubit state q is either g (ground) or e (excited) and n refers to the Fock state with n photons. The coupling term g transfers an excitation from qubit to cavity or vice-versa. Thus it couples states $|e, n-1\rangle$ and $|g, n\rangle$ with the same total number of excitations n . Two limiting regimes can be considered depending on the detuning between qubit and cavity $\Delta_{qc} = \Omega - \omega_c$.

2.2.3.1 Dispersive regime

The dispersive regime corresponds to the limit of large detuning $\Delta_{qc} \gg g$. The transfer of excitation between the subsystems costs an energy Δ_{qc} not provided by g . As hybridization between $|e, n-1\rangle$ and $|g, n\rangle$ is weak, it is convenient to eliminate the coupling linear term. At second order, the effect of coupling is to shortly excite the system from $|q, n\rangle$ to a virtual state before putting it back to $|q, n\rangle$. Globally this leaves the system unchanged and simply leads to a renormalization of qubit and cavity frequencies. This is in the same spirit as Schrieffer-Wolff transformation performed in 1.3.1 and 1.4.1. Here the unitary transformation is :

$$U = \exp\left(\frac{g}{\Delta_{qc}}\left(\hat{a}\hat{\sigma}_+ - \hat{a}^\dagger\hat{\sigma}_-\right)\right) \quad (2.19)$$

with $\hat{\sigma}_- = |g\rangle\langle e| = \hat{\sigma}_+^\dagger$. The effective hamiltonian to second order in g is :

$$H_{eff} = \hbar\left(\omega_c + \frac{g^2}{\Delta_{qc}}\sigma_z\right)\hat{a}^\dagger\hat{a} + \frac{\hbar}{2}\left(\Omega + \frac{g^2}{\Delta_{qc}}\right)\sigma_z \quad (2.20)$$

In this picture the coupling shifts the qubit frequency by g^2/Δ_{qc} and the cavity frequency by $\sigma_z g^2/\Delta_{qc}$. The cavity resonance frequency is pulled by the coupling to the qubit and this pull is a function of the qubit state (figure 2.4c). This statement will hold when replacing "qubit" by "quantum dot circuit". Note that for a positive detuning between qubit and cavity ($\Delta_{qc} > 0$), a qubit in the ground state induces a negative cavity pull.

2.2.3.2 Resonant regime

The resonance condition between qubit and cavity corresponds to $\Delta_{qc} = 0$. Without coupling the states $|e, n\rangle$ and $|g, n+1\rangle$ corresponding to $n+1$ excitations would be degenerate. Figure 2.4d depicts, how the coupling lifts this degeneracy by $2g\sqrt{n+1}$. Indeed the subspace with $n+1$ excitations is diagonal in the maximally entangled states basis $|\pm, n\rangle = (|g, n+1\rangle \pm |e, n\rangle)/\sqrt{2}$ with eigenenergies $E_{\pm, n} = (n+1)\hbar\omega_c \pm \hbar g\sqrt{n+1}$. In a transmission experiment this pair of states $|\pm, 0\rangle$ will be resolved if the splitting is larger than the peak linewidth. This is the strong coupling regime achieved for $g > \kappa, \gamma$.

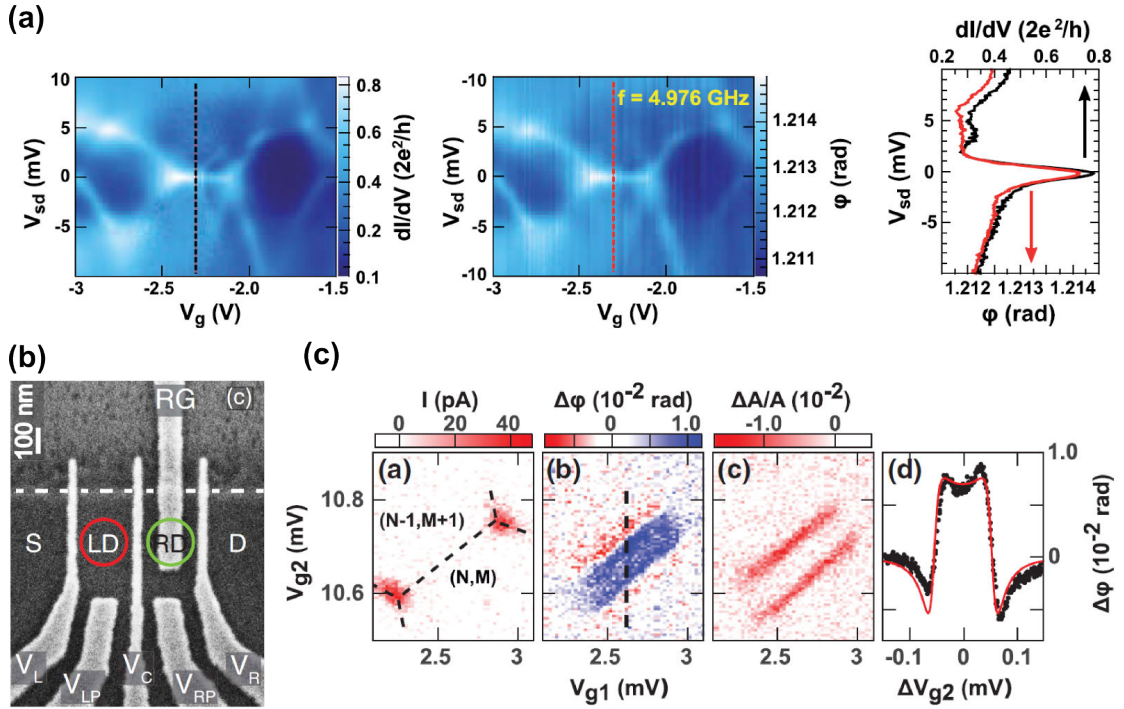


FIGURE 2.5: **Experimental manifestations of the coupling between quantum dot circuits and cavity photons.** (a) An asymmetric reservoirs-dominant coupling of a single quantum dot to the photonic field leads to the observation of the same features in the microwave phase ϕ as in the differential conductance dI/dV . colour plots for both quantities versus gate and bias voltages display here Coulomb diamonds and Kondo ridge, for which a line cut along the dashed lines is shown. Source : [42]. (b) SEM image of the gate structure defining a double quantum dot in a 2DEG. A gate RG on the right dot is directly contacted to the resonator, thus engineers an asymmetric coupling to left and right orbitals. Source: [43]. Such a coupling scheme leads to typical features close to a degeneracy line of a DQD stability diagram, if the charge qubit frequency comes in resonance with the cavity (c). There is current only at the triple points. The phase shift (here proportional to the frequency shift) changes sign along the detuning axis. The amplitude relative variation (here proportional to the change in cavity linewidth) is negative. Source: [52].

Higher-order pairs are even harder to resolve as they manifest themselves in the transmission spectrum as $2g/\sqrt{n}$ split peaks [104].

2.2.4 Mesoscopic circuit QED experiments

2.2.4.1 Quantum dots

Here we aim at briefly reviewing the experimental work carried out on quantum dot circuits coupled to microwave resonators over the past five years (more details in [46]). Coupling between a quantum dot circuit and microwave cavity photons was first reported for a carbon-nanotube-based single dot [42]. In this experiment the resonance frequency shift displays the same features as the differential conductance (figure 2.5a). This means

that the cavity field modulates mainly the leads chemical potentials in an asymmetric way. The coupling between a double quantum dot and cavity photons was first observed in a GaAs 2DEG [43]. This was done by increasing the photonic potential on the right dot using a top gate contacted to the resonator (figure 2.5b). As sketched on figure 2.3b this engineered asymmetric potential results in an asymmetric coupling between left and right dots. Consequently the detuning ϵ_δ is AC modulated and cavity photons couple to the charge qubit transition. Thus cavity transmission changes along the zero-detuning line (figure 2.5c). Sign changes in the cavity resonance frequency shift along the detuning axis indicates that the cavity is resonant with the charge qubit transition. Following experiments have mostly investigated a similar asymmetrically coupled double dot geometry in GaAs [50, 51] and other host materials like carbon nanotubes [49, 52], InAs nanowires [44] and graphene [53]. Photon-induced coupling between distant quantum dots was investigated with single dots [105] and double dots [106].

In general mesoscopic circuits not only shift the cavity resonance but also broadens it. Such additional dissipation caused by the circuit results in decrease of the transmitted amplitude ($\Delta A/A < 0$) like in the data of figure 2.5c. However amplitude enhancement has recently been observed in charge qubits, where transitions between the doublet emit photons [107–109].

Despite no intrinsic electric coupling and weak magnetic coupling the electronic spin can be coupled to cavity photons via spin-orbit interaction. This was first achieved very recently using artificial spin-orbit coupling provided by non-collinear ferromagnetic leads in a DQD [54].

2.2.4.2 Synthesis of non-classical states by SIS junctions

Other mesoscopic circuits like Josephson junctions or normal metal junctions can be coupled to microwave resonators. These latter are usually described as an electromagnetic environment, in which energy can be dissipated, when inelastic tunnelling occurs in the junction. If a SIS junction is DC biased with $|eV_{SD}| < 2\Delta$, Cooper pair tunnelling is blocked, unless one or several photons absorb the bias energy. Two-photon processes have been measured [45] and are predicted to produce entangled photon pairs [110] and bunching statistics [111]. Under certain conditions single-photon-assisted tunnelling is also expected to create photonic non-classical states like antibunched photons [112]. All these features are looked for experimentally. The backaction of non-classical light states on mesoscopic conductors is also investigated [113].

2.3 Linear response of circuit to microwave field

The purpose of this section is to describe how the cavity transmission changes in presence of a quantum dot circuit, which responds linearly to the microwave field. As the circuit charge susceptibility will enter the modified formula, high-finesse cavities are a powerful probe to investigate charge dynamics as will be shown in chapter 5.

2.3.1 Cavity transmission in the circuit linear response regime

We consider a coupling scheme where each QD circuit energy level i is modulated by the cavity field with the coupling strength g_i given by 2.16. There is no modulation of the lead electrochemical potentials. Modulations of tunnel couplings (γ terms of section 2.2.2) are disregarded. In such a situation the dot-cavity coupling hamiltonian given by 2.15 simplifies as :

$$H_{e-ph} = \sum_i \hbar g_i \hat{n}_i (\hat{a} + \hat{a}^\dagger) \quad (2.21)$$

The input-output formalism presented for a bare cavity in section 2.2.1 can be adapted in presence of a quantum dot circuit by replacing H_{cav} in equation 2.3 with $H_{syst} = H_{cav} + H_{e-ph} + H_{dot}$. H_{dot} describes the bare QD circuit and commutes with \hat{a} . Here we consider a monochromatic driving term, which is sufficiently large for quantum fluctuations to be negligible (photon number $n \gtrsim 10$). It is convenient to write this classical drive explicitly in the total hamiltonian :

$$H = \underbrace{H_{cav} + H_{bath} + H_{c,bath} + H_{drive}}_{H_{cav}^d} + H_{e-ph} + H_{dot} \quad (2.22)$$

with $H_{drive} = \hbar \epsilon_{in} \hat{a}^\dagger e^{-i\omega_d t} - \hbar \epsilon_{in}^* \hat{a} e^{i\omega_d t}$ ¹ and H_{bath} and $H_{c,bath}$ given by 2.4. The photonic field evolution equation thus becomes :

$$\frac{d}{dt} \hat{a}(t) = -i\omega_c \hat{a}(t) - \frac{\kappa}{2} \hat{a}(t) - i \sum_i g_i \hat{n}_i - \sqrt{\kappa_1} b_{in,1}(t) \quad (2.23)$$

with $b_{in,1}(t) \simeq \frac{i\epsilon_{in}}{\sqrt{\kappa_1}} e^{-i\omega_d t}$. As the cavity is driven with a quasi resonant classical drive, it is reasonable to treat the cavity field classically : $\langle \hat{a}(t) \rangle \simeq \bar{a} e^{-i\omega_d t}$. In this semi-classical treatment, the coupling term becomes $H_{e-p}^{sm} = \sum_i \hbar g_i \hat{n}_i (\bar{a} e^{-i\omega_d t} + \bar{a}^* e^{i\omega_d t})$. The linear response theory gives the mean response of operator \hat{n}_i perturbed linearly by H_{e-p}^{sm} :

$$\langle \hat{n}_i(t) \rangle = n_{i,0} + \sum_j g_j (\tilde{\chi}_{i,j}(\omega_d) \bar{a} e^{-i\omega_d t} + \tilde{\chi}_{i,j}(-\omega_d) \bar{a}^* e^{i\omega_d t}) \quad (2.24)$$

¹We simply have extracted from $H_{c,bath}$ (equation 2.4) the mode Q, which is driven at $\omega_d = \omega_Q$ with energy $\hbar \epsilon_{in} = -if_{Q,1} B_{Q,1}$.

with $n_{i,0}$ the unperturbed level occupation. Equation 2.24 is a definition of the susceptibility $\tilde{\chi}_{i,j}$ ² characterizing the response of the charge occupation of orbital i to a perturbation which is linear in the charge occupation of orbital j . Averaging equation 2.23 and keeping resonant terms only yields :

$$\bar{a} = \frac{-i\epsilon_{in}}{i(\omega_c - \omega_d) + \frac{\kappa}{2} + i \sum_{i,j} g_i g_j \tilde{\chi}_{i,j}(\omega_d)} \quad (2.25)$$

By definition, the cavity photon number is $n(\omega_d) = \langle \hat{a}^\dagger \hat{a} \rangle_{\omega_d}$. Here we consider a classical field, so $n = |\bar{a}|^2$, which is a function of the drive frequency. Equation 2.25 shows, that n is affected by the presence of the circuit. Usually the circuit decreases the photon number, with respect to the bare cavity photon number at resonance n_0 . We will see in chapter 5, that the charge susceptibility of a circuit accounts for photon emission, resulting in $n(\omega_d = \omega_c) > n_0$. Using $\hat{b}_{out,2}(t) = \sqrt{\kappa_2} \hat{a}(t)$ we obtain the transmission :

$$T = \frac{\langle \hat{b}_{out,2} \rangle}{\langle \hat{b}_{in,1} \rangle} = \frac{-\sqrt{\kappa_1 \kappa_2}}{i(\omega_c - \omega_d) + \frac{\kappa}{2} + i \sum_{i,j} g_i g_j \tilde{\chi}_{i,j}(\omega_d)} \quad (2.26)$$

This expression shows that the presence of the circuit changes both the cavity resonance frequency and resonance linewidth. In the case of a single orbital, characterised by a charge susceptibility $\tilde{\chi}$, the frequency shift and the cavity linewidth change are direct measurement of $g^2 \text{Re}\{\tilde{\chi}\}$ and $g^2 \text{Im}\{\tilde{\chi}\}$ respectively. In next section, we only discuss the adiabatic limit, where the tunnelling dynamics between a QD discrete state and a lead is much faster than the cavity field : $\Gamma \gg \omega_c$. Other regimes will be addressed in chapter 5.

2.3.2 Adiabatic limit

If the charge dynamics of a discrete energy level coupled to a reservoir is much faster than the cavity frequency, that is $\Gamma/\hbar \gg \omega_c$, the effect of the cavity field is no more than modulating the level energy. In the semi-classical description this writes $\epsilon_d(t) = \epsilon_d + \hbar g (\bar{a} e^{-i\omega_d t} + \bar{a}^* e^{i\omega_d t})$. In the adiabatic limit the cavity is not fast enough to probe the circuit dynamics so that the time-dependant level mean occupation involves the static function of the level occupation vs energy : $n(t) = n_0(\epsilon_d(t))$. The linear regime is given by the expansion to first order in $\hbar g \bar{a}$:

$$n(t) = n_0(\epsilon_d) + \frac{\partial n_0}{\partial \epsilon_d} \hbar g (\bar{a} e^{-i\omega_d t} + \bar{a}^* e^{i\omega_d t}) \quad (2.27)$$

²Here $\tilde{\chi}$ has the inverse dimension of g , that is the inverse dimension of a pulsation.

This development is justified for $\hbar g \bar{a} \ll k_B T, \Gamma$. Comparing expression 2.27 with 2.24 one finds :

$$\tilde{\chi}(\omega_d) = \tilde{\chi}(-\omega_d) = \tilde{\chi}(\omega_d \approx 0) = \hbar \frac{\partial n_0}{\partial \epsilon_d} \quad (2.28)$$

Recalling the general relationship $\tilde{\chi}(-\omega_d) = \tilde{\chi}^*(+\omega_d)$, equation 2.28 means that $\tilde{\chi}$ is real. The effect of the circuit comes down to a shift of the resonance frequency related to the static charge occupation, but no dissipation is induced. This is the same effect, as previously described in section 2.2.3. Here the frequency shift is given by the sign of $\frac{\partial n_0}{\partial \epsilon_d}$, which is negative. Indeed we have seen in section 1.2.1.1 that the number of electrons increases with the gate voltage and $\epsilon_d = -e\alpha(V_g - V_g^0)$.

2.4 Master equation treatment of coherent coupling between cavity and circuit electronic transitions

2.4.1 Isolated two-level system

We consider a mesoscopic circuit, where a single transition between electronic states is close to resonance with the cavity. The quantum dot is assumed to be "closed", so that electronic transport between the dot states and the reservoirs can be neglected. Under this approximation the system is described by a generalized Jaynes-Cummings hamiltonian H_{JC}^d including dissipation :

$$H_{JC}^d = H_{cav}^d + H_{qubit}^d + H_c \quad (2.29)$$

In addition to dissipation-less H_{cav} and H_{qubit} of 2.18 H_{cav}^d and H_{qubit}^d contain coupling terms to baths, which account for both microwave drive and dissipation. For the cavity a microscopic description of H_{cav}^d (defined by 2.22) has been given as the starting point of the input-output theory (equations 2.4). It yields a photon damping κ and a driving term ϵ_{in} (defined in previous section 2.3) in the photonic field evolution equation (in magenta in equation). Similarly the qubit decay is phenomenologically described by a relaxation rate γ and a dephasing rate Γ_ϕ . The terms in equation corresponding to the evolution of the qubit alone appear in blue. $H_{coupling}$ is unchanged compared to the Jaynes-Cummings hamiltonian. It couples the qubit operators and cavity field time evolution via the terms in cyan in the equations. In the rotating frame of the driving

field oscillating at ω_d the coupled set of evolution equation writes within the RWA :

$$\frac{d}{dt} \langle \hat{a} \rangle = - \left(i\Delta_{cd} + \frac{\kappa}{2} \right) \langle \hat{a} \rangle - i\epsilon_{in} - ig \langle \hat{\sigma}_- \rangle \quad (2.30)$$

$$\frac{d}{dt} \langle \hat{\sigma}_- \rangle = - \left(i\Delta_{qd} + \frac{\gamma}{2} + \Gamma_\phi \right) \langle \hat{\sigma}_- \rangle + ig \langle \hat{a} \hat{\sigma}_z \rangle \quad (2.31)$$

$$\frac{d}{dt} \langle \hat{\sigma}_z \rangle = -\gamma (\langle \hat{\sigma}_z \rangle + 1) - 4ig \operatorname{Im} \left\{ \langle \hat{a}^\dagger \hat{\sigma}_- \rangle \right\} \quad (2.32)$$

This system of equations can be solved directly if we make again the semiclassical approximation, replacing \hat{a} by $\bar{a} \equiv \langle \hat{a} \rangle$ (valid for $n \gtrsim 10$). Here, it allows to decouple the operators means $\langle \hat{a} \hat{\sigma}_z \rangle = \bar{a} \langle \hat{\sigma}_z \rangle$ and $\langle \hat{a}^\dagger \hat{\sigma}_- \rangle = \bar{a}^* \langle \hat{\sigma}_- \rangle$. In the stationary regime, this leads to:

$$\bar{a} = \frac{-i\epsilon_{in}}{i\Delta_{cd} + \frac{\kappa}{2} + ig^2 \frac{\langle \hat{\sigma}_z \rangle}{\Delta_{qd} - i\Gamma_2}} \quad (2.33)$$

We can test the limiting case of a non-dissipative circuit for which $\Gamma_2 = 0$. The cavity resonance frequency is shifted by $\frac{g^2 \langle \hat{\sigma}_z \rangle}{\Delta_{qd}}$, while the linewidth is unchanged, in agreement with the Jaynes-Cummings description of section 2.2.3. Interestingly the cavity field for the qubit 2.33 has the very same structure as equation 2.25 obtained in previous section in the linear theory framework. By analogy we can define $\chi_{qb} = \frac{\langle \hat{\sigma}_z \rangle}{\Delta_{qd} - i\Gamma_2}$ with $\Gamma_2 = \gamma/2 + \Gamma_\phi$. When the qubit is in the ground state, $\langle \hat{\sigma}_z \rangle = -1$ and $\chi_{qb} = \chi_{qb,0} = \frac{-1}{\Delta_{qd} - i\Gamma_2}$. Using this formulation one obtains :

$$\bar{a} = \frac{-i\epsilon_{in}}{i\Delta_{cd} + \frac{\kappa}{2} + ig^2 \chi_{qb}(\omega_d)} \quad (2.34)$$

$$\langle \hat{\sigma}_z \rangle = \frac{-1}{1 - \frac{4|\bar{a}|^2 g^2 \operatorname{Im} \{ \chi_{qb,0}(\omega_d) \}}{\gamma}} \quad (2.35)$$

$$\langle \hat{\sigma}_- \rangle = g\chi_{qb}(\omega_d)\bar{a} \quad (2.36)$$

When the drive is resonant with the qubit, the cavity frequency is unchanged. Only the cavity linewidth is affected. For a qubit in the ground state, it is broadened by an additional damping equal to g^2/Γ_2 . From the equation 2.35, we see the power dependence of $\langle \hat{\sigma}_z \rangle$. At low drive ϵ_{in} , the qubit is in the ground state $\langle \hat{\sigma}_z \rangle \approx -1$. Increasing the driving power leads to an increase in $\langle \hat{\sigma}_z \rangle$, which ultimately saturates at 0, meaning equilibrated mean populations between excited and ground states. In this limit, equation 2.33 shows that the qubit becomes transparent for the cavity field, thus the bare cavity transmission is expected to be recovered. This hand-waving reasoning about the dependence of $\langle \hat{\sigma}_z \rangle$ and \bar{a} as a function of ϵ_{in} (or equivalently versus the bare cavity photon number $n_0 = 4\epsilon_{in}^2/\kappa^2$), is confirmed by numerically solving the implicit polynomial equation on $|\bar{a}|^2$, obtained from equations 2.34 and 2.35.

2.4.2 Case of a three-level system in a ladder geometry

In this section, we use the same formalism and semiclassical assumption as above to treat the interaction between a three-level system in a ladder geometry and the cavity field. Such a level structure will be important to interpret data in section 6.3.2. Transition 1 between states $|A\rangle$ and $|B\rangle$ and transition 2 between $|B\rangle$ and $|C\rangle$ are both close to resonant with the cavity. For each state $x \in (A, B, C)$ we define $\hat{\sigma}_x = |x\rangle\langle x|$. The relaxation transition operators write $\hat{\sigma}_{1-} = |A\rangle\langle B|$ for transition 1 and $\hat{\sigma}_{2-} = |B\rangle\langle C|$ for transition 2. We use the same notations as in previous section, with an additional index $i \in (1, 2)$ to refer to the parameters of transition i . In the drive rotating frame and within the RWA, the system evolution is governed by the coupled set of equations, in the semiclassical regime :

$$\frac{d}{dt} \langle \hat{a} \rangle = - \left(i\Delta_{cd} + \frac{\kappa}{2} \right) \langle \hat{a} \rangle - i\epsilon_{in} - ig_1 \langle \hat{\sigma}_{-1} \rangle - ig_2 \langle \hat{\sigma}_{-2} \rangle \quad (2.37)$$

$$\frac{d}{dt} \langle \hat{\sigma}_{-1} \rangle = - \left(i\Delta_{qd1} + \frac{\gamma_1}{2} + \Gamma_{\phi,1} \right) \langle \hat{\sigma}_{-1} \rangle + ig_1 \langle \hat{a} \rangle (\langle \hat{\sigma}_B \rangle - \langle \hat{\sigma}_A \rangle) \quad (2.38)$$

$$\frac{d}{dt} \langle \hat{\sigma}_{-2} \rangle = - \left(i\Delta_{qd2} + \frac{\gamma_2}{2} + \Gamma_{\phi,2} \right) \langle \hat{\sigma}_{-2} \rangle + ig_2 \langle \hat{a} \rangle (\langle \hat{\sigma}_C \rangle - \langle \hat{\sigma}_B \rangle) \quad (2.39)$$

$$\frac{d}{dt} \langle \hat{\sigma}_A \rangle = \gamma_1 \langle \hat{\sigma}_B \rangle + 2g_1 \text{Im} \left\{ \langle \hat{a}^\dagger \rangle \langle \hat{\sigma}_{-1} \rangle \right\} \quad (2.40)$$

$$\frac{d}{dt} \langle \hat{\sigma}_B \rangle = -\gamma_1 \langle \hat{\sigma}_B \rangle + \gamma_2 \langle \hat{\sigma}_C \rangle - 2g_1 \text{Im} \left\{ \langle \hat{a}^\dagger \rangle \langle \hat{\sigma}_{-1} \rangle \right\} + 2g_2 \text{Im} \left\{ \langle \hat{a}^\dagger \rangle \langle \hat{\sigma}_{-2} \rangle \right\} \quad (2.41)$$

$$\frac{d}{dt} \langle \hat{\sigma}_C \rangle = -\gamma_2 \langle \hat{\sigma}_C \rangle - 2g_2 \text{Im} \left\{ \langle \hat{a}^\dagger \rangle \langle \hat{\sigma}_{-2} \rangle \right\} \quad (2.42)$$

It is convenient to define $\langle \hat{\sigma}_{z1} \rangle = \langle \hat{\sigma}_B \rangle - \langle \hat{\sigma}_A \rangle$ and $\langle \hat{\sigma}_{z2} \rangle = \langle \hat{\sigma}_C \rangle - \langle \hat{\sigma}_B \rangle$. In the stationary regime, equations 2.37, 2.38 and 2.39 result in :

$$\bar{a} = \frac{-i\epsilon_{in}}{i\Delta_{cd} + \frac{\kappa}{2} + ig_1^2 \chi_{qb1}(\omega_d) + ig_2^2 \chi_{qb2}(\omega_d)} \quad (2.43)$$

$$\langle \hat{\sigma}_{-i} \rangle = g_i \chi_{qbi}(\omega_d) \langle \hat{a} \rangle \text{ for } i \in (1, 2) \quad (2.44)$$

which are the two-transition generalization of equations 2.34 and 2.36. The three-level ladder geometry plays a role in setting the level populations. By definition, the probabilities $\langle \hat{\sigma}_x \rangle$ for the system to be in state x , fulfil the condition $\langle \hat{\sigma}_A \rangle + \langle \hat{\sigma}_B \rangle + \langle \hat{\sigma}_C \rangle = 1$. Using this relationship in addition to the stationary equations 2.40, 2.41, 2.42, we obtain

all three $\langle \hat{\sigma}_x \rangle$ as a function of the cavity field, or equivalently :

$$\langle \hat{\sigma}_{z1} \rangle = \frac{\gamma_1}{2|\bar{a}|^2 g_1^2 \chi_{qb1,0}(\omega_d)} \langle \hat{\sigma}_B \rangle \quad (2.45)$$

$$\langle \hat{\sigma}_{z2} \rangle = \frac{-\gamma_2}{\gamma_2 - 2|\bar{a}|^2 g_2^2 \chi_{qb2,0}(\omega_d)} \langle \hat{\sigma}_B \rangle \quad (2.46)$$

$$\langle \hat{\sigma}_B \rangle = \frac{1}{3 - \frac{\gamma_1}{2|\bar{a}|^2 g_1^2 \chi_{qb1,0}(\omega_d)} + \frac{\gamma_2}{\gamma_2 - 2|\bar{a}|^2 g_2^2 \chi_{qb2,0}(\omega_d)}} \quad (2.47)$$

Combining equations 2.45, 2.46, 2.47 with equation 2.43 leads to an implicit polynomial equation on $|\bar{a}|^2$. It can be solved numerically, as a function of the drive pulsation to plot cavity spectra. The evolution of the spectra, when the driving amplitude ϵ_{in} is increased, differs from the single transition case. In particular, the cavity field maximal amplitude may evolve in a non-monotonic way. Starting from a certain vacuum value, the field maximal amplitude can first decrease before increasing up to recovering the bare cavity spectrum, when the mean populations of the three states A, B, C are equilibrated to 1/3.

Chapter 3

Experimental methods

3.1 Nanofabrication	62
3.1.1 Sample description and outlook of the fabrication process	62
3.1.2 Sample cleaning	64
3.1.3 Patterning of gold alignment crosses, contacting pads and sample number	65
3.1.4 Niobium coplanar wave-guide resonator and circuit bonding pads and pre-contacts	66
3.1.5 Carbon nanotube stamping	67
3.1.6 Patterning of the device electrodes	71
3.1.7 Sample mounting and wire-bonding	71
3.2 Measurement setup	72
3.2.1 Cryogenics	72
3.2.2 DC measurements	78
3.2.3 Microwave measurements	80

Devices studied in this thesis are carbon nanotube quantum dots embedded in microwave superconducting coplanar wave-guide resonators. Their fabrication was part of this thesis work, which has been carried out in the clean room of ENS. The sample design and fabrication process are described in section 3.1, and fabrication recipes are gathered in Appendix B. The samples were studied at low temperature, in a new dilution cryostat which had to be wired prior to measurements. This part of the setup is the object of section 3.2.1. Transport and microwave measurements are respectively explained in 3.2.2 and 3.2.3.

3.1 Nanofabrication

3.1.1 Sample description and outlook of the fabrication process

At the very end of the fabrication process our samples are 10mm * 5mm chips, on which carbon nanotube quantum dot circuits are sitting in the electric field of a microwave superconducting coplanar wave-guide (CPW) resonator (figure 3.1). Such resonator is the microwave on-chip version of an optical Fabry-Perot cavity. It consists of a CPW transmission line¹, which is cut at both ends by identical finger gaps (figure 3.1a). These capacitances are the electrical counterparts of non-perfect optical mirrors, which allow photons to be mainly trapped in the cavity, although they have a finite probability to enter or leave it via input/output ports. The bigger the capacitances, the higher the couplings to external modes κ_i defined in previous chapter. As we use $\frac{\lambda}{2}$ resonators, there are two antinodes of the electric field, where we can place our quantum dot circuits. There, the cavity ground plane is interrupted on one side to leave some space for the carbon nanotube device and its five contact and gate electrodes. Among these DC lines the central electrode can also be operated at microwave frequencies, as can be seen from the bonding pads in figure 3.1a. For fabrication reasons it is more convenient to handle square chips, so that in practice we fabricate two samples on a 10mm * 10mm chip, as shown in figure 3.1b. Each sample is labelled CPSRES#X, X being L/R for the left/right side of the chip. On each chip four quantum dot circuits can be placed, one in each of the four Upper(U)/Lower(L) and Right(R)/Left(L) corners (hence the labelling UR, UL, LL, LR employed in figure 3.1b). A zoom on the right resonator lower ground opening (LR) is displayed on figure 3.1c, where the quantum dot device is circled in white. This Scanning Electron Micrograph has been coloured artificially to highlight the steps of the sample fabrication. All patterns with the same colour are done during

¹This geometry corresponds to ground/insulator/central conductor/insulator/ground, which is no more than the planar version of a coaxial cable, obtained from a longitudinal cut.

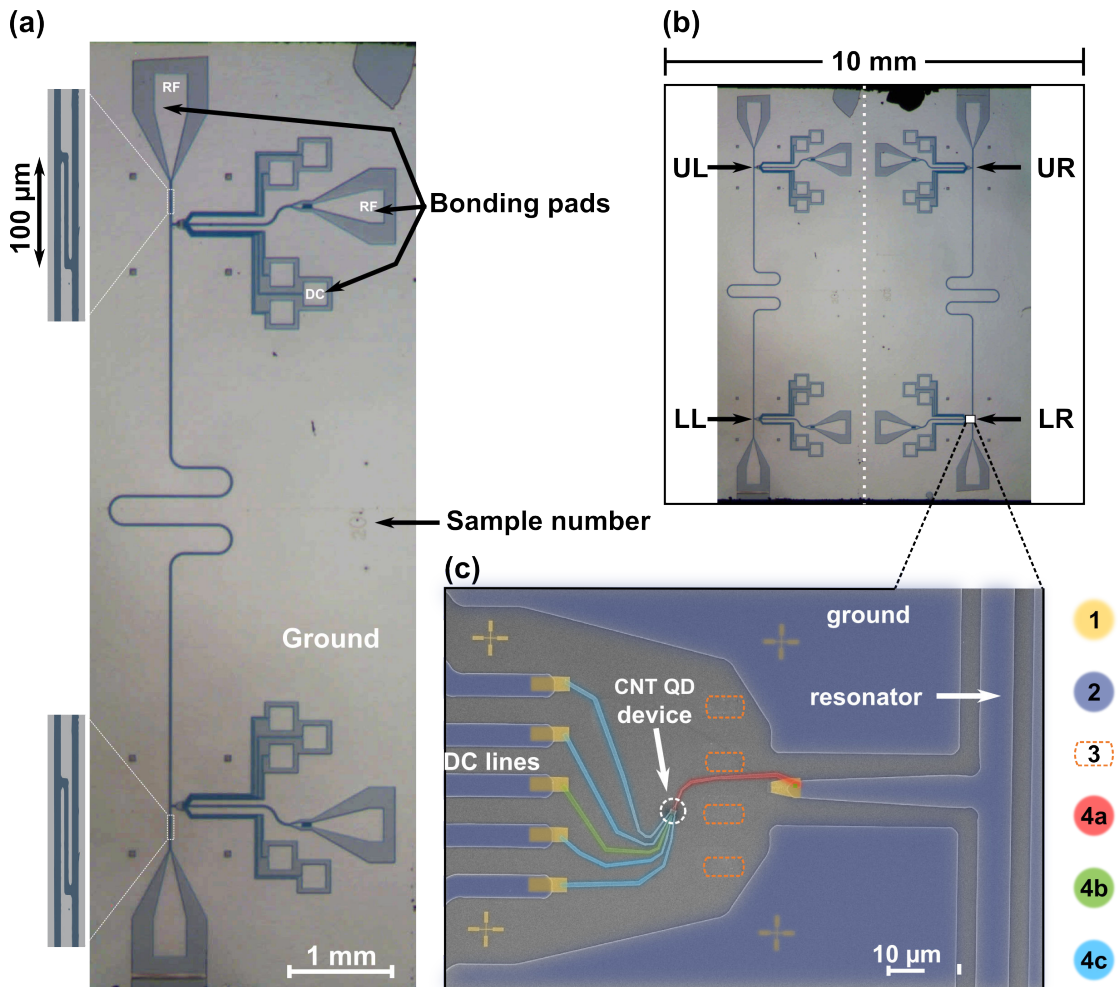


FIGURE 3.1: **Sample description.** (a) is an optical image of our microwave cavity. It is a coplanar waveguide transmission line (see central zoom) interrupted at both ends by finger gap capacitances (up and down zooms). 50 Ohm impedance matching bonding pads enable to connect the cavity to input and output ports. At the two maxima of the cavity electric field one ground plane is opened to leave space for the device and its electrodes. The square bonding pads are used to connect 5 DC lines. The central line can also be addressed in the microwave range, hence the presence of a 50 Ohm adapted bonding pad. In practice 10mm * 10mm chips are handled, on which two samples are fabricated, with four areas to place devices (b). (c) is a zoomed SEM picture of the lower right (LR) area, where the carbon nanotube (CNT) quantum dot (QD) device is circled in white. Features which are patterned simultaneously are colourized with the same artificial colour. Numbers in the legend are indicative of steps ordering. Number 3 is the carbon nanotube stamping step, materialized by the mesas stamping imprints underlined in orange.

the same step. Steps are performed following the legend number ordering. They are simply outlined here, and are further described in the following subsections.

0. **Sample cleaning**

1. **Patterning of gold alignment crosses, contacting pads and sample number (yellow)** using standard lift-off electronic lithography (technique detailed in 3.1.3).
2. **Niobium coplanar wave-guide resonator and circuit bonding pads and precontacts (blue)** fabrication combining etching and lithography.
3. **Carbon nanotube stamping** : carbone nanotubes are grown on a separate quartz substrate containing mesas, which are stamped in the resonator ground openings. The stamping procedure leads to the transfer of carbon nanotubes onto the sample. It may occasion mesa imprints, underlined with orange dotted lines.
4. **Patterning of the device electrodes** : after the localization of nanotubes various electrodes can be patterned using electronic lithography. Here ² the number of steps is set by the number of different employed materials.

This process meets both the need for high quality factor cavities ($Q \sim 10^4$) and for working carbon nanotube devices. Combining these elements is an experimental challenge, which has been fostering intense development work in the team before I started. It resulted in the stamping technique [114], from which I benefited to realise the samples presented in this thesis.

3.1.2 **Sample cleaning**

Our 10mm * 10mm chips are obtained by dicing undoped high-resistivity Si/SiO_2 wafers. The silicon dioxide layer is 500nm thick, while total thickness is around 500 μ m. As wafers are covered by a protection resist layer for dicing, it is necessary to remove this resist prior to any fabrication step. Our cleaning procedure consists in two successive 5 min ultrasonic bath in acetone, followed by a 5 min ultrasonic bath in isopropyl alcohol (IPA).

²without using angle evaporation

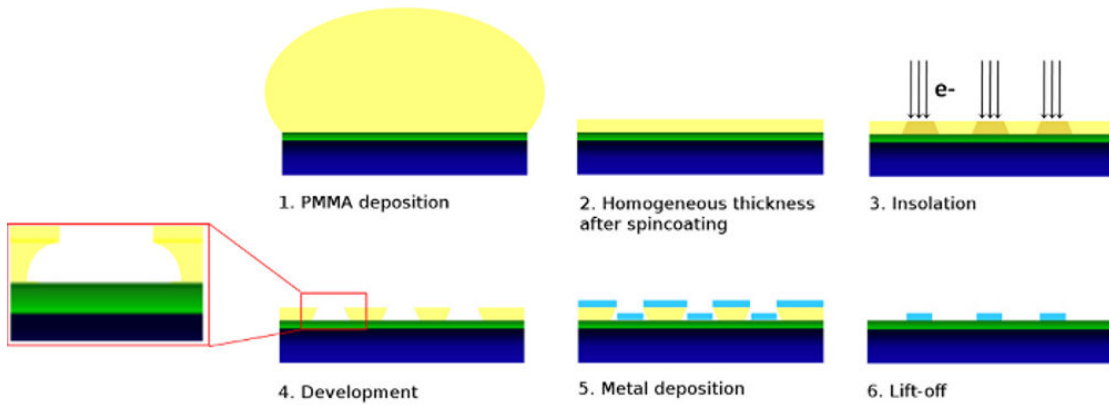


FIGURE 3.2: **Principle of lift-off positive electronic lithography.** The areas insulated in step 3 correspond to the metallic patterns in the final step 6.

3.1.3 Patterning of gold alignment crosses, contacting pads and sample number

All yellow patterns of figure 3.1 are realised in this first step using lift-off positive electronic lithography. The principle of this technique is summarized in figure 3.2 and is described below.

- Resist deposition** An electro-sensitive resist is deposited on the sample. Poly-methyl methacrylate (PMMA) is used. To obtain a 500 nm thick resist layer (sketch 2 of figure 3.2), we put a few PMMA drops on the sample (sketch 1 of figure 3.2) and place it in a spin-coater, where it is rotated during 30s at a 4000 *turns/min* speed reached with a 4000 turns/min^2 acceleration. Then it is heated at 165°C for 15 minutes.
- Electronic lithography** The sample is then placed in a Scanning Electron Microscope (SEM). A mask drawn with the SEM software defines the areas, which are exposed to the electron beam (sketch 3 of figure 3.2). In a positive lithography insulated areas correspond to the final patterns. The step size and beam aperture are set depending on the pattern size.
- Development** Insulated PMMA is damaged and can be removed by placing the sample 2 minutes in methyl isobutyl ketone (MIBK) diluted in IPA (proportions are 1 to 3). As a result there is no more resist on the patterns (sketch 4 of figure 3.2).
- Metal deposition** A controllable metallic thin film is deposited all over the sample (sketch 5 of figure 3.2). We use an ultra-high vacuum ($P < 5.10^{-10}$ mbar) electron gun evaporator. Such a low pressure ensures the purity of the deposited metals,

and is obtained thanks to a cryogenic pump. A focused beam of accelerated electrons targets a tiny crucible containing the desired metal. The beam heats the material, causing sublimation. The rapidly cooling vapour condensates on the sample substrate and thin layers can be created with a high degree of control over thickness. The thickness is probed by the resonance frequency of a piezoelectric quartz deposition controller situated inside the chamber, which is sensitive to the mass of deposited metal. Deposition rates lie between 1.5 and 10 Å/s and depend on the material.

- **Lift-off** Acetone dissolves the remaining PMMA, which lifts the metal off except on the patterned areas, where metals stick on the substrate (sketch 6 of figure 3.2). Depending on its composition and thickness it might be necessary to warm acetone for the film to lift-off.

Yellow patterns of figure 3.1 are made of Ti(5nm)/Au(40nm) using this technique. Large alignment crossed (not visible) and sample number are lithographed using a 120µm beam aperture. Fine alignment crosses and contacting pads are lithographed with 10µm aperture. These pads made out of noble metal ensure the contact between large and fine electrodes, in contrast to Nb that gets oxidized.

3.1.4 Niobium coplanar wave-guide resonator and circuit bonding pads and precontacts

Both the coplanar waveguide resonator and the large circuit structures (bonding pads and precontacts) are made out of Nb by combining etching and lithography in the following process :

- **Nb deposition** Nb deposition is tricky because it has a very high sublimation temperature. This means that it is hardly compatible with lift-off processes, as resists are altered by excessive temperatures. Here 150nm thick Nb is deposited directly over the whole chip, that already has gold patterns made in step 1. Our electron gun evaporator is powerful enough to evaporate Nb. Most importantly it is equipped with cryogenic shields and sample holder cooling, which enable to keep the pressure around $10^{-9} - 10^{-8}$ mbar using liquid nitrogen circulations. This is crucial for the Nb quality, which directly affects the resonator internal losses κ_L introduced in previous chapter.
- **Positive lithography** The resist is exposed in the resonator gaps (grey-blue areas on 3.1a or equivalently grey areas on 3.1c). During the designing phase of the mask

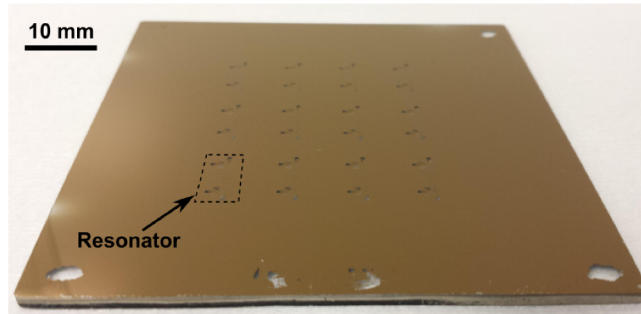


FIGURE 3.3: **Photograph of optical mask (Cr on transparent glass) fabricated to photo-lithograph resonators and large circuit structures.** Taken by M.C. Dartiailh.

it is convenient to use electronic lithography, as the mask can be changed at will. Once the design issue is settled, it is more efficient to use optical lithography, where insulation takes a few seconds compared to several hours using e-beam. Therefore one has to fabricate a physical mask from a glass plate covered with Cr, on which resonators are patterned using etching positive electronic lithography (photography on figure 3.3). We use AZ5214 as photosensitive resist. It is spin-coated on the chip, and baked. The five contacting pads on the sample have to be aligned with the lines precontacts on the mask. Sample and mask are put into contact during insulation. Developing in MIF726 removes the insulated resist.

- **Etching** Here apparent niobium areas are etched, while niobium areas covered with resist are protected. Reactive Ion Etching (RIE) with SF_6 gas is used to etch niobium. There is both a chemical and physical action of the fluor ions, which are formed and accelerated by the plasma field.
- **Resist dissolving and cleaning** The protection resist is dissolved in acetone. As some resist tends to remain on the chip, it is completely removed by a 3min long soft oxygen plasma in the RIE chamber.

3.1.5 Carbon nanotube stamping

The stamps fabrication can be done independently of the first sample fabrication steps. Mesas are patterned on quartz substrates. CNT are grown on them. Finally the quartz mesas are stamped in the ground openings of the sample resonators, which leads to the transfer of CNT. All these steps are detailed in the following subsections.

3.1.5.1 Stamps fabrication

10mm * 10mm quartz substrates are cleaned. We use lift-off positive electronic lithography³ to pattern a set of four rectangles (with typical size $10\mu\text{m} * 5\mu\text{m}$) in each corner of the quartz substrate. The 250nm thick nickel layer on the rectangles acts as a protection mask during the etching step. Indeed RIE with O_2 and CHF_3 etches SiO_2 more rapidly than Ni . To obtain flat mesas, the etching time is set so, that the final Ni thickness is higher than the square root of the Ni etched thickness. Chemical wet etching of the residual nickel is done using a $FeCl_3$ solution. The whole process results in $4.2\mu\text{m}$ high mesas.

3.1.5.2 Carbon nanotube growth

Carbon nanotubes are grown on the patterned quartz substrates by Chemical Vapour Deposition. This technique requires a catalyst. The whole recipe is designed to obtain single walled carbon nanotubes. The catalyst composition is $39\text{mg } Fe(NO_3)_3 - 9H_2O$, $7.9\text{mg } MoO_2$ and 32mg of Al_2O_3 nanoparticles diluted in 30mL of IPA. Prior deposition the catalyst flask has to be agitated with ultrasound for one hour to split molecules aggregates. After 45 minutes decantation only nanoparticles remain at the liquid surface. Two drops of catalyst are put on the chip, and dried with nitrogen flow immediately after the second one. Once catalyst is deposited, the quartz chips are placed in a special furnace dedicated to nanotubes Chemical Vapour Deposition. This furnace is a long quartz tube, in which 3 gases are injected : argon Ar (1450 sccm), dihydrogen H_2 (200 sccm) and methane CH_4 (1140 sccm). The process is the following :

- 5 min purge of the three gases
- heating under argon to obtain a 900°C temperature
- 8 min dihydrogen
- 10 min dihydrogen and methane (growth step)
- 90 min cooling under dihydrogen and argon
- final cooling under argon

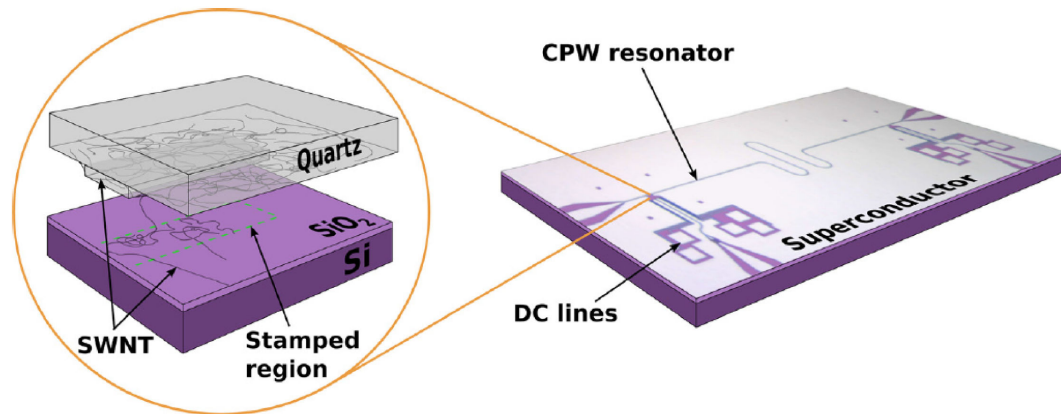


FIGURE 3.4: **Principle of CNT stamping** for combining high finesse microwave cavity with CVD-grown single wall carbon nanotubes (SWNT). The standard CVD growth is performed on a quartz substrate containing mesas which we use as stamps in order to transfer SWNT's on a clean silicon RF substrate. This can be done at chosen locations, in this case in the ground plane openings of a superconducting co-planar microwave resonator. Source: [114]

3.1.5.3 Stamping step

The principle is to flip over the quartz substrate, to align the mesas in front of the underneath sample ground openings, and to put the mesas in contact with the SiO_2 sample to transfer CNT (figure 3.4). Straightforward issues are alignment and contact. We use the alignment possibilities of the optical masker, which is normally used for optical lithography. The quartz substrate has to be fixed on a large glass plate, that can be hold by the masker. The fixing mechanism is crucial for the contact step. As planarity is never perfect, a rigid sticking makes the contact tricky. Indeed when the two substrates come closer, they tend to touch each other at other points than the mesas. In contrast a soft sticking helps in adjusting planarity, and makes the stamping easier. After trying several methods ⁴ the most reproducible and successful method consists in sticking the quartz substrate on the glass plate using double-sided tape. After stamping our sample silicon chip is imaged with the SEM (figure 3.5). Here the stamps imprints are visible. The fine alignment crosses lithographed in the first step are used in the imaging procedure to localize CNTs precisely. Usually a few CNTs have been transferred (figure 3.5 b), and we choose long and accessible single-walled CNTs to host the devices.

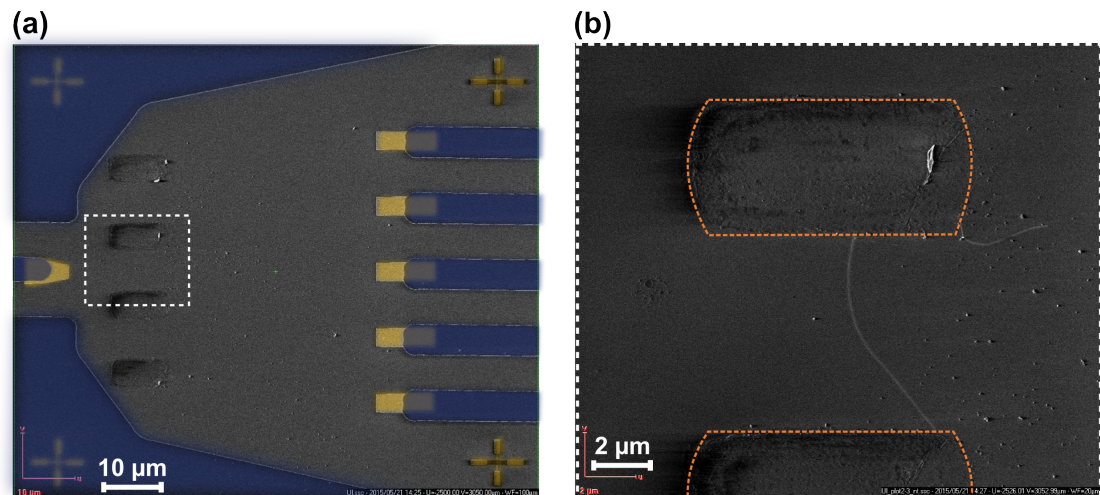


FIGURE 3.5: **CNT localization after stamping.** (a) is a SEM picture of a resonator ground opening area after stamping. The colour code is the same as for figure 3.1. Stamping imprints of the four mesas are visible. A dotted white square borders the zoomed area shown in (b). Here the stamping imprints are underlined with dotted orange lines. The contrast of transferred CNTs has been artificially enhanced for clarity.

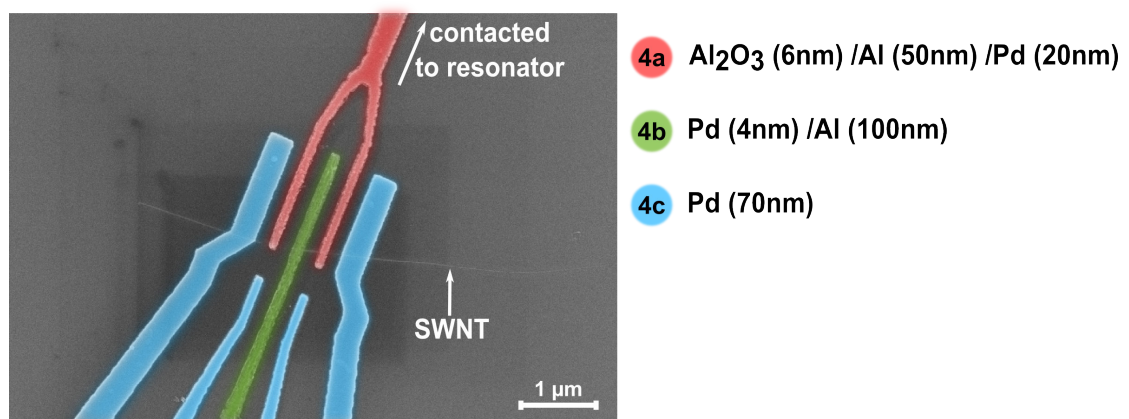


FIGURE 3.6: **Device electrodes patterning steps for our final CPS design.** The SEM picture is colorized with the same color code as 3.1. The SWNT contrast is artificially enhanced. Three successive processes of lift-off positive electronic lithography are performed on the CNT, one for each material. The coupling fork-shape top gate (red) is fabricated first. Then the superconducting central electrode (green) is patterned. Finally normal outer contacts and side gates are made simultaneously.

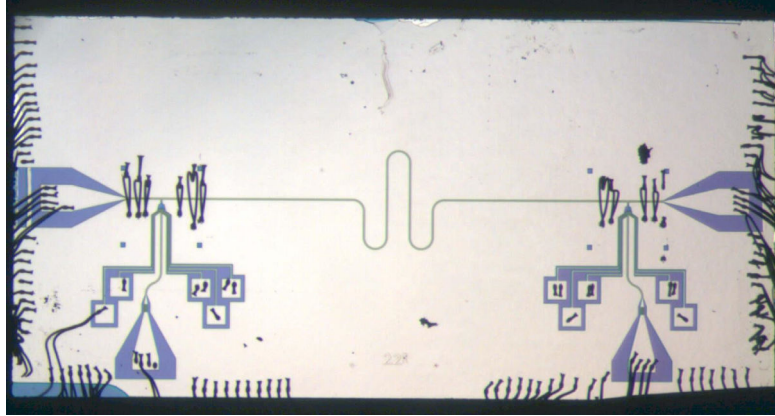


FIGURE 3.7: **Sample optical image after measurement showing wire bonds locations**

3.1.6 Patterning of the device electrodes

Electrodes are patterned using lift-off positive electronic lithography (section 3.1.3). The localization images are inserted in the SEM software, making it easy to draw an appropriate mask contacting precontact lines to the CNT. The whole process is repeated for each material composing the device. Our final Cooper pair splitter design, which corresponds to the studies presented in chapter 5 et 6 (sample CPSRES32R), requires three steps, which are labelled 4a,b,c in 3.1 and 3.6. The first one (4a) consists in fabricating a fork-shape top gate, which is directly contacted to the resonator central conductor. It is made of $Al_2O_3(6nm)/Al(50nm)/Pd(20nm)$. The second one (4b) is the central superconducting electrode $Pd(4nm)/Al(100nm)$. We use aluminium as a superconductor and a thin layer of Pd, which enables to contact CNTs and gets superconducting by proximity effect. The last step (4c) patterns 70nm thick Pd side gates and contact electrodes. Prior thinking of step 4a to enhance the coupling of the CPS to the cavity field, we were only performing step 4b and 4c. This is the case of the sample studied in chapter 4 (CPSRES20R).

3.1.7 Sample mounting and wire-bonding

Final chips are cut into two samples R/L using a diamond tip scribe. After a final cleaning step in IPA, samples are glued on the sample holder with PMMA. Microbonding 25 μm diameter aluminium wires connects the cavity and device electrodes to the sample holder lines. During microbonding the operator should be connected to electrical ground at all times to avoid any electrostatic jolt to nanotubes, which would damage them.

³similarly to 3.1.3 with an additional aluminium layer deposition before lithography to avoid charging effects

⁴like gluing with PMMA, with and without PDMS

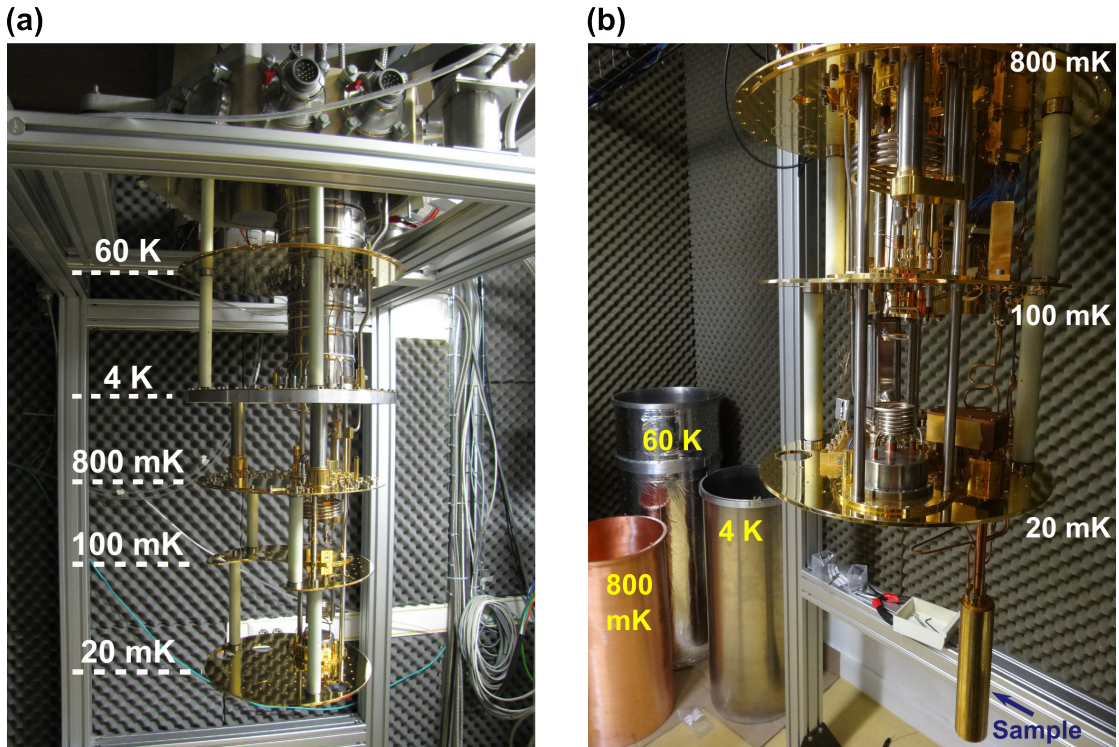


FIGURE 3.8: **Empty (a) and wired (b) cryostat.** White labels indicate the cryostat plates temperatures and the yellow ones the shields temperatures. The sample is inside the cylinder indicated in blue.

Figure 3.7 displays an optical image of a sample after measurement. The bonding traces show numerous bondings, which role is to obtain a well-defined ground. In particular bondings jumping over the cavity line are crucial to observe a resonance.

3.2 Measurement setup

Our measurement setup is designed to simultaneously perform low-noise transport measurements of the device and microwave cavity transmission measurements at low temperature.

3.2.1 Cryogenics

Temperature sets the upper limit for the resolvable energy scales. In order to study a CPS device, we crucially need to resolve the Pd/Al superconducting gap, which is of the order of $100\mu\text{eV}$. Taking into account Fermi distribution width gives the condition $3.5k_B T \ll \Delta$ equivalent to $T \ll 330\text{mK}$. This justifies the use of a dilution refrigerator, which provides a base temperature around 20mK. This temperature range also enables to reach the cavity quantum regime, where the thermal photon number $\frac{1}{e^{\hbar\omega_c/k_B T} - 1} \ll 1$

or equivalently $T \ll 400\text{mK}$. Several months of this thesis have been spent in designing and realizing the wiring of a dry Cryoconcept dilution refrigerator. The photograph of figure 3.8 shows that it is made of successive plates, which are colder from top to bottom. A pulse tube provides the cooling power for the first and second stage at 60K and 4K. The next stages rely on the thermodynamic properties of a mixture of ^4He and ^3He . The still sets the temperature of the 800mK stage. The next stage is around 100mK and the last one hosts the mixing chamber (MC), which sets the refrigerator base temperature. The wiring scheme is sketched on figure 3.9. Our technical choices for DC and microwave lines are presented and explained in the following subsections. They are guided by the quest for the best quality measurements, while keeping the refrigerator working.

3.2.1.1 Precautions imposed by the cryostat

All elements introduced in the cryostat have to be thermalised by anchoring at a given stage. For this reason all mechanical pieces are made out of oxygen free high conductivity (OFHC) copper, and are gold plated to prevent oxidation. Additionally cryogenic grease (ApiezonN) is used to make better thermal contact between pieces. The thermal conduction between stages should be as low as possible, which explains the use of resistive manganin wires and relatively attenuating CuBe microwave cables. As the 60K, 4K and 800mK stages are equipped with shields, it is crucial to prevent any radiation going through these stages. Pieces are designed in a way that avoids straight paths for photons ("Mexican hat"-shaped thermalization pieces for the RF amplifier power supply on figure 3.12c, trapeze-shaped clamps on figure 3.10a). This is also one justification for the U-shape of microwave cables, as shown on figure 3.12.

3.2.1.2 DC lines

DC lines are either used to polarise gate electrodes or to apply a bias voltage and measure current through the device. DC wiring is designed having in mind two major issues : thermalization and protection from noise.

Thermalization The refrigerator temperature corresponds to the temperature of phonons. For our electrical measurements this is the temperature of electrons, that matters. This is why a lot of effort is put to thermalise DC lines at each cryostat temperature stage.

- **60K ; 4K ; 800mK stages** Stainless steel flexible coaxial cables are pressed at each stage in golden copper clamps as shown in figure 3.10a.

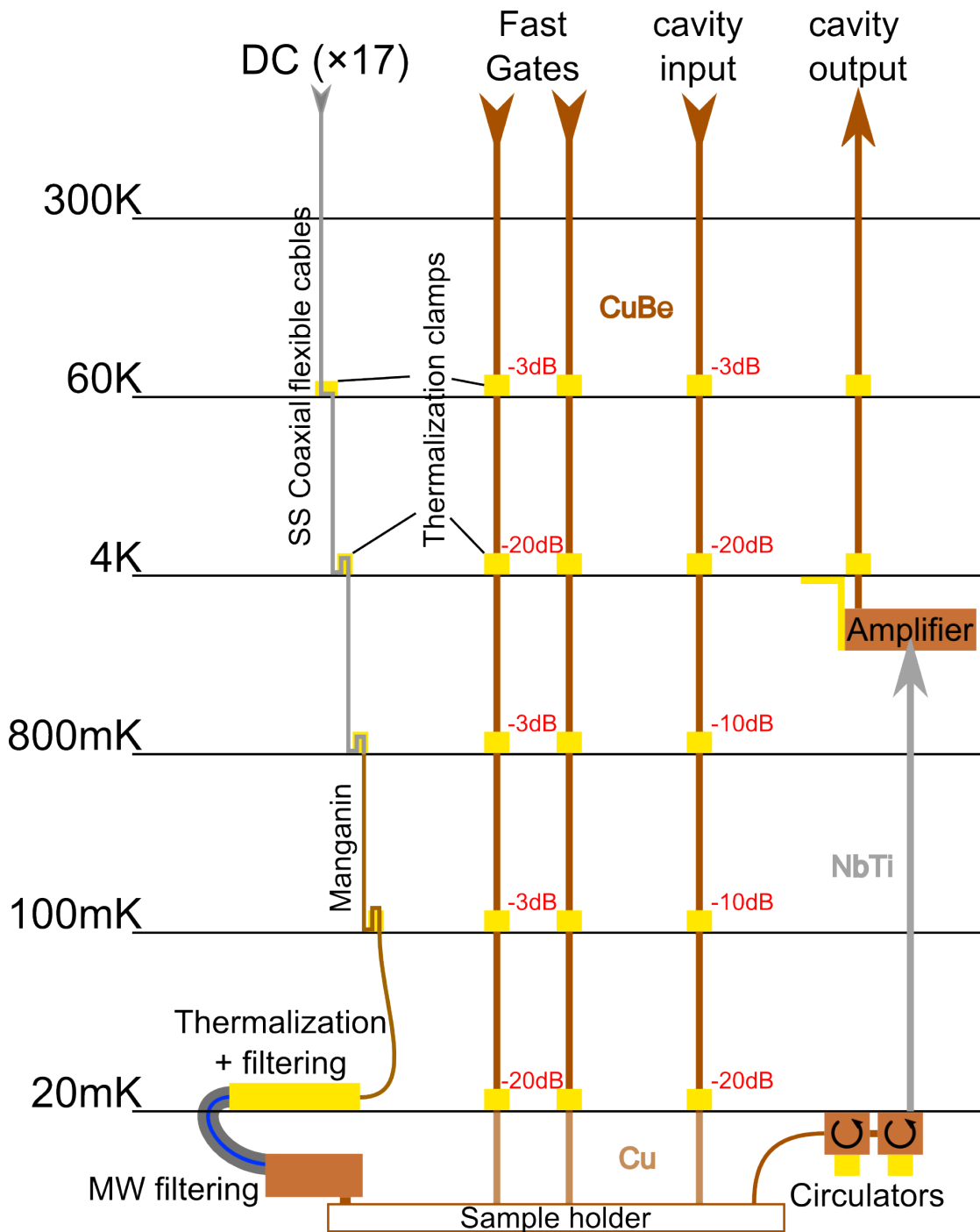


FIGURE 3.9: **Cryostat wiring scheme.** There are 17 identical DC lines and 4 microwave (MW) lines corresponding to cavity input and output and two fast gates. Microwave wiring is done using CuBe (brown), Cu (light brown) and NbTi (grey) semi-rigid cables. Thermalization elements are depicted in yellow. Red numbers indicate the value of discrete attenuators at each stage.

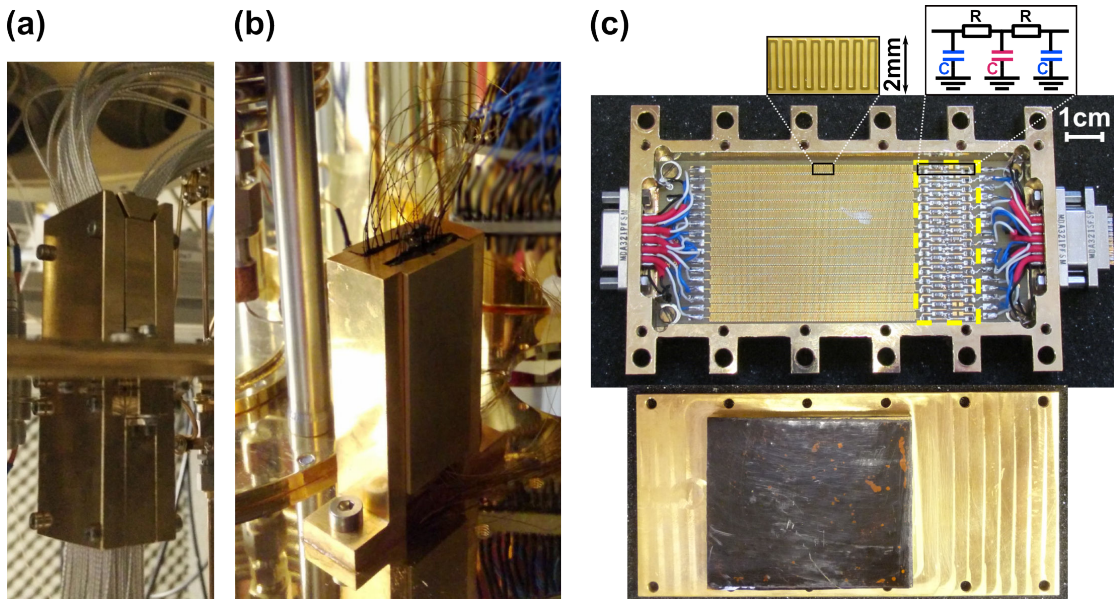


FIGURE 3.10: **Techniques for thermalizing DC wires.** (a) Clamps for thermalizing stainless steel coaxial cables at 60K, 4K and 800mK. (b) Clamps for manganin wires glued with stycast (black epoxy). (c) Lithographed meanders on PCB for thermalization at 20mK and on-chip cms components ($R=1\text{k}\Omega$, blue $C=1\text{nF}$, pink $C=2.2\text{nF}$) forming second-order low-pass filters (surrounded in yellow). The lines are thermalised by a block shaped in the copper lid, which is covered with a kapton sheet (orange) glued with stycast (black).

- **100mK stage** Manganin wires are glued with stycast⁵ between a gold plated copper piece and a brass piece (figure 3.10b).
- **20mK stage** As the material thermal conductance decreases with temperature, the thermalization length increases. Therefore we use micro-lithographed meanders on a PCB, displayed on figure 3.10c. They are thermalised by pressing a copper block covered with a $200\mu\text{m}$ thick kapton sheet, which is glued with stycast. Kapton satisfies the joint need for electrical insulation and acceptable thermal conductance. Thermalization occurs over 40cm, which exceeds the estimated thermalization length of 14cm⁶.

Noise minimization The following elements are meant to minimize noise either by metallic shielding or by filtering.

- **Stainless steel coaxial cables** are used between 300K and 800mK to protect the wires from the black body radiation of the cryostat shields.

⁵This epoxy is compatible with cryogenic temperature and has the particularity to have a thermal contraction close to copper.

⁶Such value gives an indication of the relevant order of magnitude but is very uncertain, as they are few measurements of thermal conductivities at such low temperature. In addition for copper it is extremely sensitive to the metal purity.

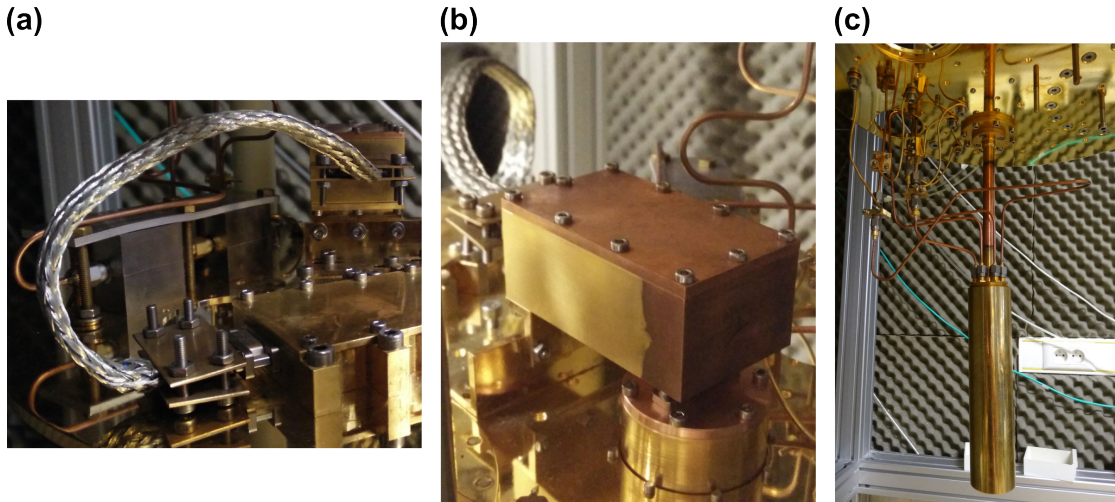


FIGURE 3.11: **Techniques for minimizing noise in DC wires.** (a) A metallic braid shields the DC wires from the electromagnetic field between the thermalization/filtering block and the microwave filtering block photographed in (b). (c) shows that DC wires stay shielded to the very end by metallic tubes, when they reach the sample.

- After the thermalization meanders on the PCB there are second-order low-pass filters so-called **Pi filters**(figure 3.10c).
- **A metallic braid** shields the wires coming out the thermalization/filtering box before they go in a microwave filtering box (figure 3.11a).
- **The microwave filtering box** is shown on figure 3.11b. Inside wires are twisted to increase their length and the box is filled⁷ with ecosorb CRS 117, a microwave absorbent.
- A copper tube finally shields the lines and the sample (figure 3.11c).

3.2.1.3 Microwave lines

There are three incoming lines (the cavity input line and two fast gate lines) and one outgoing line (cavity output line). They satisfy radically different requirements, which are presented below.

Incoming lines To reach the quantum regime for a non-driven cavity both strong attenuation and thermalization are important. Indeed the cavity is exposed to the thermal noise of a 50Ω resistor at 20mK plus the 50Ω thermal noise at all stages temperatures, each attenuated by the following attenuators. All microwaves cables and attenuators

⁷Note that the wires soldering should not be covered with ecosorb, as thermal-induced mechanical constraints break the soldering. Therefore we designed holed plastic partitions to protect plugs, while letting wires going through.

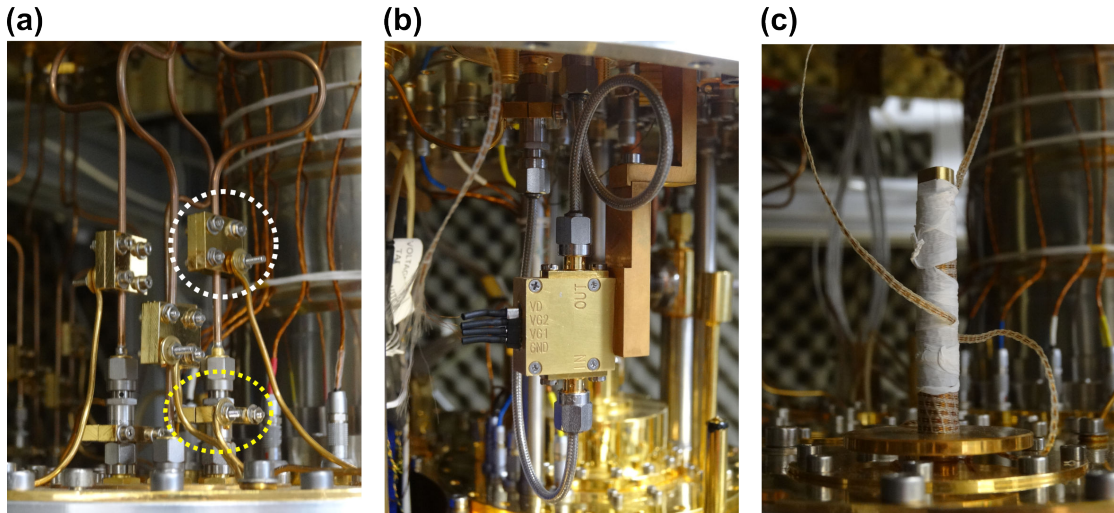


FIGURE 3.12: **Techniques for microwave wiring.** (a) shows the thermalization clamps for microwave cables (white circle) and for attenuators (yellow circle) and their anchoring using gold plated copper wires. The U-shape cable portions are visible at the top of the picture. (b) displays a cryogenic amplifier powered by two twisted pairs BeCu wires, which are thermalised on a rod shown in (c). The large circle rod base acts as a "Mexican hat" shadowing the small holes, which let the wires going through the plate. The amplifier displayed here is connected in a 4K-test configuration, which explains why the NbTi cable is not visible.

are thermalised with clamps, which are thermally anchored to a cryostat stage with gold plated copper thick wire (figure 3.12a). The attenuation values given on 3.9 are indicative of the lines transmission, but do not provide accurate calibration of the cavity drive, or of the microwave amplitude applied to fast gates. In-situ power calibration schemes are required, as chapter 5 will illustrate.

Outgoing line The cavity output line carries the signal of interest, that is the cavity transmission. As a result attenuation is highly undesirable. For this reason a superconducting NbTi microwave wire is used between 20mK and 4K. There it goes in a 35dB gain cryogenic amplifier (figure 3.12b), which only adds a 4K thermal noise to the signal. To prevent the amplifier noise from going backward onto the sample, two circulators are placed in series at 20mK before the NbTi cable. These are chiral components, which have 18dB attenuation in one direction. The amplifier is power supplied using two twisted pairs BeCu wires⁸, which are thermalised at 60 and 4K using "Mexican-hat shaped" pieces (figure 3.12c).

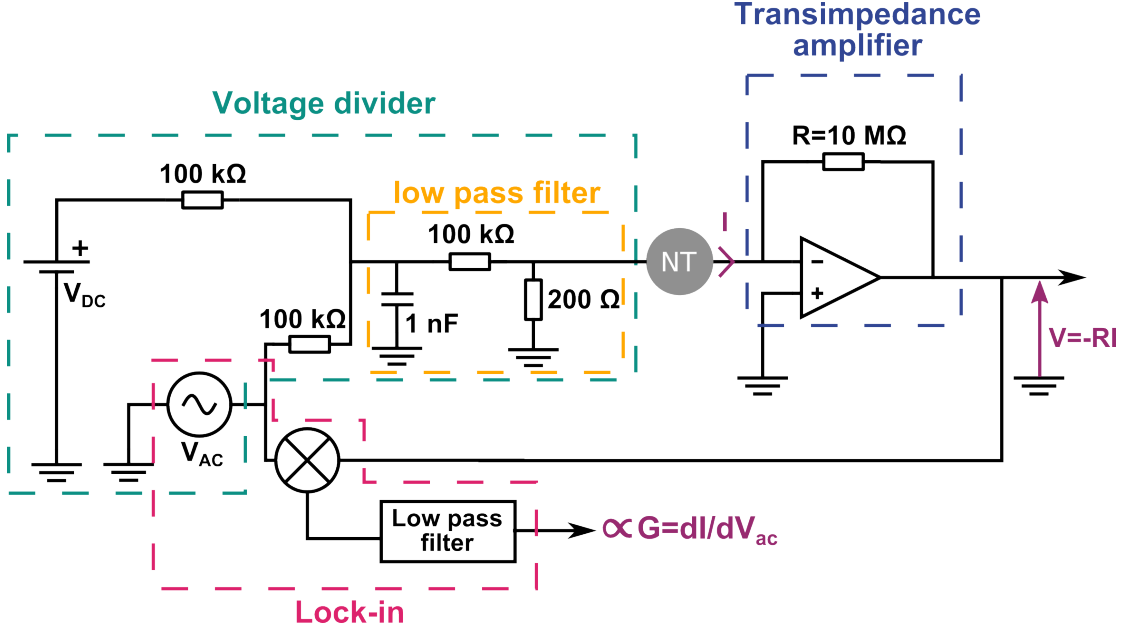


FIGURE 3.13: Low noise transport measurements setup.

3.2.2 DC measurements

3.2.2.1 Low-noise detection

The setup addressing the carbon nanotube is represented on figure 3.13. Using synchronous detection the differential conductance G can be measured in addition to the current I . The nanotube is polarised by the output voltage V_{bias} of a voltage divider adding a continuous voltage V_{DC} typically between $-1.5V$ and $1.5V$ and a small alternative voltage $V_{AC} = 15mV$, at frequency typically of the order of hundred Hz.

$$V_{bias} \approx \underbrace{\frac{2 V_{DC}}{3 \cdot 1000}}_{V_{SD}} + \underbrace{\frac{2 V_{AC}}{3 \cdot 1000}}_{V_{AC}'}$$

After the divider, the small AC voltage is $V_{AC}' = 10\mu V$ ⁹. The source-drain continuous voltage V_{SD} typically lies between $-1mV$ and $1mV$. The current coming out the nanotube is amplified with a home-made analogical amplifier with gain 10^7 . Basically it can be viewed as a transimpedance amplifier (surrounded in dotted blue on figure 3.13), composed of an operational amplifier and a resistance $R = 10^7 M\Omega$. Consequently, $V_{out}(t, V_{sd}, V_g) = -R * I(t, V_{bias}, V_g)$ with :

$$I(t, V_{bias}, V_g) = I(V_{SD}, V_g) + \frac{dI}{dV}(V_{SD}, V_g) V_{AC}' \cos(\omega t) \quad (3.1)$$

⁸ $10\Omega/m$

⁹Such energy corresponds to $3.5k_B T$ with $T \approx 34mK$, thus should not cause any extra broadening.

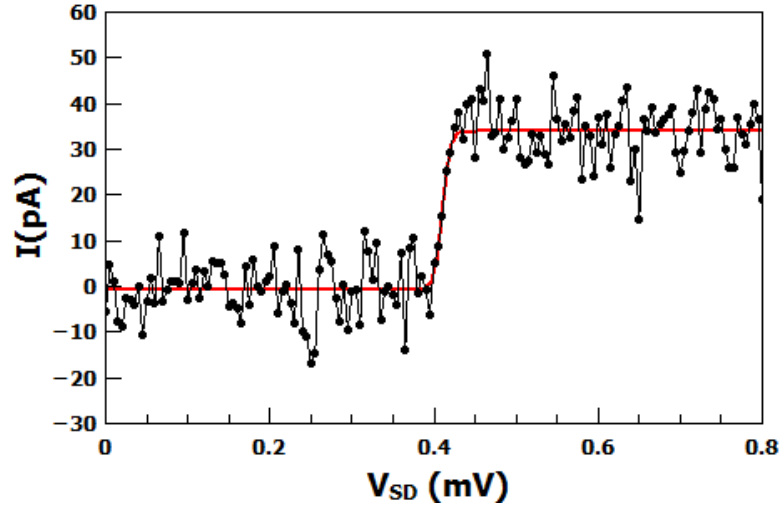


FIGURE 3.14: **Electronic temperature upper bound.** In the Coulomb blockade regime the width of current steps sets an upper bound to the electronic temperature. Here the red curve fitting the experimental curve (black) corresponds to $T_{el} = 50 \pm 21mK$.

In the lock-in the output voltage is multiplied with the local oscillator alternative voltage and the total signal goes through a low-pass filter, so that we measure a signal proportional to the differential conductance :

$$\langle V_{out}(t) V_{AC} \cos(\omega t) \rangle \rightarrow -R * \frac{dI}{dV}(V_{sd}, V_g) V_{AC}' \quad (3.2)$$

The advantage to measure at finite frequency is to get rid of high low-frequency noise (below $10Hz$) and $50Hz$ noise. The noise we get is the noise density of a frequency window centred on the used AC-frequency (here $77, 77Hz$) and wide like the filter bandwidth. The AC-frequency is chosen to minimize noise. Devices are first tested at room temperature to check if CNTs are electrically connected, before being cooled down at cryogenic temperature.

3.2.2.2 Electronic temperature

As discussed in section 1.2.1.2 and 1.2.1.3, the current step width, or the low-bias conductance FWHM, roughly corresponds to $\max(3.5k_B T, \Gamma)$ for a quantum dot in the Coulomb blocked regime. This gives an indication on the maximal value of the electronic temperature. On figure 3.14 a current step in the Coulomb blockade regime is fitted using the expression given by 1.15. The extracted electronic temperature is $T_{el} = 50 \pm 21mK$, which validates the thermalization technical choices ¹⁰.

¹⁰at least for the cryostat lines 11 and 14 used as source and drain for this measurement.

3.2.3 Microwave measurements

The microwave setup drives the cavity and measures its transmission properties (figure 3.15). More precisely we measure the in-phase (I) and out-of-phase (Q) quadratures of the transmitted signal, from which we deduce the signal phase and amplitude.

The RF source provides power at ω_{LO} in a [1; 20] GHz frequency range. The signal is split into a reference signal and an excitation signal. Using a mixer the excitation signal is modulated at the Lock-in frequency $\omega_{IF} = 2577.77Hz$. The amplitude of the modulation V_{IF} sets the power of the microwave modulated signal at $\omega_{LO} \pm \omega_{IF}$ ¹¹. Discrete room temperature attenuation Att is chosen depending on the desired cavity input power. Then the signal goes in the cryostat input line ($\approx -68dB$ attenuation) before reaching the sample. After a 4K amplification on the cryostat output line ($\approx +31dB$), the output signal is further amplified at room temperature ($\approx +62dB$). The presence of filters, circulators and attenuators contribute to the signal quality. Finally the output signal is demodulated in an IQ-mixer, using the reference signal at ω_{LO} . An IQ-mixer has two channels and introduces a 90° phase shift on one channel. This separates the two signal quadratures. After demodulation at frequency ω_{IF} in the Lock-In, charge and current amplitudes are extracted :

$$I = A \cos(\varphi) \quad Q = -A \sin(\varphi)$$

from which the modulus A and the phase φ of the transmitted signal $A_{out} \equiv Ae^{j\varphi}$ can be deduced :

$$A = \sqrt{I^2 + Q^2} \quad \varphi = -\arctan\left(\frac{Q}{I}\right)$$

For a bare cavity the transmission T is given by equation 2.10. Making the substitution $i \rightarrow -j$ to account for opposite Fourier transform sign conventions between quantum mechanics and electrical engineering, we obtain :

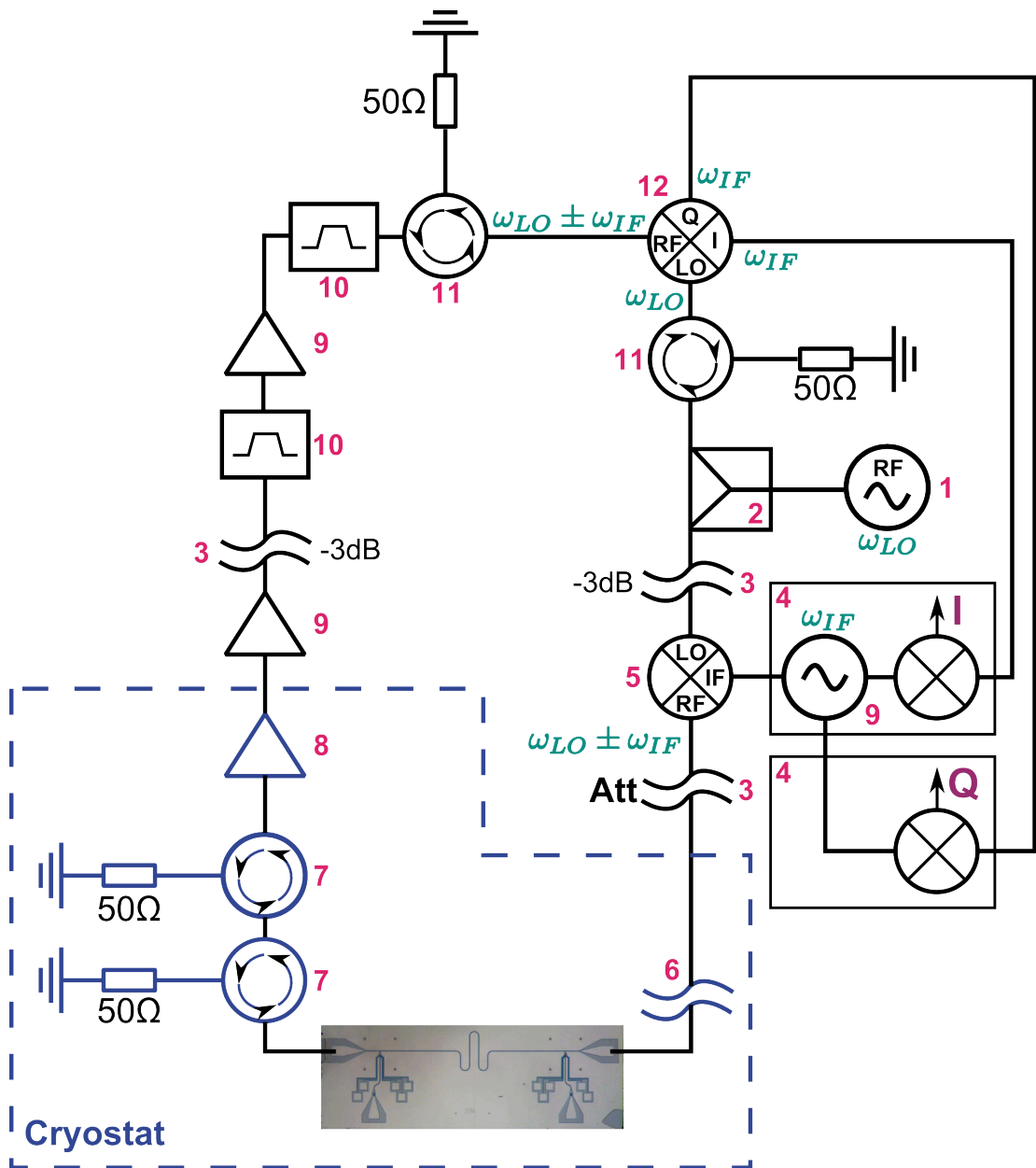
$$A = \frac{\kappa_1 \kappa_2 A_{in}}{\sqrt{(\omega - \omega_c)^2 + \left(\frac{\kappa}{2}\right)^2}} \quad (3.3)$$

and

$$\varphi = \arg\left(-\frac{\sqrt{\kappa_1 \kappa_2} A_{in}}{j(\omega - \omega_c) + \frac{\kappa}{2}}\right) \quad (3.4)$$

Figure 3.16 displays a measurement of the amplitude and phase of the transmitted signal for a bare cavity with around 120 photons (points) and the fitting curves (plain lines) given by 3.3 and 3.4. The square of the transmitted signal amplitude is expected to

¹¹For optimal power control V_{IF} should lie between 56 and 200 mV



- | | | |
|--|---|---|
| 1 Agilent Source E8257D | 5 Mixer Marki M10412LA | 9 Amplifier |
| 2 6dB power splitter 5336
Picosecond Pulse Labs | 6 XMA attenuators | 10 High pass filter VHF-3500
minicircuit |
| 3 Attenuators | 7 Cryogenic circulators
Quinstar XTE0812KC | 11 Circulator AEROTEK
H60-1FFF |
| 4 Lock-in SR7265 | 8 Cryogenic amplifier
Caltech | 12 IQ mixer Marki 4509L |

FIGURE 3.15: Microwave measurement chain of the two quadratures I and Q of the resonator transmitted signal. The dashed blue line encloses the part of the setup inside the cryostat. Pulsations are indicated in green to illustrate the modulation/demodulation scheme.

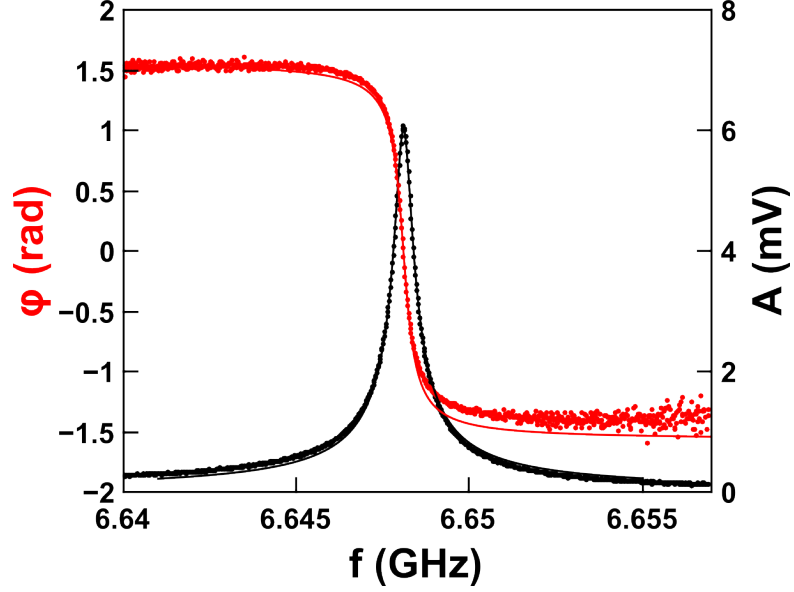


FIGURE 3.16: **Amplitude and phase of the resonator transmitted signal** for $n \approx 120$ photons in the resonator (points). The amplitude A peaks at the resonance frequency, while the phase φ makes a π shift. Fitting the amplitude with 3.3 gives $f_c = \omega_c/2\pi = 6.64809$ GHz and $\Delta f_{-3dB} = \kappa/2\pi = 522$ kHz, thus $Q \approx 12700$. The plain lines correspond to 3.3 and 3.4 with these fitting parameters.

be a Lorentzian, which peaks at the resonance frequency $f_c = \omega_c/2\pi$. The FWHM Δf_{-3dB} is indicative of the cavity quality, routinely quantified by the quality factor $Q \equiv \frac{f_c}{\Delta f_{-3dB}} = \frac{\omega_c}{\kappa}$. The phase exhibits a π shift across the resonance. Here $f_c = 6.64809$ GHz and $Q = 12700$. We estimate the bare cavity photon number at resonance n_0 from the bare cavity spectrum, combined with rough calibration of our input and output lines, as explained in Appendix C. In presence of the nanocircuit the cavity transmission is modified. Consequently the relevant quantities to measure the influence of the nanocircuit are the phase shift $\Delta\varphi = \varphi - \varphi_0$ and the amplitude relative variation $\Delta A/A_0 = (A - A_0)/A_0$ at the resonance frequency $f = f_c$, the zero index referring to bare cavity signals.

Chapter 4

Dynamics of Kondo effect at finite frequency

4.1	Predictions and existing measurements on Kondo dynamics	84
4.2	Kondo phenomenology	85
4.2.1	Sample	85
4.2.2	Resonance in absence of excitation	86
4.2.3	Phenomenology under microwave excitation	87
4.3	Power-frequency dependance of Kondo conductance peak under microwave excitation	88
4.3.1	In situ microwave amplitude calibration	88
4.3.2	Scaled amplitude-frequency conductance map	90
4.3.3	Ansatz proposed for quantitative analysis	92
4.4	Test of universality	93

We explore the transport properties of a single dot in the Kondo regime under microwave excitation. We start by mentioning theoretical work on the expected Kondo resonance behaviour and by reviewing existing experiments probing this situation. Section 4.2 presents our measurements of the Kondo resonance at equilibrium and qualitative behaviour under microwave excitation. Section 4.3 contains a quantitative study and modelling of the Kondo conductance maximum as a function of excitation frequency f and excitation amplitude V_{AC} . Last section 4.4 addresses the universality property of this frequency-power dependence.

4.1 Predictions and existing measurements on Kondo dynamics

What happens to the Kondo resonance in a quantum dot, if the leads Fermi level and/or the dot electrochemical potential is modulated at frequency f with amplitude V_{AC} ? This question, conveniently referred to as the "AC Kondo" problem, has raised much theoretical interest [63, 115–120] and has been so far investigated in three experiments in GaAs-based 2DEG quantum dots¹[59–61]. Theoretical studies on the "AC Kondo" predict two main effects: the appearance of satellite Kondo peaks at multiples of hf away from the central main Kondo resonance and a decrease in the central Kondo peak due to photonic-induced spin-decoherence. There has been a debate on whether the satellite peaks could be observed, before the Kondo resonance completely vanishes. Experimentally Elzerman et al did not observe satellites [59], whereas Kogan et al did [60].

Kaminski et al predicted that the conductance at the Kondo resonance is a function of the scaled dimensionless parameters $V = \frac{eV_{AC}}{k_B T_K}$ and $F = \frac{hf}{k_B T_K}$ [63]. This means, that even the irradiation-induced decoherence of the Kondo state is governed by a unique energy scale T_K . Such a property is referred to as universality, because the physical law describing the effect does not depend on the system microscopic properties. Two kinds of couplings of the AC field to the dot can be distinguished: AC modulation of the energy level carrying the spin and AC modulation of the bias between source and drain. For an AC modulation of the dot energy level ("gate-type" coupling), the conductance is almost unaffected at low frequencies, and decreases all the more that frequency increases. An AC modulation of bias gives the opposite frequency dependence : conductance is maximally reduced for low frequencies and gradually recovers its unperturbed value when the excitation frequency increases. Testing these predictions requires to measure the frequency-amplitude dependence of the AC Kondo conductance. This is experimentally very challenging, as it requires the ability to send a constant excitation amplitude on

¹To our knowledge, excluding the work presented in this thesis.

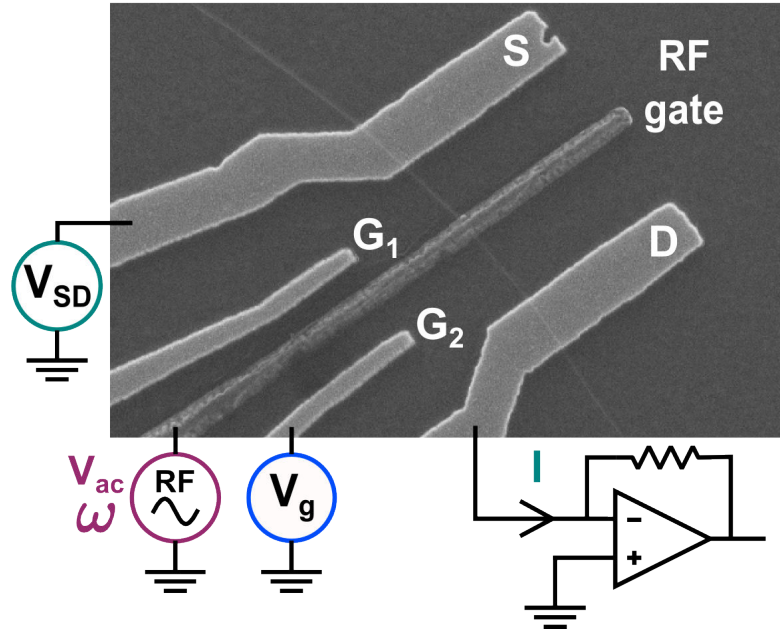


FIGURE 4.1: **SEM picture of the device studied in this chapter** (CPSRES20LR). It behaves as a single dot, which can be biased by applying V_{SD} on the source electrode, while the current is measured through the drain electrode. A DC gate voltage V_G is applied on a side gate. A microwave excitation V_{AC} at frequency f can be applied on the central top gate.

the sample, while changing the frequency. In practice microwave setups naturally do not provide this : at fixed source power, the power on the sample is frequency dependent. Therefore in-situ calibration is required. Two experiments proposed calibration criteria based on assumptions about the Kondo response itself [59, 61]. While this strong assumption allowed Hemingway et al. [61] to observe qualitative frequency dependence, it prevented them from testing the AC Kondo joint frequency-amplitude dependence and the resulting scaling properties. This calls for a better microwave amplitude control, which is achieved in our experiment by an independent in-situ calibration. This allows us to perform a quantitative study of the AC Kondo and to show preliminary results on universality.

4.2 Kondo phenomenology

4.2.1 Sample

Figure 4.1 shows the sample, on which the measurements presented in this chapter have been carried out. The process fabrication is the one described in section 3.1 with steps 4b and 4c for electrodes patterning (figure 3.6). The two outer normal electrodes were connected to the CNT, yielding a room temperature resistance of $71k\Omega$. In contrast the

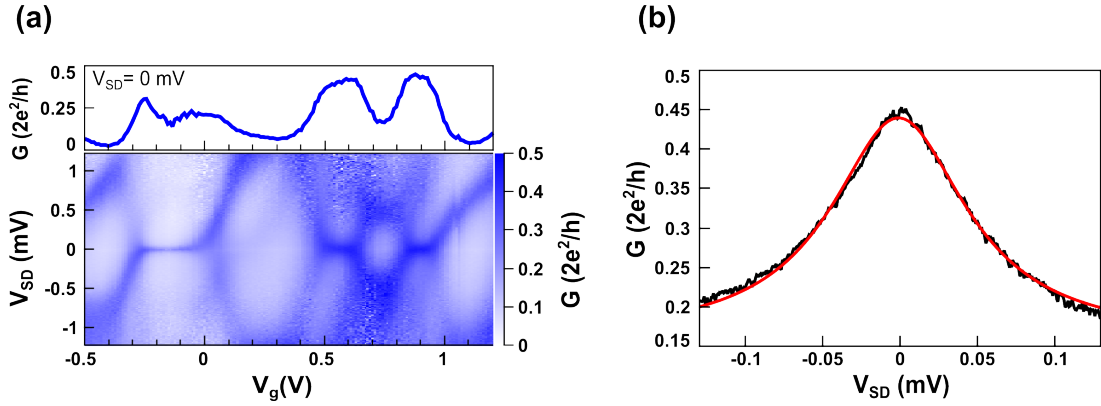


FIGURE 4.2: **Kondo phenomenology at equilibrium.** (a) A conductance colour plot versus gate and bias voltage shows characteristic Kondo ridges. (b) displays a Kondo resonance conductance peak (black line) at equilibrium ($V_{ac} = 0$). The red line is a Lorentzian fit parametrized as given by 4.1 with $k_B T_K = 32.7 \mu\text{eV}$, $G_{OFF} = 0.281(2e^2/h)$, $G_{BG} = 0.159(2e^2/h)$. Here data is plotted after a shift of V_{SD} by $x_c = 0.128\text{meV}$.

central superconducting electrode was disconnected, and acts as a top gate, which can be addressed by a microwave source. This is the excitation mode we use to perform our study of the AC Kondo. Transport measurements as a function of the two side gates show a single dot behaviour². In the following a single side gate is operated with gate voltage V_g . A DC bias voltage V_{SD} can be applied between the two normal reservoirs. Current I and differential conductance G are measured as explained in 3.2.2 with $V'_{AC} = 10\mu\text{V}$. The dot device is embedded in a microwave superconducting resonator, but in this chapter the latter is neither used as a probe, nor as a microwave excitation mode. No coupling to the cavity field is observed, which explains, why cavity signal measurements are not shown here.

4.2.2 Resonance in absence of excitation

Transport measurement in absence of microwave excitation displays Kondo ridges, which indicate that the sample is in the Kondo regime (figure 4.2a). The Kondo resonance conductance peak can be fitted by a Lorentzian curve centred on x_c with amplitude G_{OFF} plus a background conductance G_{BG} ³ (figure 4.2b). The peak width is related to the Kondo temperature and the following fitting parametrization sets our practical

²In the gate-gate plane a current colour plot exhibits parallel lines with a single slope.

³In the Kondo regime, it is common to observe a background conductance, in addition to the Kondo resonant peak [84]. For instance, there could be a contribution of cotunnelling, which would evolve over the scale $U \approx 1\text{meV} \gg k_B T_K$, which can be considered as flat over the Kondo resonance versus bias voltage.

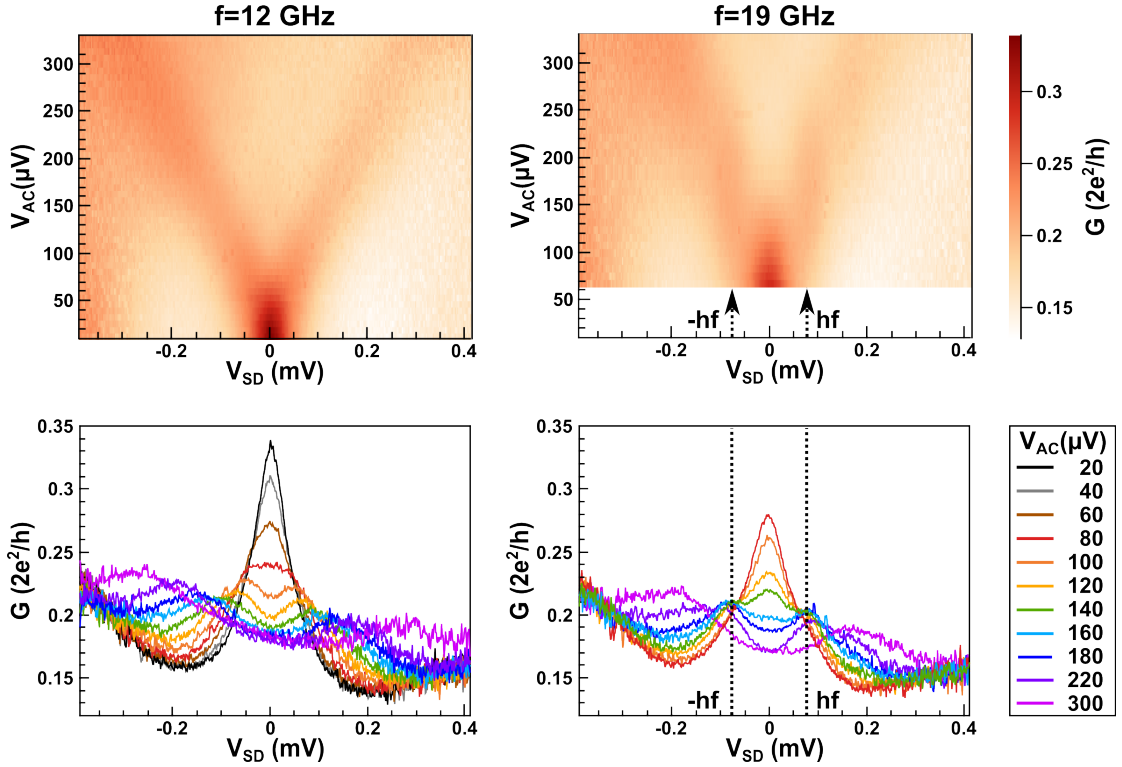


FIGURE 4.3: **Kondo phenomenology under microwave excitation.** Data are shown for two excitation frequencies: $f=12\text{GHz}$ on the left and $f=19\text{GHz}$ on the right. The upper panels are colour plots of the conductance versus bias voltage V_{SD} and excitation voltage V_{AC} . The lower panels show linear cuts of the same data. The lines colour encodes the excitation voltage, and the colour code applies to both frequencies.

definition of T_K :

$$G = G_{BG} + \frac{G_{OFF}}{1 + \frac{3}{8} \left(\frac{eV_{SD} - x_c}{k_B T_K} \right)^2} \quad (4.1)$$

This parametrization is chosen to recover the $SU(2)$ coefficient of the (quadratic) Fermi liquid description at low energy [86].

4.2.3 Phenomenology under microwave excitation

Figure 4.3 shows how the Kondo resonance conductance peak is modified by a microwave excitation. Data are shown for two excitation frequencies: $f=12\text{GHz}$ on the left and $f=19\text{GHz}$ on the right. The upper panels are colour plots of the conductance versus bias voltage V_{SD} and excitation voltage V_{AC} . The lower panels show linear cuts of the same data. The lines colour encodes the excitation voltage, and the colour code applies to both frequencies.

The Kondo resonance conductance peak decreases, when V_{AC} increases. Above a certain excitation voltage several peaks are observed. This is where measurements qualitatively

differs between 12 and 19 GHz. At 12 GHz the Kondo resonance peak splits and the splitting increases with V_{AC} . At 19 GHz three peaks are simultaneously observed for $V_{AC} = 140\mu V$ (green curve). These are the central peak at $V_{SD} = 0mV$ plus two satellite peaks at $\pm hf$. Over a certain range of excitation voltage the two satellite peaks locked at $\pm hf$ are visible (light and dark blue curves). In the colour plot, it manifests itself by two vertical lines at $\pm hf$. For $V_{AC} > 200\mu V$ the splitting between the two peaks increases like for $f=12$ GHz. Comparing lines cuts with the same colours ie the same excitation voltage, it is clear that the drop in conductance at the Kondo resonance quantitatively differs between 12 and 19 GHz. This is analysed in details in the next section.

4.3 Power-frequency dependance of Kondo conductance peak under microwave excitation

4.3.1 In situ microwave amplitude calibration

To study the Kondo response under microwave excitation, it is crucial to know the microwave voltage applied on the sample. Therefore a calibration of the absolute excitation voltage is needed. In practice, at constant source power, the microwave voltage on the sample depends on the source frequency. This issue is commonly encountered and hard to avoid, because of parasite resonant modes coming from e.g. wire bonds, sample holder. As the Kondo AC response is predicted to be frequency dependent, it is highly valuable to calibrate the relative excitation voltage between frequencies.

Our in-situ calibration method consists in measuring the current rectification under microwave excitation in the Coulomb regime. Assuming that the AC excitation simply modulates the DC current-voltage characteristic $I(V)$ ⁴ leads to the following expression of the measured current :

$$\underbrace{\langle I(V_{SD} + V_{AC} \cos \omega t) \rangle}_{I_{ON}} = \underbrace{I(V_{SD})}_{I_{OFF}} + \frac{1}{4} \frac{d^2 I}{dV_{SD}^2} V_{AC}^2 \quad (4.2)$$

which is expressed to lowest order in the excitation voltage on the sample V_{AC} ⁵. For each frequency a proportionality coefficient $c(f)$ links the sample voltage to the source voltage : $V_{AC} = c(f)V_{AC,source}$. Two calibration methods were combined to obtain the values of $c(f)$ for 61 frequencies between 2.4 and 20 GHz (figure 4.4d). The first method

⁴This is reasonable in our case since $(U \approx 1meV, \Gamma \approx 200\mu eV) \gg \omega$.

⁵This is valid if V_{AC} explores the linear part of the characteristic $G(V_{SD})$, leading to $V_{AC} \ll U \approx 1meV$.

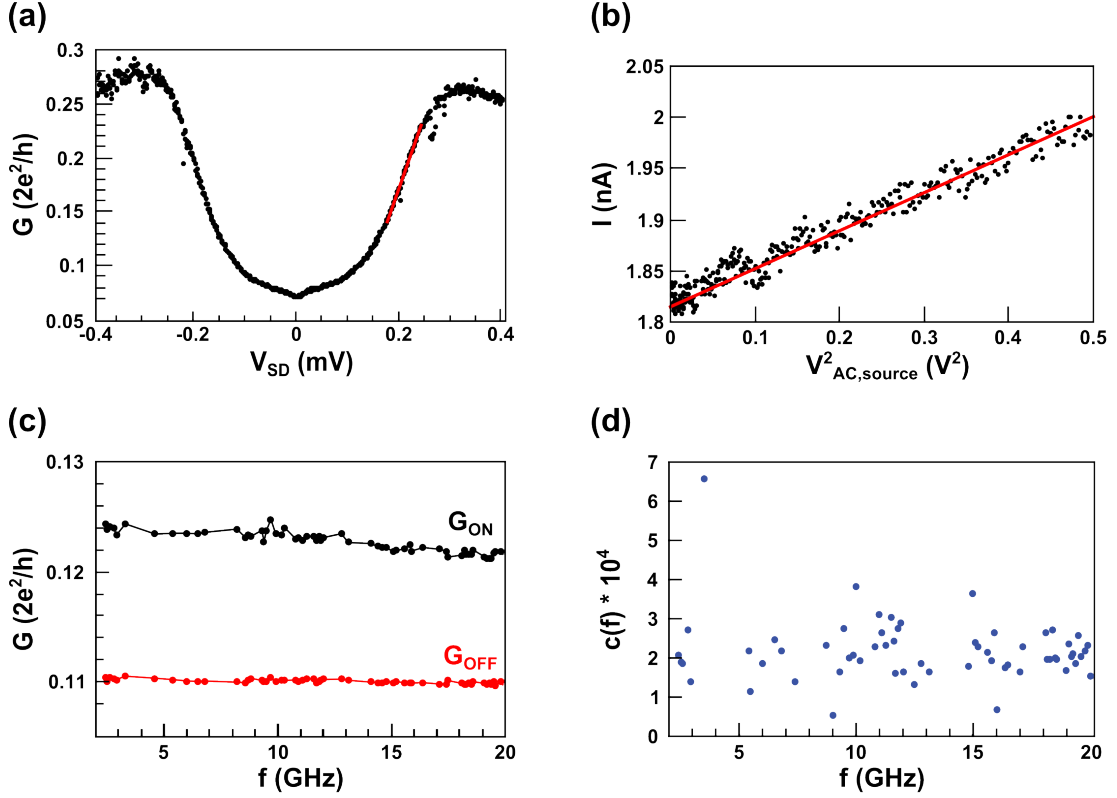


FIGURE 4.4: **Excitation amplitude calibration.**(a) The local slope of the conductance G versus bias voltage gives $\frac{d^2I}{dV_{SD}^2}$. Here around $V_{SD} = 0.207\text{mV}$, $\frac{d^2I}{dV_{SD}^2} = 1.0 \cdot 10^{-1} \text{A/V}^2$. (b) Knowing this value, the slope p of the current I as a function of the square source amplitude $V_{AC,source}$ in the linear regime yields the amplitude calibration coefficient $c(f) = \sqrt{4p/\frac{d^2I}{dV_{SD}^2}}$. Here for $f=20\text{GHz}$ $p = 0.372\text{nA/V}^2$ hence $c(f = 20\text{GHz}) = 1.2 \cdot 10^{-4}$.(c) shows an iterative relative amplitude calibration. For each frequency the conductance is successively measured with and without microwave excitation. Calibration coefficients $c_n(f)$ are used to set a $V_{AC} \approx 200\mu\text{V}$ for each frequency. The new coefficient set $c_n(f)$ are deduced from 4.4 with G instead of I . (d) plots the calibration coefficients $c(f)$ used to obtain the excitation amplitudes V_{AC} for data presented on figure 4.5.

provides a reliable absolute calibration. In absence of excitation ($V_{AC} = 0$) $\frac{d^2I}{dV_{SD}^2}$ is measured at $V_{SD,0}$ on the side of a Coulomb diamond. This is the local slope of the conductance as a function of bias voltage near $V_{SD,0}$, as depicted on figure 4.4a. Figure 4.4b shows the current at $V_{SD,0}$ as a function of V_{AC}^2 . We focus on the low excitation regime, where the dependence is linear in agreement with 4.2. Knowing $\frac{d^2I}{dV_{SD}^2}$ at $V_{SD,0}$, the slope gives access to $c(f)$. Applying this method for each frequency is time-consuming and the sample working point may change between first and last measured frequencies. Relative calibration is performed more rapidly and reliably using a second method. The source voltage is fixed and the frequency is swept. Current is successively measured with (ON current I_{ON}) and without (OFF current I_{OFF}) microwave excitation for each frequency point. Calibration coefficients for different frequencies are related by current

rectification ratios : ⁶

$$\frac{c(f_2)^2}{c(f_1)^2} = \frac{I_{ON}(f_2) - I_{OFF}}{I_{ON}(f_1) - I_{OFF}} \quad (4.3)$$

Relative calibration can be refined by iterating the procedure. We apply a source voltage $V_{AC,source}(f) = V_{AC,0}/c_n(f)$ calculated to apply a constant excitation voltage $V_{AC,0} \approx 200\mu V$. The new relative calibration is deduced from :

$$\frac{c_{n+1}(f_2)^2}{c_{n+1}(f_1)^2} = \frac{c_n(f_2)^2 I_{ON}(f_2) - I_{OFF}}{c_n(f_1)^2 I_{ON}(f_1) - I_{OFF}} \quad (4.4)$$

This relation holds replacing the current I by the differential conductance G . Figure 4.4c shows the conductance ON and OFF measurement, which defined the final relative calibration for some frequencies. To see if our calibration is valid at all gate voltages, we measure the conductance as a function of gate voltage at finite bias ($V_{SD}=0.203mV$) with $V_{AC} = 100\mu V$. In majority, curves measured at different excitation frequencies superpose all over the gate range. This means that for most frequencies, the excitation mainly applies to the dot bias voltage. For some frequencies, curves do not superpose over the entire gate range. In this case, the AC excitation a priori applies to both the dot energy level and bias voltage, possibly with different phases. This mixed regime does not correspond to the well controlled situation we want to study. The corresponding frequencies are excluded from the frequency set used for the AC Kondo study. Details about this frequency selection procedure are given in Appendix D.

4.3.2 Scaled amplitude-frequency conductance map

Gathering all measurements of the Kondo peak conductance under microwave excitation forms a database of 5189 sets of ($f, V_{AC,source}, G$). Appendix D details the various measurement types and data extraction procedures. The amplitude calibration coefficients $c(f)$ plotted on figure 4.4d are used to calculate the excitation amplitude V_{AC} from $V_{AC,source}$. The equilibrium Kondo peak under study is the one plotted on figure 4.2b. As the peak is slightly evolving between measurements, it is first measured at equilibrium prior measuring under excitation. Thus G_{BG} , G_{OFF} and T_K are obtained for each data from the equilibrium resonance fit 4.1 (see Appendix D for the parameter table). This allows to calculate the excitation scaled frequency F and scaled amplitude V :

$$F = \frac{hf}{k_B T_K} \quad V = \frac{eV_{AC}}{k_B T_K} \quad (4.5)$$

The conductance under excitation G_{ON} is obtained by subtracting the background conductance G_{BG} . We assume G_{BG} not be changed by the excitation, as $(hf, eV_{AC}) \ll U$.

⁶This is valid for frequencies with $c(f)$ such, that the lowest-order expansion 4.2 applies.

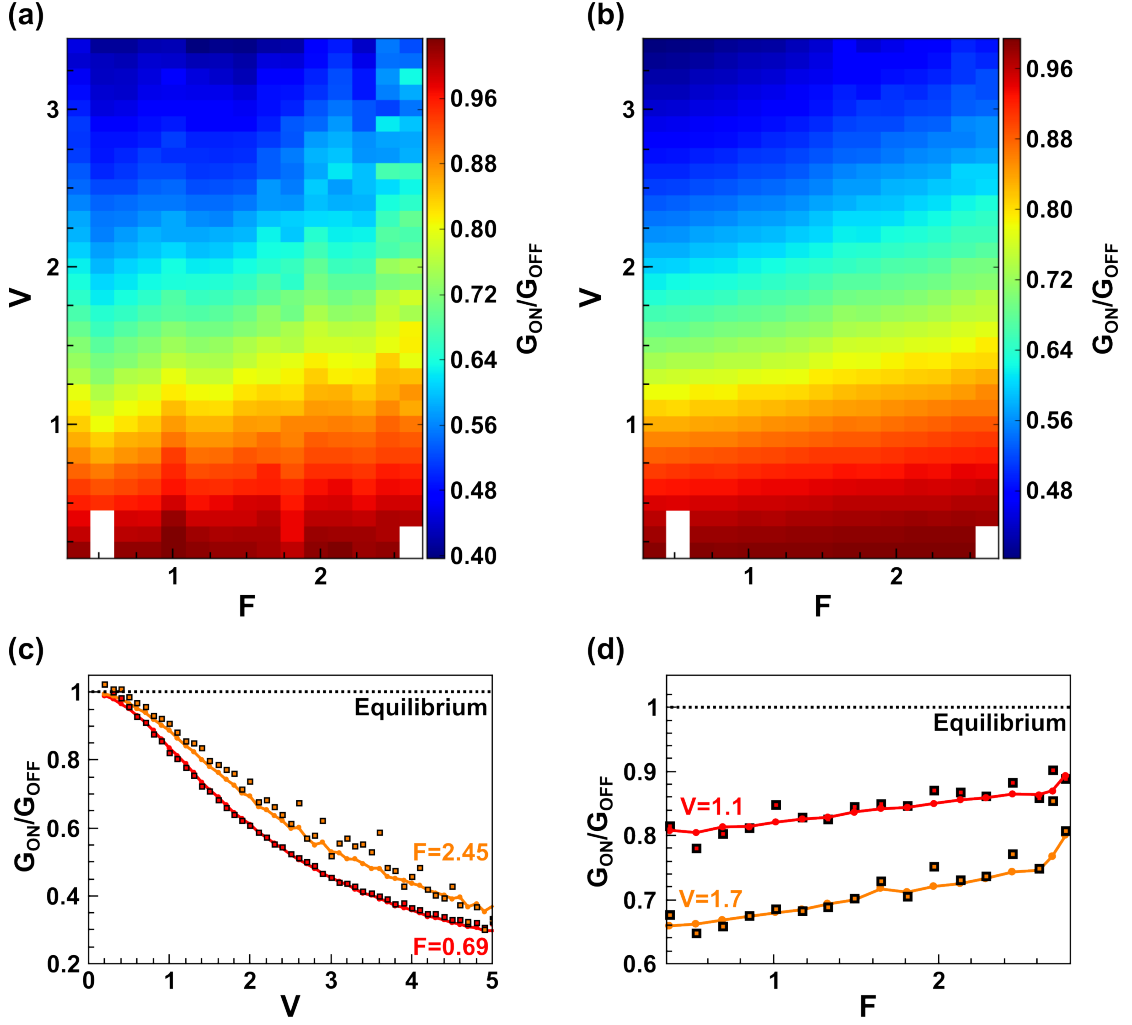


FIGURE 4.5: **Scaled Amplitude-frequency evolution of Kondo resonance.**(a) Experimental averaged normalized conductance colour plot as a function of excitation scaled amplitude V and scaled frequency F . (b) Similar map of the averaged normalized conductance calculated using the Ansatz formula 4.7. (c) Linear cuts at $F=0.69$ (red) and $F=2.45$ (orange). (d) Linear cuts at $V=1.1$ (red) and $V=1.7$ (orange). In both c and d panels squares correspond to data points, while dots linked by full lines correspond to the Ansatz. The black dashed line indicates the equilibrium reference.

This assumption is validated by figure 4.3, where conductance curves for all V_{AC} values merge at high bias voltage. For comparison between data, it is relevant to normalize G_{ON} by the equilibrium conductance G_{OFF} :

$$\frac{G_{ON}}{G_{OFF}} = \frac{G - G_{BG}}{G_{OFF}} \quad (4.6)$$

The F - V normalized conductance map is represented on figure 4.5a. Because data points are not uniformly spaced in the F - V plane, we choose a regular grid and create a matrix by averaging data points in the same cell. Cells with no data points remain blank. Here the cell size in F is $\Delta F = 0.16$ and in V $\Delta V = 0.1$. Linear cuts at fixed F and fixed V are

plotted respectively with squares on figure 4.5c and d. An horizontal black dashed line at 1 recalls the equilibrium value. As already shown on figure 4.3, the Kondo conductance peak decreases, when the amplitude excitation increases. We observe that this behaviour is frequency-dependant : the higher the frequency, the lower the excitation-induced drop in Kondo conductance. This trend is more pronounced for $F > 1$, while G_{ON}/G_{OFF} is rather flat for $F < 1$.

4.3.3 Ansatz proposed for quantitative analysis

We use the following Ansatz to quantitatively describe our data :

$$\frac{G_{ON}}{G_{OFF}}(V, F, G_{OFF}) = \frac{1}{\sqrt{1 + \frac{3}{8}V^2\alpha(F, G_{OFF})}} \quad (4.7)$$

with

$$\alpha(F, G_{OFF}) = \frac{1}{\sqrt{1 + \left(\frac{16}{3} \frac{a}{\pi} \frac{G_{OFF}}{2e^2/h} \frac{1}{F}\right)^{-2}}} \quad (4.8)$$

where $a \sim 1$ is a dimensionless parameter. Expression 4.7 bridges the low-frequency adiabatic limit and the low-amplitude high-frequency limit predicted in [63] in the case of AC bias (formula (74)). Indeed $\lim_{F \rightarrow 0} \alpha(F) = 1$. In this limit, formula 4.7 becomes frequency-independent and corresponds to the adiabatic averaging of the equilibrium Kondo Lorentzian peak⁷. In the opposite limit $F \gg 1$ and for $V \ll 1$ formula 4.7 leads to :

$$\frac{G_{ON}}{G_{OFF}} = 1 - a \frac{\hbar}{\tau' k_B T_K} \quad (4.9)$$

which is equation (74) of [63] with :

$$\frac{\hbar}{\tau' k_B T_K} = \frac{1}{\pi} \frac{G_{OFF}}{2e^2/h} \frac{V^2}{F} \quad (4.10)$$

which is equation (72) of [63] without the logarithmic term $1/(\ln F)^2$ in factor. However the presence of the logarithm in the formula validity parameter range has too little influence to be tested in our experiment.

The agreement with experimental data is best for $a=4.4$. We use $\frac{G_{ON}}{G_{OFF}}(V' = bV)$ with $b=1.1$. The latter corrects a reasonable global absolute calibration error of 10%. For each experimental data set of (F, V) we calculate the value of G_{ON}/G_{OFF} predicted by the Ansatz using the corresponding G_{OFF} experimental value. An F-V colour map of

$$\frac{1}{T} \int_0^T \frac{1}{1 + \frac{3}{8}V^2 \cos^2(\omega t)} dt = \frac{1}{\sqrt{1 + \frac{3}{8}V^2}}$$

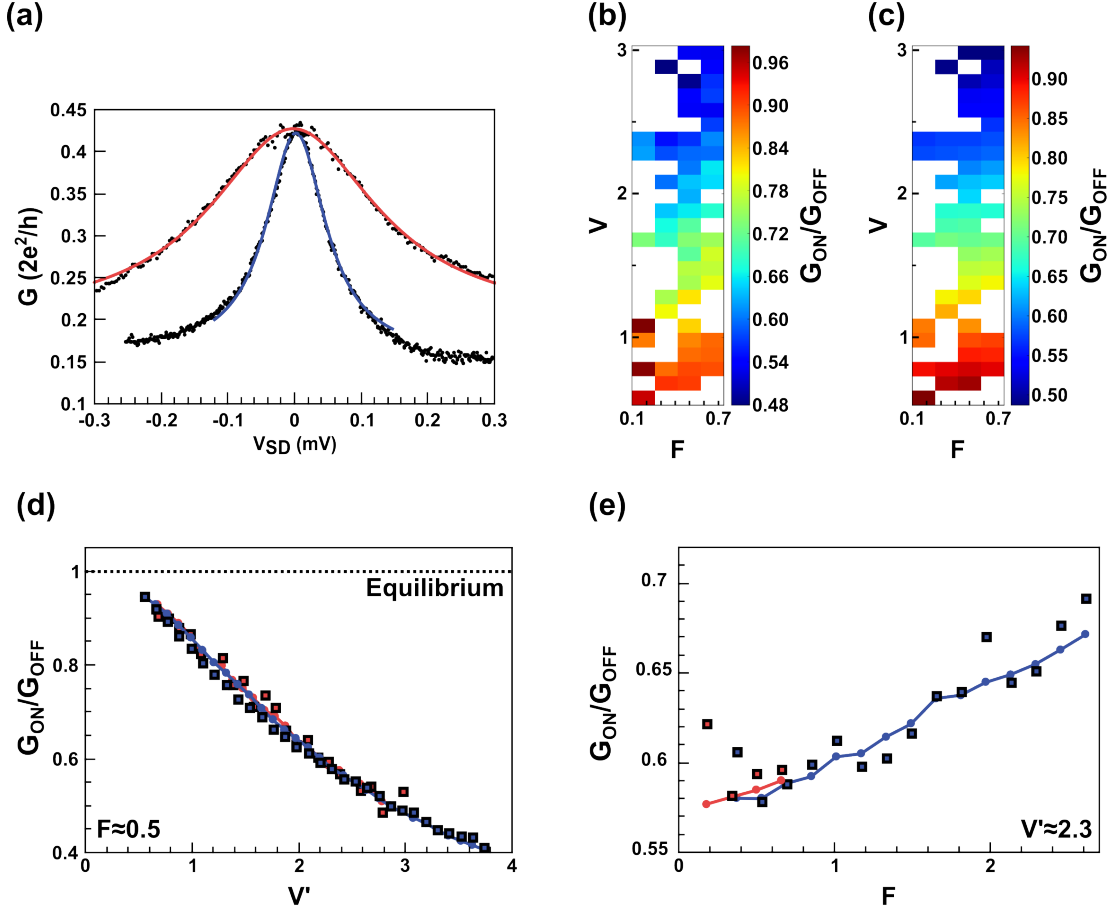


FIGURE 4.6: **Investigation of universality.**(a) displays thin and wide equilibrium Kondo resonances (black dots), which are fitted with expression 4.1. The thin peak fit in blue plain line yields parameters close to 4.2b and given in the table D.1 (file 3) in appendix. The wide peak fit in pink yields $k_B T_K = 95 \mu\text{eV}$, $G_{OFF} = 0.229(2e^2/h)$, $G_{BG} = 0.196(2e^2/h)$. Experimental (b) and Ansatz (c) F-V normalized conductance map for the wide peak. Comparison of V-dependence (d) and F-dependence (e) of G_{ON}/G_{OFF} for wide (pink) and thin (blue) Kondo peaks to investigate universality. Squares correspond to experimental data, while dots linked by plain lines plot the Ansatz.

the Ansatz normalized conductance is obtained similarly to the experimental map and is displayed on figure 4.5b. It shows a good agreement with experimental data, which is confirmed by the linear cuts of figure 4.5c and d, where the Ansatz is represented with dots linked by plain lines.

4.4 Test of universality

A central prediction of Kaminski et al. is the universality of the Kondo peak response to an AC excitation. This means that the frequency f and amplitude V_{AC} are not the relevant parameters to describe G_{ON}/G_{OFF} , but instead F and V , which are frequency and amplitude scaled by the Kondo temperature. In previous section, we have investigated

the functional form of $G_{ON}/G_{OFF}(F, V)$ but we have not demonstrated scaling versus Kondo temperature. The variations in T_K were too small for that. Here we present data measured during a different cryostat run on a Kondo peak with $k_B T_K = 95 \mu eV$. Fitted with the pink line on figure 4.6a, it is three times wider than the peak fitted in blue and studied in previous section. On the one hand, this is an advantage because T_K scales are very different and scaling should be tested unambiguously. On the other hand, the investigated scaled frequency range is also three times smaller. Indeed our microwave source delivers up to 20GHz frequencies, so we are limited to $F \lesssim 0.84$.

Because of thermal cycling the microwave amplitude calibration changed, and a new sets of coefficients $c(f)$ was determined and used to obtain V_{AC} . The experimental normalized conductance F-V map for the wide Kondo peak is displayed on 4.6b. We were able to collect 189 data sets, which is much less than for the thin peak. This explains, why there are more blank cells than in 4.5, although the cell size is the same ($\Delta F = 0.16$ and $\Delta V = 0.1$). Figure 4.6c shows the corresponding Ansatz map, calculated with $a=4.4$ determined in section 4.3.3, and $b=1$ (no global absolute calibration adjustment). We observe a good agreement, which is in favour of $G_{ON}/G_{OFF}(F, V)$ being a universal function of F and V. To further investigate universality, it is useful to plot G_{ON}/G_{OFF} for wide and thin peaks on the same graph as a function of scaled quantities F and V^8 and see whether curves collapse. Figure 4.6d shows the V-dependence for the $F \approx 0.5$ linear cut. Following the colour code of panel a, pink and blue respectively refers to wide and thin peak. Squares correspond to experimental data, while dots linked by plain lines plot the Ansatz. As expected the two Ansatz curves merge, up to small discrepancies due to slightly different G_{OFF} values. For both peaks, experimental data collapse well onto this curve. This validates the universal amplitude dependence at low frequency. Figure 4.6e focus on the F-dependence at $V' \approx 2.3$ and uses the same colour code as graph c. As mentioned above, the scaled frequency range for the wide peak is narrow, so that pink data comes down to four points. They fall reasonably well on the blue data (except the first pink point) and confirm a flat adiabatic behaviour at low frequency. This is consistent with a universal frequency dependence, although universality in the pronounced frequency-dependant regime $F > 1$ could not be investigated.

To conclude our experiment realised on a CNT-based quantum dot provides further understanding of the AC Kondo problem. We report the second observation of radiation-induced Kondo satellite peaks, primarily observed in GaAs 2DEG [60]. Using an independent in-situ amplitude calibration, we provide the first quantitative measurement of the amplitude-frequency dependence of the Kondo conductance with an AC bias. The

⁸The use of $V'=bV$ is required to compare data from thin and wide peaks, that were taken in different runs, with different calibrations. $b=1.1$ for the thin peak and $b=1$ for the wide peak.

Kondo resonance is found to be less affected at higher excitation frequencies, in agreement with Kaminski et al theoretical paper [63]. We describe our data quantitatively using an Ansatz, which bridges expressions given in this paper for two limiting regimes of parameters. Measurement on two Kondo resonances with very different T_K allows to make some statements on universality. We find a good scaling of G_{ON}/G_{OFF} with the scaled amplitude $V = \frac{eV_{AC}}{k_B T_K}$. In the more limited parameter range we could explore, our data is also consistent with a scaling of G_{ON}/G_{OFF} with the scaled frequency $F = \frac{hf}{k_B T_K}$.

Chapter 5

Charge dynamics of a single level coupled to fermionic reservoirs

5.1	An S-QD-N device embedded in a microwave resonator	97
5.2	Equilibrium charge dynamics in a N-dot junction at finite frequency	99
5.2.1	Cavity signals as a probe of charge susceptibility	99
5.2.2	Investigation of charge relaxation universality	101
5.3	Non equilibrium charge dynamics in an S-dot-N bijunction	104
5.3.1	Crossed measurement of dot conductance and cavity response	104
5.3.2	Photon-assisted tunnelling between a dot and a superconductor	107
5.4	Summary and discussion	108

Circuit QED techniques have been recently put forward to investigate the electronic dynamics in mesoscopic circuits. As discussed in 2.2.4 most experiments with quantum dots used the coupling to the cavity as a probe of the circuit *internal* dynamics, with the prospect of building qubits. Nevertheless, mesoscopic circuits are inseparable from the existence of electronic reservoirs with Fermi seas, which contributes to the richness of the field. Indeed the large variety of materials (e.g superconductors or ferromagnets) that can be used results in a large variety of physical effects from spin-dependent transport to Andreev Bound States. In this context, it is crucial to understand how tunnelling processes between a discrete energy level and the continuum of states of a reservoir can affect cavity photons. This situation is epitomized by a single quantum dot circuit coupled to a cavity, a case which has been studied elusively so far [42, 62, 105].

In this chapter, we present experimental data and theoretical modelling of the behaviour of a single quantum dot in a carbon nanotube, coupled to normal metal (N) and superconducting (S) reservoirs, and embedded in a high finesse microwave cavity. We first study a dot discrete orbital coupled only to the N reservoir (section 5.2). This allows us to investigate the universality of the charge relaxation. As presented in 2.1.1, this effect had so far been observed only in the AC current through a strongly spin-polarised and non-interacting GaAs quantum dot [66]. However, the interacting case has raised an intense theoretical activity recently because Coulomb blockade is ubiquitous in quantum dots[67, 68, 121–125]. Here, we present the first experiment on the universality of charge relaxation in the spin-degenerate interacting case. In addition our data provides the first measurement of the dependence of the charge relaxation resistance on the dot orbital energy. Finally we are able to study, how dissipation evolves going to the non-adiabatic regime. In section 5.3 the dot level is also coupled to the S reservoir. For both N-dot and N-dot-S experimental situations the cavity response is described in terms of the quantum dots charge susceptibility, as described in 2.3. This approach was recently suggested [69–72] to treat the open contact limit as an alternative to existing theoretical modelling, which disregard fermionic reservoirs or assume tunnel rates much smaller than temperature.

5.1 An S-QD-N device embedded in a microwave resonator

The device geometry is visible in figure 5.1b and figure 3.6: a carbon nanotube is contacted to a superconducting contact (S) surrounded by two normal metal (N) contacts, following the fabrication process detailed in section 3.1. In the regime of parameters considered here, the whole nanotube section between the two N contacts forms a single

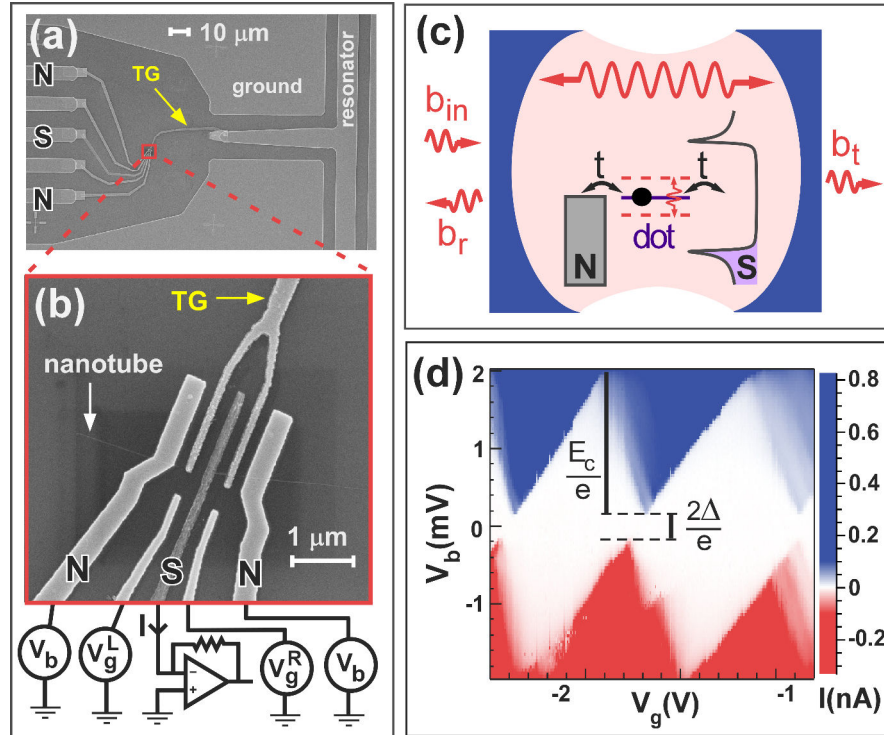


FIGURE 5.1: Panels (a) and (b): Scanning electron micrograph of the microwave resonator and the quantum dot circuit. Panel (c): Principle of our setup. The dot level is tunnel coupled to the N and S reservoirs and modulated by the cavity electric field. Panel (d): Current through the S contact versus the effective gate voltage V_g and the bias voltage V_b .

quantum dot¹. An effective gate voltage V_g ² is used to tune the dot level orbital energy ε_d . We connect the S contact to ground and we apply the same bias voltage V_b to the two N contacts, which can thus be considered as an effective single contact³. The dot is capacitively coupled to the central conductor of a superconducting coplanar waveguide cavity through a top gate TG (see figure 5.1a). Using the setup presented in section 3.2.3, we measure the phase φ and amplitude A of the transmitted signal at a pulsation ω_{RF} equal to the bare cavity pulsation $\omega_0 \sim 2\pi \times 6.65$ GHz. The cavity quality factor is $Q \approx 12800$. We determine the phase shift $\Delta\varphi = \varphi - \varphi_0$ and the amplitude shift $\Delta A = A - A_0$, which are caused by the presence of the quantum dot circuit, with respect to the bare cavity transmitted signals labelled with nought subscript. Simultaneously, we measure the DC current I and differential conductance G through the dot as explained in 3.2.2. The current I shows clear signatures of Coulomb blockade with

¹For $e|V_b| > \Delta$, the current I versus V_g^L and V_g^R corresponds to a pattern of parallel lines (figure E.1 in Appendix).

² $V_g = a_L V_g^L + a_R V_g^R$, where V_g^L and V_g^R are voltages applied to side gate electrodes visible on figure 5.1b

³If one uses two N contacts with a similar structure and the same bias voltage, this only increases the effective density of states ρ_N of the normal continuum seen by the quantum dot. In this picture, the effective tunnel rate $\Gamma_N = 2\pi |t_N|^2 \rho_N$ corresponds to the sum of the tunnel rates of the two real N contacts.

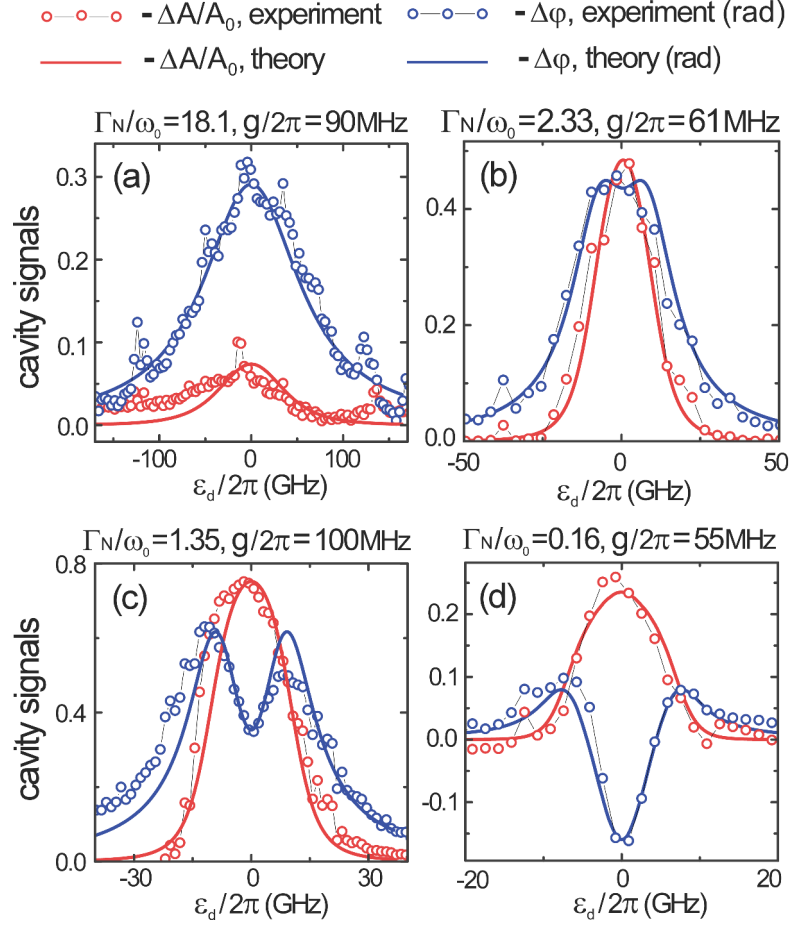


FIGURE 5.2: Measured phase shift $\Delta\varphi$ (blue dots) and reduced amplitude shift $\Delta A/A_0$ (red dots) of the microwave signal transmitted by the cavity versus the energy ε_d of the dot orbital, for $V_b = 0$ (for clarity, we have plotted the opposite of these signals). The red and blue lines show the predictions given by equations 5.2 and 5.3 for values of Γ_N and g given in the different panels and $T = 60 \text{ mK} \simeq 0.19\omega_0$.

a charging energy $E_c \simeq 1.8 \text{ meV}$ (see figure 5.1d). It also vanishes for a bias voltage V_b smaller than the gap $\Delta \simeq 0.17 \text{ meV}$ of the S contact. Therefore, for $V_b = 0$, the effect of the S contact can be disregarded and the quantum dot circuit corresponds to an effective N/dot junction, studied in section 5.2. For $e|V_b| > \Delta$, our device enables the study of quasiparticle transport in a N/dot/S bi-junction, presented in section 5.3.

5.2 Equilibrium charge dynamics in a N-dot junction at finite frequency

5.2.1 Cavity signals as a probe of charge susceptibility

A single dot level coupled to a N reservoir is the most basic configuration for studying the light matter interaction in a mesoscopic circuit. Our device realises such a situation

for $V_b = 0$ due to the absence of subgap Andreev reflections. Figure 5.2 shows the cavity signals $\Delta\varphi$ (blue dots) and $\Delta A/A_0$ (red dots) versus the energy ε_d of the dot orbital, for $V_b = 0$. We observe resonances although $I = 0$. This means that the cavity is able to reveal quasiparticle tunnelling between the dot and the N contact even if it doesn't lead to a DC current. The four panels correspond to four different dot/reservoir resonances with decreasing tunnel rates Γ_N from left to right and top to bottom. The phase shift $\Delta\varphi$ can be positive as well as negative. Such a behaviour for $\Delta\varphi$ has already been observed in [62]. For $\omega_0 \ll \Gamma_N$, the quantum dot circuit behaves as an effective capacitance. Electrons can follow very rapidly the variations of the dot potential to fill in and out the dot, proportionally to the dot density of states. This lead to a negative frequency shift, as explained in 2.3.2. In contrast, for $\omega_0 \gg \Gamma_N$, the charge current lags behind the dot potential, so that the dot behaviour becomes inductive. This directly affects the sign of the frequency shift, hence of $\Delta\varphi$. The cavity dissipation induced by the quantum dot was not studied in [62]. In contrast with the behaviour of $\Delta\varphi$, we observe that ΔA remains negative (up to experimental uncertainty), which means that the dot always damps photons. This effect is maximum, when the dot level is at resonance with the Fermi energy of the N reservoir ($\varepsilon_d = 0$). One could naively expect that ΔA , which reveals photon dissipation, will scale with Γ_N which is the only dissipation parameter in our problem. However, this intuition is wrong since ΔA becomes small when Γ_N tends to large values (see figure 5.2a). In fact, the large- Γ_N behaviour of ΔA is rather in agreement with our discussion of the adiabatic case in section 2.3.2, where dissipation ultimately vanishes.

To understand the data presented in figure 5.2 for other panels than (a), we need an expression for the charge susceptibility beyond the adiabatic limit to plug into the semi-classical linear response description of section 2.3. Writing equation 2.26 for the single orbital case, and using the electrical engineering Fourier transform sign convention, leads to the following expression for the cavity transmission⁴:

$$T = \frac{j\sqrt{\kappa_1\kappa_2}}{\omega_{RF} - \omega_0 - j\Lambda_0 - g^2\chi(\omega_{RF})} \quad (5.1)$$

with $\Lambda_0 = \kappa/2$ the bare cavity half-FWHM and $\chi(\omega) = \tilde{\chi}(\omega)^*$. The quantum dot charge susceptibility $\chi(\omega)$ at any ω can be calculated within the Keldysh formalism as explained in Appendix E.2.2. In the case of a non-interacting N/dot junction, the susceptibility $\chi(\omega)$ can be simplified as equation E.11 of Appendix E.2.2 at zero temperatures and

$$\chi(\omega) = \int_{-\infty}^{+\infty} \frac{d\omega'}{\pi\omega} \frac{\Gamma_N (f(\omega') - f(\omega' - \omega))}{(\omega' - \varepsilon_d - i\frac{\Gamma_N}{2})(\omega' - \omega - \varepsilon_d + i\frac{\Gamma_N}{2})} \quad (5.2)$$

⁴Some notations differ : the cavity resonance pulsation changed from ω_c to ω_0 and the cavity drive pulsation from ω_d to ω_{RF}

with $f(\varepsilon) = 1/(1 + \exp[\varepsilon/k_bT])$ for finite temperatures. The use of these expressions in spite of the presence of Coulomb blockade is relevant due our regime of parameters, as discussed in section 5.4. We obtain a quantitative agreement between the measured $(\Delta\varphi, \Delta A)$ and the values calculated from the transmission ratio

$$(1 + (\Delta A/A_0))e^{i\Delta\varphi} = \Lambda_0/(\Lambda_0 - ig^2\chi(\omega_0)) \quad (5.3)$$

which follows from equation 5.1 (see red and blue lines in figure 5.2). We use the same finite temperature $T = 60$ mK for all the resonances. Then, for each resonance, we use only two adjustable parameters, namely g and Γ_N . Remarkably, we obtain a good agreement with the data for a wide range of Γ_N/ω_0 ratios (see figure E.2 for supplementary resonances). The full functional form of the cavity response is accurately reproduced by our theory. Such a modelling was not possible for previous experiments combining (real or effective) single quantum dots with microwave cavities[42, 62, 105].

5.2.2 Investigation of charge relaxation universality

A deeper analysis of the cavity response can be performed by studying the cavity frequency shift $\Delta\omega_0$ and cavity linewidth shift $\Delta\Lambda_0$, which can be obtained from the experimental signals as $\Delta\omega_0 = \Lambda_0(A_0/A) \sin(\Delta\varphi)$ and $\Delta\Lambda_0 = \Lambda_0((A_0/A) \cos(\Delta\varphi) - 1)$ and modelled theoretically from $\Delta\omega_0 + i\Delta\Lambda_0 = g^2\chi(\omega_0)$ ⁵. To study the relation between $\Delta\Lambda_0$ and $\Delta\omega_0$, we define the ratio

$$\theta = \frac{\pi \omega_0}{2} \frac{(\Delta\omega_0)^2}{g^2 \Delta\Lambda_0} \quad (5.4)$$

which can be modelled theoretically as

$$\theta = \frac{\pi}{2} \omega_0 \frac{(\text{Re}[\chi])^2}{\text{Im}[\chi]} \quad (5.5)$$

The top panel of figure 5.3 shows with a dashed line $\theta_0 = \theta(\varepsilon_d = 0)$ versus Γ_N/ω_0 , calculated at $T = 0$ from equations 5.5 and E.11, for a dot level at resonance with the Fermi energy of the reservoir ($\varepsilon_d = 0$). The dot behaviour changes from inductive to capacitive when Γ_N increases. Hence, $\text{Re}[\chi]$ changes sign and θ_0 shows the minimum $\theta_0 = 0$ for $\Gamma_N \sim 0.7\omega_0$. Then, in the adiabatic limit $\Gamma_N \gg \omega_0$, θ_0 tends to 1. In fact, this limit is valid for any value of ε_d , i.e.

$$\lim_{\Gamma_N/\omega_0 \rightarrow +\infty} \theta(\varepsilon_d) = 1 \quad (5.6)$$

⁵In the linear limit where $\Delta\varphi$ and ΔA are small, one has $\Delta\omega_0 \simeq \Lambda_0\Delta\varphi$ and $\Delta\Lambda_0 \simeq -\Lambda_0\Delta A/A_0$ so that $\Delta\omega_0$ and $\Delta\Lambda_0$ reveal the cavity frequency and linewidth shifts respectively. However, since we have strong signals it is more accurate to use the non linear relations given here.

The full gray line in figure 5.3, top panel, shows $\theta(\varepsilon_d = 0)$ for the temperature $T = 60$ mK, calculated from equations 5.2 and 5.5.

It illustrates that finite temperatures affect quantitatively the behaviour of the system for low values of Γ_N , but equation 5.6 remains valid as soon as $\Gamma_N \gg k_B T$. A straightforward question is whether the non-trivial behaviour of equation 5.6 can be observed with our experiment. This equation has two important implications. First, it predicts that the $\Delta\Lambda_0$ and $(\Delta\omega_0)^2$ curves versus ε_d (or equivalently versus the dot gate voltage V_g) should be proportional in the open contact limit $\Gamma_N \gg \omega_0, k_B T$. Second, it gives the exact value of the proportionality constant between $\Delta\Lambda_0$ and $(\Delta\omega_0)^2/g^2$. The latter cannot be accessed in our experiment. Indeed, we cannot calibrate the absolute value of θ because we don't have an independent experimental determination of the parameter g . Instead, we determine g and thus θ from a fitting procedure which relies on the assumptions of our theory. Nevertheless, we can test the scaling between $\Delta\Lambda_0$ and $(\Delta\omega_0)^2$ independently of any theoretical assumption, as shown below.

For $\Gamma_N > 10\omega_0$, equations 5.2 and 5.5 predict a universal dissipation regime, corresponding to the gray area in the top panel of figure 5.3, where $\theta_0 \simeq 1$ and the scaling between $\Delta\Lambda_0$ and $(\Delta\omega_0)^2$ is closely satisfied. There is also a regime corresponding to the pink area, where $\theta_0 < 1$ but the scaling between $\Delta\Lambda_0$ and $(\Delta\omega_0)^2$ is still approximately satisfied. Finally, on the left side of the pink area, $\Delta\Lambda_0$ and $(\Delta\omega_0)^2$ do not scale at all. To illustrate the large variety of regimes achieved with our experiment, we show with crosses the fitted values of θ_0 , calculated from equations 5.2 and 5.5, for the fitting parameter Γ_N of the different resonances in figures 5.2 and E.2 and $T = 60$ mK. We find two resonances ($\Gamma_N = 18.1\omega_0$ and $\Gamma_N = 14.3\omega_0$) falling in the gray universal dissipation area. In this limit, $\Delta\Lambda_0 \sim 8g^2(\omega_0/\Gamma_N)^2/\pi\omega_0$ vanishes like $(\omega_0/\Gamma_N)^2$. This explains why the ΔA signal is significantly smaller than for other resonances (figures 5.2a and E.2). Since ΔA and thus $\Delta\Lambda_0$ become comparable to the cavity background noise, it is not possible to test the scaling between $\Delta\Lambda_0$ and $(\Delta\omega_0)^2$ for this resonance. To solve this problem, one has to use lower values for ω_0/Γ_N , which fall in the pink approximate scaling area. We have found two such resonances, for $\Gamma_N = 2.40\omega_0$ and $\Gamma_N = 2.86\omega_0$. For these resonances, the proportionality between the experimental $\Delta\Lambda_0$ and $(\Delta\omega_0)^2$ is satisfied to a good accuracy (figure 5.3c and d). Small discrepancies between these two quantities are visible in the theoretical curves (see red and blue lines in figure 5.3c) but not resolvable experimentally. Such a scaling behaviour is observed here for the first time. Finally, we can observe how the scaling behaviour breaks down for smaller tunnel rates. The crosses in the top panel of figure 5.3 show that we have tested a large number of Γ_N/ω_0 ratios in the non-universal regime. When Γ_N decreases, the $(\Delta\omega_0)^2$ peak versus ε_d first becomes wider than the $\Delta\Lambda_0$ peak (not shown), before becoming strongly non monotonic (See figure 5.3a and b).

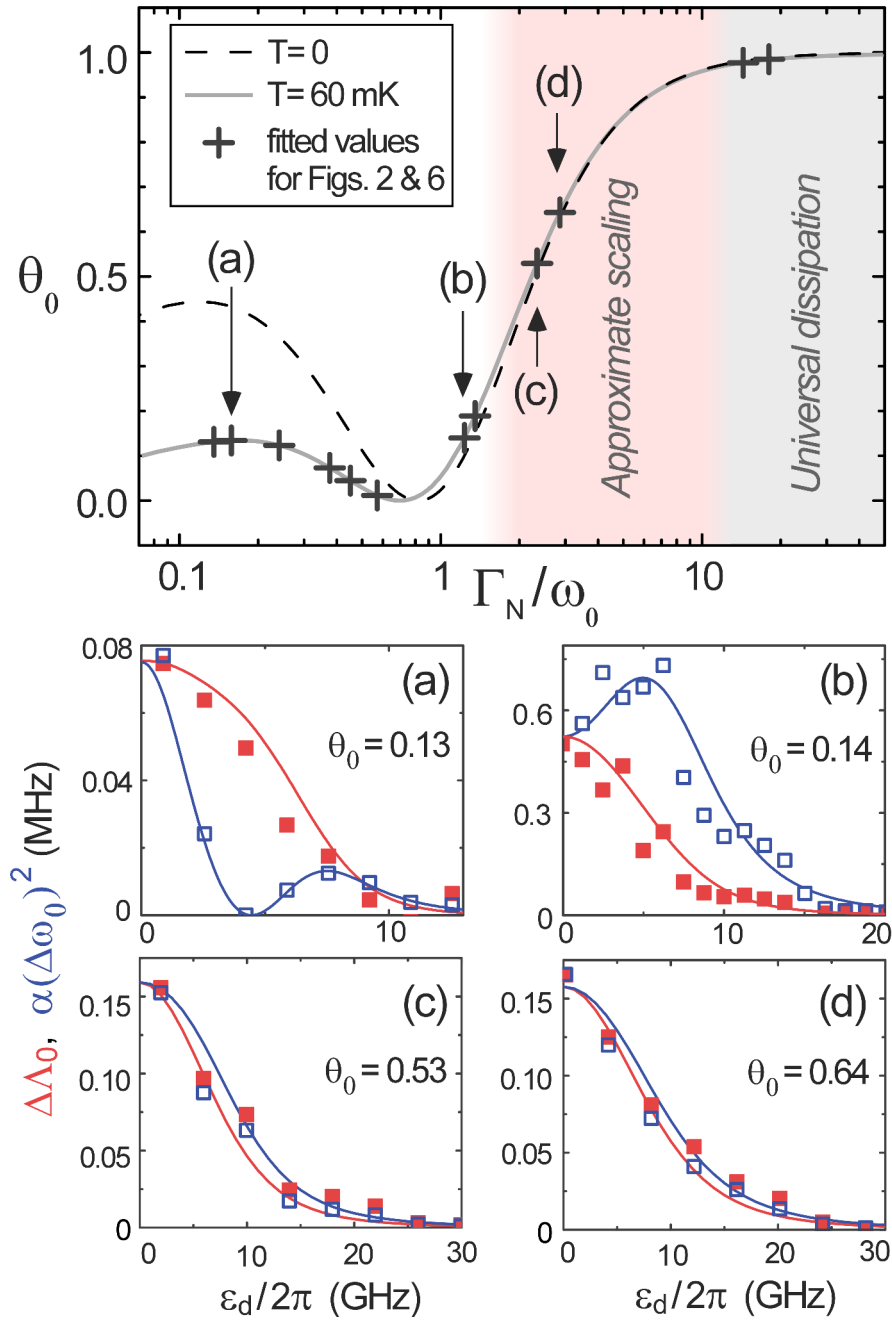


FIGURE 5.3: Top panel: Ratio $\theta_0 = \theta(\varepsilon_d = 0)$ versus the tunnel rate Γ_N , calculated from equations 5.2, 5.5, and E.11 for $T = 0$ (black dashed line) and $T = 60$ mK (gray full line). The crosses correspond to fitted values of θ_0 , calculated from equations 5.2 and 5.5 for the different resonances in figures 5.2 and E.2. Bottom panels: Comparison between the experimental $\Delta\Lambda_0$ and $(\Delta\omega_0)^2$, using the scaling factors θ_0 indicated with arrows in the top panel. We use $\Gamma_N/\omega_0 = 0.16, 1.23, 2.33$ and 2.86 from left to right and top to bottom panels. We also show as blue and red full lines the calculated $\Delta\Lambda_0$ and $(\Delta\omega_0)^2$.

The remarkable scaling between $\Delta\Lambda_0$ and $(\Delta\omega_0)^2$ in the regime $\Gamma_N \approx 2.5\omega_0$ is directly related to the universality of the AC resistance of a quantum dot circuit, which was predicted by M. Büttiker two decades ago [64, 65], and recently revisited as a Korringa Shiba relation [68, 122, 126]. More precisely, for a non-interacting N/dot junction ($E_c = 0$) excited at a frequency ω_{RF} such that $\Gamma_N \gg \omega_{RF}, k_B T$, the AC resistance has been predicted to tend to $R_{AC} = h/4e^2\theta(\epsilon_d)$, which gives $R_{AC} = h/4e^2$ with our spin-degenerate model, for any gate voltage. This effect can be understood as a quantum charge relaxation effect, which involves the internal coherent dynamics of the quantum dot. So far, the universality of the quantum charge relaxation had been observed only with a strongly spin-polarised GaAs 2-dimensional electron gas device, through the measurement of the dot AC conductance [66]. Here, we present the second example of system, i.e. a spin-degenerate carbon nanotube device, whose behaviour is consistent with this phenomenon. Indeed, the scaling behaviour between $\Delta\Lambda_0$ and $(\Delta\omega_0)^2$ reveals the independence of R_{AC} from the dot gate voltage V_g (or equivalently the dot orbital energy ϵ_d), a property which could not be probed in reference [66], and which is already valid for intermediate tunnel rates. The fact that we obtain this result in spite of Coulomb blockade is non trivial, as will be discussed in section 5.4. More generally, we demonstrate that circuit QED techniques represent a powerful way to study the quantum charge relaxation in a quantum dot, as discussed theoretically by [69]. Improvements of our setup could enable an independent experimental determination of g to test the absolute value of the right member of equation 5.6 (or equivalently R_{AC}) [105].

5.3 Non equilibrium charge dynamics in an S-dot-N bi-junction

5.3.1 Crossed measurement of dot conductance and cavity response

A common belief is that a fermionic reservoir should necessary damp cavity photons since it calls for irreversible processes. Is it possible to go against this natural trend ? To answer this question, we consider the finite bias voltage regime $V_b \neq 0$ where our device implements a N/dot/S bi-junction. This can be confirmed from the bi-junction conductance versus V_b and the dot gate voltage V_g (figure 5.4a). Like in figure 5.1d, we observe two Coulomb triangles which do not close on the $V_b = 0$ line but at $eV_b \sim \pm\Delta$, and which are shifted along the V_g axis. These features are typical of a N/dot/S structure and are due to the gap and BCS peaks in the density of states of the S contact [127–129]. The conductance resonances corresponding to an alignment between the dot level and the BCS peaks display negative differential resistance areas [128] (see red areas in figure 5.4a). This can be understood easily in the limit $\Gamma_S \ll k_B T$, where, from a Fermi's

golden rule argument, the conductance is proportional to the derivative of the BCS peak [89]. It is also interesting to notice that the conductance above the gap has a small amplitude $|G| < 0.12 \times e^2/h$, which suggests a strong asymmetry between the tunnel rates Γ_N and Γ_S to the N and S contacts. A theoretical modeling of the conductance with equation E.12 of Appendix E.2 confirms that for the dot level considered in this section, one has $\Gamma_S \ll \Gamma_N < k_B T$ (see figure 5.4b).

We have measured the cavity signals simultaneously with G (figures 5.4c and 5.4e). Here we see clearly that transport and cavity signals are qualitatively different. A crossed measurement of the two will therefore enable us to characterise the device more accurately. In agreement with section 5.2, $\Delta\varphi$ and ΔA reveal the resonance between the dot level and the Fermi energy of the N contact even inside the gap area ($e|V_b| < \Delta$), in contrast to what happens for G . Sign changes in $\Delta\varphi$ similar to those of figure 5.2d indicate that we are in a regime with $\Gamma_S, \Gamma_N \ll \omega_0$. The microwave amplitude A shows a more surprising behaviour. Indeed, the resonances of the dot level with S and N do not affect similarly the A signal. For $e|V_b| > \Delta$, the resonances with the S contact are closely followed by an area with $\Delta A > 0$, which indicates a counter-intuitive negative photon damping (or photon emission) caused by a fermionic reservoir (see dark blue areas in figure 5.4e). So far, with quantum dots circuits coupled to cavities, photo-emission had been obtained only due to tunnelling between two discrete dot levels[107–109, 130].

To model the cavity response, we use again equations E.2 and 5.3, with expressions of $\tilde{\mathcal{G}}^{r/a}(\omega)$ and $\tilde{\Sigma}^<(\omega)$ which take into account the finite Γ_S (see equations E.4–E.10 of Appendix E.2.2). We can reproduce quantitatively the three signals $\Delta\varphi$, ΔA and G versus V_b and V_g with a consistent set of parameters (see figures 5.4b, 5.4d and 5.4f). The good agreement between the data and theory is also visible in figure E.3 of Appendix E.1 for constant values of V_b . In particular, our theory reproduces well the positive ΔA areas. We take into account the lever arms determining the shift of the dot and reservoir energy levels with V_b and V_g . We also use the gap value $\Delta = 0.17$ meV given straightforwardly by the $G(V_b, V_g)$ map[129]. Then, there remains only 5 adjustable parameters: Γ_N , Γ_S , g , T , and the broadening parameter Γ_n for the BCS peaks. The multiple signals give strong constraints on the different adjustable parameters. The agreement with the data is optimal for $\Gamma_N/2\pi = 0.6$ GHz, $\Gamma_S/2\pi = 65$ MHz, $\Gamma_n/2\pi = 8$ GHz, $g/2\pi = 99$ MHz, and $T = 90$ mK. The equation E.12 used to model the dot conductance has been obtained in the absence of the cavity ($g = 0$). This approximation is relevant because the cavity brings only small corrections to this expression, not resolvable in our experiment. In contrast, $\Delta\varphi$ and A are calculated to second order in g .

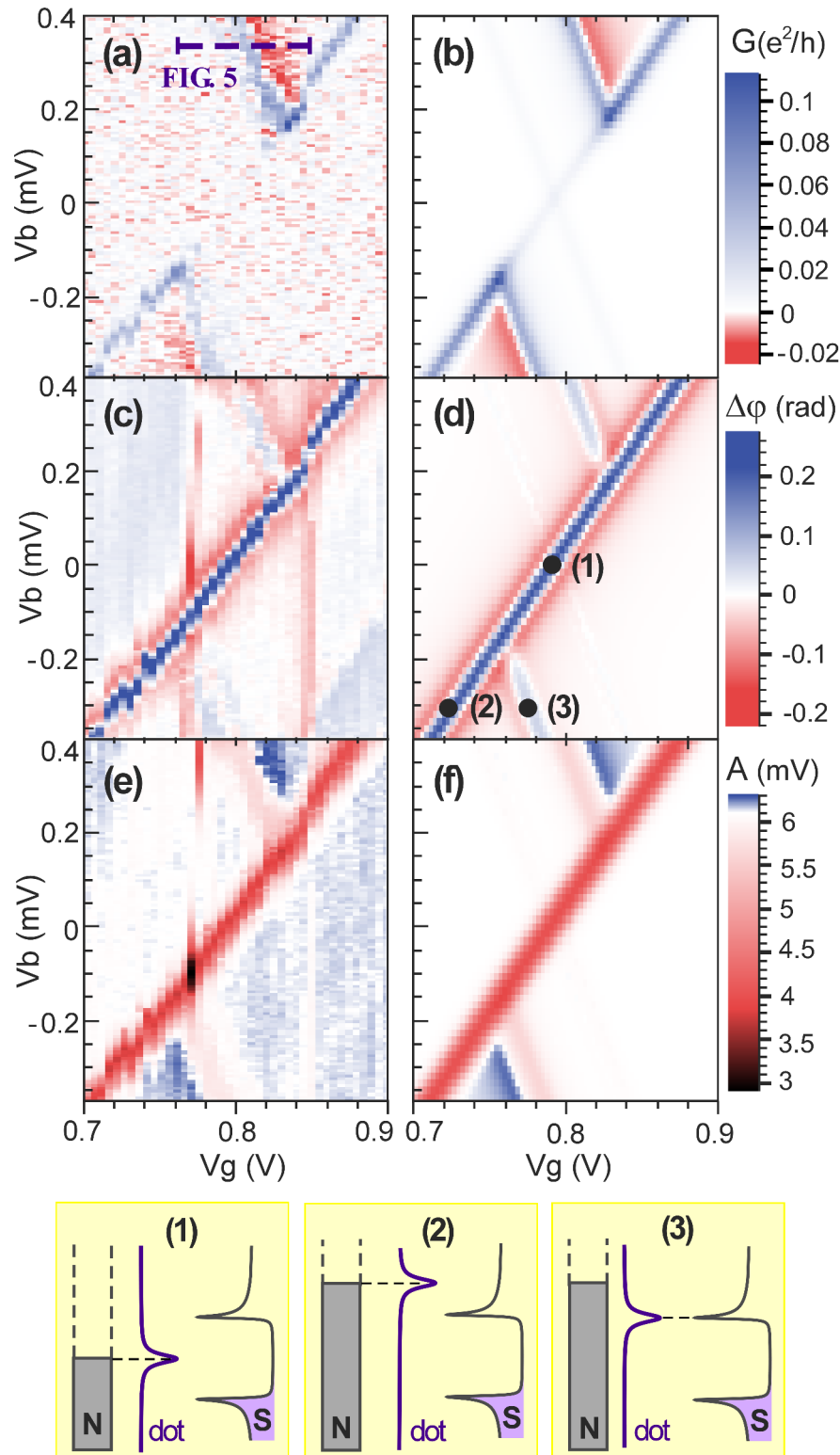


FIGURE 5.4: Panels (a), (c) and (e): Measured linear conductance G , phase shift $\Delta\phi$ and total amplitude A of the transmitted microwave signal, versus the dot gate voltage V_g and the bias voltage V_b . Panels (b), (d) and (d): Predictions from equations E.2, 5.3 and E.12, for $\Gamma_N/2\pi = 0.6$ GHz, $\Gamma_S/2\pi = 65$ MHz, $\Gamma_n/2\pi = 8$ GHz, $g/2\pi = 99$ MHz, $\Delta = 0.17$ meV, $T = 90$ mK, $\omega_0/2\pi = 6.65$ GHz, $A_0 = 6.1$ mV, and $\Lambda_0/2\pi = 0.259$ MHz. The white colour corresponds to $A = A_0$ in panels (e) and (f). Panels (1), (2) and (3): Electric potential configuration corresponding to the black points in panel (d).

5.3.2 Photon-assisted tunnelling between a dot and a superconductor

Are the $G < 0$ and $\Delta A > 0$ effects related? In order to answer this question, figure 5.5 shows A and G versus V_g for a constant bias voltage $V_b = 0.336$ mV (red dots) together with the theory for the above parameters (red lines). These signals vary smoothly due to the large value of Γ_n . It is very instructive to use a smaller BCS peak broadening parameter $\Gamma_n/2\pi = 1$ GHz for the theory (blue lines). The A signal then shows a cusp when the dot level is at resonance with a BCS peak (gray dashed line (2)) or shifted by $\pm\hbar\omega_0/\alpha$ (gray dashed lines (1) and (3)), with α the lever arm associated to V_g . This indicates inelastic tunnelling accompanied by photon absorption or emission along lines (1) and (3). More precisely, in the configuration corresponding to panel (1)/(3) of figure 5.5, the BCS peaks of the S contact reinforce the probability of photo-absorption/emission, leading to a pronounced negative/positive ΔA peak. In contrast, one keeps $\Delta A < 0$ near the N/dot resonance because the density of states of the N contact can be considered as constant. As expected, the theoretical G for $\Gamma_n/2\pi = 1$ GHz and $g = 0$ does not show cusps along lines (1) and (3) since this quantity does not take into account photon emission or absorption (see blue line in top panel of figure 5.5). Since the experimental G is dominated by this zeroth order contribution in g , it implies that the $G < 0$ and $\Delta A > 0$ effects in our data are not directly related. It is more correct to state that these effects have a common origin. More precisely, $G < 0$ is due to the fact that the DOS of S decreases with energy in certain areas, which leads to a reduction of the dot current, whereas $\Delta A > 0$ is due to the strong DOS peaks which reinforce photo-emission. It is important to replace the above results in a wider context. Photo-assisted tunnelling has been observed for 40 years in SIS junctions [57] and for 25 years in quantum dots with N contacts [58, 131, 132]. In these seminal experiments, a broad band coupling scheme was used instead of a cavity and the photo-induced current was directly measured. In this context, one novelty of our work is that we use a highly resonant microwave technique to inject and probe photons. We send a limited photonic power on the quantum dot circuit, so that the photo-induced current is not resolvable. More precisely, along lines (1) and (3), the rate of photons absorption/emission ($\Gamma_{e/a}$) by the quantum dot circuit is $\Gamma_{e/a} \simeq 2\langle n \rangle \Lambda_0 \Delta A / A_0$, with an average photon number $\langle n \rangle \sim 120$ in the cavity⁶. This gives $\Gamma_{e/a} \sim 2$ MHz, which corresponds to a photo assisted current of the order of 0.3 pA. For comparison, in [131], the photo assisted current reaches 30 pA. In spite of this, we can directly detect photo emission/absorption thanks to the cavity. This demonstrates that circuit QED techniques provide accurate tools to revisit the physics of photo-assisted tunnelling. Note that many theory papers

⁶In the semiclassical limit, by combining equations 2.23 and 2.24 with $\chi(-\omega_0) = \chi(\omega_0)^*$, one obtains a photon emission/absorption rate $\Gamma_{e/a} = -2g^2 \text{Im}[\chi(\omega_0)] \langle n \rangle$. Then, for linear cavity signals, one has $\Delta\Lambda_0 \sim g^2 \text{Im}[\chi(\omega_0)] \simeq -\Lambda_0 \Delta A / A_0$. This gives $\Gamma_{e/a} \simeq 2\langle n \rangle \Lambda_0 \Delta A / A_0$.

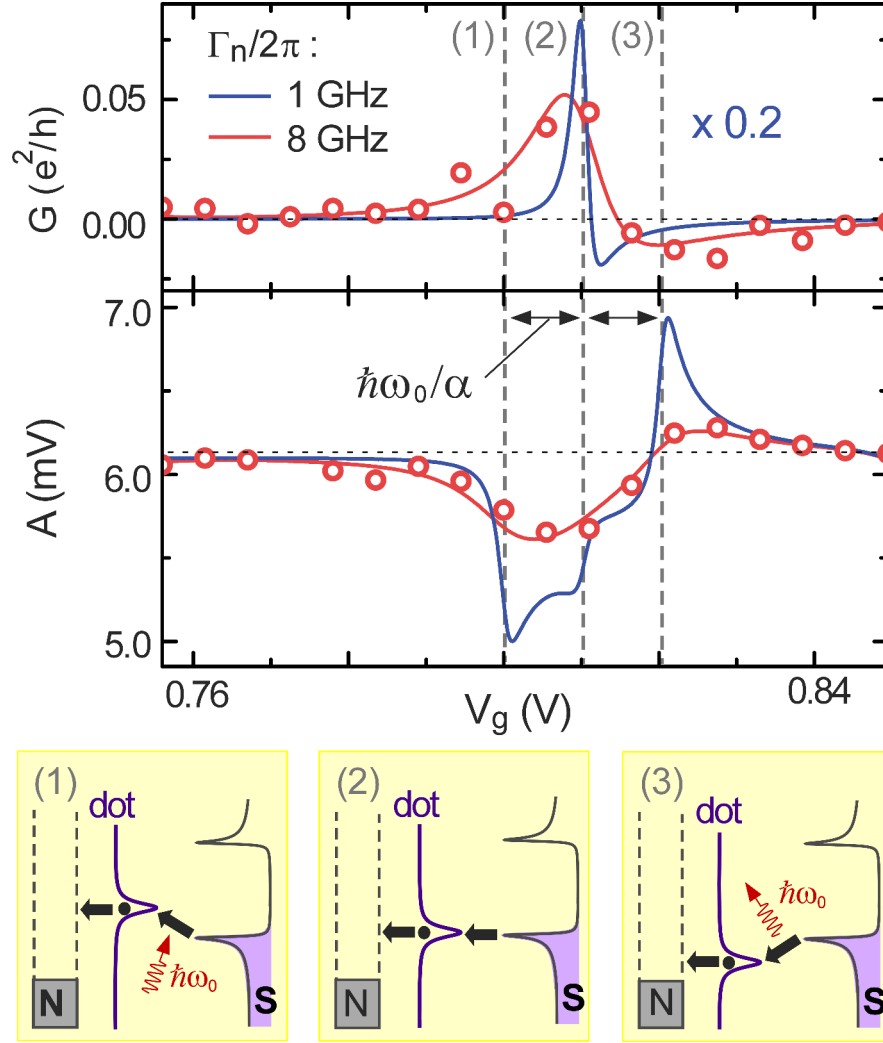


FIGURE 5.5: Conductance G and microwave amplitude A versus V_g (red dots), measured along the dashed line in figure 5.4a for $V_b = 0.336$ mV, and theory using the same parameters as in figure 5.4 and $\Gamma_n/2\pi = 8$ GHz (red lines) or $\Gamma_n/2\pi = 1$ GHz (blue lines). The theoretical G for $\Gamma_n/2\pi = 1$ GHz has been multiplied by 0.2. Panels (1), (2) and (3) illustrate the transport regimes corresponding to the gray dashed lines. In panel (2), the dot orbital is resonant with a BCS peak in the DOS of the S reservoir. In panels (1)/(3), an electron can pass from the dot orbital to the BCS peak by absorbing/emitting a cavity photon.

have studied the photo-assisted current between a quantum dot and superconductors (see for instance [133–137]), but we present the first experimental study of this case, to our knowledge.

5.4 Summary and discussion

We have studied experimentally the behaviour of a spin-degenerate N/dot/S hybrid structure based on a carbon nanotube, coupled to a microwave cavity. We have observed a large variety of effects depending on the values of the tunnel rates and on the bias

voltage applied to the device. For intermediate tunnel rates and equilibrium conditions, the cavity frequency and linewidth shifts follow a relation, which is independent of the quantum dot gate voltage. We have shown that this behaviour is related to the universality of the quantum charge relaxation resistance predicted by Büttiker et al. [64, 65], and observed only in a strongly spin-polarised GaAs quantum dot so far [66]. We have observed in a controlled way the departure from this universal regime, when the dot behaviour changes from capacitive to inductive. We have also observed negative photon damping by the quantum dot circuit, in case of out of equilibrium quasiparticle tunnelling between the dot and the BCS peaks of the S reservoir. Strikingly, all these effects can be modelled quantitatively with a single theoretical description. We can reproduce simultaneously the quantum dot conductance, together with the phase and amplitude of the microwave signal transmitted by the cavity, versus gate voltage and versus bias voltage, with only 5 adjustable parameters. This validates a description of mesoscopic QED experiments in terms of an electronic charge susceptibility.

The fact that a non-interacting theory reproduces well our data is non-trivial since we see Coulomb blockade. This approach seems relevant in our case because Andreev reflections and correlations effects induced by interactions (e.g. Kondo effect) are not visible in the experiment. In the absence of electron/hole and many-body correlations in the dot, the effect of interactions mainly comes down to decreasing the dot level occupation in comparison with the non-interacting case. More precisely, due to Coulomb blockade, the occurrence of a dot/reservoir resonance for a given spin direction is limited by the occupation of the dot by opposite spins [138]. In this picture, one can expect G and χ to have the same gate or energy dependences as in the non-interacting case (same peaks width), but with renormalized amplitudes. This renormalization can be different for the dot/N and dot/S resonances, for which the dot occupation differs. Actually, with the non-interacting theory, it is possible to tune the amplitude of the different peaks in the current and cavity signals by changing the parameters g , Γ_N , Γ_S , Γ_n and T . Therefore, we believe that for our system, these parameters can be simply viewed as effective parameters renormalized by Coulomb interactions. Note that a temperature $T = 60$ mK is optimal to interpret the low bias voltage data of section 5.2, but we need a higher temperature $T = 90$ mK to interpret the finite bias voltage data of section 5.3. This may be due to heating effects caused by $V_b \neq 0$, or to interactions since the dot occupation is modified by out-of-equilibrium transport.

It is important to note that the seminal experiment of [66] was carried out in the strongly spin polarised and non-interacting regime⁷. In contrast, we have presented the first experimental investigation of quantum charge relaxation in the spin-degenerate interacting

⁷In the samples of [66], the large top gate capacitance makes the Coulomb energy unusually small, similar to [139].

case. Our observations are consistent with recent theory works which suggest that the universality of the charge relaxation resistance R_{AC} persists in this limit[67, 68]. More precisely, our experiment confirms that R_{AC} is independent from the dot gate voltage, at least within our experimental uncertainty. Noticeably, this independence could not be probed in [66]. We have investigated the deep Coulomb blockade regime, but other interacting regimes like the Kondo limit can be studied with our technique[42].

Chapter 6

Strong coupling of a Cooper pair splitter to cavity photons

6.1	Sample and setup	112
6.2	DC transport	113
6.3	Cavity response	115
6.3.1	Resonant behaviour	115
6.3.2	Strong coupling	117
6.4	Preliminary microscopic interpretation	118
6.4.1	Three-level ladder scenario	118
6.4.2	Sub-gap transitions	120

While creating distant entangled photon pairs is routinely done in quantum optics laboratories, the equivalent for electron pairs has never been achieved. Research efforts in creating distant entangled electrons are motivated by the curiosity about if and how this could be achieved, as well as by the potential practical use of such pairs for solid-based quantum information processing. A strategy proposed in the early 2000's is to exploit Cooper pairs in superconductors and superconducting proximity effect to induce non-local superconducting correlations in quantum dots [27]. In principle, in the appropriate parameters regime, a Cooper pair splitter device will generate entanglement between two electron spins sitting in spatially separated orbitals, as introduced in section 1.4.2. In practice Cooper pair splitter devices have been originally implemented in CNT [31, 33, 88, 129] and InAs NW [30, 32, 34], more recently in graphene [36, 37] and with InAs self-assembled QD [35]. Transport measurements demonstrated an electronic beam splitter behaviour by looking at currents signals. However entanglement and coherence of the split pairs could not be probed. Recently the use of a cavity QED architecture has been proposed to investigate those properties [55, 56]. Here we present the first experimental study of a Cooper pair splitter embedded in a microwave cavity. Section 6.1 describes the sample and setup in this experiment. Simultaneous DC transport and microwave cavity measurements are shown in sections 6.2 and 6.3. Finally section 6.6 provides some elements to interpret our observations.

6.1 Sample and setup

Data presented in this chapter have been measured on the same sample as the one of chapter 5, namely CPSRES32R, although under different operating conditions. The design is recalled on 6.1 (same as figures 5.1b and 3.6) and fabrication techniques can be found in 3.1. It is a Cooper pair splitter formed in a carbon nanotube contacted to a central superconducting electrode S and two lateral normal electrodes N. Energy levels positions are tuned using two side gates G_L and G_R . A "fork-shape" floating top gate TG_{RF} is contacted to the resonator central conductor. Placed symmetrically above the two dots, it aims at simultaneously modulating the left and right dot energy levels with equal amplitude. By comparison with the asymmetric situation depicted in figure 2.3b, we target the opposite symmetric coupling regime $g_{d,L} = g_{d,R}$. Figure 6.1 also shows the specific measurement configuration used for acquiring this chapter transport data. Here the bias voltage is applied to the superconducting contact, while currents I_R , I_L and differential conductances G_R , G_L through right and left normal contacts are measured using techniques presented in 3.2.2. The issue in such a measurement is the difference between the two amplifiers offsets, which results in a spurious bias voltage between left and right normal electrodes. To minimize this effect, we used the amplifiers with the

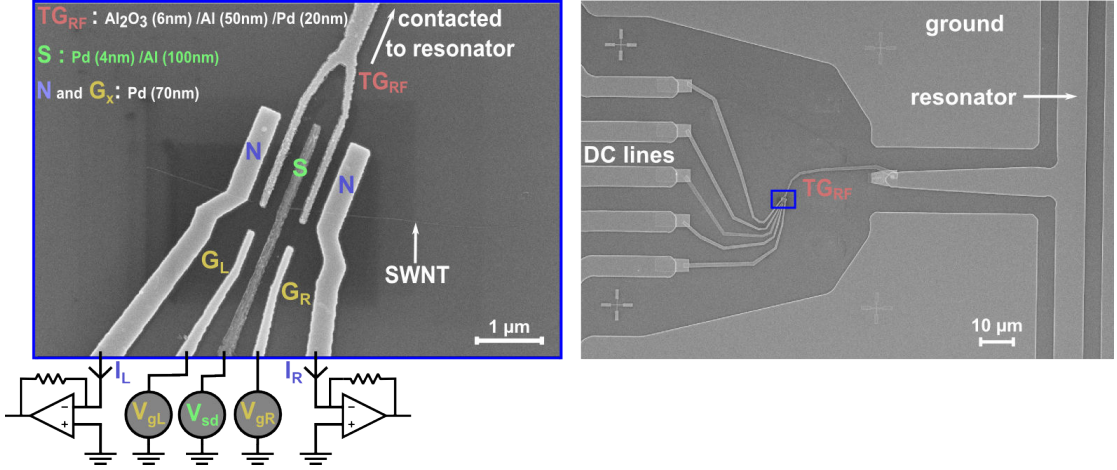


FIGURE 6.1: **Scanning electron micrograph of a Cooper pair splitter circuit embedded in a microwave resonator** (location indicated by a blue rectangle). The measurement scheme consists in biasing the central superconducting electrode, while measuring the currents and conductances through the two lateral normal electrodes.

smallest offset difference we found in our lab, namely $3\mu V$. Using the microwave setup presented in section 3.2.3, we measure the phase φ and amplitude A of the transmitted signal. The cavity quality factor is $Q \approx 12800$ for a cavity photon number $n_0 \approx 120$.

6.2 DC transport

Figure 6.2 shows the characterization of our device by transport measurements. Panels a and b are colour plots of the right and left differential conductance in the gate-gate plane for $V_{SD} = -0.16mV$. More precisely the data are measured using the orthonormal frame $V_{\Sigma}-V_{\delta}$, which results from a 42 degrees clockwise rotation of the original $V_{g,L}-V_{g,R}$ frame¹. This choice is justified by thin features in the V_{Σ} direction, which could thus be resolved in a shorter data acquisition time. G_R displays a clear avoided crossing characteristic of a double dot stability diagram, as presented in section 1.2.2.1. The G_L signal is weaker and measurable only on one orbital branch. Note that the behaviour of our device changed from single dot to double dot between chapter 5 and this chapter. This is because we use different values for side gate voltages $V_{g,L}$ and $V_{g,R}$.

Figure 6.2c and d show the right and left currents dependence versus bias voltage V_{SD} and V_{Σ} . We observe Coulomb blockade and a clear superconducting gap $\Delta \approx 150\mu V$. Note that the currents displayed here are calculated by numerical integration of the measured differential conductances : $\tilde{I}_{L/R} = \int_0^{V_{SD}} G_{L/R} dV'_{SD}$. This allows to get rid of the current due to the residual static bias voltage between left and right normal electrodes, by measuring only the current due to the modulated bias applied on the

¹For convenience the frame origin has also been translated.

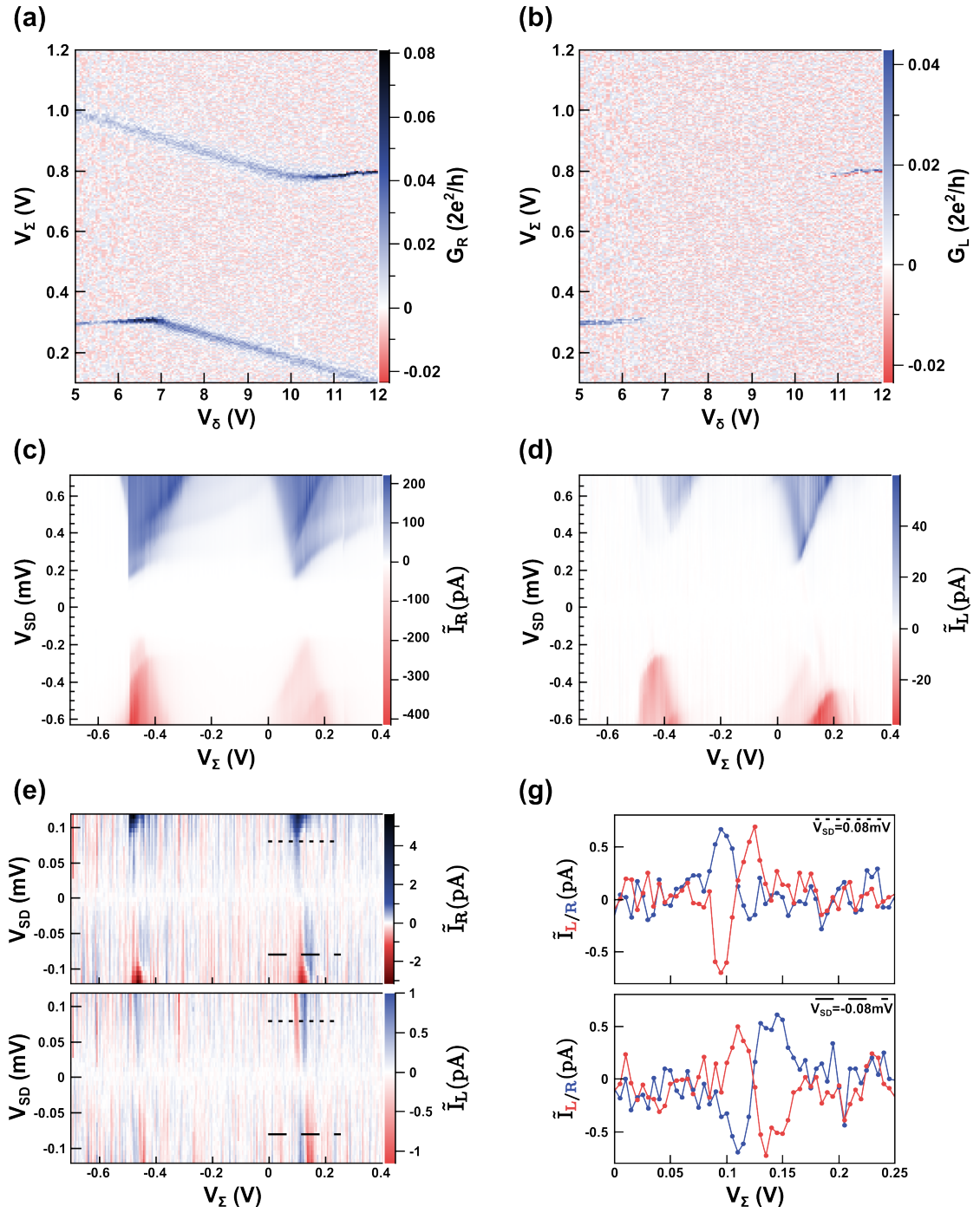


FIGURE 6.2: **Device transport measurements.**(a) and (b) are colour plots of the right and left differential conductance in the rotated gate-gate plane V_Σ - V_δ for $V_{SD} = -0.16$ mV. To make comparison easier, colours for G_R and G_L are the same on the common range. (c) and (d) show the right and left currents dependence versus bias voltage V_{SD} and V_Σ . \tilde{I} refers to the current calculated from the numerical integration of the measured conductance G . (e) show $\tilde{I}_{L/R}$ colour plots zoomed onto the sub-gap area. To make comparison easier, colours for G_R and G_L are the same on the common range. The dashes indicate the linear cuts plotted in (g).

superconductor. We have checked that the difference between measured I and calculated \tilde{I} currents is negligible at high bias voltages. However a spurious left-right current of a few pA is damageable for the study of sub-gap current signals. Figure 6.2e displays zooms of the currents colour plots c and d in the range $V_{SD} \in [-0.12; 0.12]mV$. It reveals simultaneous measurable left and right currents of a few pA below the gap. Figure 6.2g shows linear plots of $\tilde{I}_{L/R}$ along cuts at $V_{SD} = 0.08mV$ (top panel, indicated with short dashes on e) and $V_{SD} = -0.08mV$ (bottom panel, indicated with long dashes on e). They highlight correlations between left and right current resonances. For negative bias voltages \tilde{I}_L and \tilde{I}_R look opposite, while for positive bias voltages they do not.

6.3 Cavity response

We present here the changes in the cavity resonance occasioned by the Cooper pair splitter close to a degeneracy line of the stability diagram.

6.3.1 Resonant behaviour

In this section the phase and amplitude of the transmitted microwave signal are measured at a fixed frequency, equal to the bare cavity frequency f_c . Figure 6.3a and b present the cavity response, measured simultaneously as the transport colour plots a and b of figure 6.2. Cotunnelling lines, which appeared in the differential conductances, are also visible in the cavity signals. However the strongest changes in the cavity transmission occur along the degeneracy line, where there is no measurable DC transport. The cavity phase shift $\Delta\varphi$ overcomes 40 degrees in absolute value and goes from negative to positive to negative, when the zero-detuning line is crossed. This behaviour is characteristic of a resonance condition between the frequency of a circuit electronic transition and the cavity frequency. It has been observed previously for a charge qubit transition [43, 44, 50–52] and a charge-spin hybrid transition [54]. However the specific change in contrast observed along the zero-detuning line between the two triple points is unusual, and has not been reported before ². A resonance condition is also crossed in this direction, as indicated by the phase sign change. Figure 6.3c is a V_Σ - V_δ phase colour plot, similar to 6.3a but measured on a different day ³. The dotted line on 6.3c shows the line cut, where the cavity signals dependence as a function of bias voltage has been measured right after,

²A change in contrast along the zero-detuning line was reported in [109] and attributed to variable interdot tunnelling term t . However, the phase signal seems to bridge the two triple points, whereas ours does not.

³This explains the shifts in gate voltages and the different contrast of the lower cotunnelling line, which displays here a sign-changing behaviour observed and discussed in previous chapter (figure 5.2d). Indeed the parameters of carbon nanotube-based circuits are known to evolve over time due to changes in the electrostatic environment.

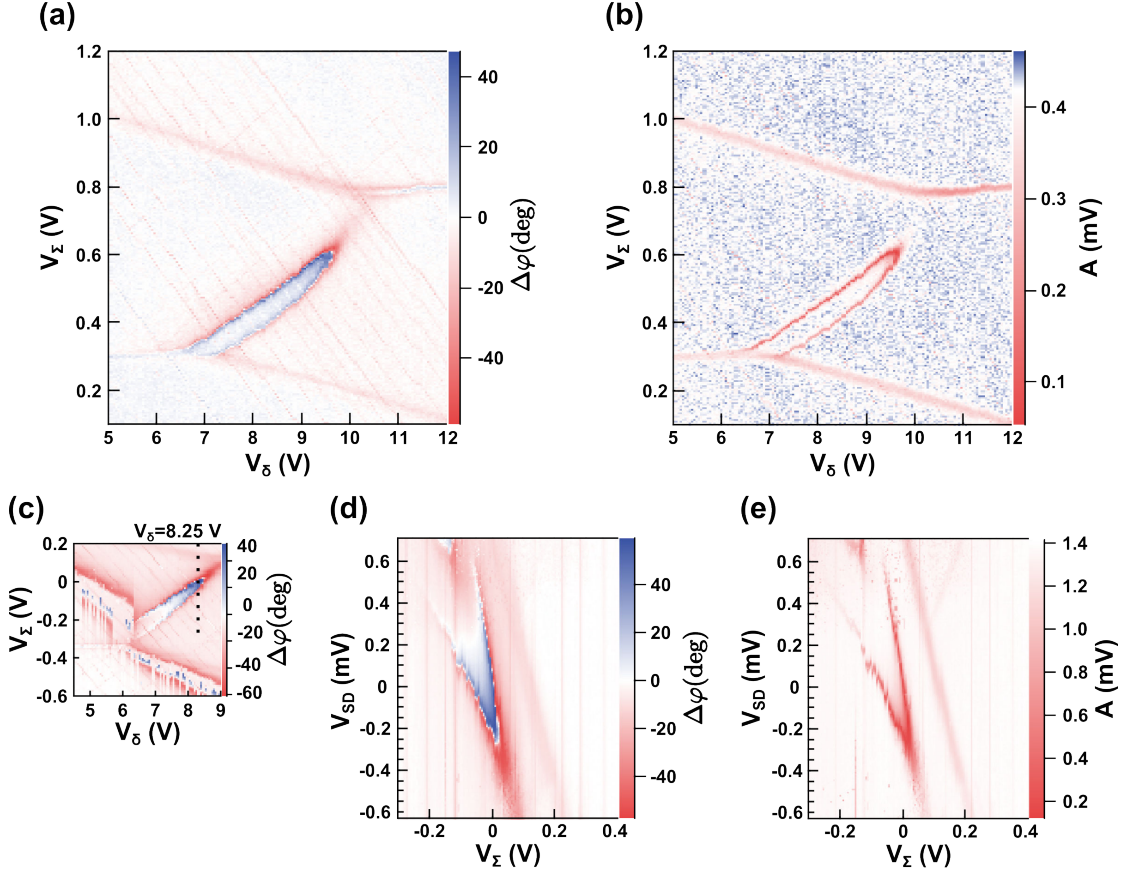


FIGURE 6.3: **Cavity measurements.** Phase shift and amplitude of the resonator transmitted signal measured simultaneously as the transport signals displayed in figure 6.2. (a) and (b) show colour plots in the V_{Σ} - V_{δ} plane for $V_{SD} = -0.16\text{mV}$, corresponding to 6.2a,b. (c) is a similar phase colour plot also measured for $V_{SD} = -0.16\text{mV}$ but on a different day than (a). It indicates with a dotted line the V_{Σ} line cut at $V_{\delta} = 8.25\text{V}$, where the bias dependence was measured right after, resulting in (d) and (e), corresponding to simultaneous transport measurements of 6.2c,d.

leading to figure 6.3d and e. These V_{SD} - V_{Σ} maps (6.3d and e) are the simultaneous cavity measurements as the transport signals of figure 6.2c and d. Note that the dotted line of 6.3c crosses the resonance condition twice and a dot-lead cotunnelling line. Remarkably, these two features can also be identified on the cavity phase shift and amplitude maps versus V_{SD} and V_{Σ} . The cotunnelling line is the shallow straight line with negative slope. Consistently with 5 it corresponds to the N-dot resonance, which is revealed by the cavity even below the superconducting gap⁴. The resonance condition appears as a "V-shape" dispersion line with a minimum, which is reminiscent of the parabolic dispersion of the transition energy between two anticrossing hybridized levels.

⁴Note that the N-dot resonance in chapter 5 corresponded to a line with positive slope, in agreement with the change in biasing contact between the two chapters.

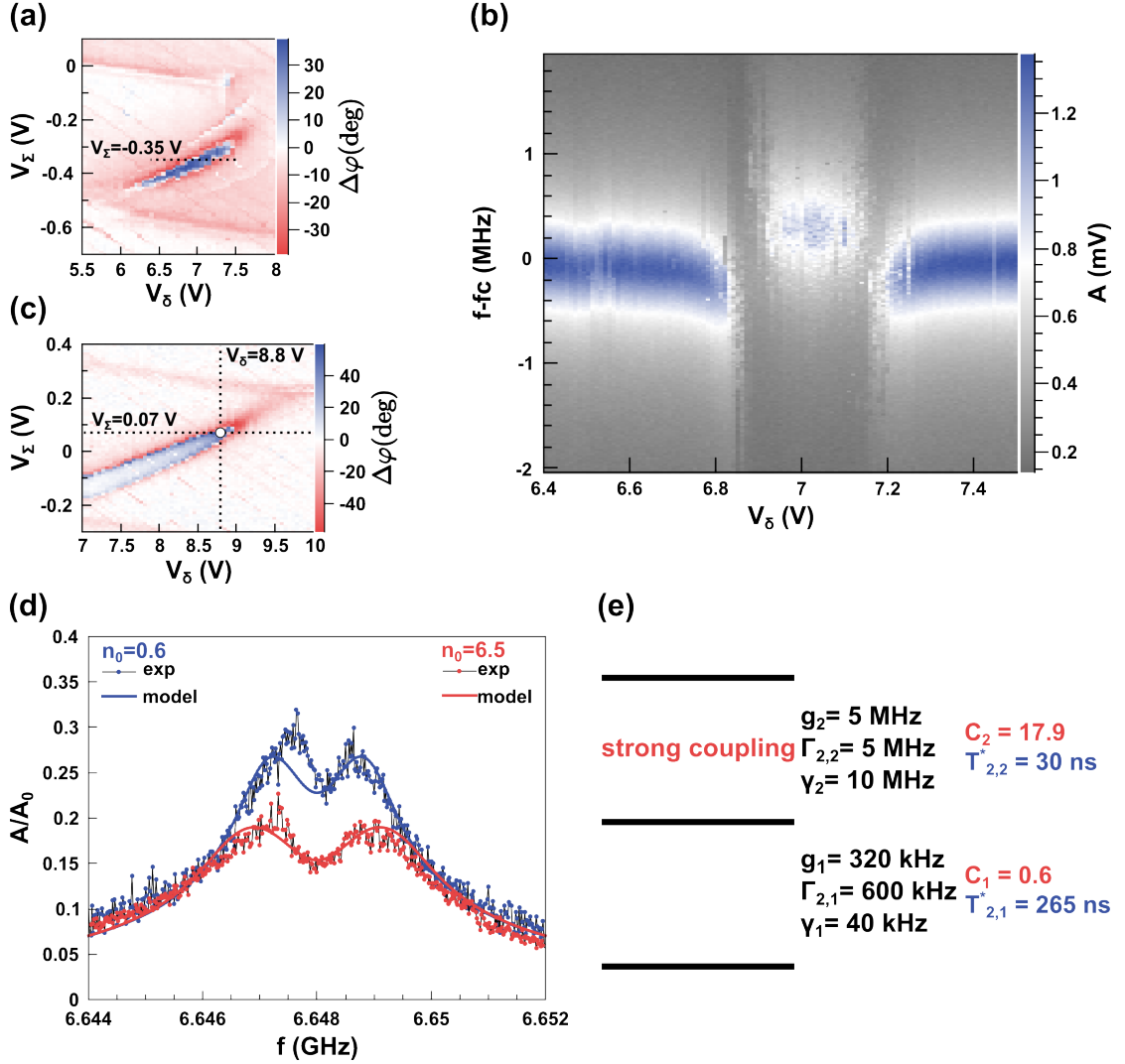


FIGURE 6.4: **Strong coupling of a CPS device transition to cavity photons.**(a) indicates with a dotted line, for which parameters the cavity spectra shown on 6.4(b) were measured.(c) The dot on the V_{Σ} - V_{δ} phase map is where amplitude spectra plotted (black lines, coloured dots) in (d) were acquired for $n_0 \approx 0.6$ (blue) and $n_0 \approx 6.5$ (pink). Plain lines correspond to the semi-classically modelled cavity response coupled to a three-level ladder. The parameters are given in black on the sketch in (e). The cooperativity C_i and coherence time $T_{2,i}^*$ of each transition i are calculated from the coupling strength g_i , the decoherence rate $\Gamma_{2,i}$ and the relaxation rate γ_i .

6.3.2 Strong coupling

An alternative way to characterize the cavity response is to measure how the full spectrum of the cavity is modified by the quantum dot circuit. This consists in measuring the cavity transmitted signal as a function of the input microwave frequency for different sets of circuit parameters V_{Σ} , V_{δ} , V_{SD} . For a bare cavity the spectrum is fitted by a Lorentzian, which gives the resonance frequency and width and the setup transmission (see section 3.2.3). In principle the circuit induces dispersion and dissipation on the cavity, which can directly be identified by looking at the cavity modified spectrum. Figure

6.4a indicates with a dotted line in the V_Σ - V_δ plane, the parameters for which cavity spectra are shown on 6.4b. When V_δ goes from 6.4 to 7.5V, it crosses the resonance condition twice. At these points the cavity spectrum is most strongly affected, because of its hybridization with the device electronic states. At the contrast maximum in the V_Σ - V_δ phase map (circle on figure 6.4c), the cavity spectrum shows two resolvable peaks (figure 6.4d), which is the signature of strong coupling between the cavity photonic mode and the Cooper pair splitter electronic states. We observed the Rabi splitting for two cavity input power, expressed in terms of corresponding photon numbers for a bare cavity : $n_0 = 0.6$ (blue dots) and $n_0 = 6.5$ (pink dots). These numbers are estimated from setup transmission measurements detailed in Appendix. The evolution of spectra as a function of n_0 is not the one expected for a two-level transition strongly coupled to a cavity mode. In this case, and for our parameter range, an increase in the photon number would result in the merging of the two peaks into the single bare cavity resonance peak (see discussion in 2.4.1). Instead the opposite behaviour is observed : the curve measured for $n_0 = 6.5$ shows a larger splitting and lies below the curve for $n_0 = 0.6$. This can be reproduced invoking a three-level ladder scenario, depicted on figure 6.4e. Assuming that the two transitions are resonant with the cavity, the semi-classical master equation treatment exposed in section 2.4.2 leads to the plain lines plotted in 6.4d. The parameters used to simultaneously reproduce both curves are given in black on figure 6.4e. There are the coupling strength g_i , the decoherence rate $\Gamma_{2,i}$ and the relaxation rate γ_i of each transition i . From these parameters the cooperativity $C_i = \frac{2g_i}{\kappa\Gamma_{2,i}}$ and coherence time $T_{2,i}^* = 1/\Gamma_{2,i}$ of each transition i are calculated. The first transition is much less coupled and much more coherent than the second one, which is the one in the strong coupling regime.

6.4 Preliminary microscopic interpretation

In this section we provide some arguments to interpret the microscopic nature of the electronic transitions coupled to the cavity field.

6.4.1 Three-level ladder scenario

In principle, carbon nanotubes are characterized by a four-fold orbital degeneracy, due to doubly degenerate spin and valley degree of freedom. The valley can be pictured as the electron orbital moment orientation, corresponding to clockwise or counter-clockwise "electron movement" around the nanotube. The two possible states for the valley are usually labelled K and K'. The three-level ladder structure of the spectrum could originate from the splitting of valley degeneracy $\Delta_{K,K'}$. It is common to observe valley

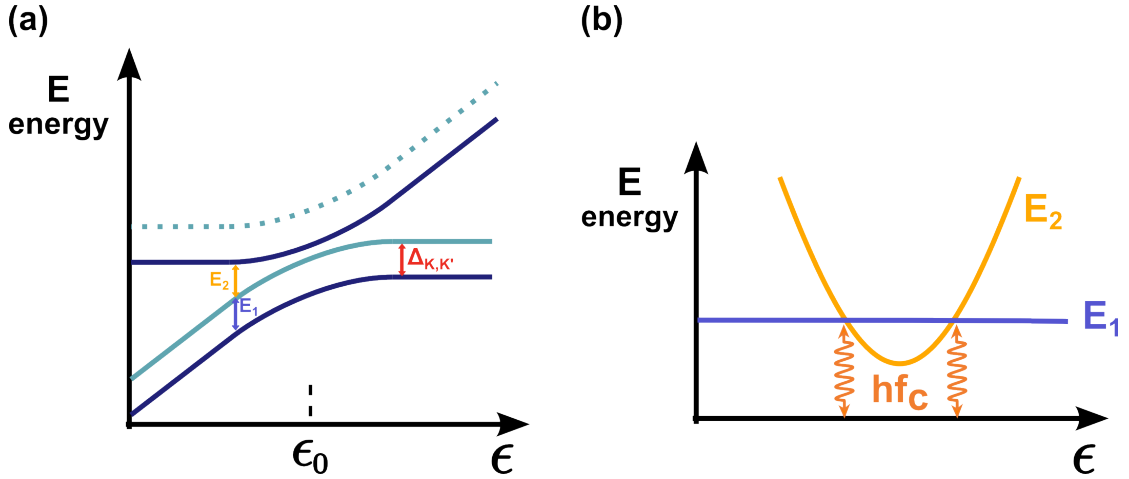


FIGURE 6.5: **Explanation for a ladder scenario.**(a) In a simplified treatment the effect of a splitting $\Delta_{K,K'}$ comes down to splitting the original dark blue spectrum made of two anticrossing levels. If $\Delta_{K,K'} \sim hf_c$, and both parameters are also close to the original minimal level anticrossing, two transitions may be resonant with the cavity (Here we ignore the dotted fourth level).(b) Dispersion relations of the transition energies E_1 and E_2 as a function of a given electrical anticrossing parameter ϵ . The curvature of E_2 makes this second transition much more sensitive to charge noise than the first transition with flat dispersion.

splitting in carbon nanotube-based devices due to disorder in the molecular structure. Values of $\Delta_{K,K'}$ reported in the literature can be as different as $0.1\mu eV$ in [54] and $450\mu eV$ in [140], so $\Delta_{K,K'} \sim hf_c \approx 25\mu eV$ is possible. In a simplified approach, the effect of valley splitting can be seen as adding a shifted copy of energy levels to the original spectrum (figure 6.5a). These two arguments about valley splitting allow us to account for the possible existence of two resonant transitions in a ladder geometry. The valley-splitting interpretation is supported by the fact that it also provides an explanation for the couplings and coherence rates hierarchy between the two transitions. On the one hand a transition between states, which differ only by the valley internal degree of freedom, is not expected to be highly coupled to the cavity electric field. Indeed their wavefunctions are likely to be rather similar [141]. On the other hand, a flat transition energy dependence with any electrical control parameter (eg gate voltages) makes the transition much more insensitive to charge noise (E_1 flat dispersion on figure 6.5b). This would explain the long coherence time of the first transition between K, K' parallel levels. The second transition coherence time order of magnitude is compatible with the scheme of a two-level hybridized transition exposed to charge noise (E_2 curved dispersion on figure 6.5b). However, so far we have not identified the microscopic degree of freedom involved in such resonant hybridized two-level system.

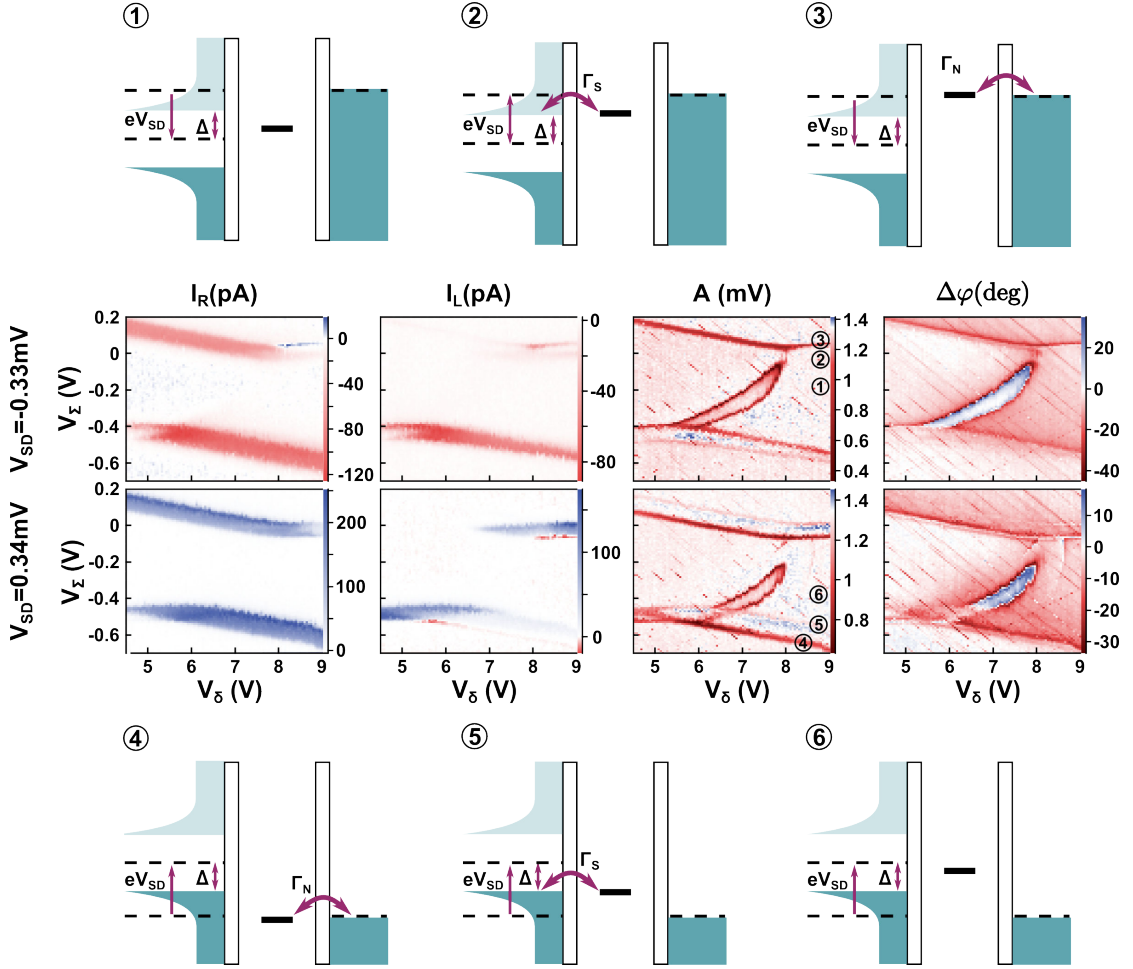


FIGURE 6.6: **Signature of subgap transitions.** Transport and cavity simultaneous measurements of V_{Σ} - V_{δ} maps for $V_{SD} = -0.33\text{mV}$ and $V_{SD} = 0.34\text{mV}$. The sketches show the circuit electric potential configuration in the parameters regime of the corresponding number position. It shows only one CPS level for explaining the geometry of the lines corresponding to resonances between CPS and leads. The unoccupied side of the superconducting density of states is depicted with a lighter colour than the occupied side.

6.4.2 Sub-gap transitions

We analyse here how the evolution of V_{Σ} - V_{δ} maps as a function of bias voltage is informative about the circuit ground state level position, relatively to the superconducting gap. For $|V_{SD}| > \Delta$ current can flow if a device discrete level lies between a BCS peak and the normal electrochemical potential, with filled states on one side and empty states on the other (like for instance in sketch 2 of 6.6). The areas of the V_{Σ} - V_{δ} plane, where this condition is fulfilled are the two stripes in the currents maps on figure 6.6. Their boundaries appear as lines in the cavity signals. It is clearer on amplitude maps, where the line with strongest contrast corresponds to the resonance with the normal contact (sketches 3 and 4), while the shallow line reveals tunnelling to the superconducting BCS peak (sketches 2 and 5). Within the stripes, the circuit ground state energy level lies

inside the superconducting gap, as depicted on sketches 1 and 6. Given that $\omega_c \ll \Delta$, the levels leading to resonant transition(s) lie all below the superconducting gap, in the central area between the lines (blank in transport). Note that the resonant signals in the cavity phase shift and amplitude vanish, when the circuit level position leaves the superconducting gap. To explain this behaviour, one can imagine two different scenarios. The device spectrum may change and the resonant transitions may not exist any more in this parameters range. Alternatively the resonant transition(s) still exist, but their coherence properties ($\Gamma_{2,i}$) and/or their population ($\langle \hat{\sigma}_{z,i} \rangle$) are modified, resulting in the observed changes in cavity transmission (see 2.4.2). To conclude the cavity shows a resonant behaviour with (a) very coherent electronic transition(s) only when the involved states lie below the gap.

In this chapter we have studied a Cooper pair splitter embedded in a microwave resonator. The cavity appears as a powerful probe, as it reveals features which are either absent or hardly resolvable in transport signals. Beyond being a powerful probe of the CPS electronic states, the photonic cavity mode strongly couples to the CPS electronic degrees of freedom. This hybridization regime had not been reached with quantum dots circuits so far. Noticeably the position of the electronic states involved in the resonant transition(s) with respect to the superconducting gap strongly affects the cavity signal contrast.

Conclusion and perspectives

Summary and conclusion

The experiments presented in this thesis illustrate, that microwaves are a powerful tool to investigate quantum dot circuits. Microwave excitations can be applied directly to the circuit electrodes. This technique has been used in some quantum transport experiments for almost fifty years (cite Tien Gordon). This is the excitation method we have employed to characterise the finite-frequency response of a single quantum dot in the Kondo regime (chapter 4). We confirm the decrease in the Kondo conductance peak and the appearance of satellite peaks, which were previously observed in similar experiments. We go further by providing the first frequency-amplitude characterisation of the Kondo zero-bias conductance. We find that the peak amplitude is more strongly reduced for low excitation frequencies. Given our frequency selection procedure, implying a microwave excitation applied on the leads, this observation matches with theoretical predictions. To model our data, we propose an Ansatz, which reproduces quantitatively the conductance dependence versus both frequency and amplitude. We also present partial experimental data testing the predicted universality of the AC Kondo response as a function of the scaled excitation parameters $eV_{AC}/k_B T_K$ and $hf/k_B T_K$. Our observations are consistent with a universal behaviour. However, this property remains to be experimentally explored over a wider scaled frequency range.

The experiments of chapters 5 and 6 belong to the young field of mesoscopic QED, as they study quantum dot circuits embedded in microwave resonators. They both illustrate that a cQED architecture offers more than a mode of circuit excitation at finite-frequency. Due to the circuit-cavity coupling, measuring the resonator transmission reveals information about the circuit, which could not be accessed by transport measurements alone. In chapter 5 the circuit is a single dot coupled to normal and superconducting leads. At zero-bias, the cavity probes the tunnelling dynamics between a dot discrete level and a normal continuum. We present the cavity response for a wide range of tunnel rates, and approach a universal dissipation regime governed by a

charge relaxation effect. Noticeably this observation concerns a spin-degenerate interacting system, a situation which had been intensively studied theoretically but never experimentally. At finite bias, the cavity reveals photon-assisted tunnelling between the dot and the BCS peaks of the superconducting reservoir. This physical effect was never studied experimentally before, even with DC transport. Here, we report the possibility of photon emission by a dot coupled to reservoirs, against the common idea that reservoirs are synonym of dissipation. In chapter 6 we present the first implementation of a Cooper pair splitter in a microwave resonator. We observe the resonant coupling between electronic transitions of the device and cavity photons. From an energetic analysis, we show that this observation is conditioned to the subgap position of the electronic states involved in the resonant transition(s). Importantly, the strong coupling regime is achieved, which had never been realised before with quantum dot circuits. We provide a semi-classical modelling of the non-trivial Rabi splitting dependence with the photon number. A full interpretation of the CPS microscopic states, which are involved in this strong coupling to cavity photons, needs further analysis.

Perspectives

Further experimental investigation of Cooper pair splitters in microwave cavities is a near future perspective of this thesis work. Measuring others samples with different parameters and in various coupling regimes (e.g dispersive versus resonant) to the cavity would probably be instructive. We plan to use additional experimental knobs to perform more complete characterisations. Magnetic field comes to mind directly. It allows to investigate the spin structure of electronic states and to ultimately cross the superconducting-normal transition. While it was not yet available for this thesis experiments, it has been implemented recently in our experimental setup. In principle, applying a second microwave tone to the device enables to perform the spectroscopy of the Cooper pair splitter, a first step towards manipulation. However, it requires a better control over the driving microwave amplitude versus frequency, that we achieved in this thesis, and towards which we are working.

While most previous experiments in mesoscopic QED focused on "atomic-like" circuits, our results presented in chapter 5) show that cavity QED tools are also powerful to investigate effects involving tunnelling between a discrete level and fermionic reservoirs. Beyond the experimental observations themselves, it is the first experimental test of the cavity response theoretical description in terms of charge susceptibility. Remarkably, this formalism is able to reproduce quantitatively the large variety of effects we observe. This lays the foundations for the study of others nanocircuits coupled to cavities, involving any type of fermionic reservoirs (normal, superconducting, ferromagnetic). This opens

many possibilities. For instance, the open question of the charge susceptibility in the Kondo regime could be addressed. Cavity photons could also be instrumental in the quest of Majorana bound states in topological hybrid nanocircuits [142]. In a different perspective quantum dots are envisioned to produce non-classical states of light [143] in the spirit of what is currently looked after with SIS junctions.

Finally it is important to mention that mesoscopic QED fits in the wider context of hybrid QED. Beyond mesoscopic circuits, the coupling to microwave cavities is a topical issue for other systems, like for instance spin ensembles and nanomechanical objects. In the future, these diverse degrees of freedom are expected to be combined to take the most of their respective strengths, with the purpose of engineering quantum technologies.

Appendix A

QD-S and splitter effective hamiltonian

This Appendix gives details about the calculation of the effective hamiltonian for the S-QD system and the splitter device in the large gap limit using a Schrieffer-Wolff transformation $H_S = e^{iS} H e^{-iS}$ (see 1.4). The formula are adapted from [144].

A.1 Schrieffer-Wolff transformation

Using Baker-Hausdorff formula :

$$H_S = H + i[S, H] - \frac{1}{2}[S, [S, H]] + \dots \quad (\text{A.1})$$

writing the total hamiltonian $H = H_0 + H_t$ and choosing S linear in t yields :

$$H_S = H_0 + \underbrace{H_t + i[S, H_0]}_{\text{first order}} + \underbrace{i[S, H_t] - \frac{1}{2}[S, [S, H_0]]}_{\text{second order}} + \mathcal{O}(t^3) \quad (\text{A.2})$$

S must be an hermitian operator, which full-fills the cancellation condition :

$$i[S, H_0] = -H_t \quad (\text{A.3})$$

In this case the second order term simplifies so that :

$$H_S = H_0 + \frac{i}{2}[S, H_t] \quad (\text{A.4})$$

A.2 S-QD device

A.2.1 Check of the Schrieffer-Wolff transformation

The S-QD original hamiltonian decomposes as $H = H_0 + H_t$ with:

$$H_0 = H_d + H_{sc} = \epsilon_d \hat{n}_d + \sum_{k,\sigma} E_{k\sigma} \gamma_{k\sigma}^\dagger \gamma_{k\sigma} \quad (\text{A.5})$$

and

$$H_t = t \sum_{k,\sigma} d_\sigma^\dagger c_{k\sigma} + h.c. \quad (\text{A.6})$$

Here we present the calculation which shows that equation A.3 is satisfied by :

$$S = i \sum_{k\sigma} (X_{k\sigma} \gamma_{k\sigma} - h.c.) \quad (\text{A.7})$$

with :

$$\begin{aligned} X_{k\uparrow} &= \frac{tu_k^*}{E_k - \epsilon_d} d_\uparrow^\dagger + \frac{t^* v_k^*}{E_k + \epsilon_d} d_\downarrow \\ X_{k\downarrow} &= \frac{tu_k^*}{E_k - \epsilon_d} d_\downarrow^\dagger - \frac{t^* v_k^*}{E_k + \epsilon_d} d_\uparrow \end{aligned} \quad (\text{A.8})$$

A.3 is equivalent to :

$$\left[\sum_{k\sigma} (X_{k\sigma} \gamma_{k\sigma} - h.c.), H_0 \right] = H_t \quad (\text{A.9})$$

Because

$$\begin{aligned} [X_{k\sigma} \gamma_{k\sigma} - h.c., \hat{n}_d] &= [X_{k\sigma} \gamma_{k\sigma}, \hat{n}_d] + h.c. \\ [X_{k\sigma} \gamma_{k\sigma} - h.c., \gamma_{k'\sigma'}^\dagger \gamma_{k'\sigma'}] &= [X_{k\sigma} \gamma_{k\sigma}, \gamma_{k'\sigma'}^\dagger \gamma_{k'\sigma'}] + h.c. \end{aligned} \quad (\text{A.10})$$

it is enough to calculate $[\sum_{k\sigma} X_{k\sigma} \gamma_{k\sigma}, H_0]$.

$$[X_{k\sigma} \gamma_{k\sigma}, \hat{n}_d] = [X_{k\sigma}, \hat{n}_d] \gamma_{k\sigma} \quad (\text{A.11})$$

$$[X_{k\sigma} \gamma_{k\sigma}, \gamma_{k'\sigma'}^\dagger \gamma_{k'\sigma'}] = X_{k\sigma} \gamma_{k\sigma} \delta_{kk'} \delta_{\sigma\sigma'} \quad (\text{A.12})$$

$$[X_{k\uparrow} \gamma_{k\uparrow}, H_0] = \sum_k (\epsilon_d [X_{k\uparrow}, \hat{n}_d] + E_k X_{k\uparrow}) \gamma_{k\uparrow} = \sum_k (tu_k^* d_\uparrow^\dagger + t^* v_k^* d_\downarrow) \gamma_{k\uparrow} \quad (\text{A.13})$$

$$[X_{k\downarrow} \gamma_{k\downarrow}, H_0] = \sum_k (\epsilon_d [X_{k\downarrow}, \hat{n}_d] + E_k X_{k\downarrow}) \gamma_{k\downarrow} = \sum_k (tu_k^* d_\downarrow^\dagger - t^* v_k^* d_\uparrow) \gamma_{k\downarrow} \quad (\text{A.14})$$

H_t can be rewritten as a function of Bogoliubov operators using :

$$\begin{aligned} c_{k\uparrow} &= u_k^* \gamma_{k\uparrow} + v_k \gamma_{-k\downarrow}^\dagger \\ c_{k\downarrow} &= u_k^* \gamma_{k\downarrow} - v_k \gamma_{-k\uparrow}^\dagger \end{aligned} \quad (\text{A.15})$$

This yields :

$$H_t = \sum_k \left(t u_k^* d_{\uparrow}^\dagger + t^* v_{-k}^* d_{\downarrow} \right) \gamma_{k\uparrow} + \left(t u_k^* d_{\downarrow}^\dagger - t^* v_{-k}^* d_{\uparrow} \right) \gamma_{k\downarrow} + h.c. \quad (\text{A.16})$$

As $v_{-k}^* = v_k^*$ the first term equals A.13 and the second term equals A.14. Equations A.13 and A.16 show that other terms are equal to each other as they are simply hermitian conjugates. Formula A.9 is thus satisfied.

A.2.2 Effective hamiltonian

H_t can be expressed in the following convenient formulation :

$$H_t = \sum_{k\sigma} Y_{k\sigma} \gamma_{k\sigma} + h.c. \quad (\text{A.17})$$

with :

$$\begin{aligned} Y_{k\uparrow} &= t u_k^* d_{\uparrow}^\dagger + t^* v_k^* d_{\downarrow} \\ Y_{k\downarrow} &= t u_k^* d_{\downarrow}^\dagger - t^* v_k^* d_{\uparrow} \end{aligned} \quad (\text{A.18})$$

Using this formulation equation A.4 writes :

$$H_S = H_0 - \frac{1}{2} \left[\underbrace{\sum_{k\sigma} X_{k\sigma} \gamma_{k\sigma}}_A - h.c., \underbrace{\sum_{k'\sigma'} Y_{k'\sigma'} \gamma_{k'\sigma'}}_B + h.c. \right] \quad (\text{A.19})$$

Using $[A - A^\dagger, B + B^\dagger] = [A - A^\dagger, B] + h.c.$ only $[A, B]$ and $[A^\dagger, B]$ need to be calculated. The effective hamiltonian is obtained by projecting H_S onto the subspace where the superconductor is in the BCS ground state. Therefore $[A, B]$ is skipped and $[A^\dagger, B] = -\sum_{k\sigma} Y_{k\sigma} X_{k\sigma}^\dagger$. This results in the following effective hamiltonian for the QD :

$$H_{d,\text{eff}} = H_d - \frac{1}{2} \left(\sum_{k\sigma} Y_{k\sigma} X_{k\sigma}^\dagger + h.c. \right) \quad (\text{A.20})$$

After simplification, this formula yields the expression 1.34 given in the main text.

A.3 Cooper pair splitter

For the Cooper pair splitter, the original hamiltonian decomposes as $H = H_0 + H_t$ with:

$$H_0 = \sum_{i \in L, R} \epsilon_i \hat{n}_i + \sum_{k, \sigma} E_{k\sigma} \gamma_{k\sigma}^\dagger \gamma_{k\sigma} \quad (\text{A.21})$$

and

$$H_t = \sum_{i \in L, R} \left(t_i \sum_{k, \sigma} d_{i, \sigma}^\dagger c_{k\sigma} e^{i\mathbf{k} \cdot \mathbf{r}_i} \right) + h.c. \quad (\text{A.22})$$

The Schrieffer-Wolff transformation operator satisfying equation A.3 is :

$$S = i \sum_{i \in L, R} \sum_{k\sigma} (X_{k\sigma}^i \gamma_{k\sigma} - h.c.) \quad (\text{A.23})$$

with :

$$\begin{aligned} X_{k\uparrow}^i &= \frac{t_i u_k^* e^{i\mathbf{k} \cdot \mathbf{r}_i}}{E_k - \epsilon_i} d_{i, \uparrow}^\dagger + \frac{t_i^* v_k^* e^{-i\mathbf{k} \cdot \mathbf{r}_i}}{E_k + \epsilon_i} d_{i, \downarrow} \\ X_{k\downarrow}^i &= \frac{t_i u_k^* e^{i\mathbf{k} \cdot \mathbf{r}_i}}{E_k - \epsilon_i} d_{i, \downarrow}^\dagger - \frac{t_i^* v_k^* e^{-i\mathbf{k} \cdot \mathbf{r}_i}}{E_k + \epsilon_i} d_{i, \uparrow} \end{aligned} \quad (\text{A.24})$$

Appendix B

Nanofabrication processes

This Appendix gives details about some of the processes developed and used to fabricate our devices as explained in chapter 3. Not everything is reported but the main processes are here and can be recombined for a different goal. Some parameters are machine-dependent and should be adapted for a different tool. In the following, a is the aperture of the SEM beam; EHT is the acceleration voltage of the SEM; WF is the SEM write-field; U and V are coordinates on the SEM; US stands for ultrasonics. One layer of PMMA is baked for 15min at 165°C and is about 500nm thick.

B.1 CPSRES fabrication roadmap

***SiO₂* Sample cleaning**

5min acetone US bath

5min acetone US bath

5min IPA US bath

Alignment crosses + sample number + contacting pads lithography

lithography time (including settings): 30min/chip

deposition : Ti (5nm)/Au(40nm)

lift-off : 1-2min in warm acetone + pipette

cleaning 2min stripping RIE

Nb cavity fabrication (evaporation, positive optical lithography, RIE, cleaning)

NT Fake Stamping in cavity

NT Localisation

Coupling top gates

fine litho : layer 4

deposition :

e = 15 Angstrom Al (3s at 5 Angst/s) ;10 min oxidation

e = 15 Angstrom Al ;10 min oxidation

e = 15 Angstrom Al ;10 min oxidation

Al : e = 400 Angstrom

Pd : e = 200 Angstrom

lift-off : difficult ! 20 min in warm acetone+pipette+needle

Superconducting contact

fine litho : layer 3

deposition :

Pd : e = 40 Angstrom

Al : e = 840 Angstrom (meant to be 100nm)

lift off : 5 to 10 min in warm acetone + pipette

Normal metallic electrodes

fine lithography : layer 2

deposition : Pd : e = 700 Angstrom

lift off : 2 min in warm acetone + pipette

B.2 Quartz stamps with CNT fabrication**B.2.1 Pillar fabrication**

Detach quartz substates from wafer from inner to outer to avoid damage.

Scratch the letter F on the backside with the scribe to able further substrate orientation.

Cleaning :

5 min acetone US

5 min acetone US

5 min IPA US

1 min stripping RIE

Electronic lithography :

spin-coating : double layer PMMA 550

15nm Aluminium deposition (to avoid charging)

lithography:

- settings a=10 μ m : measure current, origin correction, angle correction, WF alignment

(100 μm x 100 μm)

- mask Quartz-wafer : layer 6 ; (U=0,05 μm ;V=0,05 μm) ; step=20nm

remove Aluminium : 1min30 KOH ; 1 min in water

development : 2min MIBK ; 30s IPA

Ni deposition : 2500 Angstrom

lift-off : 1min in warm acetone + needle + 30s US + needle ; rinse 30s in IPA

Etching : 3*30 min in RIE : prog SiO₂ (O₂+CHF₃)

Ni chemical etching by FeCl₃ :

1min FeCl₃

30s water (big becher)

2 min in water (second big becher)

5 min in water US (small becher)

Pillars are 4,2 μm high.

B.2.2 CNT growth

Carbon nanotubes are grown on the patterned quartz substrates by Chemical Vapour Deposition. This technique requires a catalyst. The whole recipe is designed to obtain single walled carbon nanotubes. The catalyst composition is 39mg $Fe(NO_3)_3 - 9 H_2O$, 7.9mg MoO_2 and 32mg of Al_2O_3 nanoparticles diluted in 30mL of IPA. Prior deposition the catalyst flask has to be agitated with ultrasound for one hour to split molecules aggregates. After 45 minutes decantation only nanoparticles remain at the liquid surface. Two drops of catalyst are put on the chip, and dried with nitrogen flow immediately after the second one. Once catalyst is deposited, the quartz chips are placed in a special furnace dedicated to nanotubes Chemical Vapour Deposition. This furnace is a long quartz tube, in which 3 gases are injected : argon Ar (1450 sccm), dihydrogen H_2 (200 sccm) and methane CH_4 (1140 sccm). The process is the following :

- 5 min purge of the three gases
- heating under argon to obtain a 900°C temperature
- 8 min dihydrogen
- 10 min dihydrogen and methane (growth step)
- 90 min cooling under dihydrogen and argon
- final cooling under argon

B.3 Nb cavity fabrication

150nm Nb **evaporation** with evaporator cooled with nitrogen

Positive optical lithography :

mask cleaning : 10min acetone US, 10min IPA US

spin-coating : resin AZ5214 with program 1 (4000-4000-30s)

baking 1min30 at 110C

exposure 8s : mask CPSRES T-geometry (capa 100 μ m) resonator number 1

development 35s in MIF developer ; rinse 1min in water

If RF pad is shinted, scratch the resist using the needle and rince under water flow (2min) until there are no dust in resonator gaps any more.

Etching (RIE) :

open SF6 valve

switch laser on and put the spot in the gap where the device will stand.

Wait until penning pressure 10nbar

parameters : EDP range = [0;7]V

Program Nb : RUN

prepare Go to > Purge

Look at EDP signal : it is flat, then it drops and when the etching is completed the slope changes (either decreases or stabilizes or rises). Wait 10s after the etching end and click on confirm to stop.

After the 2 purges, vent

close SF6 valve

Lift-off

30s agitation in first warm acetone bath

30s agitation in second warm acetone bath and 2min needle

30s rincing in IPA

Cleaning :

Stripping(RIE) : 3min

if remaining dust : 10s acetone US ; rinse with IPA

B.4 CNT stamping

Clean glass slab

5 min acetone US bath

5 min IPA US bath

Glue quartz stamp on glass slab

Use white double-sided tape.

Stick a piece of tape in the middle of the slab on the whole slab's length.

Remove the protection on the top using a scalpel.

Drop the quartz stamp on the tape

Fake stamping on the optical masker

Switch the UV lamp OFF before switching the optical masker ON.

Set the Mode : Align and expose

Arrange the glass slab on the holder so that stamp and sample are roughly aligned.

Quarter by quarter or half by half stamping can be performed.

Find the pillars.

Lift the lever to move sample closer to stamp. Turn UP to have a reasonable focus on both sample and stamp surfaces.

Perform fine alignment.

Turn the z knob to UP to stamp : *you should see interferences in the pillars that is alternation of green and pink colour. At some point, colour saturates to dark green and pillar edges are thick and black. STOP ! It may happen that pillars get crashed.*

Turn the z knob down. Pull the lever down.

When you switch the aligner off you can skip the cooling time by turning the red button (left) OFF and ON and switch the lamp back ON for the next person.

Cleaning

Detach quartz stamp from tape by sliding a thin and flexible shade in-between. This may be destructive.

Remove tape.

Clean glass slide if necessary (tape residues) :

5 min acetone US bath

5 min IPA US bath

Appendix C

Photon number evaluation

This Appendix gives details about how we estimate the bare cavity photon number at resonance $n_0 \equiv \langle \hat{a}^\dagger \hat{a} \rangle_{\omega=\omega_c}$ (see chapter 5 and 6).

All transmission are given at $f = 6.648GHz \approx f_c$. S_{21} refers to the transmission coefficient of the measured element. It can be measured directly with a vectorial network analyser (VNA).

C.1 Input power P_{in} calibration

C.1.1 Conversion loss measurement

The RF power going out the mixer is controlled by the IF voltage V_{IF} .

$$P_{RF} = P_{IF} - CL$$

The conversion loss CL has been calibrated by measuring the output power of the mixer using a power meter. There was a discrete attenuation A and a small flexible cable of estimated attenuation -0.5 dB in-between the mixer and the power meter. The measured power is related to the CL by the following formula :

$$P_{powermeter} = P_{IF} - CL + A + cable\ att$$

From measurements shown in table C.1.1 we deduce :

$$CL = 7\text{ dB}$$

V_{IF} (V)	P_{IF} (dBm)	A (dB)	cable att (dB)	$P_{\text{powermeter}}$ (dBm)	CL (dB)	comment
0.2	-0.97	-40	-0.5	-49	7.5	
0.2	-0.97	0	-0.5	-8.7	7.2	
0.1	-7	0	-0.5	-14.5	7	
0.002	-41	0	-0.5	-29	-12	noise dominates
0.02	-21	0	-0.5	-26	4.5	noise starts to dominate

FIGURE C.1: conversion loss measurement table

C.1.2 Cable calibration

C.1.2.1 Room temperature cable

From data sheet of green Radiall 1m cable R286301073 :

$$S_{21}(\text{RT cable, in}) = -0.9 \text{ dB}$$

C.1.2.2 Cryogenic cavity input line transmission

The transmission of line 5 (cavity input line) is measured from cryostat head down to tube input at room temperature.

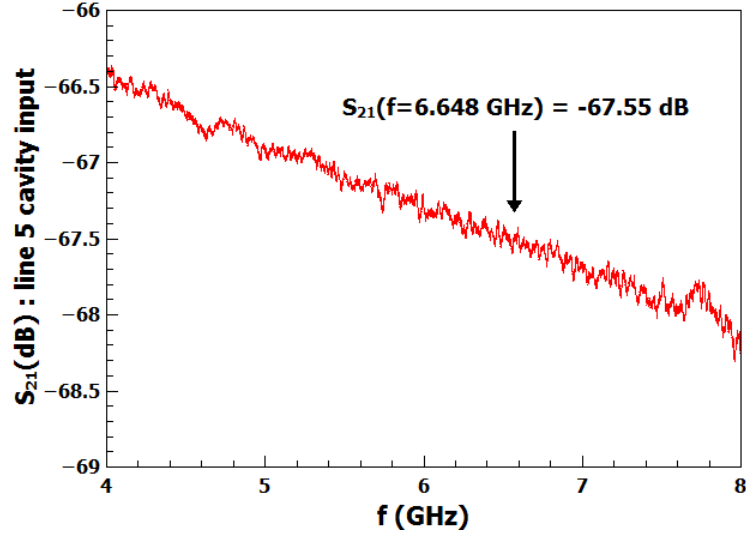


FIGURE C.2: room temperature transmission of cavity input line measured with the VNA

The transmission of the flexible cable going from the tube entry to the sample holder cavity input port (figure C.3) has to be added to obtain the global attenuation from cryostat input to sample holder input port. Thus the global input line attenuation is :

$$S_{21}(\text{cryo line, in}) = -68.1 \text{ dB}$$

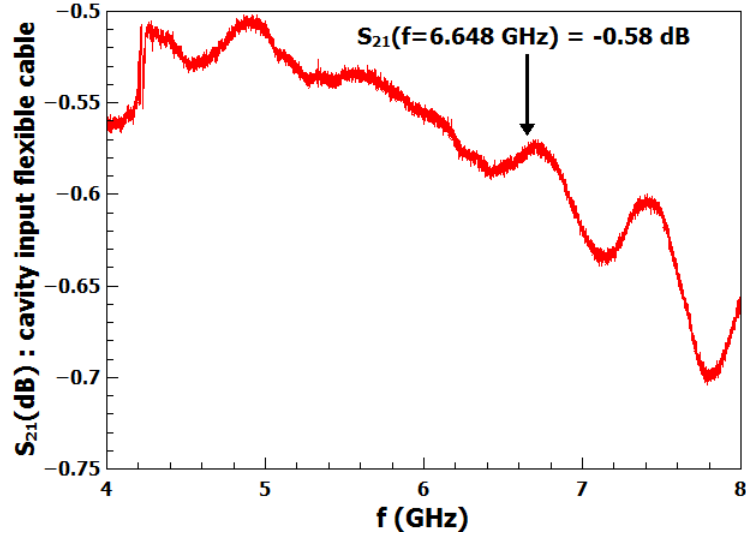


FIGURE C.3: room temperature transmission of the flexible cable cavity input line measured with the VNA

C.1.3 Conclusion

The sample holder input power P_{in} in dBm is given by the following formula :

$$P_{in} = P_{IF} - CL + A + S_{21}(\text{RT cable, in}) + S_{21}(\text{cryo line, in})$$

Fixed parameters

$$CL = 7 \text{ dB cf C.1.1}$$

$$S_{21}(\text{RT cable, in}) = -0.9 \text{ dB cf C.1.2.1}$$

$$S_{21}(\text{cryo line, in}) = -68.1 \text{ dB cf C.1.2.2}$$

variable parameters

$$P_{IF} = 10 \log_{10} \left(\frac{V_{IF}^2}{50 * 10^{-3}} \right) \text{ with } V_{IF} \text{ the oscillator rms voltage (V) on the quadrature I LockIn.}$$

A is the discrete attenuation (dB, negative value) placed at the mixer output.

C.2 Output power P_{out} calibration

C.2.1 Output transmission calibration

C.2.1.1 Cryogenic cavity output line transmission

Following the output line upwards one finds 2 copper semi-rigid cables, two shielded circulators, a copper semi-rigid cable, a dissipationless NbTi cable, a cryogenic amplifier, a flexible cable and 2 CuBe cables.

From sample holder to cryogenic amplifier Figures C.4, C.5, C.6, C.7 show the transmission of the 4 elements between the sample holder and the cryogenic amplifier. The resulting transmission of this part is :

$$S_{21}(\text{MC} - 4\text{K}, \text{out}) = -1.9 \text{ dB}$$

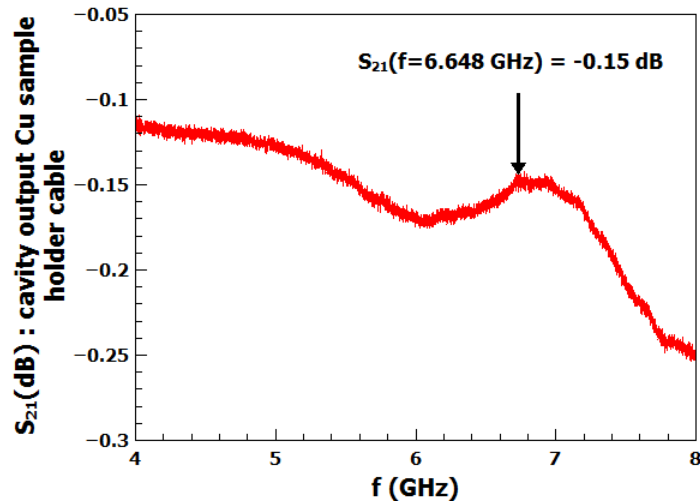


FIGURE C.4: room temperature transmission of the Cu sample holder cavity output cable measured with the VNA

From cryogenic amplifier to cryostat head To check that the amplifier works at cryogenic temperature, we measured with the VNA the transmission of the input line section from 300K to 4K connected via a flexible cable to the output line section from 4K to 300K (including the amplifier).

$$S_{21, meas} = A + S_{21}(300 - 4\text{K}, in) + S_{21}(cable) + S_{21}(4 - 300\text{K}, out)$$

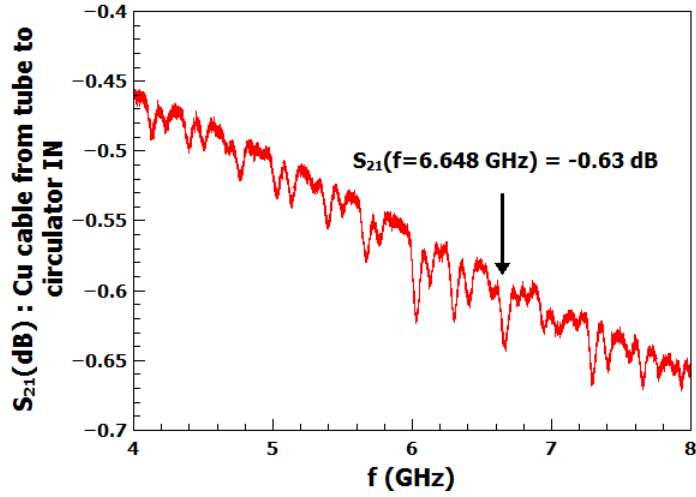


FIGURE C.5: room temperature transmission of the Cu cable from tube to circulator input measured with the VNA

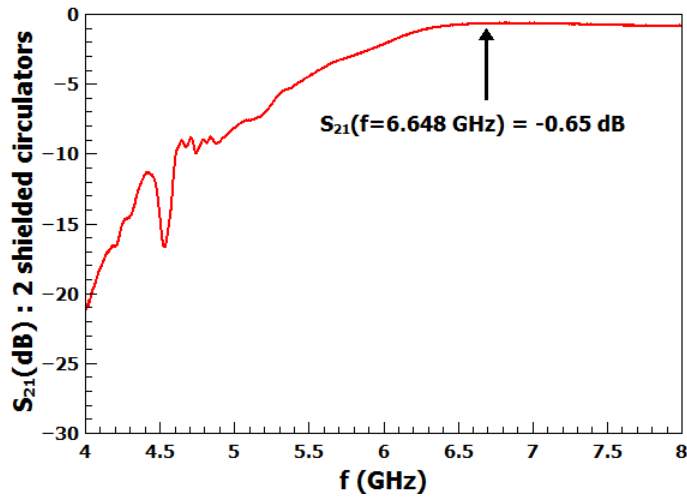


FIGURE C.6: room temperature transmission of the 2 shielded circulators measured with the VNA

$A = -40 \text{ dB}$ is a discrete attenuator added to work in the amplifier linear regime.

$S_{21}(\text{cable}) \approx -0.5 \text{ dB}$ (estimation from similar cable measurement)

$S_{21}(300 - 4\text{K}, \text{in}) = -25.1 \text{ dB}$ from room temperature transmission measurement (see figure C.9) of fast gate lines 300-4K section which are identical to the input line 300-4K section.

From that we deduce the 300-4K output line transmission :

$$S_{21}(4 - 300\text{K}, \text{out}) = 33.1 \text{ dB}$$

The transmission of the global output line in the cryostat results in :

$$S_{21}(\text{cryo line}, \text{out}) = (\text{MC} - 4\text{K}, \text{out}) + (4 - 300\text{K}, \text{out}) = -1.9 + 33.1 = 31.2 \text{ dB}$$

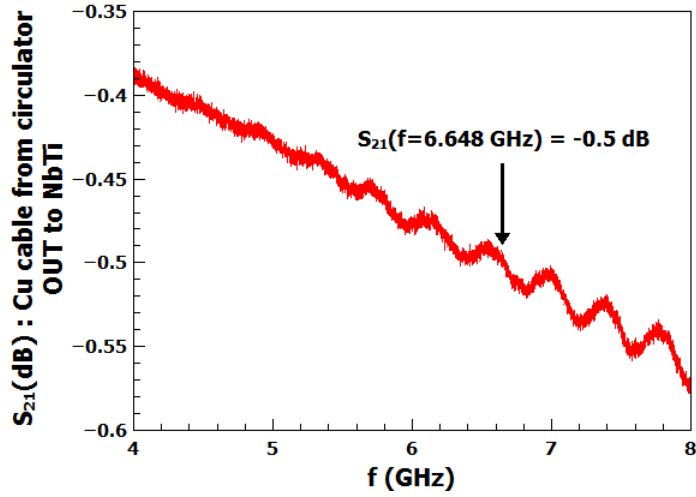


FIGURE C.7: room temperature transmission of the Cu cable from circulator output to NbTi cable measured with the VNA

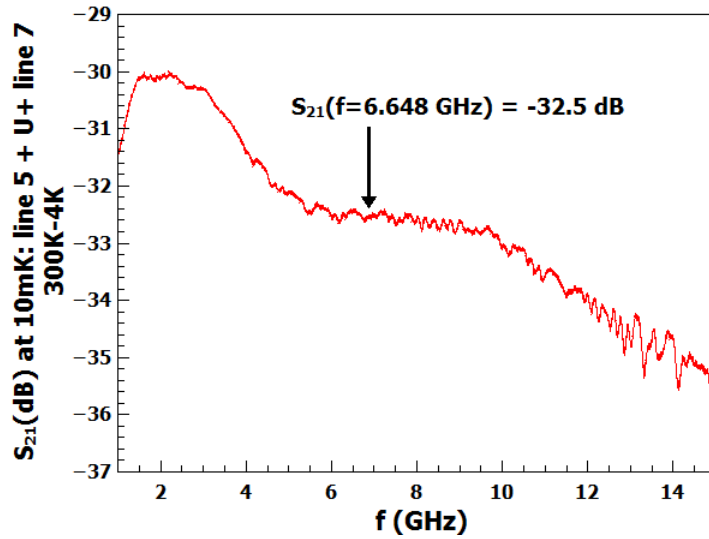


FIGURE C.8: Transmission at 10mK of the 300K-4K sections of the input and output lines connected via a flexible cable

C.2.1.2 Room temperature cable transmission

Like in C.1.2.1 from data sheet of green Radiall 1m cable R286301073 :

$$S_{21} (RT \text{ cable}, out) = -0.9 \text{ dB}$$

C.2.2 RF table transmission

The RF table transmission is calibrated by linking the mixer output to the amplifier input using a small flexible cable and a discrete attenuator of known attenuation A (dB).

The measured output power is : $P_{out,meas} = 10 \log_{10} \left(\frac{amplitude^2}{50 * 10^{-3}} \right)$ with $amplitude =$

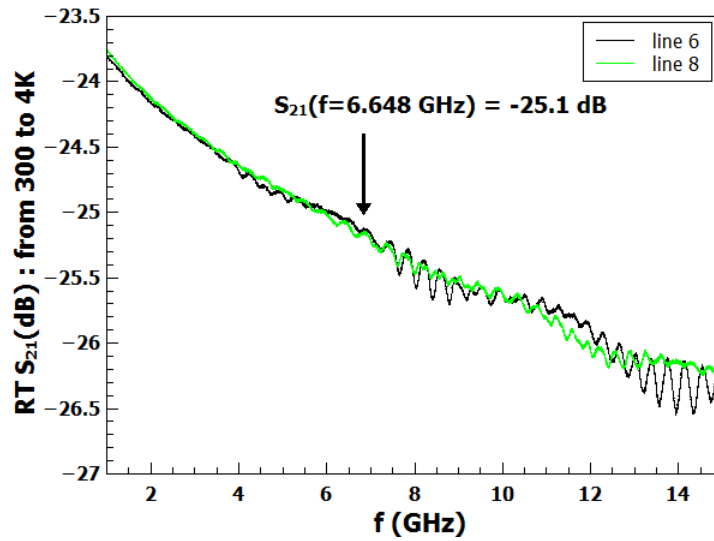


FIGURE C.9: Transmission at room temperature of the 300K-4K sections of fast gate lines representative for the input line 300-4K transmission

$$\sqrt{I^2 + Q^2}.$$

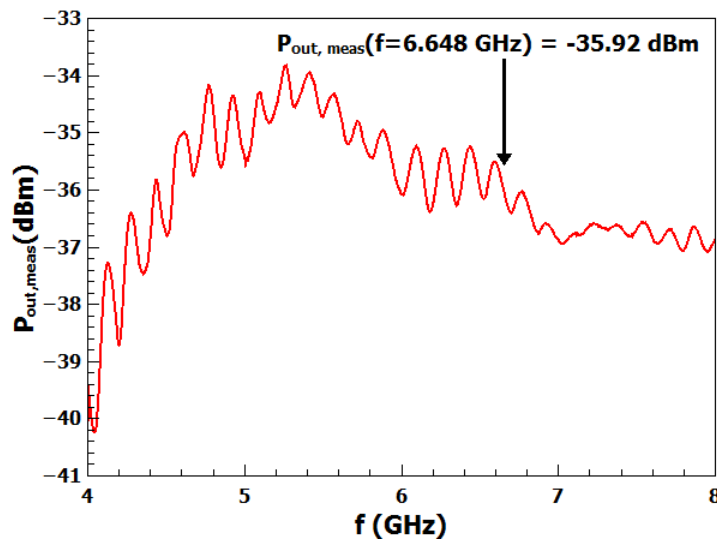


FIGURE C.10: Calibration of RF table transmission

It is related to the table transmission as follows :

$$P_{out, meas} = P_{IF} - CL + A + S_{21}(cable) + S_{21}(RF\ table)$$

With $V_{IF} = 0.2V$ and $A = -90\ dB$, we measure $P_{out, meas} = -35.9\ dB$ (see figure C.10). Knowing $CL = 7\ dB$ and $S_{21}(cable) = -0.5\ dB$ (see figure C.11), one deduces :

$$S_{21}(RF\ table) = 62.6\ dB$$

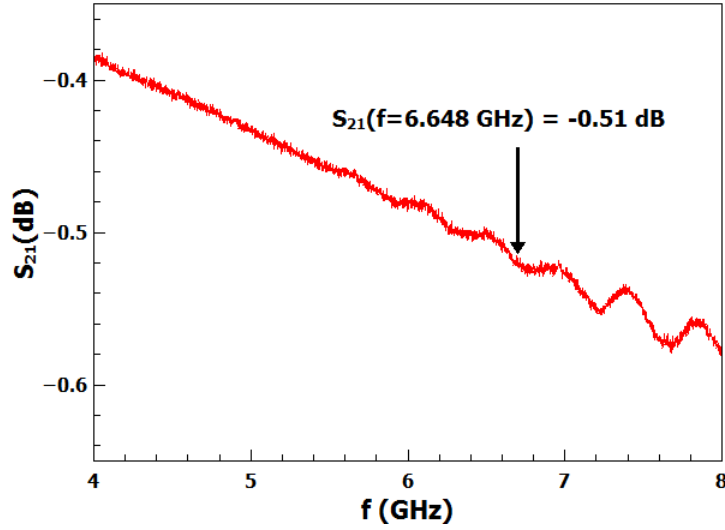


FIGURE C.11: Transmission of cable used for RF table calibration

C.2.3 Conclusion

From measured amplitude (V) the sample output power (dBm) is calculated as follows :

$$P_{\text{out}} = P_{\text{out,meas}} - S_{21}(\text{RF table}) - S_{21}(\text{RT cable, out}) - S_{21}(\text{cryo line, out})$$

Measurement

$$P_{\text{out,meas}} = 10 \log_{10} \left(\frac{\text{amplitude}^2}{50 * 10^{-3}} \right)$$

$$\text{amplitude} = \sqrt{I^2 + Q^2}$$

Fixed parameters

$$S_{21}(\text{RT cable, out}) = -0.9 \text{ dB } \text{C.2.1.2}$$

$$S_{21}(\text{RF table}) = 62.6 \text{ dB } \text{C.2.2}$$

$$S_{21}(\text{cryo line, out}) = 31.2 \text{ dB } \text{C.2.1.1}$$

C.3 Photon number

The average photon number in the cavity is computed from the input and output power of the cavity expressed in W and the cavity resonance parameters :

$$n = \frac{\sqrt{P_{\text{in}} P_{\text{out}}}}{h f_c \pi \Delta f_{-3\text{dB}}}$$

with f_c the bare resonance frequency of the cavity and Δf_{-3dB} the resonance width at half maximum. Relevant parameters for sample CPSRES32R measurement are presented on figure C.12.

meas period	V-IF(V)	DiscAtt (dB)	sweep number	f0(MHz)	lambda0 (MHz)	A(V)	Q	Pin (dBm)	Pout (dBm)	S21 (dB)	n
1	0.2	-20	4	6,648.055	0.2105	0.07665	15,791	-97	-102.2	-5.2	18,905.5
1 before B	0.2	-40	4	6,648.08075	0.25875	0.0060325	12,847	-117	-124.3	-7.3	121
1 after B	0.2	-40	1	6,643.789	0.294	0.00479	11,299	-117	-126.3	-9.3	84.6
2	0.2	-40	2	6,647.9665	0.2735	0.005555	12,154	-117	-125	-8	105.5
3	0.2	-40	1	6,648.039	0.276	0.005244	12,044	-117	-125.5	-8.5	98.6
1	0.056	-40	1	6,648.085	0.284	0.00155	11,704	-128	-136.1	-8.1	7.9
3	0.056	-40	1	6,648.042	0.302	0.001347	11,007	-128	-137.3	-9.3	6.5
3	0.2	-50	2	6,648.0235	0.268	0.0015345	12,403	-127	-136.2	-9.2	9.4
3	0.056	-50	1	6,648.045	0.325	0.000409	10,228	-138	-147.7	-9.6	0.6

FIGURE C.12: Photon number and cavity parameters table for various measurement parameters applied to CPSRES32R

Appendix D

Supplementary materials on AC Kondo

This Appendix gives details about the experiment presented in chapter 4.

D.1 Raw data description

The AC response of a thin Kondo peak ($T_K \approx 30\mu eV$) was studied during a first measurement run. This corresponds to data files 0 to 6 ; 13 to 16 ; 18 and 19 in the table presented in figure D.1. From these files 5189 sets of $(f, V_{AC,source}, G)$ on the Kondo resonance have been extracted and used for the analysis. After a thermal cycling the sample displayed a thick Kondo peak ($T_K \approx 95\mu eV$). 189 data points were extracted from files 9 and 12 and used in the analysis.

Data types are explicitly indicated by the file name. They are three fold. Grayscale f2-Vac are measurements on the Kondo resonance peak, where the frequency is the sweeping loop, while the excitation voltage is the incremental loop. GrayscaleVgf2OnOff are gate sweeps for different frequencies at constant V_{AC} , the RF power being successively switched ON and OFF between sweeps. Multigrayscale-VsdP2-f2 are three loops measurements with the excitation frequency as external loop, the excitation voltage or power as intermediate loop and the bias voltage as internal loop.

D.2 Power calibration and frequency set

Frequency sets and calibration coefficients differ between thick and thin peaks because of thermal cycling. Calibration of the thin peak frequencies was obtained by combining

Filename	#	T_K (μeV)	G_{BG} ($2e^2/h$)	G_{OFF} ($2e^2/h$)	x_c (mV)	std-Tk	std-GBG	std-GOff	std-xc
20140905_grayscalef2Vac_powercal_005_av10_averaged	0	24.6	0.138	0.2	0.127	0	0	0	0
20140908_grayscalef2Vac_powercal_003_av50_averaged	1	29.7	0.16	0.266	0.132	0	0	0	0
20140910_grayscalef2Vac_powercal_001_av500_averaged	2	30.8	0.164	0.256	0.128	0	0	0	0
20140912_grayscalef2Vac_powercal_001_av250_averaged	3	33.3	0.156	0.266	0.122	0	0	0	0
20140915_grayscalef2Vac_powercal_001_av100_averaged	4	33.1	0.156	0.274	0.127	0	0	0	0
20140916_grayscalef2Vac_powercal_001_localav40	5	32.7	0.159	0.281	0.128	0	0	0	0
20140916_grayscalef2Vac_powercal_002_localav40	6	32.7	0.159	0.281	0.128	0	0	0	0
20141001_grayscalef2VacOnOff_powercal_001_localav5_av1	9	95	0.196	0.229	0.118	0	0	0	0
20141002_grayscaleVgf2OnOff_002_6av	12	95		0.229	0.118	0	0	0	0
20140829_multigrayscale005_VsdP2_f2	13	28.9	0.136	0.193	0.124	0.6	0.003	0.001	0.003
20140829_multigrayscale003_VsdP2_f2	14	21.8	0.169	0.265	0.124	0.9	0.01	0.005	0.001
20140901_multigrayscale001_VsdP2_f2	15	29	0.141	0.194	0.126	0.3	0.003	0.004	0.004
20140901_multigrayscale002_VsdP2_f2	16	29.6	0.145	0.193	0.123				
20140904_multigrayscale001_VsdP2_f2_powercal	18	28.2	0.134	0.195	0.123	0.4	0.0005	0.002	0.0006
20140905_multigrayscale001_VsdP2_f2_powercal	19	29.9	0.138	0.215	0.12	2	0.01	0.03	0.002

FIGURE D.1: Table of Kondo equilibrium parameters associated with each data file.

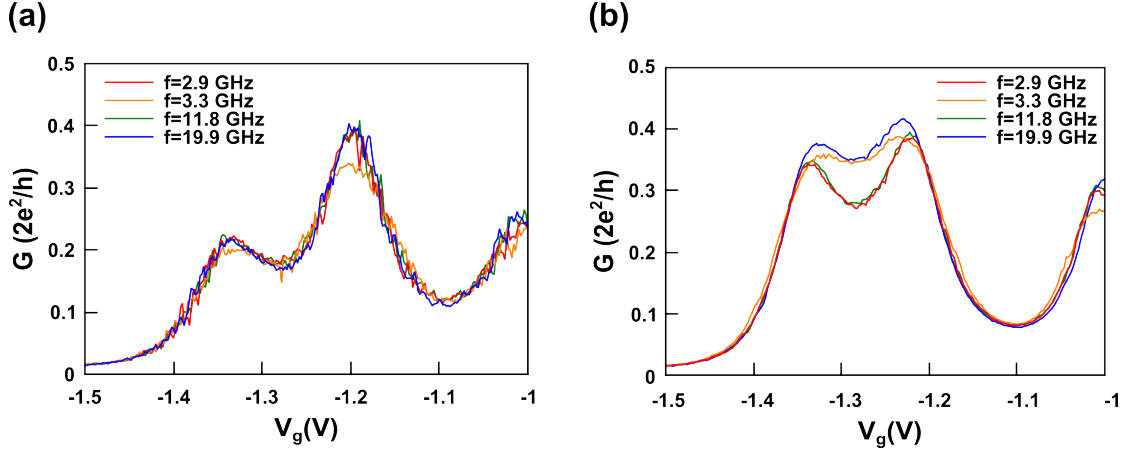


FIGURE D.2: **Selection of frequencies with gate-independent calibration.** (a) Conductance measurement at finite bias ($V_{SD} = 203 \mu V$) and under AC excitation $V_{AC} = 100 \mu V$. Curves at $f=2.9$, 11.8 and 19.9 GHz superpose at all gate voltages, while the $f=3.3$ GHz does not. (b) Conductance measurement at zero bias under AC excitation ($V_{AC} = 100 \mu V$) for the same frequencies.

absolute calibration and relative calibration methods described in the main text. The resulting $c(f)$ plotted on figure 4.4 are on the same order of magnitude. This is because they have been preselected to be, otherwise relative powers may vary over tens of dB. We make this pre-selection to get a similar power range for all frequencies from the 43dB dynamic power range of our microwave source.

Once calibration is done, we study its gate dependence. We measure the conductance as a function of gate voltage successively with excitation ON ($V_{AC} = 100 \mu V$) and OFF. This is done at finite bias $V_{SD} = 203 \mu V$ for all calibrated frequencies. As expected the curves coincide at $V_g = -1.095 V$, where calibration was performed. We keep only frequencies, which curves superpose entirely. For example we observe on figure D.2a that frequencies 2.9, 11.8 and 19.9 GHz match well at all gate voltages, while 3.3 GHz does not. As a result 3.3 GHz is excluded from the study of AC Kondo. In the post-processing of the thin peak data set, 25 frequencies were excluded starting from 86 frequencies. For the wide peak, 22 frequencies out of 59 were excluded. Frequencies remaining after this procedure correspond to an AC excitation mainly applied on the dot bias voltage. When current rectification is gate-dependent, the AC excitation very likely also applies to the dot energy level. Kaminski et al [63] predicted an opposite frequency-dependence of the AC Kondo conductance with this kind of coupling, compared to coupling to bias. G_{ON}/G_{OFF} is predicted to be decreasing with frequency instead to be increasing with frequency, as we measured. Figure D.2b shows that the Kondo conductance at 3.3 GHz is higher than at 2.9 GHz and 11.8 GHz, which is consistent with microwaves partly coupling to the gate. However we chose not to study this mixed coupling regime, as it is not easy to quantify couplings to bias and to gate separately.

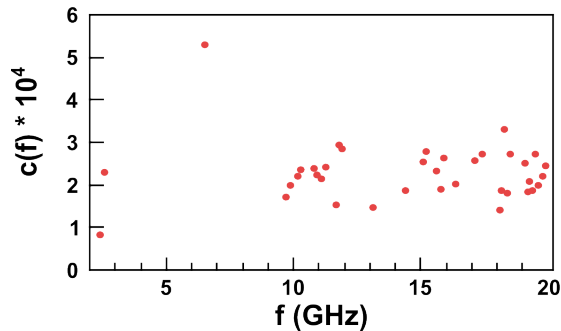


FIGURE D.3: **Calibration coefficients $c(f)$ for the measurement run of the wide peak data.**

For the wide Kondo peak calibration was performed by iterating a relative calibration obtained on thin peak. The frequency selection procedure was done. The resulting coefficients $c(f)$ are plotted on figure D.3. The thermal cycling did not change absolute calibration but relative calibration and coupling mode were modified, possibly because wire bonds moved.

D.3 Data extraction and scaling

Grayscale f2-Vac

The Kondo resonance at equilibrium is measured and fitted to obtain G_{BG} , G_{OFF} and T_K . V_{SD} and V_g are fixed on the Kondo peak during the measurement as a function of excitation frequency and amplitude. Normalization of the conductance G and scaling of f and V_{AC} are done as explained in section 4.3.2.

GrayscaleVgf2OnOff

From this measurement we extract the Kondo conductance with and without microwave excitation for each frequency. As the Kondo resonance conductance at equilibrium shifts slightly over time, we assume that the background conductance varies between sweeps, while G_{OFF} is taken constant. We use the G_{OFF} value extracted from the fit done before measurement and the measured $G_{BG}(F)$ to calculate the normalized conductance from 4.6.

Multigrayscale-VsdP2-f2

Here the equilibrium Kondo parameters are obtained for each frequency by fitting the conductance versus V_{SD} measured at the lowest excitation amplitude, provided that

$\min(V_{AC}) < 15\mu V$. This is justified by the observation that excitation amplitudes below this threshold do not affect the Kondo conductance compared to equilibrium. The conductance values on the Kondo peak are extracted by filtering the points with V_{SD} closest to the Lorentzian center fitting parameter x_c . G_{ON}/G_{OFF} , F and V are calculated with the specific fitting parameters found for the corresponding frequency. Values tabulated in the table shown on figure D.1 are averaged quantities, with standard deviation indicated in other columns.

Appendix E

Supplementary materials on charge relaxation

This Appendix gives details about the experiment presented in chapter 5.

E.1 Experimental supplementary

Although the sample CPSRES32R was designed as a Cooper pair splitter, in the parameter range of chapter 5, it behaves as a single dot connected to normal and superconducting leads. This is indicated by E.1, where current and phase colour plots as a function of left and right gate voltages show parallel lines.

In order to demonstrate further the quantitative agreement between our theoretical approach and the data, we present supplementary data together with their theoretical modelling. Figure E.2 shows the cavity signals $\Delta\varphi$ and ΔA at $V_b = 0$ for 11 different quantum

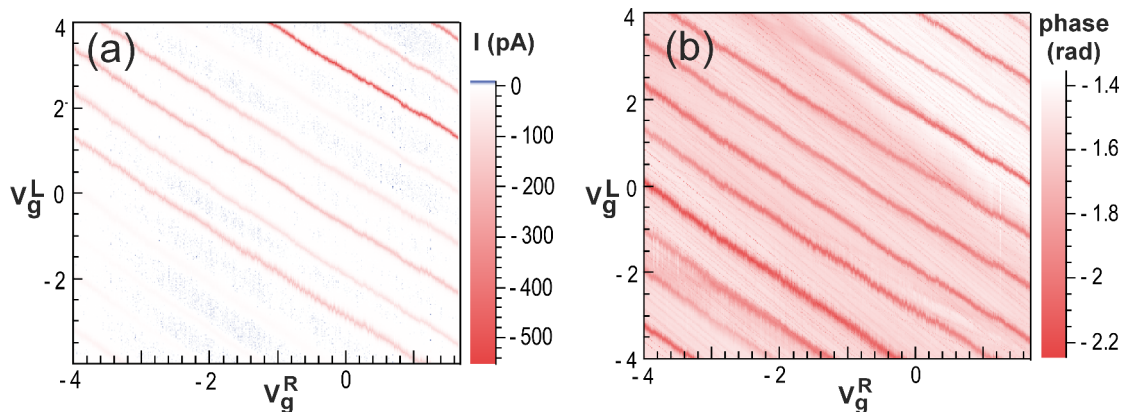


FIGURE E.1: Current I through the quantum dot (a) and phase cavity signal φ (b) versus V_g^L and V_g^R corresponding to the data of figure 5.3c and d.

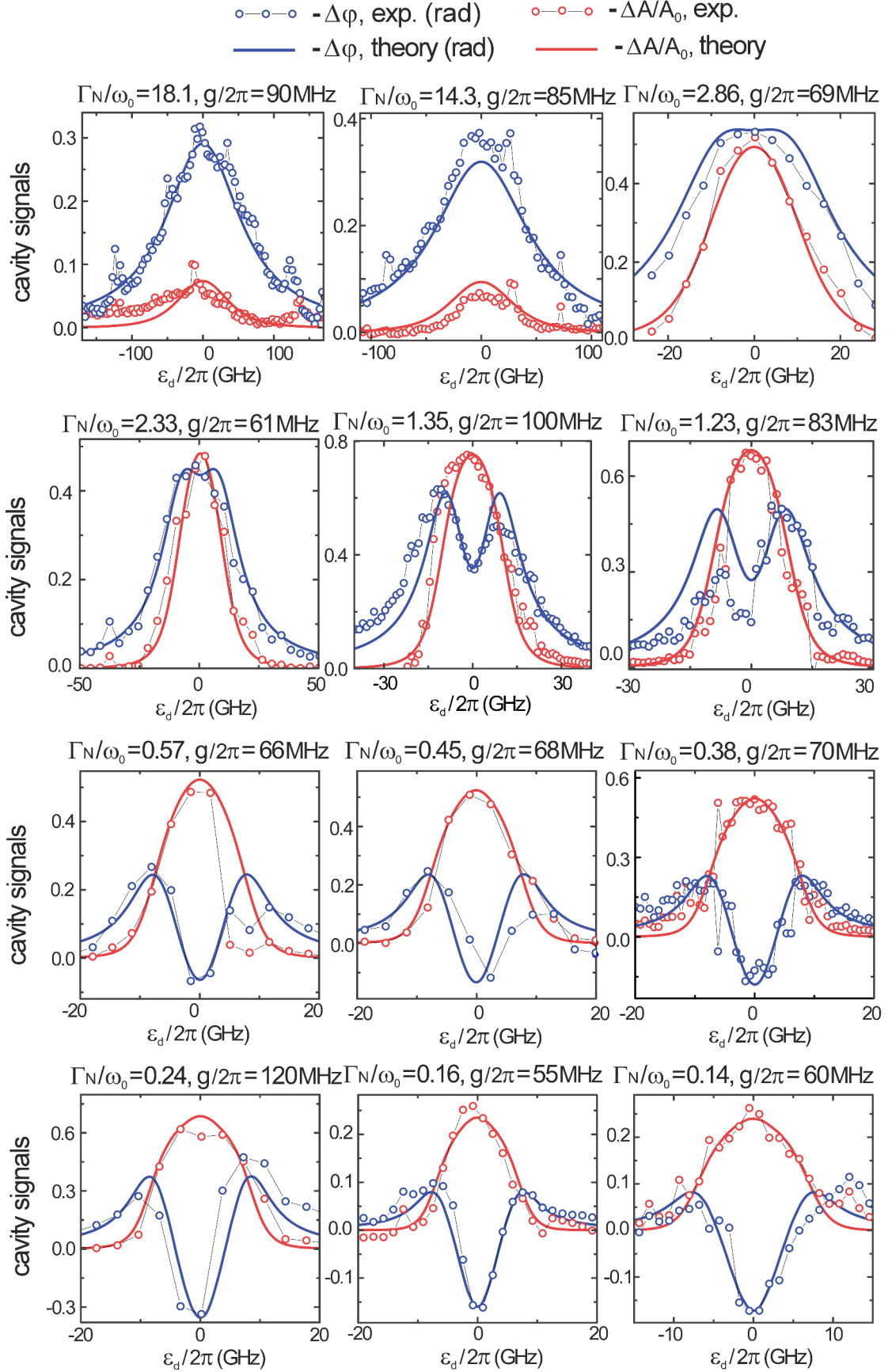


FIGURE E.2: Cavity signals $\Delta\varphi$ (blue dots) and $\Delta A/A_0$ (red dots) versus ε_d for $V_b = 0$. The red and blue lines show the predictions given by equations 5.2 and 5.3 for the values of Γ_N and g given in the different panels and $T = 60$ mK. When a resonance is shown in the main text, we indicate the corresponding figure number in purple.

dot/reservoir resonances, including those of figures 5.2 and 5.3 for completeness. Near each dot/reservoir resonance, we calibrate the bare cavity linewidth $\Lambda_0 \sim 2\pi \times 0.26$ MHz and the bare cavity transmission amplitude $A_0 \sim 6.1$ mV. For the 11 resonances studied, the dot/photon coupling g varies from $2\pi \times 55$ MHz to $2\pi \times 120$ MHz and the tunnel rate Γ_N from $2\pi \times 0.9$ GHz to $2\pi \times 120$ GHz. The average photon number $\langle n \rangle$ in our measurements is estimated from setup transmission calibration. Assuming a 6dB uncertainty we obtain a lower bound $\langle n \rangle > 20$ which ensures the validity of the semi-classical approximation used in our theory. The agreement between our theory and data also confirms that we remain in the linear response regime. Otherwise, the width of the resonances in the cavity response would not match with the theory. Figure E.3 shows the dot conductance and cavity signals, for different values of V_b , on a wider V_g -scale than in figure 5.5.

E.2 Theoretical supplementary

E.2.1 Hamiltonian of the quantum dot circuit

In chapter 5, we use $\hbar = 1$ and define most scales as pulsations. To model the behaviour of our setup, we use the total Hamiltonian 2.22, with

$$\begin{aligned}
 H_{dot} = & \sum_{\sigma} \varepsilon_d \hat{d}_{\sigma}^{\dagger} \hat{d}_{\sigma} + \Delta \sum_k \left(\hat{c}_{k\uparrow}^{S\dagger} \hat{c}_{-k\downarrow}^{S\dagger} + H.c. \right) \\
 & + \sum_{O \in \{S, N\}, k, \sigma} \left(\varepsilon_k^O \hat{c}_{k\sigma}^{O\dagger} \hat{c}_{k\sigma}^O + (t_O \hat{d}_{\sigma}^{\dagger} \hat{c}_{k\sigma}^O + H.c.) \right) \\
 & + \sum_{k, k', \sigma} \left(\varepsilon_{kk'}^n \hat{b}_{kk'\sigma}^{n\dagger} \hat{b}_{kk'\sigma}^n + (t_n \hat{b}_{kk'\sigma}^{n\dagger} \hat{c}_{k\sigma}^S + H.c.) \right)
 \end{aligned} \tag{E.1}$$

the Hamiltonian of a single quantum dot contacted to a N and a S contact. Above $\hat{d}_{\sigma}^{\dagger}$ [$\hat{c}_{k\sigma}^{O\dagger}$] creates an electron with spin σ in the orbital with energy ε_d [ε_k^O] of the dot [reservoir $O \in \{S, N\}$]. To account for the broadening of the BCS peaks in the density of states of S, we use an auxiliary reservoir n whose states can be populated by the operators $\hat{b}_{kk'\sigma}^{n\dagger}$. For simplicity, each level $k\sigma$ of S is coupled to an independent set $kk'\sigma$ of levels in n . We assume that a bias voltage V_b is applied to the N contact whereas the S contact is grounded. For simplicity, we disregard Coulomb interactions in the whole Appendix E.2.

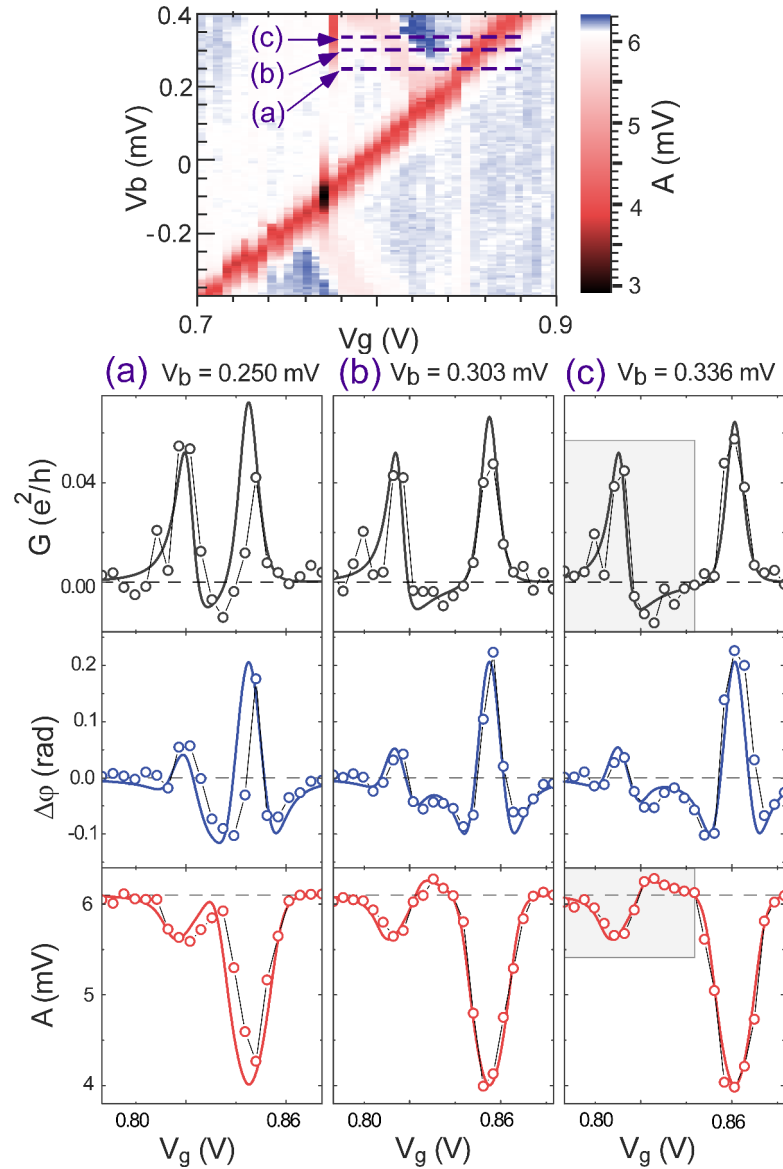


FIGURE E.3: Top panel: Measured amplitude A versus V_b and V_g , already shown in figure 5.4,c. Bottom panels: Measured conductance G (black dots), and cavity signals $\Delta\varphi$ (blue dots) and A (red dots) versus V_g , along the dashed lines in the top panel, for $V_b = 0.25, 0.303$, and 0.336 mV from left to right. The full red, blue and black lines show the predictions given by equations E.2, 5.3 and E.12, for the same parameters as in figure 5.4. The areas in the gray rectangles are enlarged in figure 5.5 of the main text.

E.2.2 Keldysh description of the quantum dot circuit

The quantum dot charge susceptibility $\chi(\omega)$ can be calculated within the time-dependent Keldysh formalism [145] as :

$$\chi^*(\omega) = -i \int \frac{d\omega}{2\pi} \text{Tr} [\check{S}(\omega) \check{G}^r(\omega) \check{\Sigma}^<(\omega) \check{G}^a(\omega)] \quad (\text{E.2})$$

with

$$\check{S}(\omega) = \check{\tau} (\check{G}^r(\omega + \omega_0) + \check{G}^a(\omega - \omega_0)) \check{\tau} \quad (\text{E.3})$$

The matrix $\check{\tau} = \text{diag}(1, -1)$ describes the structure of the photon/particle coupling in the Nambu (electron/hole) space. Note that this degree of freedom is not necessary for describing the N/dot junction, but we introduce it for treating the N-dot-S bijunction. Equation E.2 involves the retarded, advanced, and lesser Green's functions \check{G}^c of the quantum dot, with $c = r, a, <$ respectively, which have the structure

$$\check{G}^c = \begin{bmatrix} \mathcal{G}_{\hat{d}_\uparrow, \hat{d}_\uparrow}^c & \mathcal{G}_{\hat{d}_\uparrow, \hat{d}_\downarrow}^c \\ \mathcal{G}_{\hat{d}_\downarrow, \hat{d}_\uparrow}^c & \mathcal{G}_{\hat{d}_\downarrow, \hat{d}_\downarrow}^c \end{bmatrix} \quad (\text{E.4})$$

in Nambu space. For any operators A and B , we use $\mathcal{G}_{A,B}^r(t) = -i\theta(t) \langle \{A(t), B(t=0)\} \rangle$ and $\mathcal{G}_{A,B}^<(t) = i \langle B(t=0)A(t) \rangle$. From Hamiltonian E.1, one obtains[134, 146]:

$$\check{G}^r(\omega) = (\check{G}^a(\omega))^\dagger = [\omega \check{1} - \check{E}_{dot} - \check{\Sigma}^r(\omega)]^{-1} \quad (\text{E.5})$$

$$\check{G}^<(\omega) = \check{G}^r(\omega) \check{\Sigma}^<(\omega) \check{G}^a(\omega) \quad (\text{E.6})$$

with

$$\check{\Sigma}^r(\omega) = -i(\Gamma_N/2)\check{1} - i(\Gamma_S/2)\check{C}(\omega) \quad (\text{E.7})$$

$$\check{\Sigma}^<(\omega) = i\Gamma_N \check{f}_N(\omega) + i\Gamma_S f(\omega) \text{Re}[\check{C}(\omega)] \quad (\text{E.8})$$

Above, we have introduced the diagonal matrices $\check{1} = \text{diag}(1, 1)$, $\check{E}_{dot} = \text{diag}(\varepsilon_d, -\varepsilon_d)$ and $\check{f}_N(\omega) = \text{diag}(f(\omega - eV_b), f(\omega + eV_b))$. The terms $\check{\Sigma}^c(\omega)$ describe the effect of the N and S reservoirs on the quantum dot Green's functions in the large bandwidth approximation. We use tunnel rates $\Gamma_r = 2\pi |t_r|^2 \rho_r$ with ρ_r the density of states per spin direction in reservoir $r \in \{S, N, n\}$. For describing electronic correlations in the superconducting reservoir, we use

$$\check{C}(\omega) = \begin{bmatrix} G_\omega & F_\omega \\ F_\omega & G_\omega \end{bmatrix} \quad (\text{E.9})$$

with $G_\omega = -i(\omega + i\frac{\Gamma_n}{2})/D_\omega$, $F_\omega = i\Delta/D_\omega$ and

$$D_\omega = \sqrt{\Delta^2 - (\omega + i\frac{\Gamma_n}{2})^2} \quad (\text{E.10})$$

The parameter Γ_n is often omitted (see for instance [133–137, 146, 147]), but is it essential to account for the broadening of the BCS peaks which is observed experimentally.

In the case $V_b = 0$ and $\Gamma_S \ll \Gamma_N, \Delta$ the effect of the superconducting contact can be disregarded i.e. $\Gamma_S = 0$. In this limit, equation E.2 leads to

$$\chi(\omega) = \frac{-\Gamma_N}{\pi\omega(\omega - i\Gamma_N)} \text{Log}\left[\frac{4\varepsilon_d^2 + \Gamma_N^2}{4\varepsilon_d^2 - (2\omega - i\Gamma_N)^2}\right] \quad (\text{E.11})$$

for $T = 0$ and equation 5.2 for T finite. In the case $\Gamma_S \neq 0$, we evaluate $\chi(\omega)$ numerically from equations E.2, E.3 and E.4-E.10.

For completeness, we mention that the DC current through the spin-degenerate quantum dot can be calculated for $g = 0$ as[146]:

$$\begin{aligned} I = & \frac{2e\Gamma_N\Gamma_S}{h} \int d\omega (f(\omega - eV_b) - f(\omega)) [\check{\mathcal{G}}^r \text{Re}[\check{\mathcal{C}}\check{\mathcal{G}}^a]_{11} \\ & + \frac{2e\Gamma_N^2}{h} \int d\omega (f(\omega - eV_b) - f(\omega + eV_b)) |\check{\mathcal{G}}_{12}^r|^2 \end{aligned} \quad (\text{E.12})$$

This expression includes quasiparticle tunneling as well as Andreev processes. With our non-interacting approach, when Γ_S increases, subgap Andreev processes appear much more quickly than what is expected in the Coulomb blockade regime, because Coulomb interactions forbid $2e$ charge fluctuations necessary for Andreev reflections[147]. In our case, this is not a problem because we have a low Γ_S . In figure 5.4b, the onset of the non-interacting Andreev current is slightly visible, but this current is barely above the noise level of the data in the top left panel. For values of Γ_S larger than in our experiment, it would be necessary to use an interacting theory to reproduce satisfactorily the data.

Bibliography

- [1] Yuli V. Nazarov and Yaroslav M. Blanter. *Quantum transport*. Cambridge University Press, 2009. ISBN 978-0-521-83246-5.
- [2] Serge Haroche and Jean-Michel Raimond. *Exploring the Quantum: Atoms, Cavities, and Photons*. Oxford University Press, 2006. ISBN 978-0198509141.
- [3] Michael A. Nielsen and Isaac L. Chuang. *Quantum Computation and Quantum Information*. Cambridge University Press, 2011. ISBN 9781107002173.
- [4] B. J. Van Wees, H. Van Houten, C. W J Beenakker, J. G. Williamson, L. P. Kouwenhoven, D. Van Der Marel, and C. T. Foxon. Quantized conductance of point contacts in a two-dimensional electron gas. *Phys. Rev. Lett.*, 60(9):848–850, 1988. ISSN 00319007. doi: 10.1103/PhysRevLett.60.848.
- [5] S. A. Wolf. Spintronics: A Spin-Based Electronics Vision for the Future. *Science (80-.)*, 294(5546):1488–1495, nov 2001. ISSN 00368075. doi: 10.1126/science.1065389. URL <http://www.sciencemag.org/cgi/doi/10.1126/science.1065389>.
- [6] Igor Žutić, Jaroslav Fabian, and S. Das Sarma. Spintronics: Fundamentals and applications. *Rev. Mod. Phys.*, 76(2):323–410, apr 2004. ISSN 0034-6861. doi: 10.1103/RevModPhys.76.323. URL <http://arxiv.org/abs/cond-mat/0405528>.
- [7] L P Kouwenhoven, D G Austing, and S Tarucha. Few-electron quantum dots. *Reports Prog. Phys.*, 64(6):701–736, jun 2001. ISSN 0034-4885. doi: 10.1088/0034-4885/64/6/201. URL <http://stacks.iop.org/0034-4885/64/i=6/a=201?key=crossref.8812a20d6f3a272b11b3ef1a4306614f>.
- [8] Edward A. Laird, Ferdinand Kuemmeth, Gary A. Steele, Kasper Grove-Rasmussen, Jesper Nygård, Karsten Flensberg, and Leo P. Kouwenhoven. Quantum transport in carbon nanotubes. *Rev. Mod. Phys.*, 87(3):703–764, jul 2015. ISSN 0034-6861. doi: 10.1103/RevModPhys.87.703. URL <http://arxiv.org/abs/1403.6113>.

- [9] Lieven M K Vandersypen, Matthias Steffen, Gregory Breyta, Costantino S Yannoni, Mark H Sherwood, and Isaac L Chuang. Experimental realization of Shor's quantum factoring algorithm using nuclear magnetic resonance. *Nature*, 414(6866):883–887, dec 2001. ISSN 0028-0836. doi: 10.1038/414883a. URL <http://www.nature.com/doifinder/10.1038/414883a>.
- [10] D. Kielpinski, A. Ben-Kish, J. Britton, V. Meyer, M. a. Rowe, C. a. Sackett, W. M. Itano, C. Monroe, and D. J. Wineland. Recent Results in Trapped-Ion Quantum Computing. page 7, 2001. URL <http://arxiv.org/abs/quant-ph/0102086>.
- [11] A Wallraff, D I Schuster, A Blais, L Frunzio, R-S Huang, J Majer, S Kumar, S M Girvin, and R J Schoelkopf. Circuit Quantum Electrodynamics: Coherent Coupling of a Single Photon to a Cooper Pair Box. *Nature*, 431(7005):162–167, jul 2004. ISSN 0028-0836. doi: 10.1038/nature02851. URL <http://www.nature.com/doifinder/10.1038/nature02851>.
- [12] S M Girvin, M H Devoret, and R J Schoelkopf. Circuit QED and engineering charge based superconducting qubits. *Phys. Scr.*, T137(T137):014012, dec 2009. ISSN 0031-8949. doi: 10.1088/0031-8949/2009/T137/014012. URL <http://arxiv.org/abs/0912.3902>.
- [13] J. M. Raimond, M. Brune, and S. Haroche. Manipulating quantum entanglement with atoms and photons in a cavity. *Rev. Mod. Phys.*, 73(3):565–582, aug 2001. ISSN 0034-6861. doi: 10.1103/RevModPhys.73.565. URL <http://link.aps.org/doi/10.1103/RevModPhys.73.565>.
- [14] Christine Guerlin, Julien Bernu, Samuel Deléglise, Clément Sayrin, Sébastien Gleyzes, Stefan Kuhr, Michel Brune, Jean-Michel Raimond, and Serge Haroche. Progressive field-state collapse and quantum non-demolition photon counting. *Nature*, 448(7156):889–893, aug 2007. ISSN 0028-0836. doi: 10.1038/nature06057. URL <http://www.nature.com/doifinder/10.1038/nature06057>.
- [15] Samuel Deléglise, Igor Dotsenko, Clément Sayrin, Julien Bernu, Michel Brune, Jean-Michel Raimond, and Serge Haroche. Reconstruction of non-classical cavity field states with snapshots of their decoherence. *Nature*, 455(7212):510–514, sep 2008. ISSN 0028-0836. doi: 10.1038/nature07288. URL <http://www.nature.com/doifinder/10.1038/nature07288>.
- [16] Clément Sayrin, Igor Dotsenko, Xingxing Zhou, Bruno Peaudecerf, Théo Rybarczyk, Sébastien Gleyzes, Pierre Rouchon, Mazyar Mirrahimi, Hadis Amini, Michel Brune, Jean-Michel Raimond, and Serge Haroche. Real-time quantum feedback prepares and stabilizes photon number states. *Nature*, 477(7362):73–77, jul 2011.

- ISSN 0028-0836. doi: 10.1038/nature10376. URL <http://dx.doi.org/10.1038/nature10376>.
- [17] J. M. Raimond, P. Facchi, B. Peaudecerf, S. Pascazio, C. Sayrin, I. Dotsenko, S. Gleyzes, M. Brune, and S. Haroche. Quantum Zeno dynamics of a field in a cavity. *Phys. Rev. A*, 86(3):032120, sep 2012. ISSN 1050-2947. doi: 10.1103/PhysRevA.86.032120. URL <http://link.aps.org/doi/10.1103/PhysRevA.86.032120>.
- [18] Adrien Signoles, Adrien Facon, Dorian Grosso, Igor Dotsenko, Serge Haroche, Jean-Michel Raimond, Michel Brune, and Sébastien Gleyzes. Confined quantum Zeno dynamics of a watched atomic arrow. *Nat. Phys.*, 10(10):715–719, aug 2014. ISSN 1745-2473. doi: 10.1038/nphys3076. URL <http://dx.doi.org/10.1038/nphys3076>.
- [19] L. Bretheau, P. Campagne-Ibarcq, E. Flurin, F. Mallet, and B. Huard. Quantum dynamics of an electromagnetic mode that cannot contain N photons. *Science (80-.)*, 348(6236):776–779, 2015. ISSN 0036-8075. doi: 10.1126/science.1259345. URL <http://www.sciencemag.org/content/348/6236/776.abstract>.
- [20] Daniel Loss and David P. DiVincenzo. Quantum Computation with Quantum Dots. *Phys. Rev. A*, 57(1):12, 1998. ISSN 1050-2947. doi: 10.1103/PhysRevA.57.120. URL <http://arxiv.org/abs/cond-mat/9701055>.
- [21] R. Hanson, L. P. Kouwenhoven, J. R. Petta, S. Tarucha, and L. M K Vandersypen. Spins in few-electron quantum dots. *Rev. Mod. Phys.*, 79(4):1217–1265, oct 2006. ISSN 00346861. doi: 10.1103/RevModPhys.79.1217. URL <http://arxiv.org/abs/cond-mat/0610433>.
- [22] A. C. Petta, J. R. and Johnson, A. C. and Taylor, J. M. and Laird, E. A. and Yacoby, A. and Lukin, M. D. and Marcus, C. M. and Hanson, M. P. and Gossard. Coherent Manipulation of Coupled Electron Spins in Semiconductor Quantum Dots. *Science (80-.)*, 309(5744):2180–2184, sep 2005. ISSN 0036-8075. doi: 10.1126/science.1116955. URL <http://www.sciencemag.org/cgi/doi/10.1126/science.1116955>.
- [23] R. Brunner, Y.-S. Shin, T. Obata, M. Pioro-Ladrière, T. Kubo, K. Yoshida, T. Taniyama, Y. Tokura, and S. Tarucha. Two-Qubit Gate of Combined Single-Spin Rotation and Interdot Spin Exchange in a Double Quantum Dot. *Phys. Rev. Lett.*, 107(14):146801, sep 2011. ISSN 0031-9007. doi: 10.1103/PhysRevLett.107.146801. URL <http://link.aps.org/doi/10.1103/PhysRevLett.107.146801>.

- [24] K. C. Nowack, M. Shafiei, M. Laforest, G. E. D. K. Prawiroatmodjo, L. R. Schreiber, C. Reichl, W. Wegscheider, and L. M. K. Vandersypen. Single-Shot Correlations and Two-Qubit Gate of Solid-State Spins. *Science (80-.)*, 333(6047):1269–1272, sep 2011. ISSN 0036-8075. doi: 10.1126/science.1209524. URL <http://www.sciencemag.org/cgi/doi/10.1126/science.1209524>.
- [25] M. D. Shulman, O. E. Dial, S. P. Harvey, H. Bluhm, V. Umansky, and a. Ya-coby. Demonstration of Entanglement of Electrostatically Coupled Singlet-Triplet Qubits. *Science (80-.)*, 336(6078):202–205, 2012. ISSN 0036-8075. doi: 10.1126/science.1217692.
- [26] M Veldhorst, C H Yang, J C C Hwang, W Huang, J P Dehollain, J T Muhonen, S Simmons, A Laucht, F E Hudson, K M Itoh, A Morello, and A S Dzurak. A Two Qubit Logic Gate in Silicon. *Nature*, pages 1–5, 2015. ISSN 0028-0836. doi: 10.1038/nature15263. URL <http://www.nature.com/nature/journal/vaop/ncurrent/full/nature15263.html>.
- [27] Patrik Recher, Eugene V. Sukhorukov, and Daniel Loss. Andreev tunneling, Coulomb blockade, and resonant transport of nonlocal spin-entangled electrons. *Phys. Rev. B*, 63(16):165314, apr 2001. ISSN 0163-1829. doi: 10.1103/PhysRevB.63.165314. URL <http://link.aps.org/doi/10.1103/PhysRevB.63.165314>.
- [28] Martin Leijnse and Karsten Flensberg. Coupling Spin Qubits via Superconductors. *Phys. Rev. Lett.*, 111(6):060501, aug 2013. ISSN 0031-9007. doi: 10.1103/PhysRevLett.111.060501. URL <http://link.aps.org/doi/10.1103/PhysRevLett.111.060501>.
- [29] Paul G. Kwiat, Klaus Mattle, Harald Weinfurter, Anton Zeilinger, Alexander V. Sergienko, and Yanhua Shih. New High-Intensity Source of Polarization-Entangled Photon Pairs. *Phys. Rev. Lett.*, 75(24):4337–4341, dec 1995. ISSN 0031-9007. doi: 10.1103/PhysRevLett.75.4337. URL <http://link.aps.org/doi/10.1103/PhysRevLett.75.4337>.
- [30] L Hofstetter, S Csonka, J Nygård, and C Schönenberger. Cooper pair splitter realized in a two-quantum-dot Y-junction. *Nature*, 461(7266):960–963, oct 2009. ISSN 0028-0836. doi: 10.1038/nature08432. URL <http://www.nature.com/doi/10.1038/nature08432>.
- [31] L. G. Herrmann, F. Portier, P. Roche, A. Levy Yeyati, T. Kontos, and C. Strunk. Carbon Nanotubes as Cooper-Pair Beam Splitters. *Phys. Rev. Lett.*, 104(2):026801, jan 2010. ISSN 0031-9007. doi: 10.1103/PhysRevLett.104.026801. URL <http://link.aps.org/doi/10.1103/PhysRevLett.104.026801>.

- [32] L. Hofstetter, S. Csonka, A. Baumgartner, G. Fülöp, S. Dhollosy, J. Nygård, and C. Schönenberger. Finite-Bias Cooper Pair Splitting. *Phys. Rev. Lett.*, 107(13):136801, sep 2011. ISSN 0031-9007. doi: 10.1103/PhysRevLett.107.136801. URL <http://link.aps.org/doi/10.1103/PhysRevLett.107.136801>.
- [33] J. Schindele, A. Baumgartner, and C. Schönenberger. Near-Unity Cooper Pair Splitting Efficiency. *Phys. Rev. Lett.*, 109(15):157002, oct 2012. ISSN 0031-9007. doi: 10.1103/PhysRevLett.109.157002. URL <http://link.aps.org/doi/10.1103/PhysRevLett.109.157002>.
- [34] Anindya Das, Yuval Ronen, Moty Heiblum, Diana Mahalu, Andrey V Kretinin, and Hadas Shtrikman. High-efficiency Cooper pair splitting demonstrated by two-particle conductance resonance and positive noise cross-correlation. *Nat. Commun.*, 3(May):1165, 2012. ISSN 2041-1723. doi: 10.1038/ncomms2169. URL <http://dx.doi.org/10.1038/ncomms2169>.
- [35] R S Deacon, A Oiwa, J Sailer, S Baba, Y Kanai, K Shibata, K Hirakawa, and S Tarucha. Cooper pair splitting in parallel quantum dot Josephson junctions. *Nat. Commun.*, 6(May 2015):7446, 2015. ISSN 2041-1723. doi: 10.1038/ncomms8446. URL <http://www.ncbi.nlm.nih.gov/pubmed/26130172>.
- [36] Z. B. Tan, D Cox, T Nieminen, P. Lähteenmäki, D Golubev, G. B. Lesovik, and P. J. Hakonen. Cooper Pair Splitting by Means of Graphene Quantum Dots. *Phys. Rev. Lett.*, 114(9):096602, mar 2015. ISSN 0031-9007. doi: 10.1103/PhysRevLett.114.096602. URL <http://link.aps.org/doi/10.1103/PhysRevLett.114.096602>.
- [37] I V Borzenets, Y Shimazaki, G F Jones, M F Craciun, S Russo, Y Yamamoto, and S Tarucha. High Efficiency CVD Graphene-lead (Pb) Cooper Pair Splitter. pages 1–5, jun 2015. URL <http://arxiv.org/abs/1506.04597>.
- [38] J Majer, J M Chow, J M Gambetta, Jens Koch, B R Johnson, J A Schreier, L Frunzio, D I Schuster, A A Houck, A Wallraff, A Blais, M H Devoret, S M Girvin, and R J Schoelkopf. Coupling superconducting qubits via a cavity bus. *Nature*, 449(7161):443–447, sep 2007. ISSN 0028-0836. doi: 10.1038/nature06184. URL <http://www.nature.com/doi/10.1038/nature06184>.
- [39] R Barends, J Kelly, A Megrant, A Veitia, D Sank, E Jeffrey, T C White, J Mutus, Austin G Fowler, B Campbell, Y. Chen, Z Chen, B Chiaro, A Dunsworth, C Neill, P. OMalley, P Roushan, A Vainsencher, J Wenner, a N Korotkov, a N Cleland, and John M Martinis. Superconducting quantum circuits at the surface code

- threshold for fault tolerance. *Nature*, 508(7497):500–503, apr 2014. ISSN 0028-0836. doi: 10.1038/nature13171. URL <http://www.nature.com/doi/10.1038/nature13171>.
- [40] A. Imamoglu, D. D. Awschalom, G Burkard, D P DiVincenzo, D Loss, M Sherwin, and A Small. Quantum Information Processing Using Quantum Dot Spins and Cavity QED. *Phys. Rev. Lett.*, 83(20):4204–4207, nov 1999. ISSN 0031-9007. doi: 10.1103/PhysRevLett.83.4204. URL <http://link.aps.org/doi/10.1103/PhysRevLett.83.4204>.
- [41] Guido Burkard and Atac Imamoglu. Ultra-long-distance interaction between spin qubits. *Phys. Rev. B*, 74(4):041307, jul 2006. ISSN 1098-0121. doi: 10.1103/PhysRevB.74.041307. URL <http://link.aps.org/doi/10.1103/PhysRevB.74.041307>.
- [42] M. R. Delbecq, V. Schmitt, F. D. Parmentier, N. Roch, J. J. Viennot, G. Fève, B. Huard, C. Mora, a. Cottet, and T. Kontos. Coupling a Quantum Dot, Fermionic Leads, and a Microwave Cavity on a Chip. *Phys. Rev. Lett.*, 107(25):256804, dec 2011. ISSN 0031-9007. doi: 10.1103/PhysRevLett.107.256804. URL <http://link.aps.org/doi/10.1103/PhysRevLett.107.256804>.
- [43] T. Frey, P. J. Leek, M. Beck, A. Blais, T. Ihn, K. Ensslin, and A. Wallraff. Dipole Coupling of a Double Quantum Dot to a Microwave Resonator. *Phys. Rev. Lett.*, 108(4):046807, jan 2012. ISSN 0031-9007. doi: 10.1103/PhysRevLett.108.046807. URL <http://link.aps.org/doi/10.1103/PhysRevLett.108.046807>.
- [44] K. D. Petersson, L. W. McFaul, M. D. Schroer, M. Jung, J. M. Taylor, a. a. Houck, and J. R. Petta. Circuit quantum electrodynamics with a spin qubit. *Nature*, 490(7420):380–383, 2012. ISSN 0028-0836. doi: 10.1038/nature11559. URL <http://dx.doi.org/10.1038/nature11559>.
- [45] M. Hofheinz, F. Portier, Q. Baudouin, P. Joyez, D. Vion, P. Bertet, P. Roche, and D. Esteve. Bright Side of the Coulomb Blockade. *Phys. Rev. Lett.*, 106(21):217005, 2011. ISSN 0031-9007. doi: 10.1103/PhysRevLett.106.217005. URL <http://link.aps.org/doi/10.1103/PhysRevLett.106.217005>.
- [46] J. J. Viennot, M.R. Delbecq, L. E. Bruhat, M. C. Dartiailh, M. Desjardins, M. Bailargeau, A. Cottet, and T. Kontos. Towards hybrid circuit quantum electrodynamics with quantum dots. *Comptes Rendus l’Académie des Sci.*, in press, 2016.
- [47] L. Childress, A. Sørensen, and Mikhail D. Lukin. Mesoscopic cavity quantum electrodynamics with quantum dots. *Phys. Rev. A*, 69(4):042302, 2004. ISSN

- 1050-2947. doi: 10.1103/PhysRevA.69.042302. URL <http://link.aps.org/doi/10.1103/PhysRevA.69.042302>.
- [48] Mircea Trif, Vitaly N. Golovach, and Daniel Loss. Spin dynamics in InAs nanowire quantum dots coupled to a transmission line. *Phys. Rev. B*, 77(4):045434, jan 2008. ISSN 1098-0121. doi: 10.1103/PhysRevB.77.045434. URL <http://link.aps.org/doi/10.1103/PhysRevB.77.045434>.
- [49] S. J. Chorley, J. Wabnig, Z. V. Penfold-Fitch, K. D. Petersson, J. Frake, C. G. Smith, and M. R. Buitelaar. Measuring the Complex Admittance of a Carbon Nanotube Double Quantum Dot. *Phys. Rev. Lett.*, 108(3):036802, jan 2012. ISSN 0031-9007. doi: 10.1103/PhysRevLett.108.036802. URL <http://link.aps.org/doi/10.1103/PhysRevLett.108.036802>.
- [50] J. Basset, D.-D. Jarausch, a. Stockklauser, T. Frey, C. Reichl, W. Wegscheider, T. M. Ihn, K. Ensslin, and a. Wallraff. Single-electron double quantum dot dipole-coupled to a single photonic mode. *Phys. Rev. B*, 88(12):125312, 2013. ISSN 1098-0121. doi: 10.1103/PhysRevB.88.125312. URL <http://link.aps.org/doi/10.1103/PhysRevB.88.125312>.
- [51] H. Toida, T. Nakajima, and S. Komiyama. Vacuum Rabi Splitting in a Semiconductor Circuit QED System. *Phys. Rev. Lett.*, 110(6):066802, feb 2013. ISSN 0031-9007. doi: 10.1103/PhysRevLett.110.066802. URL <http://link.aps.org/doi/10.1103/PhysRevLett.110.066802>.
- [52] J. J. Viennot, M.R. Delbecq, M. C. Dartiailh, Audrey Cottet, and T. Kontos. Out-of-equilibrium charge dynamics in a hybrid circuit quantum electrodynamics architecture. *Phys. Rev. B*, 89(16):165404, 2014. ISSN 1098-0121. doi: 10.1103/PhysRevB.89.165404. URL <http://link.aps.org/doi/10.1103/PhysRevB.89.165404>.
- [53] Guang-Wei Deng, Da Wei, J.R. Johansson, Miao-Lei Zhang, Shu-Xiao Li, Hai-Ou Li, Gang Cao, Ming Xiao, Tao Tu, Guang-Can Guo, Hong-Wen Jiang, Franco Nori, and Guo-Ping Guo. Charge Number Dependence of the Dephasing Rates of a Graphene Double Quantum Dot in a Circuit QED Architecture. *Phys. Rev. Lett.*, 115(12):126804, 2015. ISSN 0031-9007. doi: 10.1103/PhysRevLett.115.126804. URL <http://link.aps.org/doi/10.1103/PhysRevLett.115.126804>.
- [54] J. J. Viennot, M. C. Dartiailh, A. Cottet, and T. Kontos. Coherent coupling of a single spin to microwave cavity photons. *Science (80-.)*, 349(6246):408–411, jul 2015. ISSN 0036-8075. doi: 10.1126/science.aaa3786. URL <http://www.sciencemag.org/cgi/doi/10.1126/science.aaa3786>.

- [55] Audrey Cottet, Takis Kontos, and Alfredo Levy Yeyati. Subradiant Split Cooper Pairs. *Phys. Rev. Lett.*, 108(16):166803, apr 2012. ISSN 0031-9007. doi: 10.1103/PhysRevLett.108.166803. URL <http://link.aps.org/doi/10.1103/PhysRevLett.108.166803>.
- [56] Audrey Cottet. Probing coherent Cooper pair splitting with cavity photons. *Phys. Rev. B*, 90(12):125139, sep 2014. ISSN 1098-0121. doi: 10.1103/PhysRevB.90.125139. URL <http://link.aps.org/doi/10.1103/PhysRevB.90.125139>.
- [57] P. K. Tien and J. P. Gordon. Multiphoton Process Observed in the Interaction of Microwave Fields with the Tunneling between Superconductor Films. *Phys. Rev.*, 129(2):647–651, jan 1963. ISSN 0031-899X. doi: 10.1103/PhysRev.129.647. URL <http://link.aps.org/doi/10.1103/PhysRev.129.647>.
- [58] L. P. Kouwenhoven, S. Jauhar, K. McCormick, D. Dixon, P. L. McEuen, Yu V. Nazarov, N. C. van der Vaart, and C. T. Foxon. Photon-assisted tunneling through a quantum dot. *Phys. Rev. B*, 50(3):2019–2022, jul 1994. ISSN 0163-1829. doi: 10.1103/PhysRevB.50.2019. URL <http://link.aps.org/doi/10.1103/PhysRevB.50.2019>.
- [59] Jeroen M Elzerman, Silvano De Franceschi, David Goldhaber-Gordon, Wilfred G. van der Wiel, and Leo P Kouwenhoven. Suppression of the Kondo Effect in a Quantum Dot by Microwave Radiation. *J. Low Temp. Phys.*, 118(5/6):375–389, 2000. ISSN 00222291. doi: 10.1023/A:1004694017738. URL <http://link.springer.com/10.1023/A:1004694017738>.
- [60] M. A. Kogan, Andrei and Amasha, Sami and Kastner. Photon-Induced Kondo Satellites in a Single-Electron Transistor. *Science (80-.)*, 304(5675):1293–1295, may 2004. ISSN 0036-8075. doi: 10.1126/science.1096377. URL <http://www.sciencemag.org/cgi/doi/10.1126/science.1096377>.
- [61] Bryan Hemingway, Stephen Herbert, Michael Melloch, and Andrei Kogan. Dynamic response of a spin-1/2 Kondo singlet. *Phys. Rev. B*, 90(12):125151, sep 2014. ISSN 1098-0121. doi: 10.1103/PhysRevB.90.125151. URL <http://link.aps.org/doi/10.1103/PhysRevB.90.125151>.
- [62] T Frey, P J Leek, M Beck, J Faist, A Wallraff, K Ensslin, T Ihn, and M Büttiker. Quantum dot admittance probed at microwave frequencies with an on-chip resonator. *Phys. Rev. B*, 86(11):115303, sep 2012. ISSN 1098-0121. doi: 10.1103/PhysRevB.86.115303. URL <http://link.aps.org/doi/10.1103/PhysRevB.86.115303>.

- [63] A. Kaminski, Yu. Nazarov, and L. Glazman. Universality of the Kondo effect in a quantum dot out of equilibrium. *Phys. Rev. B*, 62(12):8154–8170, sep 2000. ISSN 0163-1829. doi: 10.1103/PhysRevB.62.8154. URL <http://link.aps.org/doi/10.1103/PhysRevB.62.8154>.
- [64] M. Büttiker, H. Thomas, and A. Prêtre. Mesoscopic capacitors. *Phys. Lett. A*, 180(4-5):364–369, sep 1993. ISSN 03759601. doi: 10.1016/0375-9601(93)91193-9. URL <http://linkinghub.elsevier.com/retrieve/pii/0375960193911939>.
- [65] A. Prêtre, H. Thomas, and M. Büttiker. Dynamic admittance of mesoscopic conductors: Discrete-potential model. *Phys. Rev. B*, 54(11):8130–8143, sep 1996. ISSN 0163-1829. doi: 10.1103/PhysRevB.54.8130. URL <http://link.aps.org/doi/10.1103/PhysRevB.54.8130>.
- [66] J Gabelli, G Fève, J-M Berroir, B Plaçais, a Cavanna, B Etienne, Y Jin, and D C Glattli. Violation of Kirchoff’s laws for a coherent RC circuit. *Science*, 313(5786):499–502, jul 2006. ISSN 1095-9203. doi: 10.1126/science.1126940. URL <http://www.ncbi.nlm.nih.gov/pubmed/16840660>.
- [67] Minchul Lee, Rosa López, Mahn-Soo Choi, Thibaut Jonckheere, and Thierry Martin. Effect of many-body correlations on mesoscopic charge relaxation. *Phys. Rev. B*, 83(20):201304, may 2011. ISSN 1098-0121. doi: 10.1103/PhysRevB.83.201304. URL <http://link.aps.org/doi/10.1103/PhysRevB.83.201304>.
- [68] Michele Filippone, Karyn LeHur, and Christophe Mora. Giant Charge Relaxation Resistance in the Anderson Model. *Phys. Rev. Lett.*, 107(17):176601, 2011. ISSN 0031-9007. doi: 10.1103/PhysRevLett.107.176601. URL <http://link.aps.org/doi/10.1103/PhysRevLett.107.176601>.
- [69] a. Cottet, T. Kontos, and B. Douçot. Electron-photon coupling in mesoscopic quantum electrodynamics. *Phys. Rev. B*, 91(20):1–16, 2015. ISSN 1098-0121. doi: 10.1103/PhysRevB.91.205417. URL <http://link.aps.org/doi/10.1103/PhysRevB.91.205417>.
- [70] Audrey Cottet, Christophe Mora, and Takis Kontos. Mesoscopic admittance of a double quantum dot. *Phys. Rev. B*, 83(12):121311, mar 2011. ISSN 1098-0121. doi: 10.1103/PhysRevB.83.121311. URL <http://link.aps.org/doi/10.1103/PhysRevB.83.121311>.
- [71] Marco Schiró and Karyn Le Hur. Tunable hybrid quantum electrodynamics from nonlinear electron transport. *Phys. Rev. B*, 89(19):195127, 2014. ISSN 1098-0121. doi: 10.1103/PhysRevB.89.195127. URL <http://link.aps.org/doi/10.1103/PhysRevB.89.195127>.

- [72] Olesia Dmytruk, Mircea Trif, Christophe Mora, and Pascal Simon. Cavity quantum electrodynamics with an out-of-equilibrium quantum dot. pages 1–16, oct 2015. URL <http://arxiv.org/abs/1510.03748>.
- [73] S. Tarucha, D. G. Austing, T. Honda, R. J. van der Hage, and L. P. Kouwenhoven. Shell Filling and Spin Effects in a Few Electron Quantum Dot. *Phys. Rev. Lett.*, 77(17):3613–3616, oct 1996. ISSN 0031-9007. doi: 10.1103/PhysRevLett.77.3613. URL <http://link.aps.org/doi/10.1103/PhysRevLett.77.3613>.
- [74] J. M. Elzerman, R. Hanson, L. H. Willems van Beveren, B. Witkamp, L. M. K. Vandersypen, and L. P. Kouwenhoven. Single-shot read-out of an individual electron spin in a quantum dot. *Nature*, 430(6998):431–435, jul 2004. ISSN 0028-0836. doi: 10.1038/nature02693. URL <http://www.nature.com/doi/10.1038/nature02693>.
- [75] Io Kulik and Ri Shekhter. Kinetic Phenomena and Charge-Discreteness Effects in Granulated Media. *Zhur. Eksper. Teoret. Fiz.*, 41(2):308–316, 1975. ISSN 0044-4510. URL http://jetp.ac.ru/cgi-bin/dn/e/_041/_02/_0308.pdf.
- [76] T Hayashi, T Fujisawa, H D Cheong, Y H Jeong, and Y Hirayama. Coherent Manipulation of Electronic States in a Double Quantum Dot. *Phys. Rev. Lett.*, 91(22):226804, nov 2003. ISSN 0031-9007. doi: 10.1103/PhysRevLett.91.226804. URL <http://link.aps.org/doi/10.1103/PhysRevLett.91.226804>.
- [77] K. D. Petersson, J. R. Petta, H. Lu, and a. C. Gossard. Quantum Coherence in a One-Electron Semiconductor Charge Qubit. *Phys. Rev. Lett.*, 105(24):246804, dec 2010. ISSN 0031-9007. doi: 10.1103/PhysRevLett.105.246804. URL <http://link.aps.org/doi/10.1103/PhysRevLett.105.246804>.
- [78] Gang Cao, Hai-Ou Li, Tao Tu, Li Wang, Cheng Zhou, Ming Xiao, Guang-Can Guo, Hong-Wen Jiang, and Guo-Ping Guo. Ultrafast universal quantum control of a quantum-dot charge qubit using LandauZenerStückelberg interference. *Nat. Commun.*, 4:1401, jan 2013. ISSN 2041-1723. doi: 10.1038/ncomms2412. URL <http://www.nature.com/doi/10.1038/ncomms2412>.
- [79] Zhan Shi, C. B. Simmons, Daniel R. Ward, J. R. Prance, R. T. Mohr, Teck Seng Koh, John King Gamble, Xian Wu, D. E. Savage, M. G. Lagally, Mark Friesen, S. N. Coppersmith, and M. a. Eriksson. Coherent quantum oscillations and echo measurements of a Si charge qubit. *Phys. Rev. B*, 88(7):075416, aug 2013. ISSN 1098-0121. doi: 10.1103/PhysRevB.88.075416. URL <http://link.aps.org/doi/10.1103/PhysRevB.88.075416>.

- [80] W.J. De Haas and G.J. Van Den Berg. The electrical resistance of gold and silver at low temperatures. *Physica*, 3(6):440–449, jun 1936. ISSN 00318914. doi: 10.1016/S0031-8914(36)80009-3. URL <http://linkinghub.elsevier.com/retrieve/pii/S0031891436800093>.
- [81] Jun Kondo. Resistance Minimum in Dilute Magnetic Alloys. *Prog. Theor. Phys.*, 32(1):37–49, jul 1964. ISSN 0033-068X. doi: 10.1143/PTP.32.37. URL <http://ptp.oxfordjournals.org/cgi/doi/10.1143/PTP.32.37>.
- [82] Kenneth G Wilson. The renormalization group: Critical phenomena and the Kondo problem. *Rev. Mod. Phys.*, 47(4):773–840, oct 1975. ISSN 0034-6861. doi: 10.1103/RevModPhys.47.773. URL <http://link.aps.org/doi/10.1103/RevModPhys.47.773>.
- [83] S. Sasaki, S. De Franceschi, J. M. Elzerman, W. G. van der Wiel, M. Eto, S. Tarucha, and L. P. Kouwenhoven. Kondo effect in an integer-spin quantum dot. *Nature*, 405(6788):764–767, jun 2000. ISSN 00280836. doi: 10.1038/35015509. URL <http://www.nature.com/doi/10.1038/35015509>.
- [84] Pablo Jarillo-Herrero, Jing Kong, Herre S.J. van der Zant, Cees Dekker, Leo P. Kouwenhoven, and Silvano De Franceschi. Orbital Kondo effect in carbon nanotubes. *Nature*, 434(7032):484–488, mar 2005. ISSN 0028-0836. doi: 10.1038/nature03422. URL <http://www.nature.com/doi/10.1038/nature03422>.
- [85] J. R. Schrieffer and P. A. Wolff. Relation between the Anderson and Kondo Hamiltonians. *Phys. Rev.*, 149(2):491–492, sep 1966. ISSN 0031-899X. doi: 10.1103/PhysRev.149.491. URL <http://link.aps.org/doi/10.1103/PhysRev.149.491>.
- [86] L I Glazman and M Pustilnik. Coulomb blockade and Kondo effect in quantum dots. *Arxiv*, pages 1–22, feb 2003. URL <http://arxiv.org/abs/cond-mat/0302159>.
- [87] Thomas Delattre. *Fluctuations quantiques de courant dans les nanotubes de carbone*. PhD thesis, 2009. URL [http://tel.archives-ouvertes.fr/index.php?halsid=mn1vhnfvu1p8ds8cqqb0d5cj82&view\[_\]this\[_\]doc=tel-00528936&version=1](http://tel.archives-ouvertes.fr/index.php?halsid=mn1vhnfvu1p8ds8cqqb0d5cj82&view[_]this[_]doc=tel-00528936&version=1).
- [88] J. Schindele, A. Baumgartner, R. Maurand, M. Weiss, and C. Schönenberger. Nonlocal spectroscopy of Andreev bound states. *Phys. Rev. B*, 89(4):045422, jan 2014. ISSN 1098-0121. doi: 10.1103/PhysRevB.89.045422. URL <http://link.aps.org/doi/10.1103/PhysRevB.89.045422>.
- [89] D. C. Ralph, C. T. Black, and M. Tinkham. Spectroscopic Measurements of Discrete Electronic States in Single Metal Particles. *Phys. Rev. Lett.*, 74(16):

- 3241–3244, apr 1995. ISSN 0031-9007. doi: 10.1103/PhysRevLett.74.3241. URL <http://link.aps.org/doi/10.1103/PhysRevLett.74.3241>.
- [90] Silvano De Franceschi, Leo Kouwenhoven, Christian Schönenberger, and Wolfgang Wernsdorfer. Hybrid superconductor-quantum dot devices. *Nat. Nanotechnol.*, 5(10):703–11, oct 2010. ISSN 1748-3395. doi: 10.1038/nnano.2010.173. URL <http://dx.doi.org/10.1038/nnano.2010.173>.
- [91] Audrey Cottet. Microwave spectroscopy of a Cooper pair beam splitter. *Phys. Rev. B*, 86(7):075107, aug 2012. ISSN 1098-0121. doi: 10.1103/PhysRevB.86.075107. URL <http://link.aps.org/doi/10.1103/PhysRevB.86.075107>.
- [92] Guido Burkard, Daniel Loss, and Eugene V. Sukhorukov. Noise of entangled electrons: Bunching and antibunching. *Phys. Rev. B*, 61(24):R16303–R16306, jun 2000. ISSN 0163-1829. doi: 10.1103/PhysRevB.61.R16303. URL <http://link.aps.org/doi/10.1103/PhysRevB.61.R16303>.
- [93] P. Samuelsson and M. Büttiker. Semiclassical theory of current correlations in chaotic dot-superconductor systems. *Phys. Rev. B*, 66(20):201306, nov 2002. ISSN 0163-1829. doi: 10.1103/PhysRevB.66.201306. URL <http://link.aps.org/doi/10.1103/PhysRevB.66.201306>.
- [94] J. Börlin, W. Belzig, and C. Bruder. Full Counting Statistics of a Superconducting Beam Splitter. *Phys. Rev. Lett.*, 88(19):197001, 2002. ISSN 0031-9007. doi: 10.1103/PhysRevLett.88.197001. URL <http://link.aps.org/doi/10.1103/PhysRevLett.88.197001>.
- [95] Bertrand Reulet, Michel Ramin, H el ene Bouchiat, and Dominique Mailly. Dynamic Response of Isolated Aharonov-Bohm Rings Coupled to an Electromagnetic Resonator. *Phys. Rev. Lett.*, 75(1):124–127, jul 1995. ISSN 0031-9007. doi: 10.1103/PhysRevLett.75.124. URL <http://arxiv.org/abs/cond-mat/9502029><http://link.aps.org/doi/10.1103/PhysRevLett.75.124>.
- [96] L. Bretheau,  .  . Girit, H. Pothier, D. Esteve, and C. Urbina. Exciting Andreev pairs in a superconducting atomic contact. *Nature*, 499(7458):312–315, 2013. ISSN 0028-0836. doi: 10.1038/nature12315. URL <http://www.nature.com/doi/10.1038/nature12315>.
- [97] M. Büttiker, A. Pr etre, and H. Thomas. Dynamic conductance and the scattering matrix of small conductors. *Phys. Rev. Lett.*, 70(26):4114–4117, jun 1993. ISSN 0031-9007. doi: 10.1103/PhysRevLett.70.4114. URL <http://link.aps.org/doi/10.1103/PhysRevLett.70.4114>.

- [98] L. Bretheau, Ç. Ö. Girit, C. Urbina, D. Esteve, and H. Pothier. Supercurrent Spectroscopy of Andreev States. *Phys. Rev. X*, 3(4):041034, dec 2013. ISSN 2160-3308. doi: 10.1103/PhysRevX.3.041034. URL <http://link.aps.org/doi/10.1103/PhysRevX.3.041034>.
- [99] C. Janvier, L. Tosi, L. Bretheau, C. O. Girit, M. Stern, P. Bertet, P. Joyez, D Vion, D Esteve, M F Goffman, H Pothier, and C Urbina. Coherent manipulation of Andreev states in superconducting atomic contacts. *Science (80-.)*, 349(6253):1199–1202, sep 2015. ISSN 0036-8075. doi: 10.1126/science.aab2179. URL <http://www.sciencemag.org/cgi/doi/10.1126/science.aab2179>.
- [100] A A Clerk, M H Devoret, S M Girvin, Florian Marquardt, and R J Schoelkopf. Introduction to quantum noise, measurement, and amplification. *Rev. Mod. Phys.*, 82(2):1155–1208, apr 2010. ISSN 0034-6861. doi: 10.1103/RevModPhys.82.1155. URL <http://arxiv.org/abs/0810.4729><http://dx.doi.org/10.1103/RevModPhys.82.1155><http://link.aps.org/doi/10.1103/RevModPhys.82.1155>.
- [101] Y. Kubo, F. R. Ong, P. Bertet, D. Vion, V. Jacques, D. Zheng, a. Dréau, J.-F. Roch, a. Auffeves, F. Jelezko, J. Wrachtrup, M. F. Barthe, P. Bergonzo, and D. Esteve. Strong Coupling of a Spin Ensemble to a Superconducting Resonator. *Phys. Rev. Lett.*, 105(14):140502, 2010. ISSN 0031-9007. doi: 10.1103/PhysRevLett.105.140502. URL <http://link.aps.org/doi/10.1103/PhysRevLett.105.140502>.
- [102] D. I. Schuster, a. P. Sears, E. Ginossar, L. DiCarlo, L. Frunzio, J. J. L. Morton, H. Wu, G. a. D. Briggs, B. B. Buckley, D. D. Awschalom, and R. J. Schoelkopf. High-Cooperativity Coupling of Electron-Spin Ensembles to Superconducting Cavities. *Phys. Rev. Lett.*, 105(14):140501, 2010. ISSN 0031-9007. doi: 10.1103/PhysRevLett.105.140501. URL <http://link.aps.org/doi/10.1103/PhysRevLett.105.140501>.
- [103] a. Bienfait, J. J. Pla, Y. Kubo, M. Stern, X. Zhou, C. C. Lo, C. D. Weis, T. Schenkel, M. L. W. Thewalt, D. Vion, D. Esteve, B. Julsgaard, K. Moelmer, J. J. L. Morton, and P. Bertet. Reaching the quantum limit of sensitivity in electron spin resonance. 2015. URL <http://arxiv.org/abs/1507.06831>.
- [104] Lev S. Bishop, J. M. Chow, Jens Koch, A. A. Houck, M. H. Devoret, E. Thuneberg, S. M. Girvin, and R. J. Schoelkopf. Nonlinear response of the vacuum Rabi resonance. *Nat. Phys.*, 322(5906):6, 2008. ISSN 1745-2473. doi: 10.1038/nphys1154. URL <http://arxiv.org/abs/0807.2882>.

- [105] M.R. Delbecq, L.E. Bruhat, J.J. Viennot, S Datta, A Cottet, and T Kontos. Photon-mediated interaction between distant quantum dot circuits. *Nat. Commun.*, 4:1400, jan 2013. ISSN 2041-1723. doi: 10.1038/ncomms2407. URL <http://www.nature.com/doi/10.1038/ncomms2407>.
- [106] Guang-Wei Deng, Da Wei, Shu-Xiao Li, J. R. Johansson, Wei-Cheng Kong, Hai-Ou Li, Gang Cao, Ming Xiao, Guang-Can Guo, Franco Nori, Hong-Wen Jiang, and Guo-Ping Guo. Coupling Two Distant Double Quantum Dots with a Microwave Resonator. *Nano Lett.*, 15(10):6620–6625, oct 2015. ISSN 1530-6984. doi: 10.1021/acs.nanolett.5b02400. URL <http://pubs.acs.org/doi/10.1021/acs.nanolett.5b02400>.
- [107] Y.-Y. Liu, K.D. Petersson, J. Stehlik, J.M. Taylor, and J.R. Petta. Photon Emission from a Cavity-Coupled Double Quantum Dot. *Phys. Rev. Lett.*, 113(3):036801, 2014. ISSN 0031-9007. doi: 10.1103/PhysRevLett.113.036801. URL <http://link.aps.org/doi/10.1103/PhysRevLett.113.036801>.
- [108] Y.-Y. Liu, J Stehlik, C Eichler, M J Gullans, J M Taylor, and J R Petta. Semiconductor double quantum dot micromaser. *Science (80-.)*, 347(6219):285–287, jan 2015. ISSN 0036-8075. doi: 10.1126/science.aaa2501. URL <http://www.sciencemag.org/cgi/doi/10.1126/science.aaa2501>.
- [109] a. Stockklauser, V. F. Maisi, J. Basset, K. Cujia, C. Reichl, W. Wegscheider, T. Ihn, a. Wallraff, and K. Ensslin. Microwave Emission from Hybridized States in a Semiconductor Charge Qubit. *Phys. Rev. Lett.*, 115(4):046802, 2015. ISSN 0031-9007. doi: 10.1103/PhysRevLett.115.046802. URL <http://link.aps.org/doi/10.1103/PhysRevLett.115.046802>.
- [110] Mircea Trif and Pascal Simon. Photon cross-correlations emitted by a Josephson junction in two microwave cavities. *Phys. Rev. B*, 92(1):014503, 2015. ISSN 1098-0121. doi: 10.1103/PhysRevB.92.014503. URL <http://link.aps.org/doi/10.1103/PhysRevB.92.014503>.
- [111] Ciprian Padurariu, Fabian Hassler, and Yuli V. Nazarov. Statistics of radiation at Josephson parametric resonance. *Phys. Rev. B*, 86(5):054514, 2012. ISSN 1098-0121. doi: 10.1103/PhysRevB.86.054514. URL <http://link.aps.org/doi/10.1103/PhysRevB.86.054514>.
- [112] Juha Leppäkangas, Mikael Fogelström, Alexander Grimm, Max Hofheinz, Michael Marthaler, and Göran Johansson. Antibunched Photons from Inelastic Cooper-Pair Tunneling. *Phys. Rev. Lett.*, 115(2):027004, 2015. ISSN 0031-9007. doi: 10.1103/PhysRevLett.115.027004. URL <http://link.aps.org/doi/10.1103/PhysRevLett.115.027004>.

- [113] J. R. Souquet, M. J. Woolley, J. Gabelli, P. Simon, and A. A. Clerk. Photon-assisted tunnelling with nonclassical light. *Nat. Commun.*, 5:5562, nov 2014. ISSN 2041-1723. doi: 10.1038/ncomms6562. URL <http://arxiv.org/abs/1408.1128><http://www.nature.com/doifinder/10.1038/ncomms6562>.
- [114] J. J. Viennot, J. Palomo, and T. Kontos. Stamping single wall nanotubes for circuit quantum electrodynamics. *Appl. Phys. Lett.*, 104(11):113108, 2014. ISSN 1077-3118. doi: 10.1063/1.4868868. URL <http://scitation.aip.org/content/aip/journal/apl/104/11/10.1063/1.4868868>.
- [115] Matthias H. Hettler and Herbert Schoeller. Anderson Model Out of Equilibrium: Time-Dependent Perturbations. *Phys. Rev. Lett.*, 74(24):4907–4910, jun 1995. ISSN 0031-9007. doi: 10.1103/PhysRevLett.74.4907. URL <http://link.aps.org/doi/10.1103/PhysRevLett.74.4907>.
- [116] Avraham Schiller and Selman Hershfield. Solution of an ac Kondo Model. *Phys. Rev. Lett.*, 77(9):1821–1824, aug 1996. ISSN 0031-9007. doi: 10.1103/PhysRevLett.77.1821. URL <http://link.aps.org/doi/10.1103/PhysRevLett.77.1821>.
- [117] Tai-Kai Ng. ac Response in the Nonequilibrium Anderson Impurity Model. *Phys. Rev. Lett.*, 76(3):487–490, jan 1996. ISSN 0031-9007. doi: 10.1103/PhysRevLett.76.487. URL <http://link.aps.org/doi/10.1103/PhysRevLett.76.487>.
- [118] Y. Goldin and Y. Avishai. Nonlinear Response of a Kondo System: Direct and Alternating Tunneling Currents. *Phys. Rev. Lett.*, 81(24):5394–5397, dec 1998. ISSN 0031-9007. doi: 10.1103/PhysRevLett.81.5394. URL <http://link.aps.org/doi/10.1103/PhysRevLett.81.5394>.
- [119] Rosa López, Ramón Aguado, Gloria Platero, and Carlos Tejedor. Kondo Effect in ac Transport through Quantum Dots. *Phys. Rev. Lett.*, 81(21):4688–4691, nov 1998. ISSN 0031-9007. doi: 10.1103/PhysRevLett.81.4688. URL <http://link.aps.org/doi/10.1103/PhysRevLett.81.4688>.
- [120] a. Kaminski, Yu. Nazarov, and L. Glazman. Suppression of the Kondo Effect in a Quantum Dot by External Irradiation. *Phys. Rev. Lett.*, 83(2):384–387, jul 1999. ISSN 0031-9007. doi: 10.1103/PhysRevLett.83.384. URL <http://link.aps.org/doi/10.1103/PhysRevLett.83.384>.
- [121] Simon Nigg, Rosa López, and Markus Büttiker. Mesoscopic Charge Relaxation. *Phys. Rev. Lett.*, 97(20):206804, nov 2006. ISSN 0031-9007. doi: 10.1103/PhysRevLett.97.206804. URL <http://link.aps.org/doi/10.1103/PhysRevLett.97.206804>.

- [122] Christophe Mora and Karyn Le Hur. Universal resistances of the quantum resistance-capacitance circuit. *Nat. Phys.*, 6(9):697–701, sep 2010. ISSN 1745-2473. doi: 10.1038/nphys1690. URL <http://www.nature.com/doi/10.1038/nphys1690>.
- [123] Yuji Hamamoto, Thibaut Jonckheere, Takeo Kato, and Thierry Martin. Dynamic response of a mesoscopic capacitor in the presence of strong electron interactions. *Phys. Rev. B*, 81(15):5, 2010. ISSN 1098-0121. doi: 10.1103/PhysRevB.81.153305. URL <http://prb.aps.org/abstract/PRB/v81/i15/e153305>.
- [124] Ya. I. Rodionov, I. S. Burmistrov, and A. S. Ioselevich. Charge relaxation resistance in the Coulomb blockade problem. *Phys. Rev. B*, 80(3):035332, jul 2009. ISSN 1098-0121. doi: 10.1103/PhysRevB.80.035332. URL <http://link.aps.org/doi/10.1103/PhysRevB.80.035332>.
- [125] I. S. Burmistrov and Ya. I. Rodionov. Charge relaxation resistance in the cotunneling regime of multichannel Coulomb blockade: Violation of Korringa-Shiba relation. *Phys. Rev. B*, 92(19):195412, 2015. ISSN 1098-0121. doi: 10.1103/PhysRevB.92.195412. URL <http://link.aps.org/doi/10.1103/PhysRevB.92.195412>.
- [126] Hiroyuki Shiba. The Korringa Relation for the Impurity Nuclear Spin-Lattice Relaxation in Dilute Kondo Alloys. *Prog. Theor. Phys.*, 54(4):967–981, oct 1975. ISSN 0033-068X. doi: 10.1143/PTP.54.967. URL <http://ptp.oxfordjournals.org/cgi/doi/10.1143/PTP.54.967>.
- [127] Travis Dirks, Yung-Fu Chen, Norman O Birge, and Nadya Mason. Superconducting tunneling spectroscopy of a carbon nanotube quantum dot. *Appl. Phys. Lett.*, 95(19):192103, 2009. ISSN 00036951. doi: 10.1063/1.3253705. URL <http://scitation.aip.org/content/aip/journal/apl/95/19/10.1063/1.3253705>.
- [128] Sebastian Pfaller, Andrea Donarini, and Milena Grifoni. Subgap features due to quasiparticle tunneling in quantum dots coupled to superconducting leads. *Phys. Rev. B*, 87(15):155439, apr 2013. ISSN 1098-0121. doi: 10.1103/PhysRevB.87.155439. URL <http://link.aps.org/doi/10.1103/PhysRevB.87.155439>.
- [129] J. Gramich, A. Baumgartner, and C. Schönenberger. Resonant and Inelastic Andreev Tunneling Observed on a Carbon Nanotube Quantum Dot. *Phys. Rev. Lett.*, 115(21):216801, nov 2015. ISSN 0031-9007. doi: 10.1103/PhysRevLett.115.216801. URL <http://link.aps.org/doi/10.1103/PhysRevLett.115.216801>.
- [130] Y.-Y. Liu, J. Stehlik, M. J. Gullans, J. M. Taylor, and J. R. Petta. Injection locking of a semiconductor double-quantum-dot micromaser. *Phys. Rev. A*, 92(5):

- 053802, 2015. ISSN 1050-2947. doi: 10.1103/PhysRevA.92.053802. URL <http://link.aps.org/doi/10.1103/PhysRevA.92.053802>.
- [131] L. P. Kouwenhoven, S Jauhar, J. Orenstein, P. L. McEuen, Y. Nagamune, J. Motohisa, and H. Sakaki. Observation of Photon-Assisted Tunneling through a Quantum Dot. *Phys. Rev. Lett.*, 73(25):3443–3446, dec 1994. ISSN 0031-9007. doi: 10.1103/PhysRevLett.73.3443. URL <http://link.aps.org/doi/10.1103/PhysRevLett.73.3443>.
- [132] R. H. Blick, R. J. Haug, D. W. van der Weide, K. von Klitzing, and K. Eberl. Photon-assisted tunneling through a quantum dot at high microwave frequencies. *Appl. Phys. Lett.*, 67(26):3924, 1995. ISSN 00036951. doi: 10.1063/1.114406. URL <http://scitation.aip.org/content/aip/journal/apl/67/26/10.1063/1.114406>.
- [133] Hong-kang Zhao and G. v. Gehlen. Mesoscopic transport through a normal-metalquantum-dotsuperconductor system with ac responses. *Phys. Rev. B*, 58(20):13660–13669, nov 1998. ISSN 0163-1829. doi: 10.1103/PhysRevB.58.13660. URL <http://link.aps.org/doi/10.1103/PhysRevB.58.13660>.
- [134] Qing-feng Sun, Jian Wang, and Tsung-han Lin. Photon-assisted Andreev tunneling through a mesoscopic hybrid system. *Phys. Rev. B*, 59(20):13126–13138, 1999. ISSN 0163-1829. doi: 10.1103/PhysRevB.59.13126. URL <http://link.aps.org/doi/10.1103/PhysRevB.59.13126>.
- [135] Argo Nurbawono, Yuan Ping Feng, and Chun Zhang. Electron tunneling through a hybrid superconducting-normal mesoscopic junction under microwave radiation. *Phys. Rev. B*, 82(1):014535, jul 2010. ISSN 1098-0121. doi: 10.1103/PhysRevB.82.014535. URL <http://link.aps.org/doi/10.1103/PhysRevB.82.014535>.
- [136] C. Whan and T. Orlando. Transport properties of a quantum dot with superconducting leads. *Phys. Rev. B*, 54(8):R5255–R5258, 1996. ISSN 0163-1829. doi: 10.1103/PhysRevB.54.R5255. URL <http://link.aps.org/doi/10.1103/PhysRevB.54.R5255>.
- [137] Sam Young Cho, Kicheon Kang, and Chang-Mo Ryu. Photon-assisted quasiparticle transport and Andreev transport through an interacting quantum dot. *Phys. Rev. B*, 60(24):16874–16879, dec 1999. ISSN 0163-1829. doi: 10.1103/PhysRevB.60.16874. URL <http://link.aps.org/doi/10.1103/PhysRevB.60.16874>.
- [138] Yigal Meir, Ned S Wingreen, and Patrick A Lee. Transport through a strongly interacting electron system: Theory of periodic conductance oscillations. *Phys. Rev.*

- Lett.*, 66(23):3048–3051, jun 1991. ISSN 0031-9007. doi: 10.1103/PhysRevLett.66.3048. URL <http://link.aps.org/doi/10.1103/PhysRevLett.66.3048>.
- [139] G. Feve, A. Mahe, J.-M. Berroir, T. Kontos, B. Placais, D. C. Glatthli, A. Cavanna, B. Etienne, and Y. Jin. An On-Demand Coherent Single-Electron Source. *Science (80-.)*, 316(5828):1169–1172, may 2007. ISSN 0036-8075. doi: 10.1126/science.1141243. URL <http://www.sciencemag.org/cgi/doi/10.1126/science.1141243>.
- [140] Thomas Sand Jespersen, Jens Paaske, Koji Muraki, Toshimasa Fujisawa, Jesper Nygård, Karsten Flensberg, Kasper Grove-Rasmussen, Jens Paaske, Koji Muraki, Toshimasa Fujisawa, Jesper Nygård, and Karsten Flensberg. Gate-dependent spin-orbit coupling in multi-electron carbon nanotubes. *Nat. Phys.*, 7(4):348–353, 2010. ISSN 1745-2473. doi: 10.1038/nphys1880. URL <http://arxiv.org/abs/1008.1600><http://dx.doi.org/10.1038/nphys880>.
- [141] András Pályi, P. R. Struck, Mark Rudner, Karsten Flensberg, and Guido Burkard. Spin-Orbit-Induced Strong Coupling of a Single Spin to a Nanomechanical Resonator. *Phys. Rev. Lett.*, 108(20):206811, may 2012. ISSN 0031-9007. doi: 10.1103/PhysRevLett.108.206811. URL <http://link.aps.org/doi/10.1103/PhysRevLett.108.206811>.
- [142] Audrey Cottet, Takis Kontos, and Benoit Douçot. Squeezing light with Majorana fermions. *Phys. Rev. B*, 88(19):195415, nov 2013. ISSN 1098-0121. doi: 10.1103/PhysRevB.88.195415. URL <http://link.aps.org/doi/10.1103/PhysRevB.88.195415>.
- [143] Udson C. Mendes and Christophe Mora. Cavity squeezing by a quantum conductor. *New J. Phys.*, 17(11):113014, nov 2015. ISSN 1367-2630. doi: 10.1088/1367-2630/17/11/113014. URL <http://stacks.iop.org/1367-2630/17/i=11/a=113014?key=crossref.900696fcbd718b4c0efd349c8c168178>.
- [144] Simon E Nigg, Rakesh P Tiwari, Stefan Walter, and Thomas L Schmidt. Detecting nonlocal Cooper pair entanglement by optical Bell inequality violation. *Phys. Rev. B*, 91(9):094516, mar 2015. ISSN 1098-0121. doi: 10.1103/PhysRevB.91.094516. URL <http://dx.doi.org/10.1103/PhysRevB.91.094516>.
- [145] Antti-Pekka Jauho, Ned S. Wingreen, and Yigal Meir. Time-dependent transport in interacting and noninteracting resonant-tunneling systems. *Phys. Rev. B*, 50(8):5528–5544, aug 1994. ISSN 0163-1829. doi: 10.1103/PhysRevB.50.5528. URL <http://prb.aps.org/abstract/PRB/v50/i8/p5528{ }1>.

- [146] Qing-feng Sun, Jian Wang, and Tsung-han Lin. Resonant Andreev reflection in a normal-metalquantum-dotsuperconductor system. *Phys. Rev. B*, 59(5):3831–3840, feb 1999. ISSN 0163-1829. doi: 10.1103/PhysRevB.59.3831. URL <http://link.aps.org/doi/10.1103/PhysRevB.59.3831>.
- [147] K Kang. Multiple Andreev reflections through an interacting quantum dot. *Phys. E Low-dimensional Syst. Nanostructures*, 5(1-2):36–40, 1999. ISSN 13869477. doi: 10.1016/S1386-9477(99)00034-X. URL <http://linkinghub.elsevier.com/retrieve/pii/S138694779900034X>.